How to stay in shape: Overcoming beam and mirror distortions in advanced gravitational wave interferometers

Charlotte Zoë Bond

A thesis submitted for the degree of

Doctor of Philosophy

Astrophysics and Space Research Group

School of Physics and Astronomy

College of Engineering and Physical Sciences

University of Birmingham

June 2014

Abstract

Einstein's General Theory of Relativity predicts *gravitational waves*, strains of space-time caused by objects moving through space. Detection of such waves is the goal of the Laser Interferometer Gravitational-Wave Observatory (LIGO), a completely new type of detector based on laser interferometry. The direct observation of a gravitational wave has so far eluded scientists due to noise in the detectors masking the small length changes caused by passing gravitational waves. LIGO is currently being upgraded to *Advanced LIGO*, with the aim to improve the sensitivity to gravitational waves by a factor of 10 across a wide range of frequencies. It is expected that the first direct detection of a gravitational wave will occur shortly after Advanced LIGO is brought online.

The upgrade to Advanced LIGO will significantly increase the complexity of the instrument, introducing more mirrors and significantly amplifying the circulating power. For Advanced LIGO to reach design sensitivity it is crucial that the behaviour of the interferometer in the presence of deviations from the design parameters is well understood. In particular we must understand the impact of distortions of the laser beam, such as those caused by interactions with mirrors which deviate from an ideal sphere. Many features of advanced detectors will have a strong effect on the shape of the beam: thermal aberrations of the mirrors; high finesse cavities which increase the interactions between the beams and distorted mirrors; and the addition of a signal recycling mirror. To predict the shape of the beam we require realistic models which can accurately model the distortions and trace them through complicated optical setups. This thesis details the modelling of beam and mirror distortions in such interferometers, applying this to the commissioning of Advanced LIGO and investigations of technologies for future detectors.

The model developed and used throughout this thesis is the modal model: using higher order Gaussian modes to describe distortions of the beam. The basis of this model is reported here and used to model Advanced LIGO. The model exploits the fact that a well behaved interferometer acts as a series of resonators for the fundamental Gaussian mode. Any small distortion of the beam can be described by a finite number of additional modes. Tests of the modal model against other methods are detailed, supporting the results and conclusions reported here.

An Advanced LIGO model was developed throughout my Ph.D. and here I document several specific commissioning tasks, related to spatial distortions of the beam. These tasks demonstrate the behaviour of the interferometer in various configurations (power recycled, dual recycled, with and without arm cavities) as well as answering specific questions. For example, modelling of the Livingston LIGO interferometer in the intermediate power recycled Michelson stage identified power loss at the beam-splitter as the explanation behind low power buildup in the interferometer. In another task the distortion of the output beam of the full Advanced LIGO configuration allowed acceptance of the coatings of the end test masses.

Modal models are also used to investigate technologies for future detectors. In this thesis I report a feasibility study into the higher order Gaussian mode LG_{33}, proposed as a potential input beam for future detectors to suppress mirror thermal noise. The degenerate nature of optical cavities for the resonance of higher order modes results in unacceptably low beam purity. The simulation results in this investigation are complimented by the derivation of an analytic expression which identifies mirror shapes which degrade the purity of LG_{33}, and other high order modes. This expression is used to derive mirror requirements for the future use of LG_{33} in a potential upgrade of Advanced LIGO or for the envisaged European detector: the Einstein Telescope.

For my Mum, Dad and little sister

Acknowledgements

Firstly I'd like to acknowledge my supervisor, Andreas Freise, who introduced me to the subject of gravitational wave detection when I was a first year undergraduate. Thanks for seeing my potential and for all the help and support you have given me. I consider myself very fortunate to have had Andreas as a supervisor, and I'd like to thank him for the many opportunities and interesting projects I've had over the years. Not only has Andreas pushed me to become a better researcher, but he has created a fun and welcoming group at the University of Birmingham, one which I am proud to have been a part of.

Many thanks go to the gravitational wave group in Birmingham, for their friendship as well as project help. To all my colleagues, past and present: Daniel Brown, Paul Fulda, Ludovico Carbone, Mengyao Wang, Frank Brückner, Rebecca Palmer, Keiko Kokeyama, Dee Lodhia, thanks and all the best in the future.

I'd like to give a special mention to Ludo Carbone, for all his help and patience in the lab, and for his continued friendship and supplies of Belgium beer. I'd also like to thank Paul Fulda for his help and invaluable encouragement throughout my Ph.D., especially during recent commissioning tasks. No acknowledgements would be complete without mentioning Dan Brown, without whom a lot of this work would not have been possible. Thanks for answering my many late night bug reports.

Many others at the University of Birmingham have helped me along the way, particularly David Stops, our go-to computing expert, and Alberto Vecchio. I also extend my gratitude to my colleagues in the LVC: Kentaro Somiya, Hiro Yamamoto, GariLynn Billingsley, Stefan Hild, Peter Veitch, David Ottaway and many others. Thanks also go to my examiners Jon Goldwin and Giles Hammond.

I've been lucky enough to make some great friends over the course of my Ph.D.: thanks to little Trevor Sidery, the sad man Carl Haster, Rory 'mmmmm' Smith and the gossip King Mark Burke for some unforgettable times in staff house. Also to Konstantinos 'special k' Kolokythas, Chris Collins, Mat Turnball, Dan Brown, Paul Fulda, Ludo Carbone, Chiara Mingarelli, Maggie Lieu, Kat Grover, Ben Aylott and Will Vousden.

For helping me to forget about physics, I'd like to thank all my friends in Birmingham, Witney and further afield. Particularly to my 'wife' Sophie Chipperfield, for copious amounts of wine and sympathy over the years. To my 139 peps, old and new, particularly the originals: girl Sam, Matt, Ben, Rich and Soph, thanks for distracting me from the waves. To Azumi, my old lab partner, and Bobby, I look forward to more evenings of good food, wine and gossip. And to my friends from home: Becky, Rachel, Claire, Karen, Lucy, Emma and Hannah.

I wouldn't be where I am today without the continued support of my family. This is for you. To my Mum who is always there to give advice thorough the highs and lows and keep me balanced on the important things in life; my Dad who first got me excited about maths and science, but always let me find my own path; and my little sister Rosie, the best sister who is always there for me. To Granny, Grandma and my extended family and to those who are no longer with us: my Grandad, the first Dr. Bond and my Grandpa, the one and only Lionel Bennett. I know you would have been so proud.

Contents

List of Figures

Chapter 1

Introduction

1.1 Gravitational waves

The existence of gravitational waves were predicted in 1916 as a consequence of Einstein's Theory of General Relativity [1]. These waves are often described as 'ripples' in space-time, predicted by the wave-like solutions of Einstein's field equations. These 'ripples' are distortions of space-time generated by large masses accelerating through space with some non-spherically symmetric motion. The effect of a passing gravitational wave on a ring of free test particles is illustrated in figure 1.1. Here the space between the particles is stretched and squashed at the frequency of the gravitational wave. The amplitude of such a wave is [2]:

$$h(r) = \frac{2G}{c^4}\frac{1}{r}\frac{\mathrm{d}^2 I}{\mathrm{d}t^2} \tag{1.1}$$

where G is the gravitational constant, c is the speed of light, r is the distance from the source and I is the quadrupole moment of the source. The quantity $\frac{\mathrm{d}^2 I}{\mathrm{d}t^2}$ is related to the mass of the source and the non-spherically symmetric component of its speed [3]. h is often referred to as the gravitational wave strain, a dimensionless quantity which describes how space is distorted by a passing wave. A measurement

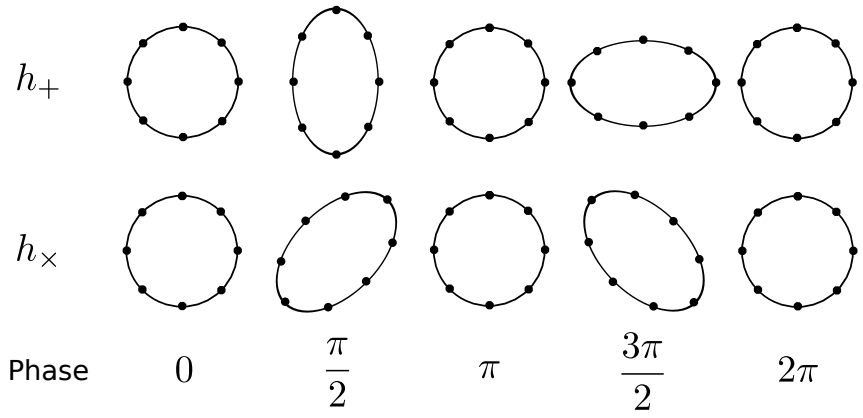

Figure 1.1: Diagram illustrating the effect of a passing gravitational wave on a ring of test particles. Space is 'stretched and squashed' perpendicular to the direction of propagation.

of length L will deviate by δl in the presence of a gravitational wave [2]:

$$\delta l = hL \tag{1.2}$$

From measurements of this change in length the amplitude of passing gravitational waves can be inferred. This is the basic premiss behind modern gravitational wave detectors: to directly measure h by detecting small changes in length over large distances.

1.1.1 Evidence for gravitational waves

Indirect evidence of gravitational waves was first presented in 1975 by Hulse and Taylor [4]. This evidence comes from observations of a binary star system, PSR B1913+16, which consists of a pulsar and another neutron star. The existence of the pulsar within this binary allows very accurate monitoring of the dynamics of the system. Observations carried out for over 30 years show a decay in the orbit, as the two stars spiral in towards each other. This loss of energy in the system matches the predicted energy lost through gravitational wave radiation. This is shown in figure 1.2 where the change in the orbital period is plotted, from 1975 to 2005 [5].

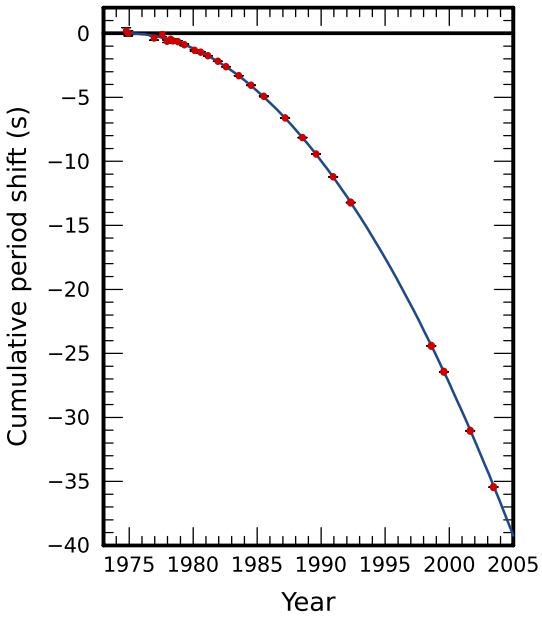

Figure 1.2: Shift in orbital period of the binary system PSR B1913+16 [4] over 30 years [5]. The observed data (red markers) matches the prediction of gravitational waves (blue trace) to within 0.2%.

The measured data agrees with the prediction of gravitational waves to within 0.2%. This is impressive evidence for gravitational waves, especially given the agreement of the measurement over such a long time period.

1.1.2 Sources of gravitational waves

The direct detection of a gravitational wave has so far eluded the scientific community due to the extremely small nature of the spatial disturbances caused by a gravitational wave. It is important to note the very small factor $\frac{G}{c^4} \sim 8 \times 10^{-45}$ in equation 1.1. To produce a gravitational wave strain of even 10^{-21} at the Earth the GW source must have considerable mass and be moving at relativistic speeds to overcome the stiffness of space-time. Such dramatic astrophysical events close enough for observation are rare and detection can become a waiting game.

Events involving black holes and neutron stars in binary in-spirals would be one potential class of source capable of producing such a strain. These compact bodies fulfil the requirements of massive objects and when interacting in a tight

binary produce the necessary speeds to generate large gravitational waves [2]. As the dynamics of such systems are well understood, from observations such as those made by Hulse and Taylor [4], their characteristic gravitational wave signal is also easier to search for in the measurement data. Black hole – black hole (BH – BH), neutron star – black hole (NS – BH) and neutron star – neutron star (NS – NS) inspirals are promising sources for initial detection. However, even these events will only cause a small variation in measurable length and we therefore require very accurate detectors to measure these small distortions.

Other potentially observable sources of gravitational waves include *continuous wave* sources, such as those which would be emitted from a rapidly rotating neutron star with 'mountains' on its surface [3]. In this case the mass of the star and speed of the rotation must be large to produce a sizeable wave, whilst the distortion of the surface satisfies the criteria that the motion is asymmetric. Other less well understood sources include the collapse of stars during supernova and the Stochastic background of gravitational waves left over from the Big Bang [2].

1.1.3 Ground based detectors

The direct detection of a gravitational wave has long been the goal of scientists across the world. Current detectors are ground based *interferometers* which very accurately measure changes in length over large distances. The gravitational wave community is an international collaboration based around a network of detectors positioned across the world. This includes the two LIGO detectors in America [6; 7], the Virgo detector in Italy [8] and GEO600 in Germany [9]. Currently under construction is KAGRA in Japan [10] and a LIGO detector is also destined for India within the next few years [11]. Individual gravitational wave detectors are sensitive to waves from a large fraction of the sky and provide virtually no directional information for short signals. The presence of multiple detectors allows for triangulation of gravitational

wave sources, using the observed time delay of a signal at different detectors to locate the probable source location in the sky [12]. For accurate triangulation an even global distribution would be an advantage. Multiple detectors are also required to boost the overall gravitational wave signal measured and to protect against false alarms in individual detectors.

The detection of gravitational waves will be significant for several reasons. Firstly, it will be a further confirmation of Einstein's General Theory of Relativity as a robust description of gravity and interesting from a purely theoretical point of view. Secondly, the detection of gravitational waves will have significant implications for astronomy: it will open up a new window on the universe. The gravitational wave spectrum will provide new information about different astrophysical phenomena, complimenting the electro-magnetic spectrum. For example, one of the most exciting sources for gravitational waves are black holes. Detection of GWs would allow direct observations of the dynamics and evolution of black holes. There is also some potential that some distant objects could be observed using GWs where the EM radiation is too faint. Finally, gravitational radiation reacts very weakly with matter, and so could carry virtually unaltered data from source to observer, with the exception of lensing effects.

1.2 LIGO

The direct detection of a gravitational wave has not been achieved with first generation detectors (ground-based interferometers). Several detectors are currently undergoing upgrades to become *second generation* or *advanced* detectors with a factor of 10 improvement in sensitivity. One such detector is the American Advanced LIGO detector, the second generation of the Laser Interferometer Gravitational-Wave Observatory (LIGO) [7]. LIGO consists of two interferometers, one in Livingston, LA and one in Hanford, WA. Advanced LIGO and other gravitational wave detectors

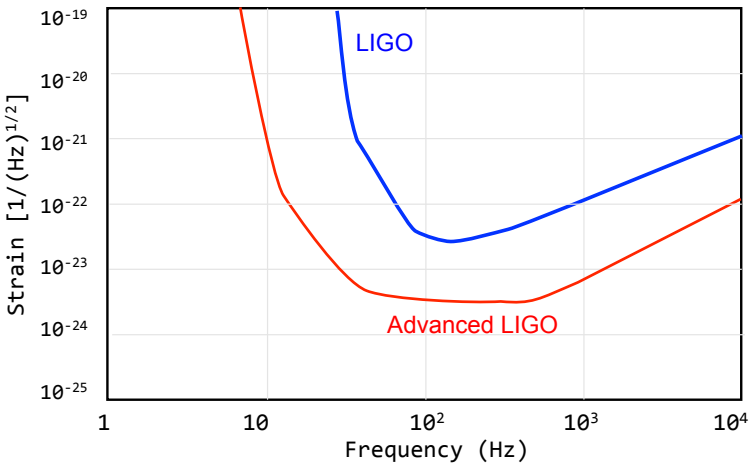

Figure 1.3: Predicted sensitivity curves for Enhanced and Advanced LIGO. Advanced LIGO aims to increase the sensitivity by a factor of 10 across a broad frequency band. Plot courtesy of Harald Lück.

are based on the structure and basic principles of a Michelson interferometer.

The original LIGO detector reached a peak sensitivity of around $2 \times 10^{-23} \frac{1}{\sqrt{\text{Hz}}}$ at around 200 Hz [7; 13]. LIGO was the most sensitive gravitational wave interferometer, due to the large distance ($\sim 4\,\text{km}$) over which the strain of space is measured. This peak sensitivity was achieved in *Enhanced* LIGO [14] which implemented several advanced technologies to improve on the sensitivity of Initial LIGO. Several of these technologies will be used in Advanced LIGO, such as higher laser powers, a DC readout scheme and output mode cleaners. Other important upgrades include the addition of a signal recycling mirror, larger beam sizes and using materials with improved optical properties.

The upgrades to LIGO aim to achieve a factor of 10 improvement in the sensitivity of the detector across a broad range of gravitational wave frequencies [15], see figure 1.3. In the following sections the principles of gravitational wave interferometry and the improvements in sensitivity for advanced detectors are outlined, providing a background to the work presented in this thesis.

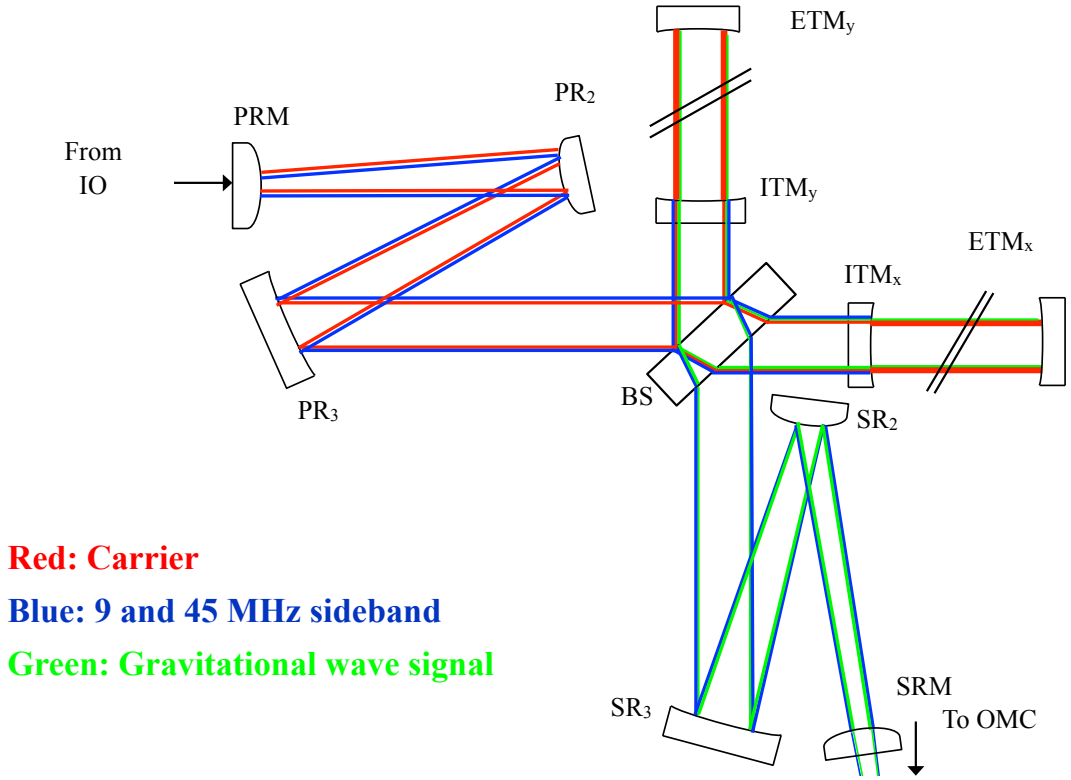

Figure 1.4: The core optics of the Advanced LIGO gravitational wave detector: a dual recycled, Fabry-Perot Michelson [16]. PR refers to power recycling, SR to signal recycling, BS to the beam-splitter, ETM to the end test masses and ITM to the input test masses. Each recycling cavity consists of three mirrors, the recycling mirrors (PRM and SRM) which reflect the beam back into the interferometer and 2 mirrors which make up the 'mode matching telescope' (PR_3/PR_2 and SR_3/SR_2). The red lines indicate the carrier light, the blue lines refer to the radio frequency sidebands used for control and the green lines refer to the signal sidebands.

1.2.1 Core optics

The configuration of the core optics of Advanced LIGO is shown in figure 1.4 [16]. The basis of the interferometer is the Michelson interferometer, with the addition of power and signal recycling and two mirror cavities in the arms. This configuration is chosen to enhance the effect of a gravitational wave on the output of the detector and reduce sources of noise in the interferometer.

Advanced LIGO and other ground based detectors are based on the *Michelson interferometer*, in which two light beams, which have travelled along different optical

paths, are interfered in order to extract the difference in phase between the two fields. In Advanced LIGO the central Michelson consists of a beam-splitter (BS) and input and end test masses (I/ETMs) which make up the *Fabry-Perot cavities*. The detector is designed with dual recycling: power recycling to enhance the power in the interferometer and signal recycling to either enhance the gravitational wave signal for a particular frequency of broaden the detector bandwidth. Initial LIGO incorporated power recycling, using a single mirror to reflect the light exiting the interferometer towards the input laser back into the detector. Advanced LIGO adds signal recycling and in both cases uses additional mirrors to mode match the beams between the main detector and the recycling mirrors, and to produce stable recycling cavities.

1.2.2 Michelson interferometer

Figure 1.5 shows a diagram of a simple Michelson interferometer, without arm cavities. The basic premiss of a Michelson is to compare the phase of the light travelling along the two arms of the interferometer. A change in length, such as that caused by a passing gravitational wave, will cause a change in phase in one or both of the light fields. As the phase cannot be directly measured the relative phase of the light fields is extracted from the interference of the beams at the output (anti-symmetric) port. The output signal for such a simple Michelson, with a 50:50 beam-splitter and completely reflective mirrors is [17]:

$$P_{out} = P_0 \cos^2 (\Delta\phi + \phi_{op}) \tag{1.3}$$

where P_0 is the input laser power and $\Delta\phi$ is the difference in phase between the light travelling in the x arm and the light traveling in the y arm. A change in phase in either arm will result in a change in this output signal and in general we can write $\Delta\phi = k\Delta L$. ϕ_{op} refers to the initial operating point of the interferometer,

the state when the phase is equal in both arms ($\Delta\phi = 0$). For gravitational wave interferometry, and other areas of precision measurement, the Michelson is operated on, or very near to, the dark fringe, performing a null measurement where any signal at the output should indicate the presence of a gravitational wave. In this representation $\phi_{op} = \frac{\pi}{2}$. The light at the output port is the differential (or anti-symmetric) measurement of the two arms whilst the light reflected back towards the laser is the common (or symmetric) light from the two arms.

A gravitational wave produces some time varying change in length of a particular path. Assuming optimal orientation of the gravitational wave the change in length is given by:

$$\delta L = L\ h(t) \tag{1.4}$$

where L is the unmodulated length and $h(t)$ is the time varying strain of the gravitational wave signal:

$$h(t) = h_0 \cos{(w_g t)} \tag{1.5}$$

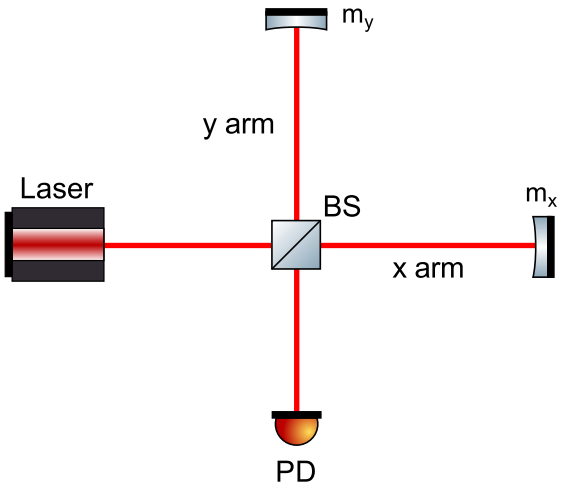

Figure 1.5: A simple Michelson interferometer. The beam-splitter (BS) splits the laser light onto two different paths: the x and y arms. The light in each arm is reflected back to the beam-splitter by a mirror ($m_{x/y}$). The input of the detector is the laser beam, entering to the left of the beam-splitter, often referred to as the input, or symmetric, port. The output of the detector is measured using a photodiode (PD) at the output, or antisymmetric, port, shown below the beam-splitter.

where h_0 is the amplitude of the gravitational wave and w_g is its angular frequency. The additional phase incurred by light during a round-trip of this path depends on this length change and the round-trip time, $\tau = \frac{2L}{c}$ [18]:

$$\begin{aligned}\delta\phi &= \frac{kL}{\tau} h_0 \int_{t-\tau}^{t} \cos\left(w_g t\right)\, \mathrm{d}t \\ &= \frac{wh_0}{2} \int_{t-\frac{2L}{c}}^{t} \cos\left(w_g t\right)\, \mathrm{d}t \\ &= \frac{wh_0}{w_g} \cos\left(w_g t - w_g \frac{L}{c}\right) \sin\left(w_g \frac{L}{c}\right)\end{aligned} \tag{1.6}$$

(see appendix A). It is this phase that gravitational wave interferometers aim to measure. For an optimally polarised gravitational wave the phase incurred in the y arm will have the same magnitude but opposite sign to that incurred in the x arm, maximising the signal at the output.

The phase modulation, $\delta\phi$, of the light in the arms will be very small. This modulation can be described as the introduction of two signal sidebands [17] (see appendix A). The majority of the light remains at the same frequency as the laser, while the effect of the gravitational wave signal is contained in sidebands at $f_0 \pm f_g$, where f_0 is the laser frequency and f_g is the frequency of the gravitational wave. On the dark fringe the carrier light is reflected back towards the laser, whilst the sidebands produced in each arm exit through the antisymmetric port. The amplitude of the sidebands are proportional to $\frac{wh_0}{w_g} \sin\left(\frac{w_g L}{c}\right)$, so to maximise the output for a particular frequency, an arm length of $L = \frac{c}{4f_g}$ would be best. As most strong gravitational wave signals are expected at frequencies below 1 kHz, this leads to an optimal arm length > 75 km. Even optimising in this way results in very small phase changes (10^{-9} rad for $h_0 = 10^{-21}$). This small phase change is difficult to measure when other effects, *noises*, easily cause such phase changes. Arm lengths of this magnitude are not feasible for ground based detectors but should be as long as possible. Currently the longest detector is LIGO, with arm lengths of 4 km. It

is important to note that the sideband amplitude becomes 0 when $f_g = \frac{c}{2L}$, i.e. the period of the gravitational wave is equal to, or a multiple of, the round-trip light travel time.

1.2.3 Fabry-Perot arm cavities

As described above, the long arms required to maximise a gravitational wave signal are impractical for current detectors. To increase the time the light spends inside the arms, increasing the interaction with gravitational waves and the signal sidebands, we add input test masses to form Fabry-Perot cavities (figure 1.6). These are linear cavities consisting of two mirrors which act as a resonator for the laser light. Light from the beam-splitter is incident on the ITM (input mirror) which allows a proportion of the light to enter the cavity. The light power builds up in the cavity and in the case of gravitational wave detectors the mirrors are chosen to achieve a very high circulating power. The reflective properties of the cavity can be described by the finesse of a cavity, which determines the power build-up. For a high finesse cavity [17]:

$$F \approx \frac{\pi}{1 - r_I r_E} \tag{1.7}$$

Figure 1.6: A Fabry-Perot cavity, as used in place of the end mirrors in Michelson interferometers for gravitational wave detectors. The cavity acts as a resonator, enhancing the light inside. The light reflected and transmitted from the cavity depends on the optical properties of the two mirrors: the input test mass (ITM) and end test mass (ETM).

r_I and r_E refer to the reflectivity of the input and end test masses. The power in the gravitational wave sidebands is proportional to the power in the arms so to maximise the gravitational wave signal the length and finesse of the arm cavities should be made suitably large. The arm cavities of Advanced LIGO are 4 km long with a finesse of 450.

1.3 Upgrading to Advanced LIGO

The detection of a gravitational wave has so far been limited by noise in the interferometer, masking the signal from a gravitational wave. Advanced LIGO aims to decrease these noise effects on the output signal by a factor of 10 [15]. In figure 1.7 the different noises for Advanced LIGO are plotted against frequency. The majority of the frequency band is limited by quantum noise: radiation pressure noise at low

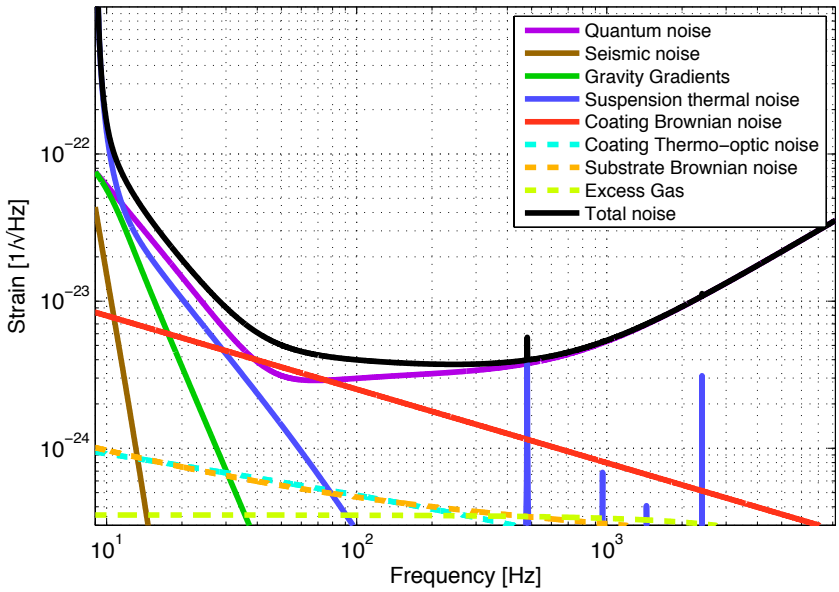

Figure 1.7: Sources of noise in Advanced LIGO at different frequencies, for broadband signal recycling during high power operation. The sensitivity is limited at most frequencies by quantum noise: radiation pressure noise at low frequencies and shot noise at high frequencies. At around 50 Hz coating Brownian thermal noise is the limiting noise source, with suspension thermal noise, seismic noise and gravity gradient noise forming a wall at around 10 Hz [19].

frequencies and shot noise at high frequencies. Brownian thermal noise of the test masses is a limiting factor mid band and seismic, gravity gradient and suspension thermal noise limit the detection at very low frequencies.

1.3.1 Reducing noise

Seismic and gravity gradient noise

At frequencies below 10 Hz the dominant noise is seismic noise originating from vibrations of the ground surrounding the detector which are transferred to the test masses via their suspensions. In Advanced LIGO the suspension systems are formed of four stage pendulums which aim to decouple vibrations in the desired frequency band from the test masses. This limiting seismic cutoff frequency is reduced from ~ 40 Hz in Initial LIGO, to 10 Hz [20; 21] using these sophisticated suspensions.

Gravity gradient noise is a result of variations in gravitational forces experienced by the test masses. Changes in the mass distribution around the mirrors, such as seismic activity, results in changing gravitational forces acting on the mirrors and variations in displacement. In first generation detectors gravity gradient noise was not a significant noise source, but due to the reduction of other noises at low frequencies gravity gradient noise should approach the overall noise level at frequencies lower than 10 Hz [22].

Thermal noise

In the $10 - 200$ Hz range one of the main noise sources is thermal noise This incorporates several different types of thermal noise, but the dominating effects are suspension thermal noise at low frequencies and coating Brownian noise mid-band (see figure 1.7).

The pendulum and violin modes of the mirror suspensions can be excited by thermal vibrations, which couple into mirror displacement [23; 24]. To reduce the

suspension noise to similar levels as the radiation pressure noise (see below) fused silica suspensions are used in place of the steel wires used in Initial LIGO. This high quality material confines excitation of the modes of the suspensions to a narrow frequency band, resulting in sharp peaks in suspension thermal noise at specific frequencies (see figure 1.7).

Coating Brownian thermal noise is expected to be a limiting source of noise at around 100 Hz in advanced detectors. The brownian motion of the atoms in the mirror coatings excite the elastic modes of the mirror surface, introducing apparent fluctuations of the mirror position, as seen by the incident laser beam [25; 26]. In Advanced LIGO larger beams in the arms more effectively average over the thermal distortions of the mirror surfaces than the small beams used in Initial LIGO, reducing thermal noise in the interferometer. In chapter 3 this particular noise is discussed in more detail, in the context of using higher order Laguerre-Gauss modes to reduce the thermal noise even further.

Quantum noise

Quantum noise is expected to be the limiting noise source at most frequencies above 10 Hz. Quantum noise in interferometers consists of radiation pressure noise (low frequencies) and shot noise (high frequencies). Radiation pressure noise arises from the transfer of momentum to the mirrors when photons are reflected and absorbed. The transfer of momentum results in motion of the mirrors and quantum fluctuations in the amplitude of light give rise to the radiation pressure noise. The greater the power the greater the imparted momentum, so radiation pressure noise increases with high light power. Radiation pressure noise is reduced to similar levels as seismic and suspension thermal noise at low frequencies in Advanced LIGO by using heavy mirrors (40 kg).

At most frequencies (above 100 Hz) the sensitivity is limited by shot noise. This is a sensing noise due to the quantum uncertainty of the phase of the photons hitting

the output photodiode. The shot noise, relative to the signal, in Advanced LIGO is reduced with high light power in the signal. This is achieved by increasing the input laser power by a factor of 10 (to 125 W), increases in the arm cavity finesse and the addition of a signal recycling mirror to increase the build up of power in the signal sidebands in Advanced LIGO [15].

1.3.2 Dual recycling

In Initial LIGO power recycling was used to increase the power in the interferometer, increasing the signal-to-noise ratio (SNR) for the shot noise. In Advanced LIGO both power and signal recycling are used, so called *dual recycling*. The recycling cavities are not near instability, as in Initial LIGO, but use mode-matching telescopes as seen in figure 1.4 [27].

Power recycling

As the shot noise is the limiting noise source over most of the frequency band in gravitational wave detectors it is necessary to significantly increase the power in advanced detectors. This is partially achieved using a higher laser power. However, as the interferometer is operated on the dark fringe the circulating power (minus the small amount in the signal sidebands) is reflected back towards the laser. Rather than dump this carrier light a partially reflective mirror (the power recycling mirror) is placed between the input optics and the main interferometer to reflect the beam back into the detector. This combination of high input laser power and power recycling leads to an anticipated $\sim$1 MW circulating in the arms [16].

Signal recycling

A major upgrade to LIGO is the introduction of a signal recycling mirror at the detector output. This mirror can be tuned for different types of operation: signal

recycling or broadband [3; 28]. For broadband operation (as shown in figure 1.7) the signal recycling cavity is tuned to effectively reduce the finesse of the arm cavities for the signal sidebands, increasing the bandwidth of the detector at the expense of peak sensitivity. For signal recycling the cavity is tuned to be resonant for a specific frequency, allowing the tailoring of the interferometer response for expected signals. One expected source of gravitational waves are neutron star – neutron star (NS – NS) in-spiral signals for which the interferometer can be operated with a narrower, more sensitive frequency band for observations of these specific signals [29] . The detector can be operated without the signal recycling mirror, considered as the initial mode of operation with the advantage of a simpler control scheme.

1.3.3 Mode cleaners

Input mode cleaner

LIGO uses an *input mode cleaner* placed before the laser beam enters the main interferometer [30; 31]. This is an optical cavity which filters the laser beam, stabilising the frequency of the light as the cavity acts as a resonator for a specific frequency. The light is also cleaned of spatial distortions as the beam coming directly from the laser is not the pure Gaussian beam the interferometer is designed for. The mode cleaner transmits a very pure Gaussian beam, as higher order spatial modes are not resonant in this cavity. This includes reducing the 'beam jitter', fluctuations in the centring of the beam.

Output mode cleaner

An upgrade introduced in Enhanced LIGO, an *output mode cleaner*, is used again in Advanced LIGO to filter the output of the interferometer of undesirable fields, whilst transmitting the field containing the gravitational wave signal to the output photodiode. This consists of an optical cavity with carefully chosen parameters to

filter out spatial modes of the light field entering the anti-symmetric port (created through interactions with the surface distortions of mirrors in the detector) as well as the radio frequency control sidebands [32].

1.3.4 Signal readout

The power in the gravitational wave signal sidebands will be very small, so to detect them on the photodiode they are beaten against a local oscillator [29]. To prevent excess phase noise the local oscillator is provided by carrier light leaking into the dark port [33], by applying some small offset (*DC offset*) from the dark fringe. Advanced LIGO will use 100 mW of local oscillator [34].

1.4 Project motivation

The work detailed in this thesis focuses on the potential impact of distortions of the light fields in advanced detectors on the projected sensitivity. Previous models used to predict the sensitivity of Advanced LIGO assume that the beams are pure, fundamental Gaussian beams. In practice the beams will be distorted, as interactions with real mirrors and imperfect optics will shape the beams in the detectors. We must include the effects of these distortions in our models. Understanding the impact of these distortions is particularly important for commissioning of advanced interferometers and designing future detectors.

The operation of gravitational wave interferometers depends on the interference of light, whether this is constructive interference of the carrier to build up power in the detector, or the beating of sidebands with the carrier light for control of the interferometer (radio frequency sidebands) and readout of the gravitational wave signal (signal sidebands). Spatial distortions of the beam can lead to:

- Lower power build up in the central interferometer.

- A degraded overlap between the leaked carrier and signal sidebands at the detection port: reduced power in the readout signal.
- Additional noise coupled to the detector photodiode.
- Complications for control of the interferometer.

We need accurate, efficient models to predict the effects of these distortions. It is important these models are ready for Advanced LIGO commissioning, as several crucial upgrades from Enhanced LIGO will have a strong effect on beam shape distortions:

- Thermal aberrations. Extremely high power in the arm cavities ($\sim 1\,\mathrm{MW}$) will heat the test masses, warping the reflective surfaces and creating lensing within the mirrors.
- Higher finesse. The higher finesse of the arm cavities and power recycling cavity will result in greater interactions between the light fields and distorted optics.
- Signal recycling. The introduction of a mirror at the anti-symmetric port will have a significant effect on the distortion of the output beam.

1.5 Thesis overview

The work detailed in this thesis falls into three categories: the development of models for current and future use in gravitational wave interferometry; commissioning of Advanced LIGO; and work towards future detection techniques.

In chapter 2 the approach used throughout this thesis is outlined: the modal model. All results presented here use this method, which uses higher order modes to describe the effects of beam distortions. In this chapter the behaviour of different

interferometer configurations in the presence of mirror surface distortions are investigated, building from individual optics to the full Advanced LIGO dual recycled configuration. A large proportion of this chapter will appear shortly in the Living Review article *Interferometer Techniques for Gravitational-Wave Detection* [35].

Chapter 3 details work carried out for future GW detectors, specifically the potential of reducing thermal noise using higher order Laguerre-Gauss beams. In this investigation it was demonstrated that the degenerate nature of optical cavities for higher order Gaussian modes results in highly distorted beams in the arm cavities. I derived an analytic expression to calculate the mirror requirements for the use of such a mode. The results of this investigation were published in [36] and have been highly influential in the field, with this analytic approach adopted in [37] and [38].

The model modal was used throughout this thesis, in the form of the interferometer simulation tool FINESSE [39]. During my Ph.D. I helped develop FINESSE, rigourously testing it against analytics and other simulation methods. The results of these tests and other technical information relevant to the simulations carried out in this thesis are reported in chapter 4.

Finally, in chapter 5 the results of various commissioning tasks I have lead, or been involved with, are summarised. These tasks combine to form an understanding of the behaviour of the overall interferometer in the presence of beam distortions as well as answering specific questions, for example accepting the coatings of the end test masses. These results are published in a number of dedicated LIGO documents: [40; 41; 42; 43; 44].

Chapter 2

Modelling realistic interferometers with higher order modes

For the commissioning of advanced interferometers, and the design of future gravitational wave detectors, their behaviour in the presence of distorted mirrors and beams must be well understood. To model the effect of beam shape distortions, and to understand their impact on interferometer performance, I use the modal model. This chapter details this particular approach: expanding beam distortions in terms of higher-order Gaussian modes. In particular we focus on two sets of complete functions, Hermite-Gauss and Laguerre-Gauss modes, as a method for describing distortions mathematically. This approach can give accurate and intuitive results, when used appropriately, to describe the performance of gravitational wave detectors in the presence of mirror surface distortions and other spatial aberrations. This decomposition via Gaussian modes will be used as the main tool throughout the investigations detailed in this thesis. The extensive work on modal methods and the beam shape behaviour of advanced GW detectors detailed here will be published in the upcoming Living Review *Interferometer Techniques for Gravitational-Wave Detection* [35].

This chapter serves to describe the simulation methods used throughout my

thesis, as well as overview the behaviour of advanced gravitational wave detectors in the presence of defects which affect the shape of the beam. These investigations build on simple defects, misalignment and mode mismatch, to include the effects of thermal distortions and lensing in the interferometer test masses. The effects on simple interferometer subsystems are investigated, building to the full dual recycled Advanced LIGO configuration and the phenomenon of *mode healing*, as reported at the 2013 Amalid conference [45].

2.1 Laser beams as Gaussian modes

2.1.1 The fundamental beam

The beam produced from a real laser is not a plane wave, but has some intensity distribution, typically a roughly circular beam with a bright spot near the centre. For an idealised laser with just one frequency component the light field can be described as [17]:

$$E(x, y, z) = u(x, y, z) \exp(-\mathrm{i}\, kz) \tag{2.1}$$

where k is the wavenumber of the laser light, z is the distance along the optical axis and $u(x, y, z)$ describes the spatial properties of the field. An ideal laser beam would resemble the intensity pattern of a *Gaussian beam*. Figure 2.1 shows the intensity and amplitude distribution of a typical Gaussian beam, often characterised by the beam spot size, w, the radius at which $\sim 86\%$ of the light power is contained (the beam intensity drops to $\frac{1}{e^2}$).

The use of cavities in advanced interferometers provides the basis for the mathematical description of laser beam shapes as Gaussian modes. A well designed cavity is a perfect optical resonator for a particular Gaussian mode. The beams spot size, w, determines the the width of the beam and the intensity distribution of a beam

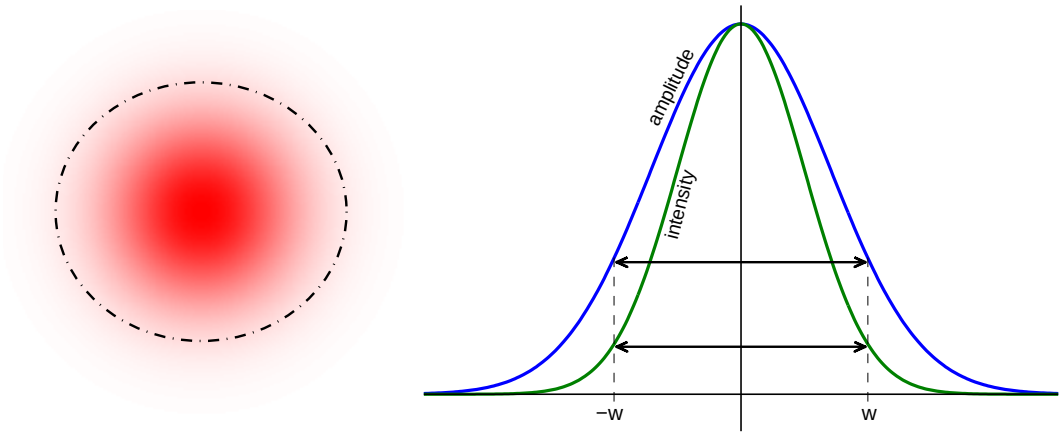

Figure 2.1: A typical laser beam intensity pattern (left) and the intensity and amplitude distributions of a normalised Gaussian beam (right). A Gaussian beam is characterised by its spot size, w, the radius at which the intensity falls to $\frac{1}{e^2}$ ($\sim 14\%$) of the peak intensity.

with total power P is given by [46]:

$$I(r,z) = \frac{2P}{\pi w^2(z)} \exp\left(-\frac{2r^2}{w^2(z)}\right) \tag{2.2}$$

As the beam propagates the beam spot size changes, with the minimum size known as the *beam waist*.

The intensity and shape of the laser beam are only one aspect of the light field. In the case of Gaussian modes the wavefront, or phase front, of the beam is curved and is expressed by a radius of curvature, R_C. As the beam propagates the curvature of the wavefront changes, becoming flat at the waist. To achieve perfect resonance in an optical cavity the curvature of the wavefront must match the curvature of the mirrors at their positions on the optical axis. The beam whose curvatures match the mirrors of a cavity is the cavity eigenmode. In figure 2.2 an optical cavity as a Gaussian beam resonator is illustrated, where the beam is the cavity eigenmode. The symmetric cavity geometry requires the beam waist to be located at the centre of the cavity.

Including the phase of the Gaussian beam, the transverse component of the

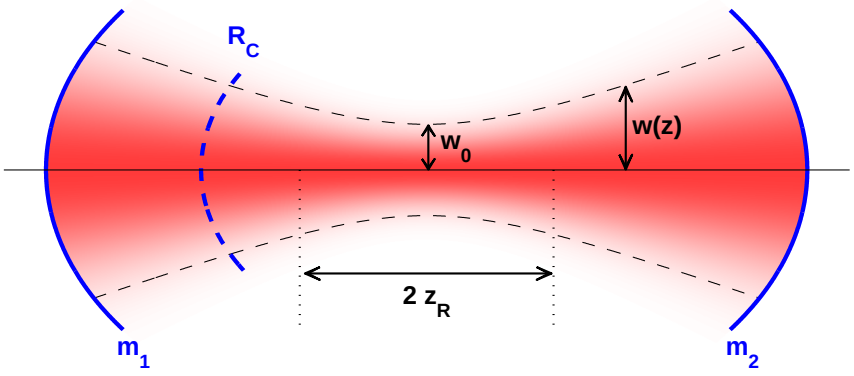

Figure 2.2: A Gaussian beam resonating in a two mirror cavity formed by m_1 and m_2. The intensity of the beam is shown in red, illustrating the change in beam size as the beam propagates. The smallest beam spot size is the waist, w_0. The radius of curvature of the beam wavefront is shown in blue (exaggerated for illustration). The eigenmode of the cavity will have a wavefront R_C which matches the curvature of the two mirrors. Also shown is the Rayleigh range, z_R, the distance which encompasses the near field.

normalised light field is given by [46]:

$$u(x,y,z) = \sqrt{\frac{2}{\pi}}\frac{1}{w(z)}\exp\left(\mathrm{i}\,\psi(z)\right)\exp\left(-\mathrm{i}\,k\frac{x^2+y^2}{2R_C(z)} - \frac{x^2+y^2}{w^2(z)}\right) \tag{2.3}$$

Such a beam is known as the *fundamental Gaussian beam*, or 00 mode, to distinguish it from higher-order Gaussian modes we will introduce later. A generic field u should have units of, for example, the electric field (for agreement with equation 2.1). However, a common convention in interferometery is to give the light field the units of $\sqrt{W}/m$. The power in any light field is then simply:

$$P = AA^* \tag{2.4}$$

where A is the amplitude of the light field. The normalised field shown in equation 2.3 has an amplitude of $1\sqrt{W}$.

The beam spot size depends on the position along the optical axis and the beam

waist:

$$w(z) = w_0\sqrt{1 + \left(\frac{z}{z_R}\right)^2} \tag{2.5}$$

where z_R is the Rayleigh range, the distance around the beam waist in the near field:

$$z_R = \frac{\pi w_0^2}{\lambda} \tag{2.6}$$

In the far-field, at a distance much greater than the Rayleigh range from the waist, the equation for the beam spot size becomes linear:

$$w(z) \approx w_0\frac{z}{z_R} = \frac{z\lambda}{\pi w_0} \tag{2.7}$$

The wavefront of the beam is described by a radius of curvature which changes as the beam propagates:

$$R_c(z) = z + \frac{z_R^2}{z} \tag{2.8}$$

At the beam waist ($z = 0$) the wavefront is flat ($R_C = \infty$). As the beam propagates through the far-field the wavefront becomes more curved. In the far field $R_C \approx z$. The final phase component of the light field is the *Gouy phase*:

$$\psi(z) = \tan^{-1}\left(\frac{z}{z_R}\right) \tag{2.9}$$

Often, when considering a particular beam, with a given curvature and size, we refer to the *Gaussian beam parameter*, q, a complex entity which contains all the information about the beam at a particular position:

$$q(z) = \mathrm{i}\, z_R + z \quad \text{or} \quad \frac{1}{q(z)} = \frac{1}{R_C(z)} - \mathrm{i}\,\frac{\lambda}{\pi w^2(z)} \tag{2.10}$$

2.1.2 Cavity stability

There are only particular combinations of cavity parameters (length and mirror curvatures) which form a stable resonator for a Gaussian beam. Small beam spot sizes diverge much faster than large spots, so require shorter cavities to avoid the beams becoming too large. Large beams diverge much less rapidly and can have longer stable cavities. This is one reason for the large beams in gravitational wave detectors, due to the long arms required to maximise the gravitational wave signal. The stability parameter, for an individual mirror is [46]:

$$g = 1 - \frac{L}{R_C} \tag{2.11}$$

where L is the length of the cavity and R_C is the radius of curvature of the mirror. For a two mirror cavity the overall stability is given by the product of the individual g-factors, $g_1 g_2$. A stable cavity has $0 \leq |g_1 g_2| \leq 1$.

2.2 Describing beam distortions with higher order modes

In an ideal interferometer the laser beams would be perfect fundamental Gaussian modes, with curvatures matching those of the mirrors they interact with. Distortions from these ideal beams can impact the interferometer performance, reducing the power buildup and coupling extra noise to the detection photodiode. In a real interferometer there are many aspects which affect the shape of the beam, distorting it from the typical round Gaussian. To model these distortions different beam shapes can be described by *higher order modes*.

Simple imperfections of a Gaussian beam can be described by the addition of a single higher-order mode (HOM). Higher order modes have the same basic proper-

ties of the fundamental Gaussian beam, with two exceptions: HOMs have different intensity patterns from the simple spot of the 00 mode and different order modes pick up extra multiples of the Gouy phase as they propagate. An example of a simple distortion is a misaligned beam. A Gaussian beam whose centre has been shifted from the optical axis can be described by the addition of a small amount of an order 1 Hermite-Gauss mode. The left panel in figure 2.3 illustrates this. This distortion is a first order effect. As long as the misalignment is small it can be described by this single order 1 mode. A larger misalignment requires more HOMs to accurately recreate the distorted beam.

Another simple imperfection is known as a mode-mismatch. This refers to a change in the spot size of a Gaussian beam, or its radius of curvature. This effect can be described by the addition of a single order 2 Laguerre-Gauss mode, LG_{10}. Such an effect is illustrated in the right panel of figure 2.3. The combination of LG_{00} and LG_{10} results in a Gaussian beam with a smaller or larger spot size. As with misalignment, the greater the distortion effect the more higher order modes

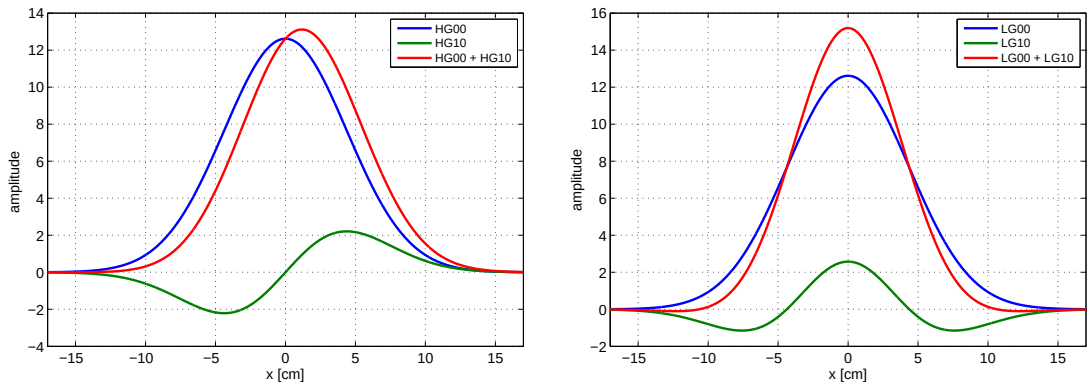

Figure 2.3: **Left:** Amplitude distributions of a fundamental Gaussian beam (HG_{00}), order 1 Hermite-Gauss beam (HG_{10}) and sum of the two modes. The resulting sum is a good description of a misaligned fundamental beam. The majority of the power is in the 00 mode, with 4% power in the order 1 mode. **Right:** Amplitude distributions of a fundemental Gaussian beam (LG_{00}), order 2 Laguerre-Gauss beam (LG_{10}) and sum of the two modes. The sum is a good description of a fundamental Gaussian beam with a smaller beam spot size. The power in the order 2 mode is 4% of the total 1 W power.

are required to recreate the field accurately.

Misalignment and mode-mismatch are two examples of very simple beam distortions, which can be described using one higher-order mode. More complicated distortions of the beam require many more modes.

2.3 Higher-order modes

2.3.1 Hermite-Gauss modes

A suitable set of modes to explain distortions with rectangular symmetry are the Hermite-Gauss (HG) modes. These are a set of orthogonal functions with the same basic properties as the fundamental beam, but with different intensity patterns. The HG modes are characterised by indices n and m, which refer to the number of dark fringes imposed on the Gaussian beam in the x and y directions. $n+m$ is the order of the mode, with n, $m \geq 0$. The amplitude distributions of some of these modes are shown in the left panel of figure 2.4. The fundamental mode is represented by $n = 0$, $m = 0$. As discussed previously, the addition of an HG_{10}/ HG_{01} mode can describe a first order distortion in x/y. Higher order distortions can be described by higher-order modes. The complete form of the Hermite-Gauss modes is [17; 47]:

$$u_{nm}(x,y,z) = \frac{1}{\sqrt{2^{\,n+m-1}\; n!\; m!\; \pi}} \frac{1}{w(z)} \exp\left(\mathrm{i}\,(n+m+1)\psi(z)\right) \\ H_n\left(\frac{\sqrt{2}x}{w(z)}\right) H_m\left(\frac{\sqrt{2}y}{w(z)}\right) \exp\left(-\mathrm{i}\,\frac{k(x^2+y^2)}{2R_C(z)} - \frac{x^2+y^2}{w^2(z)}\right) \tag{2.12}$$

where the main differences to the 00 mode (equation 2.3) are highlighted. H_n refer to the Hermite polynomials and give the HG modes their specific beam shape. The other crucial difference from the 00 mode is the additional multiples of the Gouy phase. The beam spot size, w, is still the radius at which the 00 intensity drops to $\frac{1}{e^2}$, with all modes in the same family defined by this spot size and sharing the

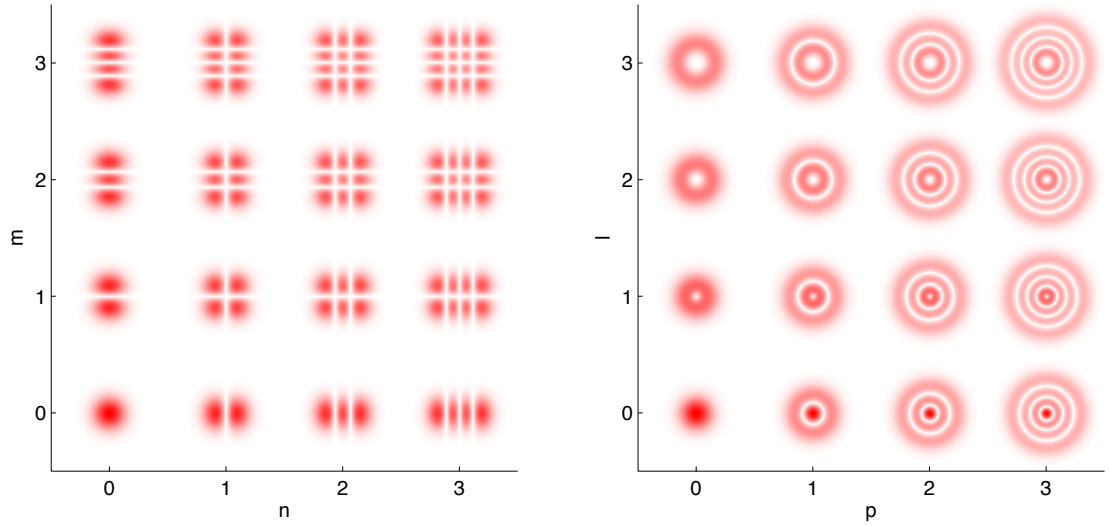

Figure 2.4: Amplitude distributions of the first Hermite-Gauss (left) and Laguerre-Gauss modes (right). The Hermite-Gauss modes are described by indices n and m, which refer to the dark fringes in x and y. The Laguerre-Gauss modes are described by radial index p, the number of radial dark fringes and azimuthal index l, which gives the width of the central dark spot and the spiral phase. The 00 modes represent the fundamental mode.

same wavefront curvature. However, as HOMs have different intensity distributions w does not correspond to an intensity of $\frac{1}{e^2}$ for each mode. The parameters w, z_R, ψ and R_C are given by the same relations as for the fundamental mode (see section 2.1.1).

2.3.2 Laguerre-Gauss modes

For distortions with spherical symmetry, such as mode-mismatch, the Laguerre-Gauss (LG) modes are the most suitable. These modes are described by radial index p, which determines the number of radial dark fringes and azimuthal index l, which determines the width of the central dark spot and the spiral phase of the mode. The order of the LG modes is given by $2p + |l|$, with $p \geq 0$. The amplitude distributions of the first few LG modes are shown in the right panel of figure 2.4.

The LG modes are given by [17]:

$$u_{pl}(r,\phi,z) = \frac{1}{w(z)}\sqrt{\frac{2p!}{\pi(|l|+p)!}}\exp\left(\mathrm{i}\left(2p+|l|+1\right)\psi(z)\right) \\ \left(\frac{\sqrt{2}r}{w(z)}\right)^{|l|} L_p^{|l|}\left(\frac{2r^2}{w^2(z)}\right)\exp\left(-\mathrm{i}\,\frac{kr^2}{2R_C(z)} - \frac{r^2}{w^2(z)} + il\phi\right) \tag{2.13}$$

with the main differences from the 00 mode highlighted. $L_p^{|l|}$ refer to the Laguerre polynomials which, along with the factor $\left(\frac{\sqrt{2}r}{w(z)}\right)^{|l|}$, give the modes their unique shape. Again there are extra multiples of the Gouy phase, related to the order of the mode. In addition to this there is an additional spiral phase, related to the azimuthal index l. Note that this is the only component of the mode which depends on the sign of l. w, ψ and R_C are given by the same realations for the fundamental mode (see section 2.1.1).

2.3.3 Higher-order mode expansion

Any paraxial beam can be expressed as a sum of Hermite or Laguerre-Gauss modes. An expansion, in terms of Hermite-Gauss modes, of the arbitrary field $u(x,y,z)$, can be written as [17]:

$$u(x,y,z) = \sum_{n,m} c_{nm} u_{nm}(x,y,z) \tag{2.14}$$

c_{nm} refer to coefficients which describe the amplitude and phase of each HG mode in the field $u(x,y,z)$. The Hermite-Gauss (and Lagurre-Gauss) modes are orthonormal so the coefficients can be calculated from an inner product with the relevant HG (or LG) mode:

$$c_{nm} = \int_{-\infty}^{\infty}\int_{-\infty}^{\infty} u(x,y,z)\; u^*_{nm}(x,y,z)\;\mathrm{d}x\;\mathrm{d}y \tag{2.15}$$

In the same way any HG mode can be expressed as a sum of LG modes of the same order, and vice versa, a convenient conversion for some simulations. An LG mode can be expressed as (see appendix B.1, [48]):

$$u_{p,l}^{LG}(x,y,z) = \sum_{k=0}^{N} (-1)^p (\mp \mathrm{i})^k \; b(|l|+p,p,k) \; u_{N-k,k}^{HG}(x,y,z) \tag{2.16}$$

where $N = 2p + |l|$ is the order of the mode, $\mp$ is $-\mathrm{sign}(l)$ and b are real coefficients given by:

$$b(n,m,k) = \sqrt{\frac{(N-k)!k!}{2^N n!m!}} \; (-2)^k P_k^{n-k,m-k}(0) \tag{2.17}$$

$P_n^{\alpha,\beta}$ are the Jacobi polynomials, calculated as:

$$P_n^{\alpha,\beta}(x) = \frac{1}{2^n} \sum_{j=0}^{n} \begin{pmatrix} n+\alpha \\ j \end{pmatrix} \begin{pmatrix} n+\beta \\ n-j \end{pmatrix} (x-1)^{n-j} (x+1)^j \tag{2.18}$$

Similarly the HG modes can be expressed as a sum of LG modes:

$$U_{n,m}^{HG}(r,\phi,z) = \sum_{j=0}^{N} (-1)^p (\pm \mathrm{i})^m \; b(|l|+p,p,m) \; U_{p,l}^{LG}(r,\phi,z) \tag{2.19}$$

where $l = 2j - N$, $p = \frac{1}{2}(N - |2j - N|)$, $N = n + m$ and $\pm$ refers to the sign of l. The coefficients b are in the same form as given in equation 2.17.

When expressing an individual LG mode as a sum of HG modes, or vice versa, only a finite number of modes are needed for a complete expansion: the modes of the same order as the target mode. For example, the order 2 mode LG_{10} is described only by the order 2 Hermite-Gauss modes. To describe some generic beam as a sum of modes could require a large number of higher order modes. This is inelegant and does not make for good understanding of beam behaviour. The reason we can use such an expansion for gravitational wave interferometers is that the eigenmodes formed by the optical cavities will act as resonators for light in the cavity eigenmode,

filtering out most of the light in higher-order modes. For such well behaved systems the light fields can be described by a finite number of modes.

The key to expanding a beam as a finite sum of HOMs is to select the appropriate Gaussian beam parameter for the expansion. In the case of gravitational wave detectors the best beam parameters are, generally, the eigenmodes of the cavities. As the light in the eigenmodes will be enhanced, the expansion should require fewer higher-order modes to recreate the real beams. In *modal models* any defects in the interferometers, such as mode-mismatches, misalignments and mirror surface distortions, are described as coupling into higher-order modes.

2.3.4 Coupling into higher-order modes

Distortions of the beam can happen at any point in the interferometer where the beam interacts with a mirror. For example, when a beam is reflected from a distorted mirror it picks up some additional phase:

$$u_{refl}(x, y, z) = u(x, y, z) \exp\left(2\mathrm{i}\, k n_1 Z(x, y)\right) \tag{2.20}$$

where $Z(x, y)$ describes the distorted surface height, n_1 is the index of refraction for the incident and reflected fields and $u(x, y, z)$ describes the undistorted reflected beam. To describe this distorted beam in terms of Gaussian modes the coupling coefficients are calculated as described in equation 2.15. For the Hermite-Gauss modes the coupling is given by [17]:

$$k_{nm}^{\text{refl.}} = \int_{-\infty}^{\infty}\int_{-\infty}^{\infty} u(x, y, z) \exp\left(2\mathrm{i}\, k n_1 Z(x, y)\right) u_{nm}^{*}(x, y, z)\ \mathrm{d}x\ \mathrm{d}y \tag{2.21}$$

Similarly, for transmission through a distorted surface we have [17]:

$$k_{nm}^{\text{trans.}} = \int_{-\infty}^{\infty}\int_{-\infty}^{\infty} u(x, y, z) \exp\left(\mathrm{i}\, k (n_2 - n_1) Z(x, y)\right) u_{nm}^{*}(x, y, z)\ \mathrm{d}x\ \mathrm{d}y \tag{2.22}$$

This process of distorting the beam is refereed to as coupling into other modes, as the action of reflection from a distorted surface creates modes other than those contained in the incoming beam. For the case of gravitational wave detectors the distortion of the mirror surfaces, and defects such as misalignment and mode mismatch, are tightly controlled. In realistic setups the lower order distortions, such as misalignment and mode mismatch, and low spatial distortions are greater than high spatial frequency distortions. As the order of the distortions is related to the order of the coupled mode this allows us to accurately model realistic interferometers with a finite number of low order modes. Modelling using modal methods, if the correct Gaussian parameters are chosen for the expansion, should typically only require modes up to order 10 [49].

2.4 Simulating interferometers with higher order modes

The modal model used throughout this thesis is FINESSE [39; 49], an interferometer simulation tool created by Andreas Freise which I have helped develop over my Ph.D. (see chapter 4). This uses coupling coefficients calculated for individual mirrors to recreate the higher order mode behaviour of complex optical systems, represented as a series of optical components connected via nodes. In this section the basic premiss of the simulation method is outlined.

2.4.1 Resonant cavities

Interferometers such as Advanced LIGO are based on resonant cavities, such as the arm and recycling cavities. A simplified diagram of a two mirror cavity is shown in figure 2.5, showing the fields at different points. Taking a simplified plane wave view the steady state behaviour can be derived. The different fields can be expressed by

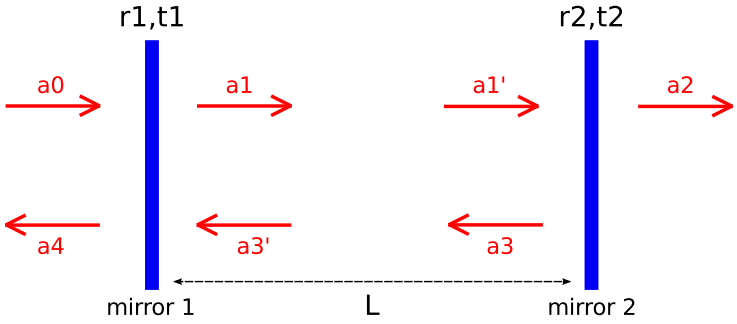

Figure 2.5: Simple diagram of a two mirror, or Fabry-Perot, cavity showing the light fields at different points in the cavity. The parameters of the cavity are the length (L), reflection coefficients (r_1, r_2) and transmission coefficients (t_1, t_2).

a series of simultaneous equations:

$$\begin{aligned} a_1 &= \mathrm{i}\, t_1 a_0 + r_1 a_3' \\ a_1' &= a_1 \exp(-\mathrm{i}\, kL) \\ a_2 &= \mathrm{i}\, t_2 a_1' \\ a_3 &= r_2 a_1' \\ a_3' &= a_3 \exp(-\mathrm{i}\, kL) \\ a_4 &= r_1 a_0 + \mathrm{i}\, t_1 a_3' \end{aligned} \tag{2.23}$$

where t_1/t_2 and r_1/r_2 refer to the amplitude transmission and reflection coefficients of the two mirrors and L is the separation of the mirrors. In the lossless case $t^2 + r^2 = T + R = 1$, (conservation of the power at a mirror). The 90° phase added on transmission ($\mathrm{i}\, t$) satisfies overall power conservation [17].

Three fields of particular interest are the transmitted field (a_2), the reflected field (a_4) and the circulating field (a_1). For the circulating field we have:

$$a_{circ} = a_1 = \mathrm{i}\, t_1 a_0 + r_1 r_2 \exp(-2\mathrm{i}\, kL) a_1 \tag{2.24}$$

and rearranging for a_1:

$$a_{circ} = \frac{\mathrm{i}\, t_1}{1 - r_1 r_2 \exp\left(-2\mathrm{i}\, kL\right)} a_0 \tag{2.25}$$

In our models we define the amplitude of the light field as $\sqrt{P}$, where P is the power of the light field. The circulating power is:

$$P_{circ} = |a_{circ}|^2 = \frac{T_1}{1 + R_1 R_2 - 2 r_1 r_2 \cos\left(2kL\right)} P_0 \tag{2.26}$$

where P_0 is the power of the incident field ($|a_0|^2$) and R and T refer to the reflected and transmitted power coefficients. Light builds up inside the cavity when it is resonant for the laser wavelength. The maximum in circulating power occurs when $2kL = N \times 2\pi$: the round-trip cavity length, $2L$, is a multiple of the wavelength. For simplicity in subsequent simulations we define the tuning as the phase $\phi = Lk$. The cavity is resonant at $\phi = N \times 180°$ and anti-resonant at $\phi = (2N + 1) \times 90°$. Alternatively the frequency of the laser can be tuned to be resonant for a certain cavity [17]:

$$2kL = 2\pi f \frac{2L}{c} = \frac{2\pi f}{\mathrm{FSR}} \tag{2.27}$$

where FSR is the *free-spectral range* ($\frac{c}{2L}$) of the cavity, the frequency spacing between resonances, as shown in figure 2.6. In this example the cavity produces very narrow resonance fringes, a result of the high reflectivities of the mirrors. A close up of a resonance peak shows the *full-width-half-maxima* (FWHM), or line-width of the cavity. A measure of the selectiveness of the cavity is the *finesse*, the ratio of the FSR to FWHM [17]:

$$\mathcal{F} = \frac{\mathrm{FSR}}{\mathrm{FWHM}} = \frac{\pi}{2\sin^{-1}\left(\frac{1 - r_1 r_2}{2\sqrt{r_1 r_2}}\right)} \tag{2.28}$$

The cavities in gravitational wave (GW) detectors are high finesse cavities which

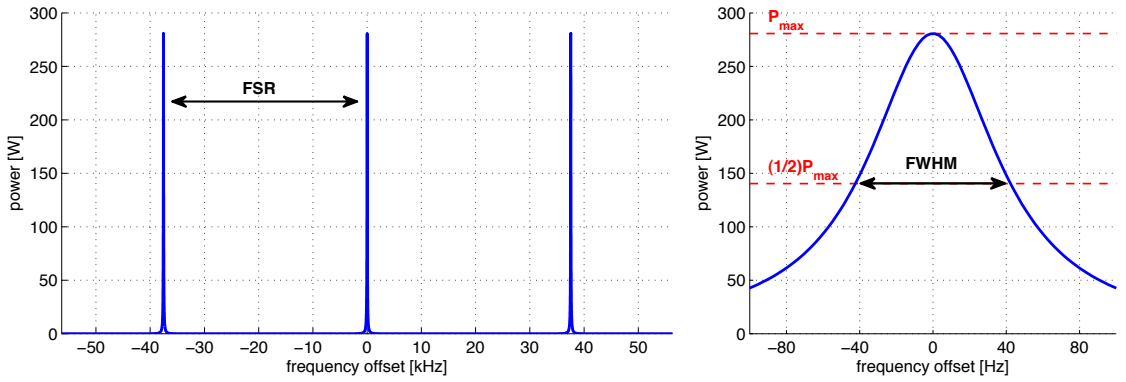

Figure 2.6: Power circulating inside a high finesse cavity as the frequency of the laser is tuned around the resonant frequency. The circulating power over several resonant fringes is shown (left). The seperation between subsequent resonances is the *free-spectral-range* (FSR). In this case the FSR is the 37.5 kHz of an Advanced LIGO arm cavity. The high finesse of the cavity results in very narrow fringes. Also shown is a zoom into a resonance peak (right), showing the line-width, or full-width-half-maxima (FWHM) of the cavity.

filter undesired frequencies and spatial modes from the light. In this case the finesse can be approximated to:

$$\mathcal{F} \approx \frac{\pi\sqrt{r_1 r_2}}{1 - r_1 r_2} \approx \frac{\pi}{1 - r_1 r_2} \tag{2.29}$$

In the same way the transmitted field is derived:

$$a_{trans} = a_2 = -\frac{t_1 t_2}{1 - r_1 r_2 \exp\left(-2\mathrm{i}\, kL\right)} a_0 \exp\left(-\mathrm{i}\, kL\right) \tag{2.30}$$

and the transmitted power:

$$P_{trans} = |a_{trans}|^2 = \frac{T_1 T_2}{1 + R_1 R_2 - 2 r_1 r_2 \cos\left(2kL\right)} P_0 \tag{2.31}$$

The transmitted power looks similar to the circulating power, with the added transmission of the end mirror. The reflected field is a combination of the light directly reflected from the input mirror and that leaking through this mirror from inside the

cavity:

$$a_{refl} = a_4 = \left(\frac{r_1 - r_2(R_1 + T_1)\exp(-2\mathrm{i}\,kL)}{1 - r_1 r_2 \exp(-2\mathrm{i}\,kL)} \right) a_0 \tag{2.32}$$

The reflected power is given by:

$$P_{refl} = |a_{refl}|^2 = \left(\frac{R_1 + R_2(R_1 + T_1)^2 - 2r_1 r_2 (R_1 + T_1)\cos(2kL)}{1 + R_1 R_2 - 2r_1 r_2 \cos(2kL)} \right) P_0 \tag{2.33}$$

In figure 2.7 examples of the power and phase of the circulating, transmitted and reflected fields are shown. The circulating and transmitted fields are maximised on resonance, while the reflected field is reduced by the out-of-phase light leaking from the cavity. The sum of reflected and transmitted power gives the total input power ($1\,W$) in the lossless example shown here. Three different cases are considered: under-coupled ($T_1 < T_2$); impedance matched ($T_1 = T_2$); and over-coupled ($T_1 > T_2$). For impedance matched all the power is transmitted on resonance. The arm

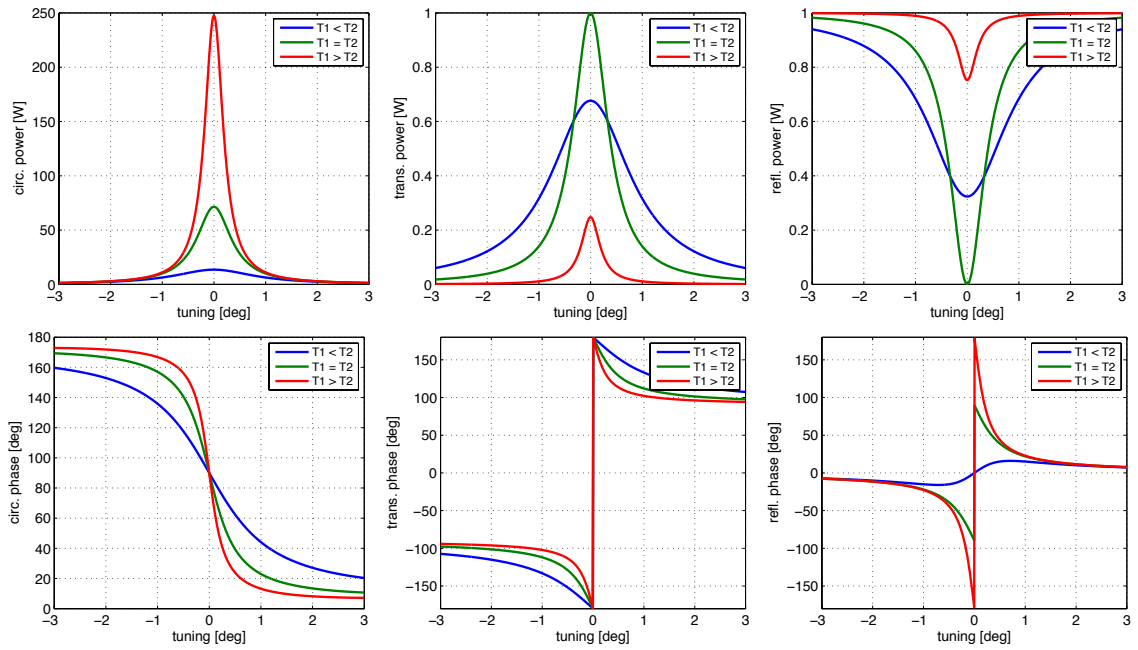

Figure 2.7: **Power** (top) and **phase** (bottom) of the fields circulating (left), transmitted (centre) and reflected (right) from a cavity as the length is tuned. 3 cases are shown with $T_1 = 1.4\%$: 1) under-coupled ($T_1 < T_2$); 2) impedance matched ($T_1 = T_2$) and 3) over-coupled ($T_1 > T_2$). These are also representative of low to high finesse (from 1 to 3).

cavities of Advanced LIGO are strongly over-coupled (see parameters in table 2.1) to the point where the cavity reflects almost all the power on resonance. The difference between the reflected beam on and off resonance is the change in sign of the field, as shown by the flip of the phase on resonance.

parameter	value
length [m]	3994.5
FSR [kHz]	37.5
T_1	1.4%
T_2	5 ppm
finesse	445
FWHM [Hz]	84

Table 2.1: Basic parameters for Advanced LIGO arm cavities [16].

2.4.2 Higher order modes in cavities

Compared to a plane wave a Gaussian beam picks up an extra phase as it propagates, the Gouy phase:

$$\psi(z) = \tan^{-1}\left(\frac{z}{z_R}\right) \tag{2.34}$$

The total Gouy phase accumulated by a Gaussian mode depends on the order of the mode: $(n+m+1)\psi(z)$ where $n+m$ is the mode order. This additional phase means cavities are resonant for different order modes at different tunings. The Gouy phase accumulated in a round trip of a cavity is:

$$\Psi = 2(\psi_2 - \psi_1) = 2\left(\tan^{-1}\left(\frac{z_2}{z_R}\right) - \tan^{-1}\left(\frac{z_1}{z_R}\right)\right) \tag{2.35}$$

where the Raleigh range is $z_R = \frac{\pi w_0^2}{\lambda}$. $\frac{\Psi}{2}$ gives the separation of HOM resonances in a cavity. The relevant parameters for an Advanced LIGO arm cavity are given in table 2.2. The curvatures of the input and end test masses (ITM and ETM) are carefully chosen so that low order HOMs are not resonant at the same tuning as the 00 mode. Figure 2.8 shows the amplitude of different order modes in an Advanced

parameter	value
ITM R_C [m]	1934
ETM R_C [m]	2245
w_0 [cm]	1.2
w_1 [cm]	5.3
w_2 [cm]	6.2
z_1 [m]	-1834
z_2 [m]	2160
$\frac{\Psi}{2}$ [°]	24.3

Table 2.2: Higher order mode parameters for Advanced LIGO arm cavities [16]. $w_{0,1,2}$ refer to the beam sizes of the cavity eigenmode at the waist (0); at the input test mass (1, ITM); and at the end test mass (2, ETM). Ψ is the round trip Gouy phase.

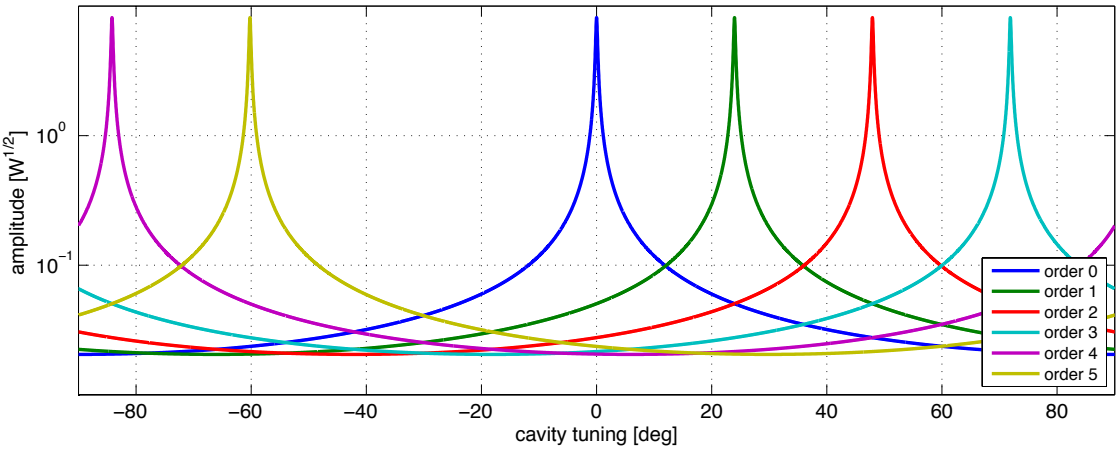

Figure 2.8: Simulated scan of an Advanced LIGO arm cavity, with different order (0 - 5) HG modes injected into the cavity. The amplitudes of the individual modes are detected as the cavity is scanned. The total power injected is 1 W, distributed evenly between the 6 modes.

LIGO cavity, with HOM resonances separated by 24.3°. For this plot the incident laser beam is made up, in equal parts, of the 6 higher order modes shown and no higher-order modes are created inside the cavity. A well designed Fabry-Perot cavity will naturally act as a higher order mode filter, due to the different resonance conditions. The cavity can be operated for one particular order, enhancing this mode and suppressing other order modes. Generally we want to enhance the 0 order fundamental beam. Such a cavity effectively acts to suppress distortions of

the beam. This technique is used in so called *mode-cleaners*, before the beam is sent into the main interferometer, ensuring a high purity Gaussian 00 mode.

2.4.3 Simple defects

A misaligned cavity

The simplest example of an imperfect cavity is a misaligned cavity, where one of the mirrors, or the incoming beam, is misaligned with respect to the optical axis. This can be represented with a few higher-order modes, with the majority of the distortion of the beam expressed by the order 1 Hermite-Gauss modes. The circulating power for an Advanced LIGO arm cavity simulated with a misalignment of 0.3 μrad of the end mirror is shown in figure 2.9. The majority of the power remains in the fundamental mode at the main resonance peak, shifted slightly from 0° tuning. The misalignment of the cavity causes coupling into the order 1 Hermite-Gauss mode, HG_{10}, which is resonant at around 25°. A small contribution from an order 2 mode, HG_{20}, is needed as the misalignment is relatively large. As the distortion (the

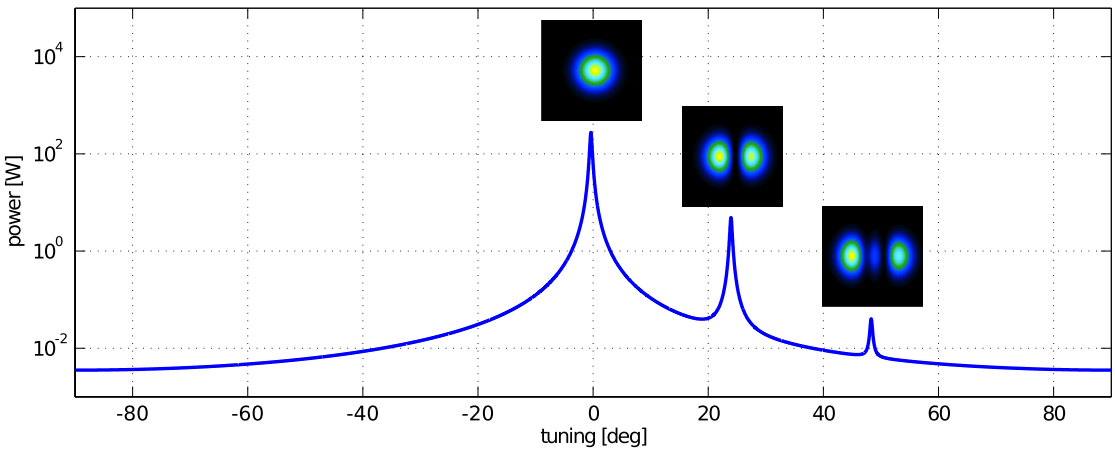

Figure 2.9: Power in a simulated Advanced LIGO arm cavity with a 0.3 μrad misalignment of the end mirror. For each peak in the power an image of the circulating beam is shown. The 00 mode is dominant in the cavity, resonant at some small shift from 0°. The misalignment results in coupling into an order 1 mode, HG_{10}, resonant at $\sim 25°$, and with some coupling into the order 2 mode, HG_{20}, resonant at $\sim 50°$.

misalignment) acts along the x-axis, the distortion of the beam is along the x-axis and the coupled modes are of the form HG_{n0}.

The order of the modes can be determined easily by the resonant tuning (subsequent modes are separated by 24.3°) and the shape of the beams. For a more detailed analysis of the exact mode content the beam can be decomposed into individual Gaussian modes.

A mode-mismatched cavity

A mode-mismatched cavity is an example of a second order distorted cavity. As previously demonstrated the effects of mode-mismatch are primarily described by the second order LG mode, LG_{10}. Again an Advanced LIGO arm cavity was simulated, this time with a mode-mismatch of 25% between the beam spot size of the cavity eigenmode and the spot size of the laser beam. The circulating power, detected as the cavity length is tuned, is plotted in figure 2.10. This mode-mismatch results in

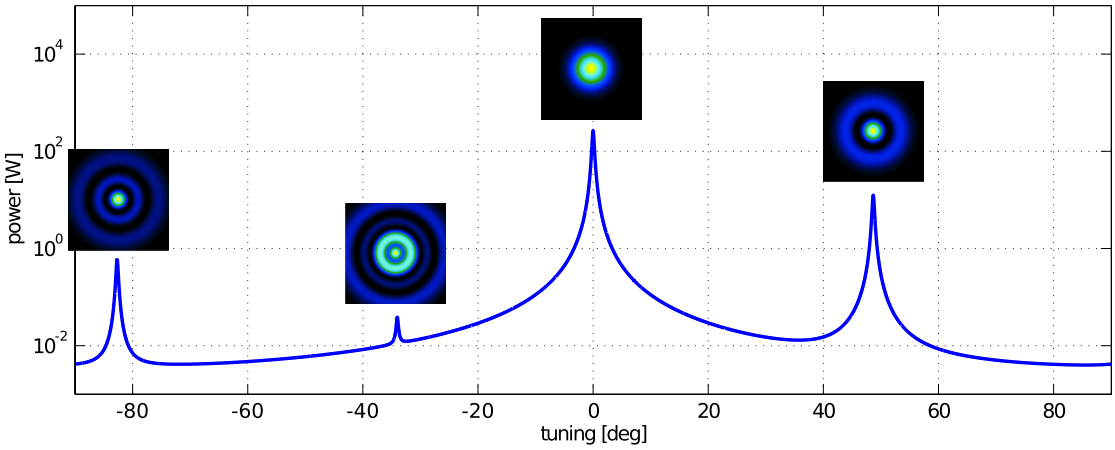

Figure 2.10: Power in an Advanced LIGO arm cavity where the injected laser beam is mismatched to the cavity. The mismatch is purely in beam spot size, with the injected beam 25% larger than the eigenmode of the cavity. For each peak in power an image of the circulating beam at that tuning is shown. Most of the power is in the 00 mode of the cavity eigenmode, resonant at 0°. At different tunings the higher-order Laguerre-Gauss modes which make up the input beam (in the cavity basis) are resonant: the order 2 LG_{10} mode at $\sim 50°$; the order 4 LG_{20} mode at $\sim -80°$ and the order 6 LG_{30} mode at $\sim -30°$.

higher-order LG modes injected into the cavity, in the basis of the cavity eigenmode. The 00 mode is still the dominant mode in the incoming laser beam, resonant at 0°. The mode-mismatch is predominantly described by the second order mode LG_{10}, resonant at $\sim 50°$. As the mode-mismatch is relatively large the addition of this order 2 mode is not sufficient to recreate the incoming beam in the cavity basis and the fourth order mode, LG_{20}, and sixth order mode, LG_{30}, are also required. At each of the resonant peaks the beam is primarily made up of the resonant mode, but there will be some component in other modes. As the mode mismatch is cylindrically symmetric the higher-order modes produced have no azimuthal component and are of the form LG_{p0}.

2.4.4 Mirror surfaces

Previous sections have shown examples of cavities with simple defects, which can be described analytically. For designing and commissioning of real detectors we want to represent more arbitrary defects, in particular the deviation of the mirror surfaces from a perfect sphere. In the case of interferometer design this will help to set requirements on the polishing and coating of the mirrors. For the commissioning process this will aide in identifying the output beam shape and other effects of distortions, such as lower than expected power build-up (see chapter 5 for commissioning examples).

Types of distortion

There are a range of different types of distortion we need to model for gravitational wave interferometers. In practise this modelling is done with a variety of different simulation tools, not just modal models. Several categories of mirror imperfections are:

- Misalignment and mode-mismatch.

- Distorted surfaces and substrates of mirrors, lenses etc.
- Non-uniform absorption/ reflection of optical components.
- Apertures created by the finite size of the optics.

The effects investigated in this thesis are a combination of simple mismatches/misalignments, mirror surface effects and aperture effects, although FINESSE can model the effects of non-uniform absorption/reflection. I focus on the effects of mirror surface and misalignment/mismatch, as the apertures are designed to be large enough for the incident beams. Mirror surface distortions can be further categorised into different types of distortion:

- Measured deviation from a perfect sphere. This deviation is measured under controlled conditions before the mirror is installed in the interferometer.
- Environmental effects. Once a mirror is installed in the detector there are processes which can effect the shape of the mirror. Of particular interest are thermal effects.
- Scratches and point defects.

The modal model employed in FINESSE is most suited to describing the effects of environmental distortions and the measured deviation of the mirror surfaces. Scratches and point defects are high-spatial frequency defects, which require high order modes to recreate and are more suited to simulations which don't rely on a modal decomposition. The modal model is not suitable for modelling scattering outside the beam divergence.

To describe the deviation of a mirror from a perfect sphere, both for measured deviations and environmental effects, *mirror maps* are used in FINESSE. These are 2D grids representing the mirror surface height. From these surfaces the reflected and transmitted beams can be calculated and the coupling into higher order modes

evaluated numerically from equation 2.15. For each mirror a matrix of coupling coefficients describes the transformation of the incident light field. These matrices are inserted into the matrix describing the interferometer behaviour, giving the HOM content at any position within the simulated setup.

2.5 Thermal effects

As we move into the commissioning era of Advanced LIGO, and other advanced detectors, it is crucial that the behaviour of the interferometers in the presence of deviations from the ideal design parameters is well understood. I am interested in those deviations that will effect the shape of the beam. Several major differences between Initial and Advanced LIGO will have a strong effect on the beam shape: the increased power in the interferometer will lead to thermal lensing and distortions of the test masses; the high finesse of the power recycling cavity and arm cavities will increase the interaction between the light fields and the mirrors; and the introduction of a signal recycling mirror will have a strong effect on any distortions at the dark-port.

In this section the behaviour of various subsystems of the central interferometer (a dual-recycled, Fabry-Perot Michelson) are investigated in the presence of thermal distortions and lenses, culminating in investigations of the so called *mode healing* effect, as presented at Amaldi 2013 [45].

Advanced LIGO will increase the injected power into the interferometer by a factor of 10 compared with initial LIGO. Along with increases in the finesse of the power recycling and arm cavities this will lead to large powers of $\sim 1\,\mathrm{MW}$ circulating in the arms. The mirrors will absorb some of the light that interacts with them, both in reflection and transmission. For low light powers this can be modelled as a simple loss. However, when the incident power is large, as for Advanced LIGO, even the low absorption of the *state-of-the-art* mirrors ($<1\,\mathrm{ppm}$) is enough to cause

significant heating within the mirrors. The result of this heating is two effects which can significantly effect the beam shape:

1. Thermal lensing. The index of refraction of the mirror substrates is dependent on temperature. The temperature gradient induced by the absorption of the incident beam causes a change in index of refraction throughout the substrate, which is mostly described by a simple lens.

2. Thermal distortion. The heating causes the mirror to expand elastically, distorting the surface of the mirror. This can be mostly described as a change in radius of curvature of the mirror surface.

The impact of these thermal effects needs to be understood, in terms of losses in power build up in the interferometer and the higher order mode content. Interferometers work by interfering beams: either carrier fields for power build up or beating with sidebands for control and gravitational wave readout. Any higher order mode effects, particularly those which occur differentially in the arms, will degrade this interference.

2.5.1 Temperature gradient

For this investigation the temperature effects are all considered in the steady-state, once the mirrors have reached equilibrium. Simulations involving the time evolution of thermal lenses and distortions, and their effects on control and thermal compensation systems are an important part of the commissioning process, but are not considered here.

The equations for thermal fields and aberrations (lensing and distortions) are taken from the extensive work of Hello and Vinet [50; 51; 52; 53]. The temperature fields that develop in the mirrors are considered for two cases: absorption of power in the highly-reflective coatings and linear absorption in the substrate (or bulk). For

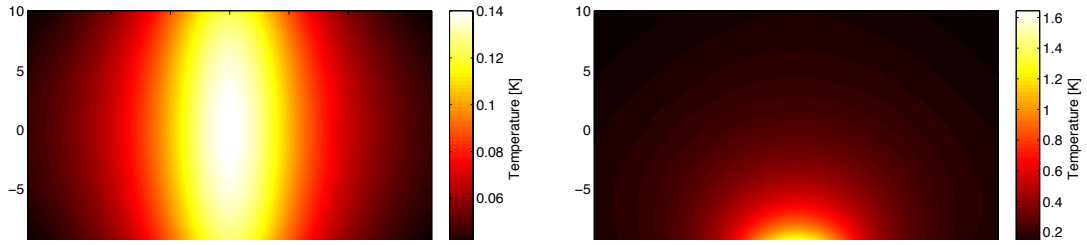

Figure 2.11: The expected excess temperature, $T(r, z)$, in an Advanced LIGO ITM substrate for absorption in the bulk (left) and absorption in the coating (right), for a beam with $w = 5.3\,\mathrm{cm}$ during high power operation. The highly reflective surface is located at a depth of $z = -10\,\mathrm{cm}$. The bulk absorbs power from the power recycling cavity (PRC) whilst the coating absorbs power from the arm cavity. The relevant thermal parameters are summarised in table 2.3.

Advanced LIGO we need only consider the coating absorption for the end mirrors (ETMs). For the ITMs we consider both coating and bulk absorption. In [53] analytic expressions for the temperature field of a mirror in thermal equilibrium are derived. Figure 2.11 shows the expected excess temperature distribution, $T(r, z)$, in an Advanced LIGO ITM for absorption in the bulk (left) and absorption in the coating (right) during high power operation. The parameters used for these and subsequent thermal calculations are summarised in table 2.3.

The overall power absorbed in the bulk is 0.1 W compared with 0.4 W absorbed in the coating. Theses similar magnitudes are a result of tight restrictions on absorption in the coating, as the power incident on the coatings is much greater ($\sim 100\times$) than that travelling through the bulk. The power absorbed by the coating is focused on the surface of the mirror ($z = -10\,\mathrm{cm}$), whereas the power absorbed by the bulk is distributed throughout the mirror.

Symbol	Parameter	Value	Units
a	radius	17	cm
h	thickness	20	cm
K	thermal conductivity	1.38	$\mathrm{Wm^{-1}K^{-1}}$
ϵ	emissivity	0.9	-
α	thermal expansion coefficient	5.4×10^{-7}	$\mathrm{K^{-1}}$
Y	Young's modulus	7.3×10^{10}	$\mathrm{Nm^{-2}}$
σ	Poisson ratio	0.17	-
dn/dT	thermal refractive index	1.1×10^{-5}	$\mathrm{K^{-1}}$
C	coating absorption	0.5	ppm
B	linear bulk absorption	200	ppm $\mathrm{m^{-1}}$
w_{ITM}	beam radius (ITM)	5.3	cm
w_{ETM}	beam radius (ETM)	6.2	cm
P_{arms}	power in the arms	740	kW
P_{PRC}	power in the power recycling cavity	5.4	kW

Table 2.3: Parameters used to calculate thermal effects in Advanced LIGO test masses. The thermal properties of the mirrors [53; 54] and beam parameters [16] are given. These refer to the design parameters of the mirrors, i.e. the absorptions are the upper limit of the requirements for the test masses and coatings.

2.5.2 Thermal lensing

The index of refraction of the fused-silica cavity mirrors are dependent on temperature, so the temperature fields which develop in the mirrors result in an inhomogeneous index of refraction. Alternatively, this effect can be described with a constant index of refraction and a lens representing the excess optical path incurred [53]:

$$Z(r) = \frac{dn}{dT} \int_{-\frac{h}{2}}^{\frac{h}{2}} T(r, z) dz \tag{2.36}$$

Figure 2.12 shows plots of the expected thermal lensing in an Advanced LIGO ITM, during high power operation. Both coating and bulk absorption contribute to the thermal lens in the ITMs. The total excess optical path is well described by a lens with focal length $f = 5\,\mathrm{km}$ in the centre region, where the beam is most intense. We can model this thermal effect by including a lens in our model and a mirror map representing the residual optical path.

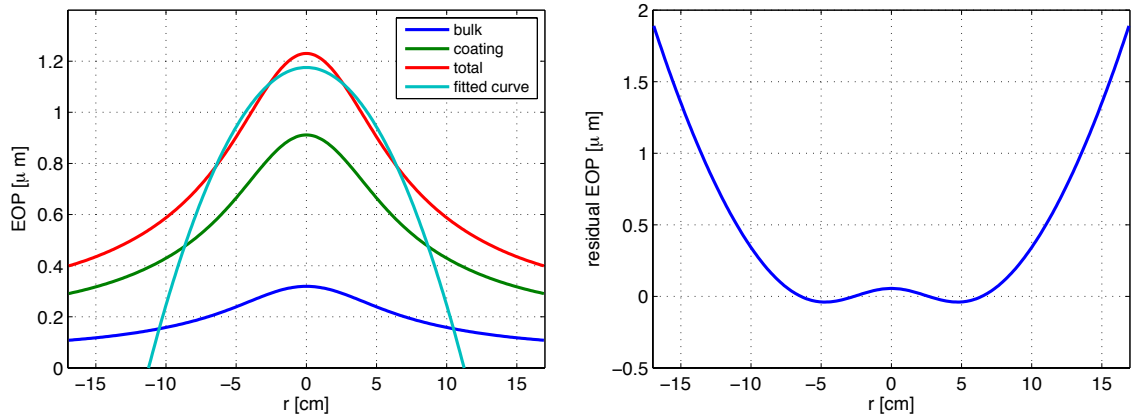

Figure 2.12: Expected thermal lensing in an Advanced LIGO ITM for high power operation. **Left:** excess optical path (EOP) for absorption in the bulk, coating and the combined EOP. Also shown is a fitted curve (weighted by the incident Gaussian beam, $w = 5.3\,\mathrm{cm}$) representing a simple lens with a focal length of 5 km. **Right:** residual EOP after the fitted curve has been removed.

For small absorptions the thermal lens scales linearly with power absorbed. Any deviation in the mirror absorptions, or the incident power, can be represented by an equivalent scaling of the lenses.

2.5.3 Thermal distortions

In figure 2.13 the expected thermal distortions of the reflecting surface of the Advanced LIGO test masses are shown. In the input mirrors there is some small contribution to the distortion by absorption in the bulk, but the majority is the result of absorption in the coating. In the case of the end mirrors the very low transmission ($T = 5\,\mathrm{ppm}$) means we can ignore any contribution from bulk absorption. In both cases the distortion, as seen by the incident beam, is well described by a change in the radius of curvature. For the ITMs this is 110 km, for the ETMs this is 160 km. As with the thermal lenses we can model these distortions as a change in radius of curvature of the test masses and use mirror maps to represent the residual distortion. For different absorptions/ incident powers the surface distortion can be calculated by scaling the distortions shown in figure 2.13.

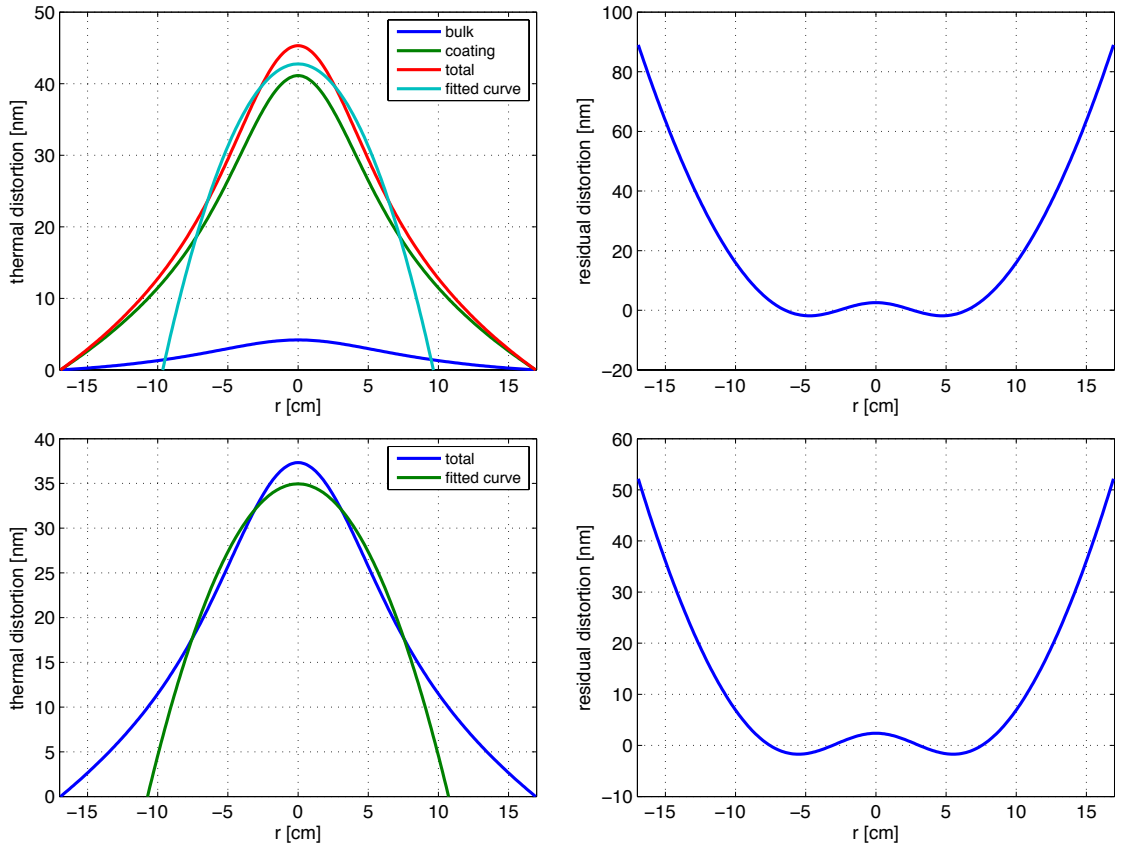

Figure 2.13: The expected thermal distortions of the reflecting surface of the ITMs (top) and ETMs (bottom) in Advanced LIGO for high power operation. **Left:** Plots showing the overall thermal deformation of the mirror surfaces. In the ITMs (top) absorption in the coating and bulk contribute to the total distortion of the surface. In the ETMs (bottom) only absorption in the coating contributes. Also shown is a fit to an ideal sphere, weighted by the incident Gaussian beam, with $R_c = 110\,\mathrm{km}$ for the ITMs and $R_c = 160\,\mathrm{km}$ for the ETMs. **Right:** The residual distortion of the ITMs (top) and ETMs (bottom) after the fitted curves have been removed. The thermal parameters used are summarised in table 2.3.

2.5.4 Thermal compensation systems

In the next sections I will include the thermal lensing and thermal distortions of the test masses into the model of Advanced LIGO. These effects can be described well as a simple lens in the mirror substrate and a change in curvature of the reflecting surfaces, characterised by a focal length, f, and radius of curvature, R_c. Both f and R_c will depend on the power in the arm-cavities and (for the input mirrors) the power in the power recycling cavity and will differ for low power (12.5 W) and high power

(125 W) operation. This means that the mode-matching between the arm-cavities and the power recycling cavity will change quite significantly, from the cold state ($f \approx \infty$), through low power ($f \approx 50\,\mathrm{km}$) and finally to high power ($f \approx 5\,\mathrm{km}$). Advanced LIGO will use *thermal compensation systems* (TCS) to correct the mirror curvatures of both test masses and the effective lens in the ITM [54; 55]. For simplicity the final design [16] was mode-matched for a 50 km lens in the ITMs to avoid using TCS during low power operation.

The thermal compensation system involves two distinct correcting mechanisms. The first is a ring-heater positioned near the AR coated surface of each test mass [56]. These are used to heat the outer edge of the mirror to produce a curvature in the opposite direction to that from heating by the beam. The ring heater also corrects some of the thermal lens in the ITM substrate. However, as the mechanisms for forming the thermal lens and thermal distortion are different they are not likely to be corrected by the same ring-heater power. An additional system is required to complete the correction of the thermal lens. This involves a compensation plate, placed in front of the ITMs, made of the same material (fused silica). A heating pattern is projected onto this plate via a CO_2 laser. This pattern is designed to heat the compensation plate in such a way as to correct any thermal lensing in the ITM [57].

The thermal compensation system, working perfectly, would correct the simple thermal lens in the ITMs and the change in curvature of both test masses, leaving just the residual lens and distortion as shown in figures 2.12 and 2.13. Initially I assume the thermal compensation systems are working perfectly, while we investigate the subsystems of the central interferometer. For final realistic simulations, and future work, the efficiencey of the TCS should be taken into account.

2.6 Arm cavities with thermal aberrations

In the following sections the higher order mode behaviour of an interferometer is illustrated, building from individual arm cavities to the full dual recycled configuration. Thermal distortions and lenses provide the mechanism for coupling into HOMs. The modal model is intuitive for such tasks.

2.6.1 Figures of merit

The arm cavities of the Fabry-Perot Michelson are tightly controlled to be as similar as possible. Any differences in the power build up or the shape of the beam will be seen at the dark port. The investigations in this thesis are primarily concerned with higher order mode content: the fraction of power in a given field in modes other than the 00 mode. This is our figure of merit for the arm cavities. Also considered is the additional loss due to scatter into HOMs, during one round trip of the cavities, and the total loss, including any mode mismatch into the cavity.

2.6.2 HOM enhancement

The coupling from an individual mirror is calculated as in 2.3.4 and represented as a coupling coefficient, k. In GW detectors the cavities are operated to enhance the 00 mode in the arms. The effect on the coupled higher order mode is not obvious and here I make an approximation of such behaviour, in the context of small couplings. Figure 2.14 shows a simple representation of coupling in a cavity. For simplicity we consider a pure 00 mode input beam (a_0), mode-matched to the cavity with the only coupling into a HOM (field b) occurring at the end mirror and described by $k_{a,b}$. The circulating 00 mode amplitude is:

$$a'_3 = \frac{\mathrm{i}\, t_1 r_2 \exp\left(-\mathrm{i}\, 2kL + \mathrm{i}\, \Psi\right)}{1 - r_1 r_2 \exp\left(-\mathrm{i}\, 2kL + \mathrm{i}\, \Psi\right)} a_0 \tag{2.37}$$

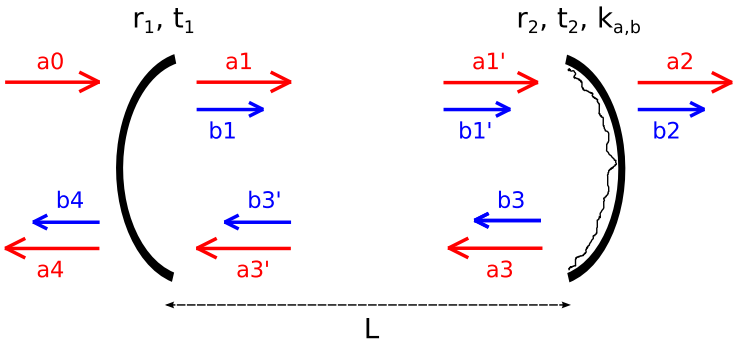

Figure 2.14: Diagram representing higher order mode coupling in a linear cavity. The field a represents the mode of the injected beam, usually the 00 mode, which is perfectly mode matched to the cavity as described by the mirror curvatures. The cavity includes some distortion of the end mirror, which couples from field a into some higher order mode represented by field b. This coupling is described by $k_{a,b}$.

(adjusted from 2.25 to include Ψ, the round trip Gouy phase). Here we make the approximation that the coupling is small enough that no power is lost from the 00 mode. This will not give exact numbers for the 00 mode, but allows simple predictions of the HOM behaviour. The set of equations needed for the circulating HOM field (b'_3) are:

$$\begin{aligned}
b'_3 &= b_3 \exp\left(-\mathrm{i}\, kL + \mathrm{i}\,(1+n+m)\tfrac{\Psi}{2}\right) \\
b_3 &= r_2 k_{a,b} a'_1 + r_2 b'_1 \\
b'_1 &= b_1 \exp\left(-\mathrm{i}\, kL + \mathrm{i}\,(1+n+m)\tfrac{\Psi}{2}\right) \\
b_1 &= b'_3 r_1 \\
a'_1 &= a_1 \exp\left(-\mathrm{i}\, kL + \mathrm{i}\,\tfrac{\Psi}{2}\right) \\
a_1 &= \mathrm{i}\, t_1 a_0 + r_1 a'_3
\end{aligned} \tag{2.38}$$

where $k_{a,b}$ is the coupling from a to b and $n+m$ is the order of b. Solving these simultaneous equations gives:

$$\frac{b'_3}{a'_3} = \frac{\exp\left(\mathrm{i}\,(n+m)\tfrac{\Psi}{2}\right)}{1 - r_1 r_2 \exp\left(-\mathrm{i}\, 2kL + \mathrm{i}\,(1+n+m)\Psi\right)} k_{a,b} \tag{2.39}$$

Setting the condition for the 00 mode resonance the HOM content of the arm is [58]:

$$\mathrm{HOM}_{\mathrm{arm}}^{\mathrm{circ.}} = \frac{|k_{a,b}|^2}{1 + R_1 R_2 - 2 r_1 r_2 \cos\left((n+m)\Psi\right)} = \epsilon \, |k_{a,b}|^2 \tag{2.40}$$

Whether the power in the mode is enhanced or suppressed depends on how close the HOM is to the resonance of the cavity. Consider the minimum (anti-resonant) and maximum (resonant) HOM content:

$$\min(\epsilon) = \frac{1}{(1 + r_1 r_2)^2} \approx \frac{1}{4} \qquad \max(\epsilon) = \frac{1}{(1 - r_1 r_2)} \approx \frac{4}{T_1^2} \tag{2.41}$$

where $R_2 \approx 1$. For the Advanced LIGO arms the maximum reduction is 0.25 and the maximum enhancement is 2×10^4. The parameters of the cavities are carefully chosen to avoid this maximum enhancement. Table 2.4 shows ϵ for different order modes in an Advanced LIGO cavity. Most of these modes will be suppressed, the only ones slightly enhanced being those close to resonance (i.e. order 7 is resonant at $\phi = 170°$).

$n+m$	1	2	3	4	5	6	7	8	9	10
ϵ	1.5	0.45	0.28	0.26	0.35	0.80	8.9	3.9	0.64	0.32

Table 2.4: Enhancement (ϵ) of higher order modes created at the ETM in an Advanced LIGO arm cavity. Modes closer to resonance are enhanced whilst those near anti-resonance are suppressed.

The HOM content in reflection can be derived:

$$\mathrm{HOM}_{\mathrm{arm}}^{\mathrm{refl.}} = \frac{T_1^2 R_2}{(r_1 - r_2(R_1 + T_1))^2} \mathrm{HOM}_{\mathrm{arm}}^{\mathrm{circ.}} \tag{2.42}$$

Setting $R_2 = 1$ this gives $\mathrm{HOM}_{\mathrm{arm}}^{\mathrm{refl.}} \approx 4 \times \mathrm{HOM}_{\mathrm{arm}}^{\mathrm{circ.}}$.

Things start to become more complicated when coupling occurs at multiple surfaces and here FINESSE is used. An Advanced LIGO cavity is simulated in FINESSE, with thermal aberrations of the test masses as described in sections 2.5.2 and 2.5.3.

4 cases are considered:

1. Perfect: no thermal aberrations and no losses, for comparison.

2. ETM distortion: the distortion on the ETM is included.

3. TM distortions: distortions on both test masses are included.

4. All aberations: all thermal aberrations are included, the distortions of the test masses and the lensing in the ITM.

For cases 2 - 4 the finite apertures of the mirrors are included. A summary of the results is shown in table 2.5, showing the power and higher order mode content of the circulating and reflected fields, and the round trip and total losses. The distortion of the ETM couples $\sim 400\,\mathrm{ppm}$ out of the 00 mode, on direct reflection, with most of this into the order 4 mode, LG_{20}. The HOM content of the circulating beam when only the ETM distortion is applied (155 ppm) agrees with the earlier analysis, as the order 4 mode is suppressed in the cavity ($\epsilon = 0.26$). The discrepancy is due to other modes in the cavity, some of which are enhanced, and second order coupling which is not included in the above approximation. The reflected HOM content is $\sim 4\times$ that of the circulating beam, as predicted.

	Case 1	Case 2	Case 3	Case 4
power (circ.) [W/W]	284	282	283	270
power (refl.) [W/W]	0.999	0.989	0.998	0.995
$\mathrm{HOM}^{\mathrm{circ.}}$ [ppm]	0	155	183	180
$\mathrm{HOM}^{\mathrm{refl.}}$ [ppm]	0	608	338	1.9%
round trip loss [ppm]	0	34	3	24
total loss [ppm]	0	34	3	343

Table 2.5: Summary of power, loss and HOM content in a simulated Advanced LIGO arm cavity for different cases: no mirror defects (case 1); thermal distortion of the ETM (case 2); thermal distortion of both mirrors (case 3); and mirror distortions and ITM thermal lensing (case 4). The power and HOM content of the circulating and reflected fields are given, as well as the total and round-trip losses.

The behaviour changes when the ITM distortion is applied. The direct coupling from the ITM is very similar to the ETM. When both distortions are applied the amplitude of a HOM in the circulating beam looks like $k_{a,b}^{\mathrm{ITM}} \exp\left(\mathrm{i}\,(n+m)\frac{\Psi}{2}\right) + k_{a,b}^{\mathrm{ETM}}$. In this example this amplitude is larger than the case of a single distortion, $k_{a,b}^{\mathrm{ETM}}$, and the intra cavity HOM content increases. We also note a drop in the HOM content of the reflected field. Deriving the HOM behaviour when the distortion is applied to the ITM has an additional coupling, of the field directly reflected from the ITM. The HOM field coming from the cavity picks up an additional minus sign, compared to the coupling on direct reflection from the cavity. Other phases are involved (round trip Gouy phase, different phases on back and front coupling) but the reflected field is roughly $4\times\mathrm{HOM}^{\mathrm{circ.}} \approx 730\,\mathrm{ppm} - 400\,\mathrm{ppm}$ (direct coupling on back reflection from ITM) $= 330\,\mathrm{ppm}$.

Notably the round trip loss decreases significantly when both distortions are applied. The distortions on each mirror are very similar in shape, scaled (in x and y) by the incident beam waist on each mirror (see figure 2.13). With equal absorptions the wavefront of the beam reflected from the distorted ETM will match well to the distorted ITM and the distorted mirrors form a common resonating mode. Although not matching the Gaussian eigenmode of the non-distorted cavity the two mirrors match well and so further distortion of the wavefront on subsequent round-trips (after the initial reflection) is greatly reduced. In the case of unbalanced distortions the beam is further distorted on each reflection, as it alternates between two different mirror shapes. Each time the beam is distorted, power is scattered into higher-order-modes, increasing the round-trip-loss. This is a somewhat counterintuitive argument as the HOM content increases with absorption on both mirrors. However, this is the mode-content in terms of the Gaussian eigenmode of the cold-cavity, not the effective mode formed by two equally distorted mirrors.

The addition of the ITM lensing has little effect on the HOM content inside the cavity. The lens causes coupling into HOMs before the light enters the cavity and

most of these modes are reflected from the cavity. This is illustrated in the significant drop in circulating power: less power is effectively injected into the interferometer. However, the lensing has a very strong effect on the mode content of the reflected beam. The thermal lens is the strongest distortion (see figure 2.12) and distorts the beam as it leaves the arm.

2.6.3 HOM and loss behaviour with scaling of thermal aberrations

The simulations of the arm cavities considered above use the absorption design values for the ITM and ETM. The real values are likely to differ from these. The lenses and surface distortions can be simply scaled to give the results for different absorptions, or for lower incident powers, such as those for low power operation.

Figure 2.15 summarises the results of simulations using a range of coating absorptions, with a constant bulk absorption in the ITM. The top two plots show the total HOM content (left) and the LG_{20} content (right) of the circulating beam. These plots illustrate that the distortion of the circulating beam depends on the total distortion of both mirrors. An individual mode (LG_{20}) displays a distinct relationship to the two absorptions, roughly $\propto C^2_{\mathrm{ITM}} + C^2_{\mathrm{ETM}}$, where C refers to the coating absorption. This could also refer to the scaling of the surface. The distortion of the beam is dominated by the order 4 mode (LG_{20}), as the levels of non-00 power are very similar to the levels of 20 power. The relationship of the total HOM content is slightly different than that of the individual LG_{20} mode, which is expected as the coupling into other modes could have a more significant contribution from second order coupling (i.e. coupling from LG_{20} into other modes). In general the HOM content is dominated by the total absorption.

The bottom left plot shows the round-trip loss incurred. This does not include loss due to transmission through the thermal lens. We find that this loss is partic-

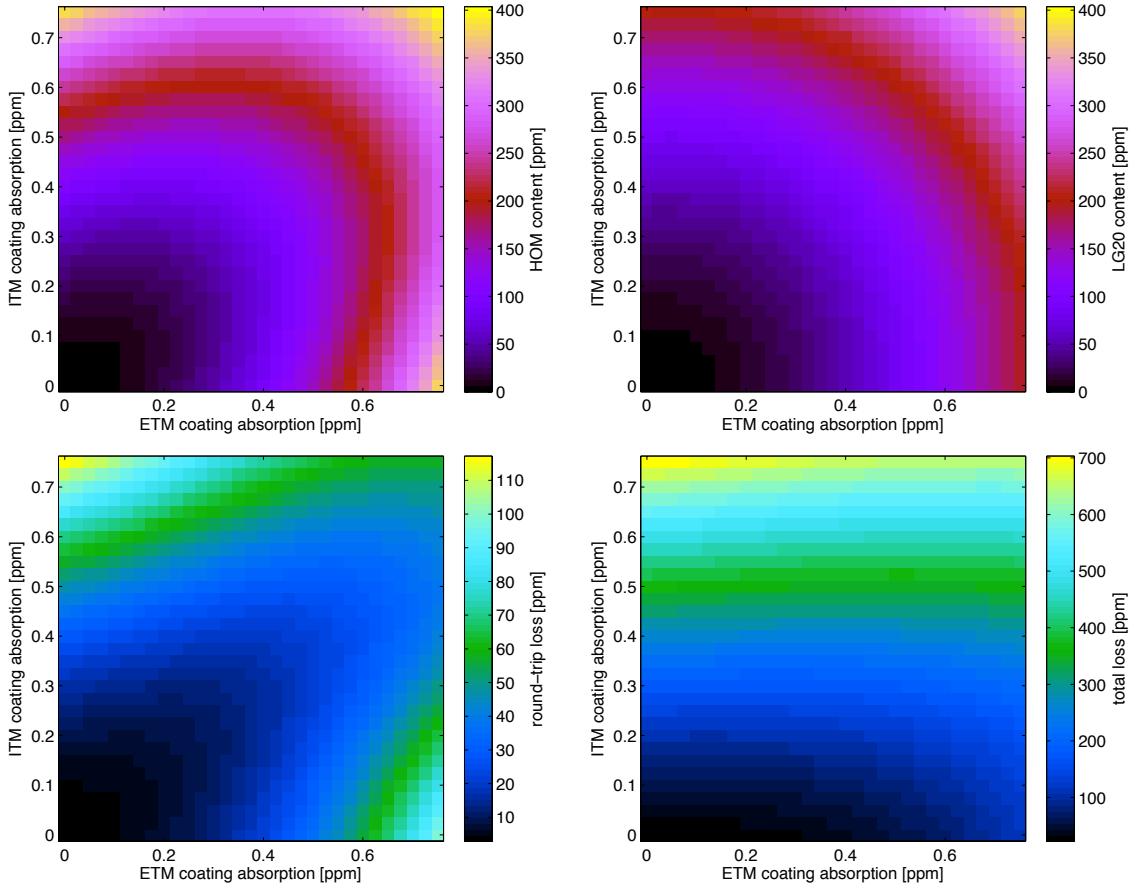

Figure 2.15: Results of simulations of Advanced LIGO arm cavities in the presence of thermal aberrations, for a range of coating ETM/ITM absorptions. Thermal surface distortions are present on both test masses and a thermal lens is present in the ITM. A constant bulk absorption (40 ppm) is applied to the ITM, so at ITM coating absorption = 0, there is some distortion and lensing of the ITM. **Top left:** HOM content of the circulating beam. **Top right:** LG20 (order 4) content of the circulating beam. **Bottom left:** round-trip loss. **Bottom right:** total loss.

ularly susceptible to the difference between the absorption of the two mirrors, so that when the two absorptions are equal the round-trip loss is much smaller. For example, for a total absorption of 0.6 ppm distributed across both mirrors we can compare the balanced case of 0.3 ppm on both mirrors, and the unbalanced case of 0.6 ppm on the ETM. For the balanced case we have a round-trip loss of ∼15 ppm, whereas the unbalanced case gives ∼60 ppm. As postulated in the previous section this is due to the similar nature of the distortions on each arm: when the absorptions are equal the wavefront of the field reflected from the distorted ETM matches the

distorted ITM. The round-trip loss is not completely balanced between the ETM and ITM absorption. This is due to the constant absorption in the bulk, creating a constant thermal distortion of the ITM. Therefore, a slightly greater absorption of the ETM is needed to balance the two mirrors. This is seen more easily at high absorptions.

The final plot (bottom right) shows the total loss in the cavity. This includes any loss incurred from transmission through the thermal lens. This power loss from transmission through the thermal lens is much greater than the round-trip loss, as the cavity effectively rejects any higher-order-modes injected into the cavity via the thermal lens. As predicted, the total loss is dominated by the absorption on the ITM. The plots shown here refer explicitly to the HOM behaviour of thermal cavities, but can be used to illustrate the behaviour for generic distortions, in terms of the common distortions of the mirrors (balanced case) and differential distortions of the mirrors (unbalanced). Simulations of thermally distorted cavities by Hiro Yamamoto give similar behaviour and numbers using a different simulation method [58].

2.7 Michelson with thermal aberrations

In this section we predict how higher order modes behave in a Michelson with Fabry-Perot arm cavities, the basis of gravitational wave detectors. The Michelson is ideally placed on the dark fringe, for the carrier light. The minimum power at the dark port is determined by any asymmetries between the two Michelson arms, as effectively the Michelson measures the destructive interference of light from each arm. In a simple plane wave model these differences would just be asymmetric losses for the two arms. This model is much too simple for these complicated instruments. Any difference in the beam shape, or higher order mode content, of the two arms will lead to imperfect interference of the two beams, and higher order modes at the dark port. This is demonstrated in figure 2.16 where the Advanced LIGO Fabry-

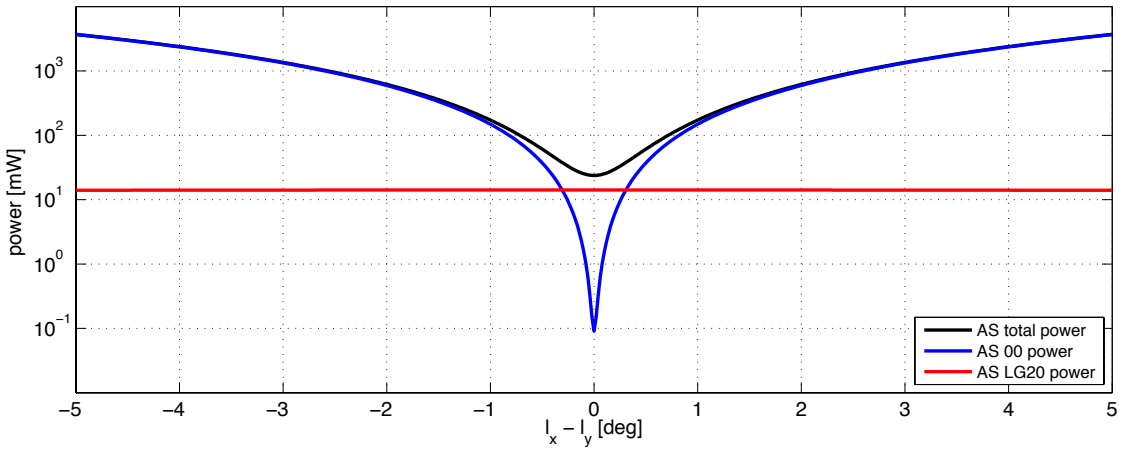

Figure 2.16: Power at the dark fringe (or anti-symmetric port, AS) of an Advanced LIGO Fabry-Perot Michelson with a thermal distorted ETM in the x arm. This distortion couples into HOMs, particularly LG_{20} and partially leaks into the dark port. The total power at AS is shown, as well as the power in the 00 mode and LG_{20} as the Michelson is tuned around the dark fringe.

Perot Michelson is simulated with asymmetric thermally distorted arm cavities: in this simple case with a thermal distortion of ETMX for 0.5 ppm coating absorption. The total power, power in the 00 mode and power in the order 4 mode, LG_{20} (the strongest coupling from this distortion), is detected as the Michelson is tuned around the dark fringe, by tuning the differential distance of the short Michelson arms ($l_x - l_y$) whilst the cavities are kept on resonance. The 00 mode on its own can achieve a much better dark fringe, down to $\sim 0.1\,\mathrm{mW}$, for an input power of 125 W. However, the higher order modes reflected from the x arm have no counter part coming from the y arm to interfere with destructively. Half of these modes will appear at the dark port. This is shown in the plot in figure 2.16. For an individual HOM the amplitude at the dark port is:

$$b_{dark} = \frac{1}{\sqrt{2}}\left(b_x - b_y\right) \tag{2.43}$$

where b_x and b_y refer to the complex amplitudes of the modes reflected from the x and y cavities. If the coupling is the same in both arms the distortions are common

and the modes are reflected back towards the laser. Any difference between the modes will appear at the dark port. The minimum power at the dark port (or anti-symmetric, AS, port) is determined by the differential mode content. This power is characterised by the *contrast defect*.

2.7.1 Contrast defect

The contrast defect is defined as the ratio of the minimum power at the dark fringe (determined by the HOMs at the dark port) to the sum of the power hitting the beam-splitter from the two arms:

$$C = \frac{P_{AS}}{P_x + P_y} \tag{2.44}$$

This ratio needs to be sufficiently low to indicate that the differential power in higher order modes is not significant compared to the power in the interferometer. In Advanced LIGO a DC offset is used to read out the gravitational wave signal: the Michelson is offset from the dark fringe allowing a small proportion of carrier light (100 mW) to leak out and act as a local oscillator. The signal sidebands will be almost exclusively in the 00 mode, as the dark fringe for the carrier is not the dark fringe for the signal. Therefore, to achieve a significant overlap the local oscillator should be as close to the 00 mode as possible. Any HOMs in the carrier at the dark port will not contribute the readout signal but will contribute to the noise.

The contrast defect depends on the differential distortions of the beam and hence the differential distortions of the mirrors in the two arm cavities. This is illustrated in figure 2.17, where the contrast defect is plotted for different thermal aberrations in the x and y arms. In each arm a constant bulk absorption of 40 ppm in the ITM substrate produces a lensing and a distortion of the ITMs. In the simulation the coating absorption is varied in each arm, for between 0 and 0.5 ppm per optic. This scales the thermal distortions of the test masses and the ITM lens. The plot shows

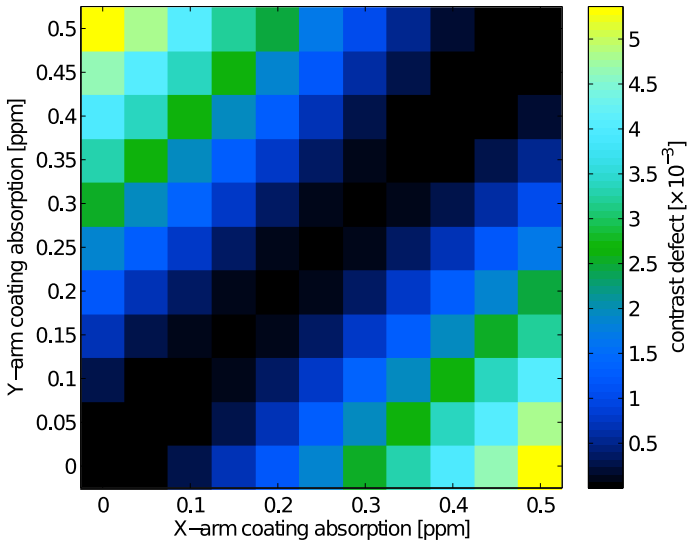

Figure 2.17: Contrast defect in a simulated Advanced LIGO Fabry-Perot Michelson with thermal aberrations of the test masses. The contrast defect is detected for different coating absorptions on the test masses in each arm, scaling the thermal distortions and ITM lens.

that the contrast defect is very small only when the absorptions for each arm are very similar, i.e. the distortions and higher order modes for each arm are similar. The total extent of the distortion (i.e. sum of x and y distortion) is not the crucial factor, but the differential distortions will determine the output mode content.

2.8 Mode-healing

The addition of a signal recycling mirror (SRM) to the detector configuration (compared to initial LIGO) can have a strong impact on the beam shape. This has been first predicted and then observed in GEO600 [59]. Differential arm distortions appear in the Michelson dark port (see previous section). The SRM forms a cavity with the rest of the interferometer. This is primarily used to enhance the signal sidebands in the interferometer. However, the effect of forming a cavity has the potential to 'heal' the beam distortions. Simply, the cavity formed by the SRM can enhance the 00 mode whilst effectively suppressing the higher order modes. The

beam at the output of the detector is effectively cleaned of unwanted spatial modes.

2.8.1 Mode-healing in Advanced LIGO

The results reported in this section were presented at the recent Amaldi conference [45]. The modal model is the ideal tool for such an investigation as the behaviour is inherently modal. The full Advanced LIGO interferometer is simulated, with higher order modes introduced with (uncorrected) thermal distortions of the end test masses. In this investigation we consider differential distortions of the ETMs, with a coating absorption of 0.3 ppm on ETMY and 0.5 ppm on ETMX. The distortions are predominantly a radius of curvature change, corresponding to 160 km for ETMX and 270 km for ETMY.

For this investigation the signal recycling cavity is tuned to be resonant for the carrier. Future investigations should explore the effect at different tunings of the SRM. The detector is operated with a constant DC offset of 100 mW of carrier power at the dark port. Ideally this should be entirely in the 00 mode. In figures 2.18 and 2.19 the results of these simulations are shown. In figure 2.18 a cross section

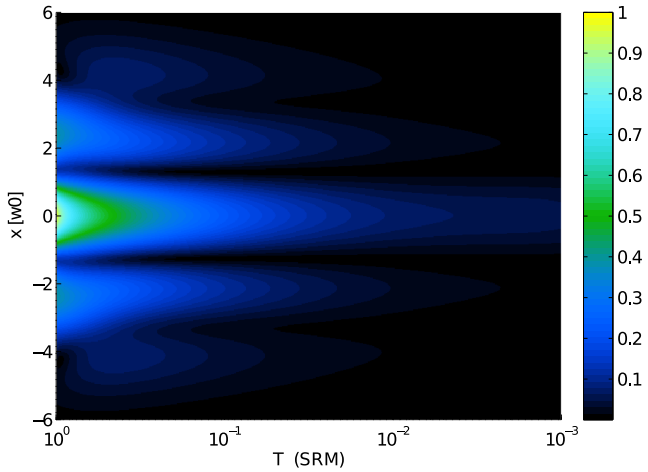

Figure 2.18: A cross section of the field at the dark port of a simulated Advanced LIGO interferometer with thermal distortions of the end test masses. The fundamental mode is masked out and the cross section is shown as the transmission of the signal recycling mirror is tuned.

of the beam at the dark port is shown, with the 00 mode masked out (i.e. just the distortion of the beam) as the SRM transmission is tuned. This is predominantly the mode mismatch HOM: LG_{10}. As the transmission is reduced the suppression of the higher order modes increases and the power in the distortion is reduced. This is further illustrated in figure 2.19, where the power at the dark port in the 00 mode and HOMs is plotted against SRM transmission. The power in the 00 mode is not significantly altered, due to the control of the interferometer to give a DC offset of 100 mW. The mode healing effect significantly favours a high finesse cavity, or low SRM transmission. However, the SRM transmission was originally chosen to optimise the shot noise. SRM transmission in Advanced LIGO (20%) still heals the beam, with $\sim \frac{1}{10}$ of the power in HOMs. The beam at the dark port is shown in figure 2.20. Without the SRM (left plot) the LG_{10} mode is clearly visible, generated from the mode mismatch in the arms and exiting the Michelson due to the differential arm distortions. When the SRM is added the mode is healed and the majority of the power is in the 00 mode.

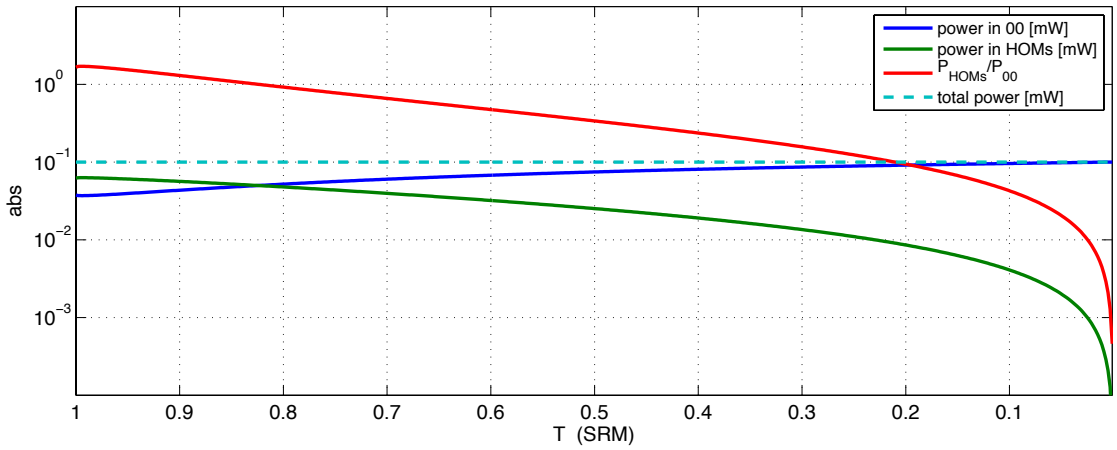

Figure 2.19: An example of mode-healing in Advanced LIGO in the presence of thermal distortions of the end test masses. The power of the fundamental mode (00) and higher order modes (HOMs) (in mW) is shown as well as the ratio of 00 power to HOM power as the SRM transmission is tuned.

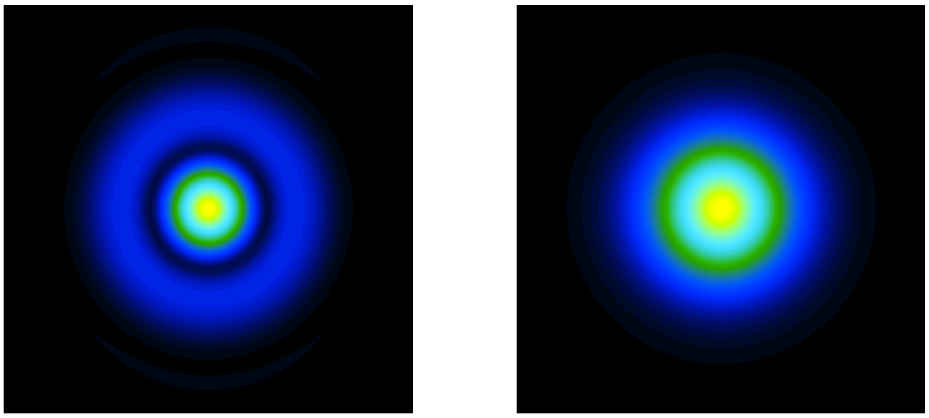

Figure 2.20: Plots of the simulated beam at the output of Advanced LIGO in the presence of differential thermal distortions. **Left:** Beam without the SRM. The mode mismatch distortion, LG_{10}, is clearly visible. **Right:** Beam with the current SRM ($T = 20\%$). The distortion of the beam is partially healed and the field is dominated by the 00 mode.

2.9 Conclusion

In this chapter I have introduced the idea of modelling beam and mirror distortions using higher order Gaussian modes. Simple distortions can be described by the addition of one HOM, an order 1 mode for misalignment (HG_{10}) and an order 2 mode for mode mismatch (LG_{10}). More arbitrary distortions, such as mirror surface distortions, require a greater number of modes. The modal model is suitable for simulations of gravitational wave detectors, as the cavities which make up these detectors ensure most of the power circulating in the interferometer is in the cavity eigenmode.

The HOM behaviour of Advanced LIGO subsystems was illustrated using the simulation tool FINESSE [49], in the presence of thermal aberrations. For the arm cavities a quasi-analytic approach suggests the maximum suppression of modes created inside an optical cavity is ~ 0.25. Simulations of these arm cavities demonstrated that the HOM content inside the arm cavities is dependent on the total arm distortion, or $Z^2_{ITM} + Z^2_{ETM}$. The round-trip loss, on the other hand, depends on the similarity of the distortion of the two mirrors, and is minimised for symmetric

distortions. We extend this behaviour to a Michelson with arm cavities, where the addition of thermal distortions contribute to junk light at the detector output. This is characterised by the contrast defect, which depends on the differential distortions of the two Michelson arms.

The final results presented in this chapter illustrate an additional benefit of signal recycling in Advanced LIGO: mode healing. The addition of a mirror at the output forms a resonant cavity with the rest of the interferometer. In the case where the cavity is resonant for the 00 mode the higher order modes in the output beam are suppressed. Investigating this effect with thermal distortions applied to the ETMs demonstrates this effect for the current SRM transmission of 20%, and would favour a lower transmission. Further investigations of this effect are planned, for different tunings of the signal recycling mirror.

Chapter 3

Potential of higher-order Laguerre-Gauss beams in gravitational wave interferometers

In this chapter I investigate the potential of a future upgrade to advanced detectors: the use of higher order Laguerre-Gauss modes. In particular I evaluate the performance of the mode LG_{33} in realistic, high finesse cavities and develop an analytical method to derive mirror requirements for higher order modes.

To reduce mirror thermal noise in future detectors the higher order mode LG_{33} has been proposed as the interferometer input beam. The cavities in GW detectors will be degenerate for higher order modes: all order 9 modes will be resonant in a cavity resonant for LG_{33}. In this chapter a simulation investigation of realistic Advanced LIGO cavities demonstrates a low purity of 88.6% of the circulating beam due to this degeneracy.

Complimenting this simulation investigation is an analytical approach: calculating the coupling between LG modes for specific mirror shapes. This approach quickly identifies the mirror shapes, described by Zernike polynomials, which couple between the order 9 modes and lead to strong distortions of the beam. Using this

new method I calculated mirror requirements for LG_{33}, restricting the amplitude of 3 Zernike polynomials to suppress distortions of the circulating beam by over a factor of 100. This work was originally published in [36] and [60].

3.1 Mirror thermal noise

The sensitivity of Advanced LIGO is expected to be limited by quantum noise at most frequencies. However, at around 100 Hz, in the most sensitive region of the interferometer, it is predicted that the limiting noise source will be thermal noise (see figure 3.1). More precisely, as there are several different thermal noises, the sensitivity is expected to be limited by thermal noise of the test masses, in particular coating Brownian thermal noise.

Mirror thermal noise arises from the Brownian motion of atoms in a mirror, which excite the elastic modes of the mirror surface. This motion of the surface is

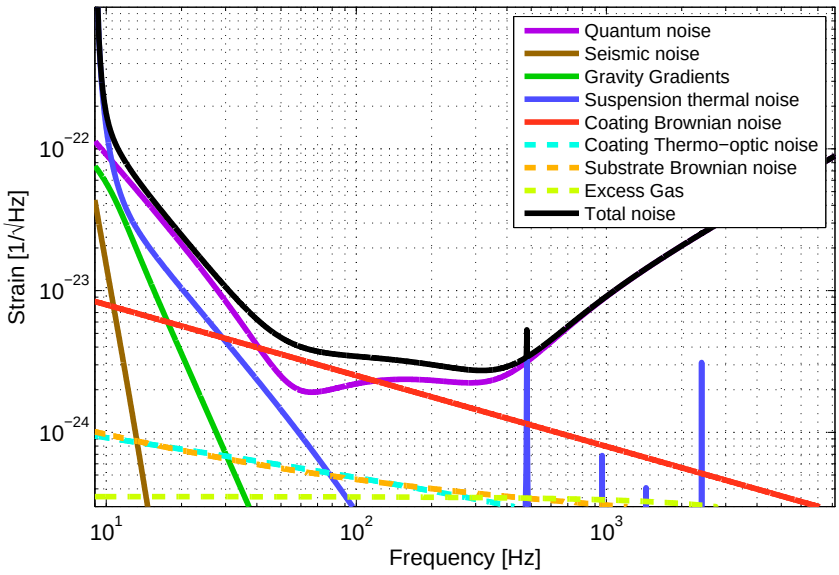

Figure 3.1: Noise curves for Advanced LIGO operating at high power (125 W input power) with the signal recycling mirror optimally tuned for Neutron Star – Neutron Star (NS – NS) inspiral GW signals [19]. The individual noises are plotted, as well as the combined total noise. Quantum noise (comprising radiation pressure noise at low frequencies and shot noise at high frequencies) is the limiting noise source at most frequencies.

interpreted by the interferometer as a displacement of the mirror, creating a change in phase which cannot be distinguished from that caused by a gravitational wave. The power spectral density of the observed displacement caused by this motion is (at low frequencies) [61; 62]:

$$S_x(f) = \frac{4k_B T}{\pi f}\Phi U \tag{3.1}$$

where k_B is Boltzmann's constant, T is the mirror temperature, f is the displacement frequency, Φ is the loss angle and U is the strain energy stored in the test mass. U is dependent on the intensity distribution of the incident beam.

There are several possible ways in which this noise could be reduced. One option is to lower the temperature of the interferometer. However, the test masses in the detectors are highly isolated, making heat extraction difficult. Other concerns include the coupling of vibrations to the test masses by cryocoolers and the unsuitability of silica at low temperatures. The advanced detector KAGRA [10] in Japan will be the first cryogenic gravitational wave interferometer and will be a good test of cryogenic technologies. However, converting Advanced LIGO into a cryogenic interferometer would be expensive and is unsuitable as a potential upgrade.

Mirror thermal noise can be reduced by using mirror materials with even higher quality factors (Q-factors) than the current test masses. High quality materials contain most of the surface motion of the mirror within narrow frequency bands around the natural resonances of the elastic modes. Careful design can ensure these are out of the detection band. Current research into suitable materials for future generation detectors is underway [63].

3.1.1 Thermal noise with different beam shapes

An alternative approach for reducing mirror thermal noise involves reducing the phase change induced by the fluctuating displacement of the mirror surface, rather

than reducing the displacement itself. This is achieved using alternative beam shapes to the currently used fundamental Gaussian beam.

The observed displacement of the test mass, due to coating Brownian thermal noise (equation 3.1), depends on U, the strain energy stored in the test mass. U is effectively the average strain energy across the surface of the mirror, weighted by the intensity of the read out beam. Current gravitational wave detectors use the fundamental Gaussian beam, whose intensity is concentrated in the mirror centre. To reduce the observed displacement a beam with a more even intensity distribution can be used to effectively average over the mirror surface fluctuations caused by thermal noise. This reduces the displacement of the mirror surface seen by the interferometer.

Several different types of readout beam have been considered for the reduction of thermal noise in this manner [53]. For example, for a flat top beam the coating strain energy is given by:

$$U_{flat} = \delta_C \frac{(1+\sigma)(1-2\sigma)}{\pi Y b^2} \tag{3.2}$$

where Y is the Young's modulus of the coating, σ is its Poisson ratio, δ_C is the thickness of the dielectric coating stack and b is the width of the beam: the strain energy, and thermal noise, is minimised by using a wide flat top beam.

Another category of beams, the Laguerre-Gauss (LG) beams result in a coating strain energy of [53]:

$$U_{Gauss} = \delta_C \frac{(1+\sigma)(1-2\sigma)}{\pi Y w^2} \alpha_p^l \tag{3.3}$$

In this case w refers to the beam spot size of the LG mode and α_p^l refers to a reduction factor associated with a particular mode. Again the strain energy is reduced with a large beam size, but for LG beams this also depends on the mode of the beam, through α_p^l. A particular advantage of Laguerre-Gauss beams, over

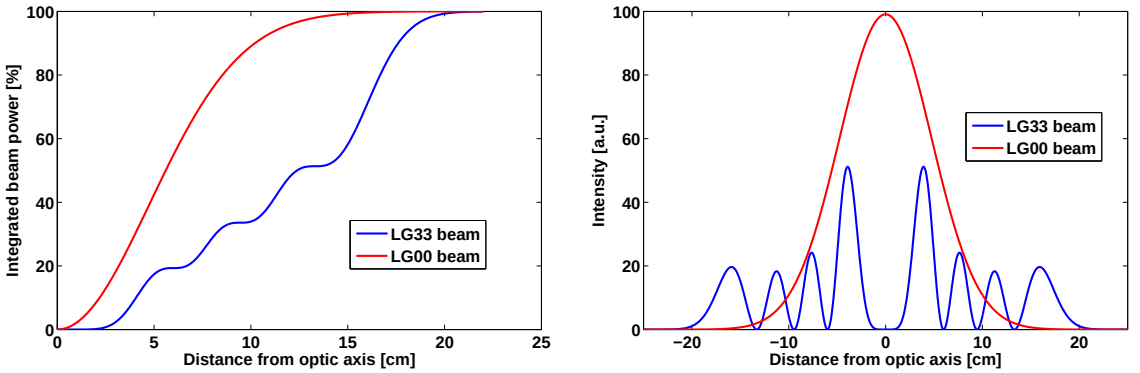

Figure 3.2: Comparing the Laguerre-Gauss mode LG_{33} and the fundamental Gaussian mode, LG_{00}. **Left:** Integrated power vs. distance from the optical axis. For the 00 mode the power is concentrated in the centre. For the LG_{33} mode the power is distributed more evenly, before dropping off sharply at 15-20 cm. **Right:** Beam intensity. Both the LG_{00} and LG_{33} beams correspond to the same total power. Images courtesy of Paul Fulda.

flat top or other beam types, is that LG modes are compatible with the current detectors, which use spherical mirrors to resonate Gaussian beams in a series of cavities. A particular higher order beam, LG_{33}, has been proposed as a candidate for thermal noise suppression [64]. Figure 3.2 shows the wide intensity distribution of LG_{33} compared to the fundamental mode. The power of the LG_{33} mode is more evenly spread over the central region and drops off steeply at the edge. In theory such a mode will reduce mirror thermal noise in future detectors.

Several different types of beam have been suggested to reduce the effects of thermal noise. These are summarised in table 3.1 with the thermal noise suppression factors calculated for Advanced LIGO. These numbers suggest that a conical beam would be the best candidate to suppress thermal noise. However, both conical and

Beam	Mirror	TN suppression
LG_{33}	Spherical	1.61
Mesa	'Mexican hat'	1.53
Conical	Conical	2.30

Table 3.1: Different beams consider to reduce the effects of mirror thermal noise in gravitational wave detectors, their required mirror shape and the thermal noise suppression as calculated for Advanced LIGO [64].

mesa beams require complex mirror shapes with well defined centres to form resonant cavities, which will require very accurate alignment. Higher order LG beams, on the other hand, are compatible with the spherical mirrors currently used in gravitational wave interferometers. It has been proposed that higher order Lagurre-Gauss beams are the best choice for the reduction of thermal noise.

3.1.2 Thermal noise with Laguerre-Gauss beams

Higher order LG modes will suppress the mirror thermal noise by different factors, α_p^l, as shown in table 3.2 [53]. In a GW detector, such as Advanced LIGO, constraints on the beam size mean α_p^l cannot be directly compared. The beam size, compared to the mirror, must not result in excess power lost over the edges of the mirror, so called *clipping loss*. LG modes require different w to achieve the same clipping loss. As w impacts the thermal noise suppression we must include this in any comparison. Using a typical clipping loss of 1 ppm (1 part-per-million) the realistic suppression factors are summarised in table 3.2 [65].

These numbers suggest there is a tradeoff in improvement in thermal noise between the higher order mode suppression factor and an increase due to smaller w. We also consider that high order modes have most of their intensity in the inner and outer ring, concentrated near the edge of the mirror. Since the edge of the mirror

Mode	α_p^l	w/w_0^0	TN suppression
LG_{00}	1	1	1
LG_{11}	0.31	0.79	1.42
LG_{22}	0.19	0.68	1.56
LG_{33}	0.14	0.61	1.63
LG_{44}	0.11	0.56	1.69
LG_{55}	0.10	0.52	1.64

Table 3.2: The suppression in coating Brownian thermal noise for different Laguerre-Gauss modes compared to the fundamental mode (LG_{00}). α_p^l refers to the suppression factor for equal beam sizes [53] and w/w_0^0 gives the beam sizes for 1 ppm clipping as a fraction of the LG_{00} radius [65].

is likely to be noisy this favours lower order modes. Consequently, the LG_{33} beam was proposed for thermal noise reduction.

3.2 Potential of the LG_{33} mode

In theory the use of an LG_{33} mode in a gravitational wave detector will reduce the observed thermal noise of the mirrors. It is important to test the behaviour of this higher order mode in setups representative of the real detectors, to compare the performance with that of the currently used fundamental beam. In particular any effects which will impact the beam shape should be investigated, as this new mode is likely to exhibit different coupling behaviour to that of the 00 mode.

3.2.1 A reminder of Laguerre-Gauss modes

The spatial distribution of the Laguerre-Gauss modes is given by [17]:

$$u_{pl}(r,\phi,z) = \frac{1}{w(z)}\sqrt{\frac{2p!}{\pi(|l|+p)!}}\exp\left(\mathrm{i}\,(2p+|l|+1)\psi(z)\right) \left(\frac{\sqrt{2}r}{w(z)}\right)^{|l|} L_p^{|l|}\left(\frac{2r^2}{w^2(z)}\right)\exp\left(-\mathrm{i}\,\frac{kr^2}{2R_C(z)} - \frac{r^2}{w^2(z)} + il\phi\right) \tag{3.4}$$

where the radial index p and azimuthal index l define the differences in shape and phase from the fundamental Gaussian beam. As well as the difference in beam shape, different order LG modes accumulate different multiples of Gouy phase, $\psi(z)$, as they propagate. A cavity resonant for the 00 mode will, for a well designed cavity, not be resonant for other modes. However, in terms of Gouy phase there is no way to separate different modes of the same order $(2p+|l|)$, meaning a cavity resonant for the LG_{33} mode will be resonant for all other modes of that order, in this case order 9.

3.2.2 Previous work

Research into the potential of the LG_{33} mode for gravitational wave detectors has been ongoing for several years. Initially a simulation investigation detailed in [65] demonstrated that the LG_{33} mode is compatible with the current methods for generating longitudinal and angular control signals. Tabletop experimental investigations in [66] and [67] used spatial light modulators and phase plates to generate an LG_{33} mode [68; 69] and demonstrated the mode-cleaning technique for an LG_{33} beam, using a linear mode-cleaner as opposed to the traditionally used triangular mode-cleaner. The prediction that an LG_{33} mode would produce similar longitudinal control signals to the fundamental mode was tested and verified experimentally. The control of a Michelson using LG_{33} was also successfully demonstrated in [67].

Previous investigations are optimistic on the outlook for LG_{33}. However, the behaviour of LG_{33} in large-scale interferometers, similar to the detectors, has yet to be investigated. In particular, the impact of realistic mirror surface distortions in the large-scale, high finesse cavities of advanced detectors has yet to be considered. Such distortions could have a significant impact on the shape and purity of the beam, due to the degeneracy of optical cavities for higher order modes. This is the subject of the investigations detailed in this chapter.

3.2.3 Higher-order mode degeneracy

The fundamental mode is the only mode of order 0 and a well designed optical cavity will ensure the next order which overlaps with the 00 resonance is a very high order unlikely to be present in the cavity. Essentially on 00 resonance the cavity is not resonant for other modes. This is not the case for higher order modes such as the order 9 mode LG_{33}. There are 10 modes of order 9, which will all share the same resonance condition, as they all accumulate 10 multiples (order + 1 = 10) of the Gouy phase as they propagate. The five unique beam shapes of the order 9

Figure 3.3: The 5 unique amplitude distributions of the order 9 Laguerre-Gauss modes ($2p + |l| = 9$). From left to right, $LG_{0\pm9}$, $LG_{1\pm7}$, $LG_{2\pm5}$, $LG_{3\pm3}$, $LG_{4,\pm1}$.

Laguerre-Gauss modes are shown in figure 3.3. Each shape has two possible modes for $\pm l$. The order 9 modes are $LG_{0\pm9}$, $LG_{1\pm7}$, $LG_{2\pm5}$, $LG_{3\pm3}$ and $LG_{4\pm1}$. A cavity tuned to be resonant for LG_{33} will also be resonant for all other order 9 modes.

This degeneracy of cavities for the order 9 modes can potentially lead to additional losses: any coupling into the other order 9 modes in the interferometer will be enhanced. This can result in highly distorted beams circulating in the cavities which make up many subsystems of the detectors: mode-cleaners, arm cavities, recycling cavities etc. Simulations have shown that the use of LG_{33} can result in a significant contrast defect [70; 71]. We aim to investigate how the expected mirror surface distortions of advanced detectors would affect the purity of an LG_{33} mode, by analytic calculation and numerical simulation, as reported in [36; 60].

3.2.4 Contrast defect

Distortions of the beam occur in the high finesse arm cavities of the detectors. The problem, for gravitational wave detectors, occurs when the beams from each arm interfere at the detection port. Optical defects, such as mirror surface distortions, differ between the two arms, resulting in different couplings and different modes in each arm. For an LG_{33} beam these differences will be enhanced if coupling occurs into the other order 9 modes. This could result in a much higher contrast defect than that achieved using the 00 mode. Contrast defect is defined as the ratio between

the power at the output and the power inside the interferometer:

$$C = \frac{P_{\mathrm{AS}}}{P_x + P_y} \tag{3.5}$$

where P_{AS} is the power at the detector output (anti-symmetric port) and P_x and P_y refer to the power hitting the beam-splitter from the x and y arms. For an LG_{33} beam the enhancement of distortions of the beam due to HOM degeneracy is likely to degrade the contrast defect in two ways. The most detrimental effect is an increase in P_{AS}, as the destructive interference between the two arms is reduced. Greater distortions of the beam will also reduce the power buildup, increasing the contrast defect.

Figure. 3.4 shows the power at the output, P_{AS}, for a Fabry-Perot Michelson interferometer with Advanced LIGO parameters [31]. The power is shown for LG_{33} and LG_{00} input beams as the differential arm length is tuned. With perfect mirrors there is no difference between the two modes and the minimum output power is determined by differential losses between the arms. When the interferometer is

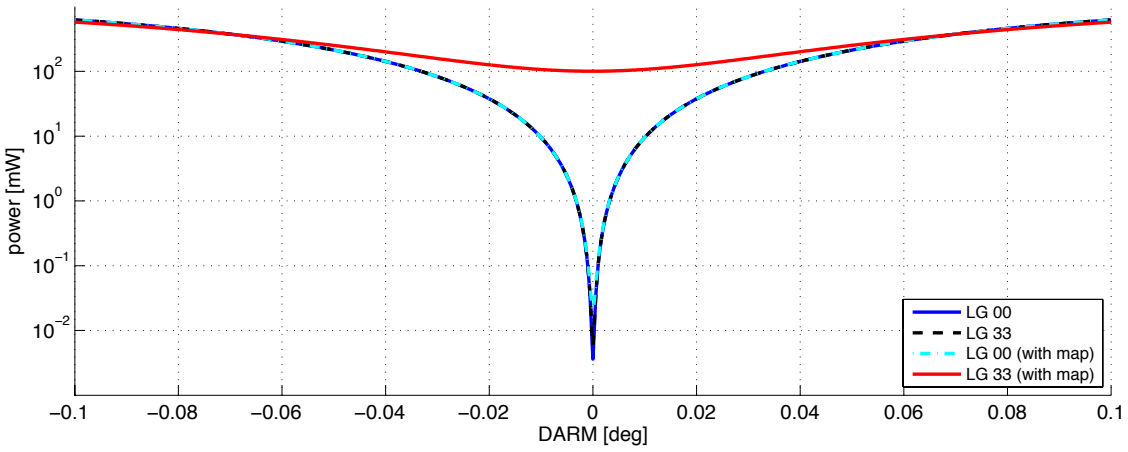

Figure 3.4: Output power in an Advanced LIGO Michelson with arm cavities as the differential arm motion (DARM $= \frac{L_x - Ly}{2}$) is tuned around the dark fringe. The interferometer is simulated for different input laser beams, LG_{33} and LG_{00}, using perfect mirrors and with an Advanced LIGO mirror map applied to the x-arm end test mass.

simulated with a distortion applied to one of the arms, in this case a *mirror map* (see section 3.3.1) applied to the end mirror of the x arm, there is a significant difference in behaviour between the two modes. When an unbalanced distortion is applied to the Michelson the output power, and hence contrast defect, for LG_{33} is significantly larger than for LG_{00}. This is due to the degeneracy of the arm cavities enhancing modes other than LG_{33} in the x arm, whilst the perfect y arm does not couple light out of the LG_{33} mode. The non-LG_{33} modes from the x arm have no counterpart to interfere with, and so appear at the dark port. This is illustrated in figure 3.5 where plots of the beam at the output of the interferometer are shown, for LG_{33} and LG_{00} in this case of unbalanced distortions. For LG_{33} the intensity pattern at the output is dominated by order 9 modes. The beam appears to be a mixture of Laguerre-Gauss and Hermite-Gauss modes, suggesting the mirror surface contains some distortions which break the cylindrical symmetry of the LG modes (as seen later in section 3.2.5). Compared to the output beam for LG_{00}, the LG_{33} beam has an intensity around 1000 times greater. Such an increase in power at the output is unacceptably high.

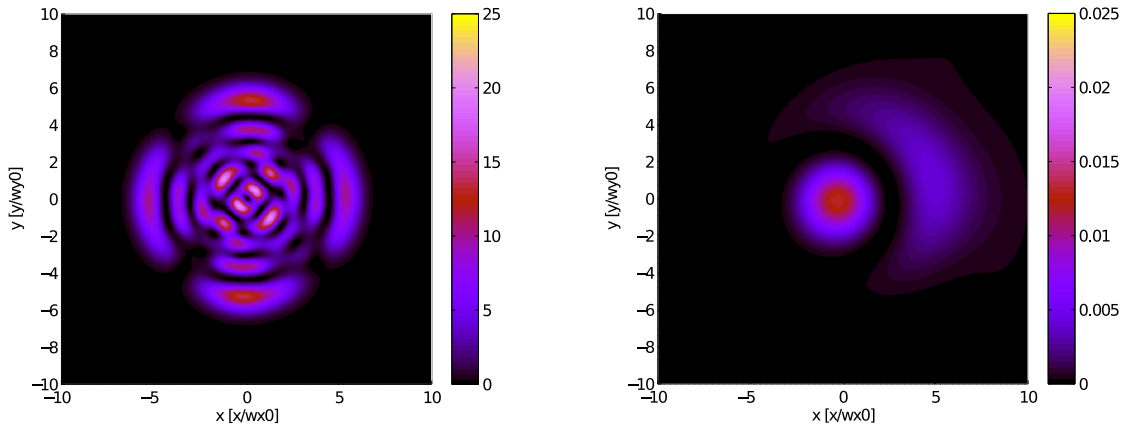

Figure 3.5: Output beam for an Advanced LIGO Fabry-Perot Michelson, with a mirror map applied to the end mirror of the x arm. The output beam is shown for an input LG_{33} beam (left) and an input LG_{00} beam (right). The power in the beam for the 00 case is around 1000 times smaller than for LG_{33}.

3.2.5 Frequency splitting

So far we have assumed that each mode of the same order will be resonant at the same cavity tuning, or laser frequency tuning. This is true for perfect cavities. For realistic cavities the distorted nature of the mirrors, coupled with the different shapes of the modes, means each mode will 'see' a slightly different cavity. This is more easily explained by the example of higher order Hermite-Gauss modes in an astigmatic cavity. The HG modes can be split into their x and y components [17; 47]:

$$u_{nm}(x, y, z) = u_n(x, z)\ u_m(y, z) \tag{3.6}$$

where the x component is given by:

$$\begin{aligned} u_n(x, y) = &\left(\frac{2}{\pi}\right)^{\frac{1}{4}} \frac{1}{\sqrt{2^n\ n! w(z)}} \exp\left(\mathrm{i}\,(n + \tfrac{1}{2})\psi_x(z)\right) \\ &H_n\left(\frac{\sqrt{2}x}{w(z)}\right) \exp\left(-\mathrm{i}\,\frac{kx^2}{2R_C(z)} - \frac{x^2}{w^2(z)}\right) \end{aligned} \tag{3.7}$$

and equivalently for the y component, u_m. The total Gouy phase accumulated by an HG mode is the sum of the phase in x and y:

$$\varphi_{nm} = (n + \tfrac{1}{2})\psi_x(z) + (m + \tfrac{1}{2})\psi_y(z) \tag{3.8}$$

The round-trip Gouy phase of a cavity is related to the cavity g-factors, i.e. in x [46]:

$$\Psi_x(z) = 2\cos^{-1}\left(\sqrt{g_{1x}g_{2x}}\right) \tag{3.9}$$

and equivalently for y. g_{1x} and g_{2x} are the factors for the two individual mirrors in the x direction. The g-factor is given by:

$$g = 1 - \frac{L}{R_C} \tag{3.10}$$

For a cavity with perfectly spherical mirrors the Gouy phase is the same in the x and y directions and all modes of a given order share the same resonance condition. In an astigmatic cavity, with slightly different curvatures in x and y, the cavity eigenmode is astigmatic and the round-trip Gouy phase is different in x and y. In this case the HG modes of a given order will have slightly different resonances, as each mode has different contributions from the x and y Gouy phases (equation 3.8). The difference in resonant tuning, or frequency, depends on the extent of the astigmatism. A large astigmatism can result in *frequency splitting*, where the difference in resonant frequencies is large enough that the resonance peaks of the different modes completely separate.

Let's consider the case of an LG_{33} beam in an astigmatic cavity. The LG_{33} mode can be expressed as a sum of Hermite-Gauss modes as summarised in table 3.3. For this example the cavity setup simulated was that of one of the 10 m arms of the Glasgow prototype interferometer [72] [1]. The design parameters for this cavity are summarised in table 3.4. This cavity was simulated with an LG_{33} input beam for two cases: 1) perfect mirrors with ETM $R_c = 15\,\mathrm{m}$; and 2) some astigmatism of the end mirror, with $R_{cx} = 15\,\mathrm{m}$, $R_{cy} = 15.5\,\mathrm{m}$ (a relativley large astigmatism to demonstrate frequency splitting). In both cases the input beam is mode matched to the design with $R_{cx} = R_{cy} = 15\,\mathrm{m}$. The intra-cavity power for these two cases is plotted in figure 3.6. The perfect case results in a single clean resonance peak

[1] The Glasgow prototype was used for further experimental investigations of LG_{33}, expanding on the work detailed in [66]. The prototype is representative of large scale interferometers, using suspended optics and a vacuum chamber. The results of this LG_{33} investigation exhibited frequency splitting suggestive of strong astigmatism [72], making this a suitable simulation example for such effects.

HG mode	9, 0	8, 1	7, 2	6, 3	5, 4	4, 5	3, 6	2, 7	1, 8	0, 9
power [%]	16.41	16.41	0	12.50	4.69	4.69	12.50	0	16.41	16.41
phase [°]	180	-90	0	-90	0	-90	0	0	0	90

Table 3.3: The power and phase of the ten order 9 Hermite-Gauss modes (indices n, m) which recreate the Laguerre-Gauss mode LG_{33} (calculated from equation 2.16).

parameter	value
ITM trans.	1%
ETM trans.	40 ppm
ETM R_c	15 m
length	10 m

Table 3.4: The design/nominal parameters for one of the arms of the Glasgow prototype interferometer [72]. The transmissions of the two mirrors are given, as well as the geometric properties of the cavity. In this case the input mirror (ITM) is flat.

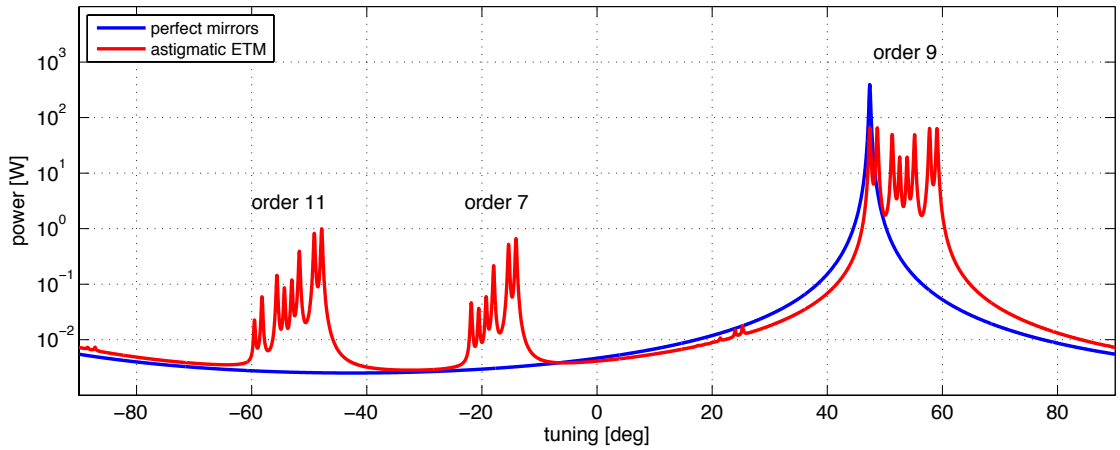

Figure 3.6: Simulated circulating power in an arm of the Glasgow prototype when an LG_{33} beam is injected into the cavity. Two cases are considered: 1) perfectly spherical mirrors and perfect mode-matching and 2) some astigmatism of the end mirror and imperfect mode matching. In case 2 the curvature (of the end mirror) in x is the nominal 15 m, whilst the curvature in y is 15.5 m, with the injected beam still matched to the 15 m case. The astigmatism results in *frequency splitting* of the LG_{33} input beam. The mode mismatch of the input beam in case 2 results in additional modes, in particular orders 7 and 11, each with $\sim 1\%$ of the power of the order 9 modes. These modes also exhibit frequency splitting.

for the order 9 mode. The astigmatic case results in splitting of this order 9 peak, as described above, due to the difference in round-trip Gouy phase for each of the HG modes which make up LG_{33}. The overall order 9 peak becomes much broader and the maximum circulating power is much lower than the perfect case, as the power in the LG_{33} mode is spread between the different HG modes over a range of tunings. The mode mismatch in this case results in additional modes injected into the cavity, particularly orders 7 and 11. The peaks of these modes also exhibit

frequency splitting.

Figure 3.7 shows a closeup of the order 9 peak. This clearly shows that the resonance peaks of the 8 HG modes which make up LG_{33} have separated. The circulating beam at each resonant tuning is shown. This shows that there is a relation between the mode indices, n and m, and the resonant frequency: modes with large n/ small m occur at lower tunings than those with small n/ large m. We can calculate the frequency splitting analytically, by considering the equations for round-trip Gouy phase in x and y. Firstly we consider the total width of a generic order, N, peak, by looking at the peaks at the two extremes of the tuning: HG_{N0} and HG_{0N}. The round-trip Gouy phase for HG_{N0} is [73]:

$$\varphi_{N0} = (N + \tfrac{1}{2})\Psi_x + \tfrac{1}{2}\Psi_y \tag{3.11}$$

and for HG_{0N} is:

$$\varphi_{0N} = \tfrac{1}{2}\Psi_x + (N + \tfrac{1}{2})\Psi_y \tag{3.12}$$

The frequency separation of these two modes, and the width of the order N peak,

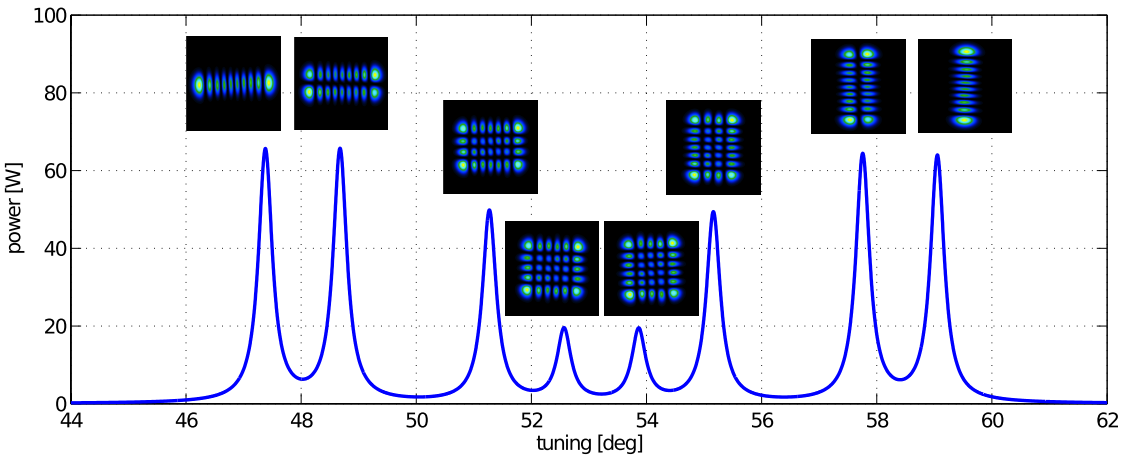

Figure 3.7: The order 9 resonance peak in a simulation of an astigmatic Glasgow prototype arm cavity. The peak exhibits frequency splitting, breaking the LG_{33} input beam into its individual Hermite-Gauss modes. Each peak corresponds to the resonance of an HG mode, from left to right: HG_{90}, HG_{81}, HG_{63}, HG_{54}, HG_{45}, HG_{36}, HG_{18} and HG_{09}.

is computed from the difference in round-trip phases:

$$f_{width} = FSR\frac{N}{2\pi}|\Psi_x - \Psi_y| \tag{3.13}$$

where the $FSR = \frac{c}{2L}$ for frequency separation and the $FSR = 180°$ for tuning separation. In our simulation of an astigmatic cavity the width of the order 9 peak is 973 kHz, or 11.7°. Similarly, the separation of neighbouring peaks can be derived:

$$\delta f = FSR\frac{1}{2\pi}|\Psi_x - \Psi_y| \tag{3.14}$$

which in our example is 108 kHz, or 1.3°. If f_{width} is greater than the line-width of the cavity the peaks begin to separate and we have frequency splitting.

The effect of the astigmatic mirror breaks the cylindrical symmetry of the cavity eigenmode. As the LG modes are cylindrically symmetric they cannot resonate in such a cavity. A more generic distortion can cause frequency splitting of a higher order mode. In the same way that the HG modes resonate in a highly astigmatic cavity, where LG modes do not, the application of a surface distortion will break a higher order mode into the appropriate modes for the resonator formed by the distorted surfaces.

The extent of the frequency splitting (f_{width} and δf) depends on the magnitude of the astigmatism, or distortion, but the effect on the resonance peak - whether the individual peaks separate or not - also depends on the finesse of the cavity, as this determines the line-width of the cavity. If the frequency splitting is greater than the line-width the peaks are effectively separate. To illustrate this we now consider a setup representative of the advanced detectors: an Advanced LIGO arm cavity. A cavity described by Advanced LIGO geometric properties (curvatures and length) was simulated with an LG_{33} input beam for a range of cavity finesses. A surface distortion was applied to the ETM and the circulating power was detected as the

cavity was scanned around the order 9 peak. This power, normalised to the peak power for each value of finesse, is shown in figure 3.8. At low finesse the power in the order 9 modes is contained in a single wide peak. As the finesse is increased the overall peak narrows, until the line-width becomes smaller than the frequency separation of the order 9 modes. For high finesse the individual mode resonances completely separate.

In theory, large frequency splitting could be an advantage, as the separation of the resonances of the LG modes would negate the degeneracy issue. However, this would require specific distortions which don't break the cylindrical symmetry of the LG modes, as asymmetric distortions result in resonators for the HG modes. The expected mirror distortions are unlikely to provide such specific frequency splitting and, as is shown in figure 3.8, at the finesse of the Advanced LIGO arm cavities (450) and with the expected mirror distortions of the real mirrors, we do not expect to see the frequency splitting required to separate the different modes.

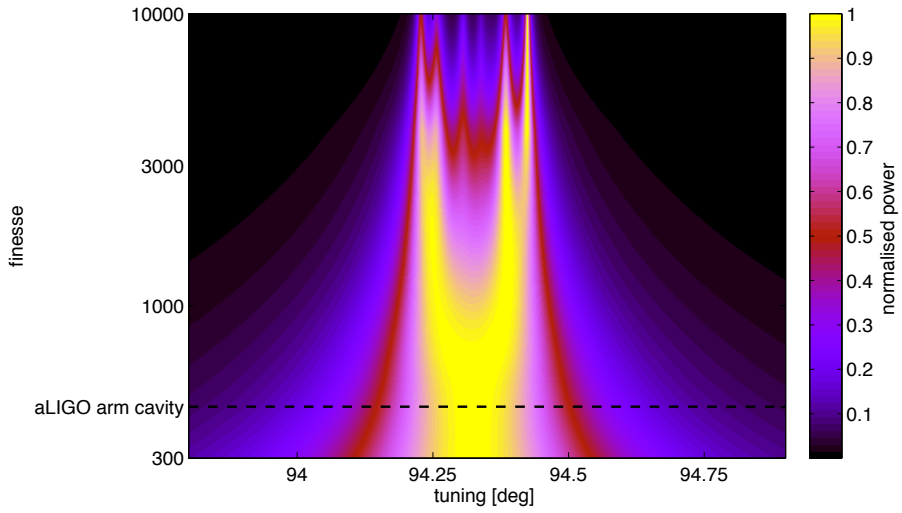

Figure 3.8: Normalised circulating power in an Advanced LIGO arm cavity simulated with an LG_{33} input beam and a distortion applied to the ETM (using an Advanced LIGO mirror map). The power is detected over the order 9 resonance peak, for a range of cavity finesses. The finesse of the Advanced LIGO arms is 450. For very high finesse the order 9 peak exhibits frequency splitting, where the peaks of individual order 9 modes separate, due to slight differences in their resonant tuning/ frequency.

3.3 Coupling between Gaussian modes

In the previous sections we have demonstrated that the degeneracy of cavities for higher order modes could result in a high contrast defect for LG_{33}. We now aim to quantify this problem, in terms of the types of surfaces which couple between order 9 modes and the behaviour of LG_{33} in realistic, high finesse cavities.

3.3.1 Methods for describing mirror surfaces

For this particular investigation the process by which coupling between the order 9 modes occurs needs to be fully understood. This requires an analysis of the mirror surfaces and methods for representing them, to conduct a simulation investigation into how particular mirror surfaces cause coupling between modes of the same order. There are several methods for representing mirror surfaces which we consider.

Mirror maps

The simplest way to represent a mirror surface is with a grid of data representing the measured surface of a real mirror, a *mirror map*. This is how mirror surfaces are implemented in the interferometer simulation FINESSE (see section 2.4.4). For this investigation we require maps representative of the mirrors used in advanced detectors, such as Advanced LIGO. An extensive database of measurements of the Advanced LIGO mirrors is available [74], as required to confirm the mirrors meet the requirements. These include maps of optical properties, such as reflectivity and transmission, as well as maps of the surface height of the mirrors. Some examples are shown in figure 3.9. These measurements correspond to the properties of the highly reflective mirror surface of a particular Advanced LIGO end test mass, ETM08. This particular mirror surface will be used extensively in the investigations detailed here, as a means of representing realistic mirror distortions.

In figure 3.9 several different types of map are shown. In all cases the different

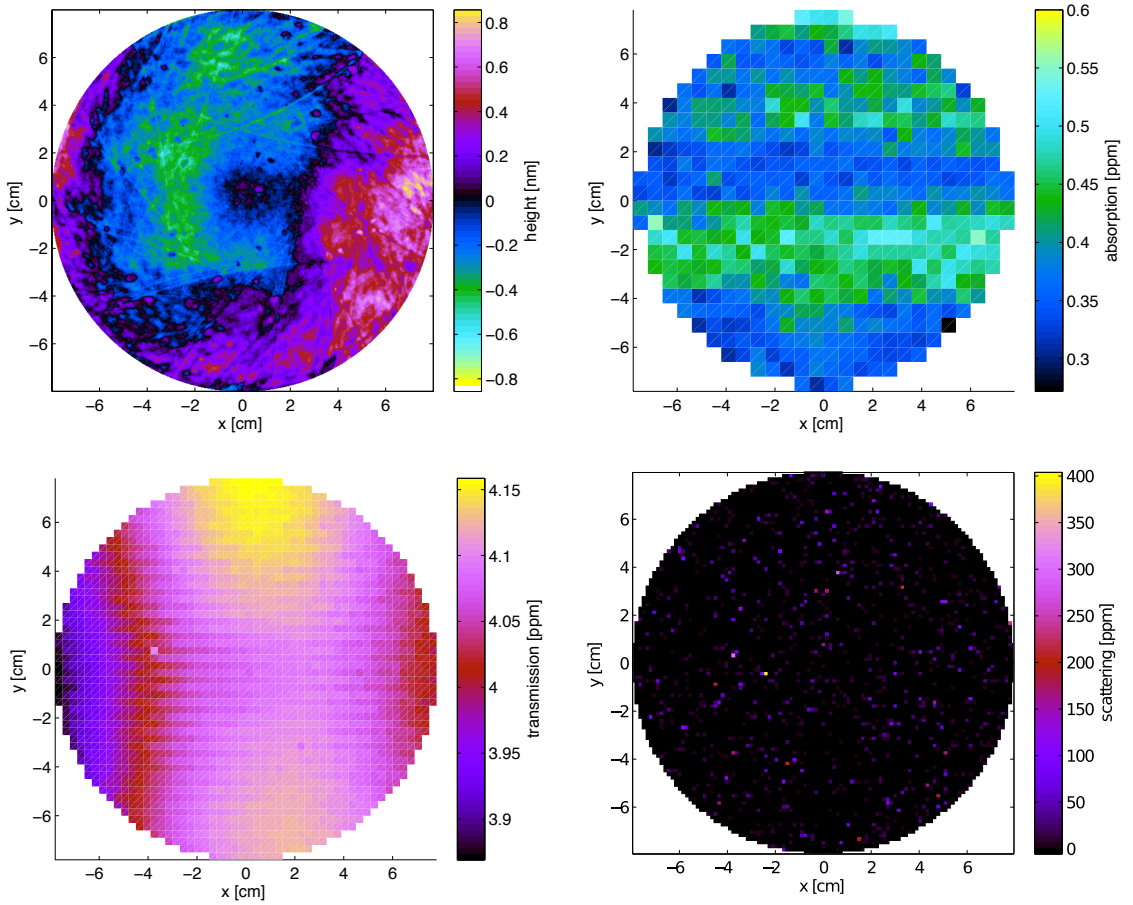

Figure 3.9: Various mirror maps measured from the Advanced LIGO end test mass ETM08 [74]. The maps refer to measurements of the highly reflective surface over the central 160 mm region. **Top left:** The surface height of the polished, uncoated substrate of the optic. **Top right:** The absorption of the coated mirror at 1064 nm. **Bottom left:** Transmission of light through the coated optic at 1064 nm. **Bottom right:** Average scatter from the coated mirror surface at 1064 nm.

properties are shown over the central region of the mirror, a diameter of 160 mm. This region requires more stringent requirements on various properties due to the concentration of the (fundamental) beam power within this area. The variation in mirror surface height (top left) is, at most, on the order of a nanometre. These maps are primarily used in commissioning tasks to do with beam shapes and HOM content, so are ideally suited for our investigation into higher order beams. The absorption (top right), transmission (bottom left) and scatter (bottom right) maps are also shown. However, it is the surface maps that we require for our investigation.

The particular map ETM08 was chosen for this investigation as this is one of the mirrors selected for use in Advanced LIGO. This mirror is also, from a simple comparison of mirror surface *rms* (root mean square), neither the best nor worst of the 4 ETMs chosen. At the time of this investigation the mirrors had yet to be coated and only maps for the polished surfaces were available. These maps are still suitable for our purposes, as they should be representative of the final mirrors, if not exactly quantitatively equivalent.

With such maps to represent the state-of-the-art mirror surfaces we can carry out simulations of LG_{33} in realistic advanced interferometer cavities, to assess the extent of the coupling between order 9 modes with the current mirrors used in advanced detectors.

Spatial frequencies

To complement simulations with mirror maps and for a proper understanding of the coupling it is useful to have an analytical description of the mirror surfaces. A commonly used method for describing surfaces is to use spatial frequencies or wavelengths. This is easier to explain in 1D rather than 2D. The distortion of a surface along the x-axis described by a single spatial wavelength is:

$$Z(x) = A\cos\left(2\pi F x + \phi\right) \tag{3.15}$$

where F is the spatial frequency, A is the amplitude of the distortion and ϕ is the initial phase of the distortion. For a purely cosine distortion $\phi = 0$, for purely sine $\phi = \frac{\pi}{2}$. A more generic distortion, such as those represented by Advanced LIGO mirrors, can be described by a sum of sines and cosines at different frequencies, F_n:

$$Z(x) = \sum_n A_n \cos(2\pi F_n + \phi_n) \tag{3.16}$$

The coefficients and phases are extracted from the discrete Fourier Transform of $z(x)$, calculated using a Fast Fourier Transform (FFT):

$$Z(k) = \sum_{n=0}^{N-1} z(n) \exp\left(-\frac{\mathrm{i}\, 2\pi(k-1)(n-1)}{N}\right) \tag{3.17}$$

where N is the number of elements in z, n is related to spatial coordinate x and k is related to spatial frequency F. This method can be adapted to a 2 dimensional surface, i.e. a mirror map, by averaging a 2D Fourier transform into a single 1D amplitude spectrum, similar to the root mean squared (rms) for each spatial frequency. In figure 3.10 this analysis for the particular map, ETM08, is shown. The amplitude of the lower spatial frequencies is significantly higher, as expected. Higher spatial frequencies occur naturally with smaller amplitudes but are also required to be very small in gravitational wave mirrors to reduce wide angle scattering out of the beam path. Low spatial frequency distortions correspond to the overall mirror shape, higher spatial frequencies refer to the *roughness* of the mirror. By using such an analysis it may be possible to identify certain spatial frequencies in the mirrors which couple between the order 9 modes.

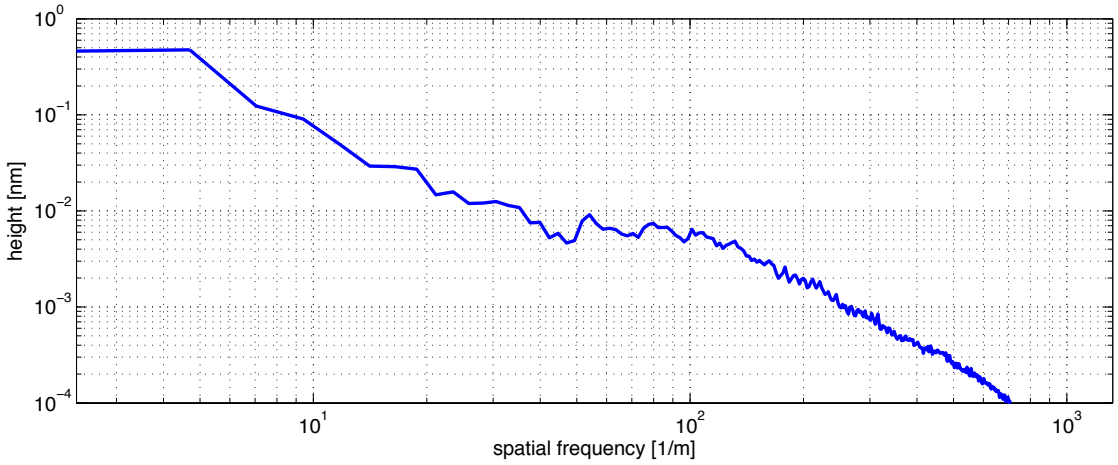

Figure 3.10: Amplitude of the different spatial frequencies present in the Advanced LIGO mirror map ETM08, calculated using a 2D FFT and computing the average for each spatial frequency. The offset, tilt and common curvature terms have been removed prior to carrying out this analysis.

Zernike polynomials

A convenient model for describing the overall shape and low spatial frequency distortions of a mirror surface are the Zernike polynomials. Zernike polynomials are a complete set of functions which are orthogonal over a unit disc, ideal for describing cylindrical mirror surfaces. These polynomials are defined by radial index, n, and azimuthal index, m, with $m \leq n$. For any index m we have [75]:

$$\begin{aligned} Z_n^{+m}(\rho,\phi) &= \cos(m\phi)R_n^m(\rho) \qquad \text{the even polynomial} \\ Z_n^{-m}(\rho,\phi) &= \sin(m\phi)R_n^m(\rho) \qquad \text{the odd polynomial} \end{aligned} \tag{3.18}$$

with ρ the normalised radial position, ϕ the azimuthal angle and $R_n^m(\rho)$ the radial function:

$$R_n^m(\rho) = \begin{cases} \sum_{h=0}^{\frac{1}{2}(n-m)} \frac{(-1)^h(n-h)!}{h!\left(\frac{1}{2}(n+m)-h\right)!\left(\frac{1}{2}(n-m)-h\right)!}\rho^{n-2h} & \text{for even } n-m \\ 0 & \text{for odd } n-m \end{cases} \tag{3.19}$$

This gives $n+1$ non-zero Zernike polynomials for each value of n. Some of the common optical features which are described by the low order Zernike polynomials are shown in figure 3.11. The simplest polynomials represent mirror defects we are familiar with: tilt (misalignment) and curvature (mode mismatch). The higher n polynomials represent higher spatial frequencies.

Odd and even Zernike polynomials describe the same shape for given n and m, with a rotation of $\frac{90^\circ}{m}$ with respect to each other. A combination of the odd and even polynomials result in the same shape rotated by a given angle with an amplitude:

$$A_n^m = \sqrt{(A_n^{-m})^2 + (A_n^{+m})^2} \tag{3.20}$$

Any surface defined over a disc can be described as a sum of Zernike polynomials,

n	m	Common name
0	0	Offset
1	± 1	Tilt in x/y direction
2	0	Curvature
2	± 2	Astigmatism
3	± 1	Coma along x/y axis

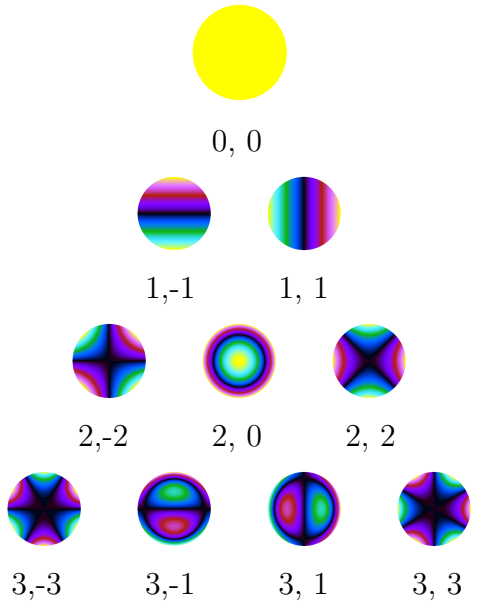

Figure 3.11: Plots of all the non-zero Zernike polynomials from $n = 0$ to $n = 3$, from odd polynomials with $m = -n$ on the far left to even polynomials with $m = n$ on the far right, in steps of 2. The colour scale represents negative surface heights with greens and blues, zero with black and positive surface heights with reds and purples.

in the same way any beam shape can be described as a sum of Gaussian modes. Higher spatial frequencies are represented by higher order polynomials. This is illustrated in figure 3.12, where the ETM08 mirror map is recreated using low order Zernike polynomials ($n \leq 20$). The overall shape of the Zernike surface looks very similar to the original map, but lacks the high spatial frequencies. These are shown

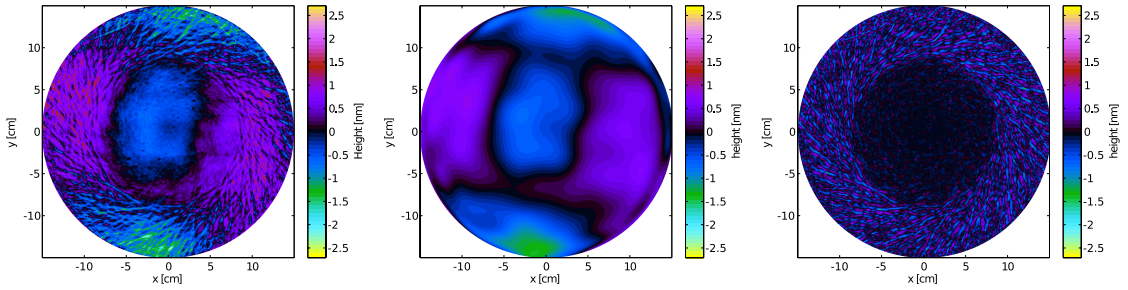

Figure 3.12: Representations of the Advanced LIGO mirror map ETM08. **Left:** Original map over 30 cm region, with offset, tilt and curvature (Z_2^0) removed. **Centre:** Map recreated from Zernike polynomials with $n \leq 20$, representing the overall shape of the mirror. **Right:** Residual surface after the Zernike map is removed, showing the higher spatial frequencies.

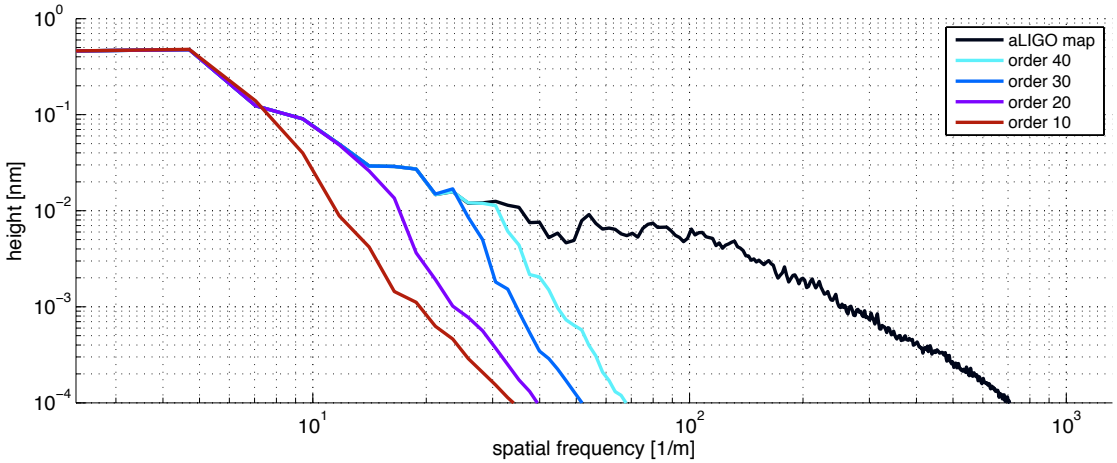

Figure 3.13: Spectra of spatial frequencies in different ETM08 maps. The spectrum for the original map is shown, as well as those for maps created from Zernike polynomials up to a given order. As more polynomials are added to the model the spectra tend to the original result.

in the residual map, which also illustrates the high polishing requirements for the central 16 cm region, compared to the total 30 cm region shown. Although high spatial frequencies can be represented by Zernike polynomials it is often convenient for mirror surface analysis to consider only the low order Zernike polynomials, with the rest of the mirror description contained in spectra of spatial frequencies. In figure 3.13 the spectrum of the ETM08 map is shown, as well as the spectra for Zernike maps recreated using polynomials up to a given order. Again this illustrates how the low order polynomials represent low spatial frequencies and including more polynomials to our model tends towards the original map.

3.3.2 Coupling from mirror surfaces

The coupling from one mode to another is described by a coupling coefficient, a complex number which describes the amplitude and phase of a particular mode in the distorted beam. For the case of reflection from a mirror, with a distorted surface described by Z, the coupling between Laguerre-Gauss modes can be calculated

as [17]:

$$k_{p,l,p',l'} = \int_S u_{p,l} \ \exp\left(2\mathrm{i}\, kZ\right) \ u^*_{p',l'} \ \mathrm{d}A \tag{3.21}$$

where $u_{p,l}$ is a mode in the incident beam and $u_{p',l'}$ is a mode in the reflected beam. In this case we assume that the distortion of the surface is small enough that it does not create a change in the beam parameter, i.e. the Gaussian parameters of the incident and reflected beam are the same. Coupling coefficients can be calculated for generic surfaces. However, we can now investigate the coupling which occurs from specific shapes and spatial frequencies, using the analytic methods for describing surfaces outlined above. The aim is to identify specific mirror surfaces which will couple between the order 9 modes.

Scattering of HOMs

In [76] Winkler presents an analytic approach to the scattering of light in the modal picture, taking the approach of describing a mirror surface using spatial frequencies and considering the x and y spatial components separately:

$$Z(x) = h_0 \cos\left(\frac{2\pi}{\Lambda}x + \phi\right) \tag{3.22}$$

where h_0 is the amplitude of the spatial distortion and Λ is the wavelength of the spatial distortion. For symmetric distortions (around $x = 0$) $\phi = 0$, for asymmetric distortions $\phi = \frac{\pi}{2}$. The approach of separating the distortions into x and y necessitates the use of the Hermite-Gauss modes, which can also be separated this way. Taking this approach, and assuming the distortion of the surface is small compared to the wavelength[1], Winkler derived an analytic expression for the coupling of an incident $n = 0$ mode into other modes. Here we expand this derivation for the case of an arbitrary incident mode.

[1] a valid assumption for advanced gravitational wave detectors, which use a wavelength of 1064 nm and state-of-the-art mirrors with distortions on the order of a nm.

The coupling from a particular spatial wavelength into a particular Hermite-Gauss mode can be separated into x ($n \to n'$) and y ($m \to m'$) coupling coefficients. For coupling between modes on reflection from a distorted surface described by Z the x coefficient is:

$$a_{n,n'} = \int_{-\infty}^{+\infty} u_n \exp\left(2\mathrm{i}\, kZ(x)\right)\, u_{n'}^*\, \mathrm{d}x \tag{3.23}$$

and similarly for y. u_n is the x component of an HG mode in the incident beam and $u_{n'}$ is the x component of a mode in the reflected beam:

$$u_n u_{n'}^* = \frac{1}{w}\sqrt{\frac{2}{\pi}}\frac{\exp\left(\mathrm{i}\,(n-n')\Psi\right)}{\sqrt{2^{n+n'}n!n'!}} H_n\left(\frac{\sqrt{2}x}{w}\right) H_{n'}\left(\frac{\sqrt{2}x}{w}\right)\exp\left(-\frac{2x^2}{w^2}\right) \tag{3.24}$$

Assuming $2kZ$ is small the exponential can be approximated:

$$\exp\left(2\mathrm{i}\, kZ\right) \approx 1 + 2\mathrm{i}\, kZ \tag{3.25}$$

The coupling coefficient becomes:

$$a_{n,n'} = \delta_{n,n'} + \int_{-\infty}^{+\infty} u_n(2\mathrm{i}\, kZ) u_{n'}^*\, \mathrm{d}x = \delta_{n,n'} + I \tag{3.26}$$

where the Kronecker delta is included for coupling back into an incident mode ($n = n'$). The integral becomes:

$$\begin{aligned} I &= C\int_{-\infty}^{\infty} H_n(v)H_{n'}(v)\exp\left(-v^2\right)\cos\left(\frac{\sqrt{2}\pi w}{\Lambda}v + \phi\right)\mathrm{d}v \\ &= C\cos\left(\phi\right)\int_{-\infty}^{\infty} H_n(v)H_{n'}(v)\exp\left(-v^2\right)\cos\left(\frac{\sqrt{2}\pi w}{\Lambda}v\right)\mathrm{d}v \\ &- C\sin\left(\phi\right)\int_{-\infty}^{\infty} H_n(v)H_{n'}(v)\exp\left(-v^2\right)\sin\left(\frac{\sqrt{2}\pi w}{\Lambda}v\right)\mathrm{d}v \end{aligned} \tag{3.27}$$

where

$$C = \frac{2\mathrm{i}\, kh_0}{\sqrt{\pi}} \frac{\exp\left(\mathrm{i}\,(n-n')\Psi\right)}{\sqrt{2^{n+n'} n! n'!}} \quad \text{and} \quad v = \frac{\sqrt{2}x}{w} \tag{3.28}$$

These two integrals can be solved using two standard identities [75]:

$$\begin{aligned}
\int_0^\infty e^{-x^2} \sin(bx) H_p(x) H_{p+2m+1}(x) \mathrm{d}x &= 2^{p-1}(-1)^m \sqrt{\pi}\; p!\; b^{2m+1} \exp\left(-\frac{b^2}{4}\right) L_p^{2m+1}\left(\frac{b^2}{2}\right) \\
\int_0^\infty e^{-x^2} \cos(bx) H_p(x) H_{p+2m}(x) \mathrm{d}x &= 2^{p-1}(-1)^m \sqrt{\pi}\; p!\; b^{2m} \exp\left(-\frac{b^2}{4}\right) L_p^{2m}\left(\frac{b^2}{2}\right)
\end{aligned} \tag{3.29}$$

for $b > 0$, where $L(x)$ refer to the Laguerre polynomials. Applying this to our problem, the integral in equation 3.27, we have:

$$b = \frac{\sqrt{2}\pi w}{\Lambda} \qquad p = \min(n, n') \tag{3.30}$$

These solutions correspond to odd couplings ($n - n'$ is odd, $m = \frac{1}{2}(|n-n'|-1)$) for asymmetric distortions (sine term) and even $n - n'$ couplings ($m = \frac{1}{2}|n-n'|$) from symmetric distortions (cosine term). We can apply these identities to solve our coupling approximation. However, to further simplify the problem the integral identities look very similar to the amplitude of the Laguerre-Gauss modes:

$$|U_{p,l}| = \frac{1}{W}\sqrt{\frac{2p!}{\pi(|l|+p)!}} \exp\left(-\frac{r^2}{W^2}\right)\left(\frac{\sqrt{2}r}{W}\right)^{|l|} \left|L_p^{|l|}\left(\frac{2r^2}{W^2}\right)\right| \tag{3.31}$$

In this case, r and W are not the radial coordinate and beam spot size as in the common definition of an LG mode, but related to the quantity $\frac{w}{\Lambda}$:

$$\frac{2r^2}{W^2} = \frac{b^2}{2} \qquad b = \frac{\sqrt{2}\pi w}{\Lambda} \quad \rightarrow \quad \frac{r}{W} = \frac{\pi w}{\sqrt{2}\Lambda} \tag{3.32}$$

We also have $p = \min(n, n')$ and $l = n - n'$. Writing the integral identities (equation 3.29) in terms of Laguerre-Gauss modes and substituting these solutions into

equation 3.27 we have[1]:

$$\begin{aligned} I &= C2^p\pi W\sqrt{\frac{p!(|l|+p)!}{2}}(\sqrt{2})^{|l|}\,|U_{p,l}|\,[\cos(\phi)\cos\left(|l|\tfrac{\pi}{2}\right)-\sin(\phi)\sin\left(|l|\tfrac{\pi}{2}\right)] \\ &= C2^p\pi W\sqrt{\frac{p!(|l|+p)!}{2}}(\sqrt{2})^{|l|}\,|U_{p,l}|\cos\left(\phi+|l|\tfrac{\pi}{2}\right) \end{aligned} \tag{3.33}$$

where:

$$p=\min(n,n') \qquad l=n-n' \qquad \frac{r}{W}=\frac{\pi}{\sqrt{2}}\frac{w}{\Lambda} \tag{3.34}$$

For simplicity we set $W=\frac{\sqrt{2}}{\pi}$ and $r=\frac{w}{\Lambda}$, the ratio of the beam spot size to the wavelength of the spatial distortion. Finally substituting in the values for C (equation 3.28) and using $p+|l|=\max(n,n')$ and $n+n'=2p+|l|$ (the order of the LG mode) we have:

$$a^1_{n,n'}=\delta_{n,n'}+\text{sign}\left(L_p^{|l|}(\pi^2r^2)\right)\frac{2\mathrm{i}\,k\;h_0}{\sqrt{\pi}}\exp(\mathrm{i}\,l\Psi)|U_{p,l}(r=\tfrac{w}{\Lambda},W=\tfrac{\sqrt{2}}{\pi})|\cos\left(\phi+|l|\tfrac{\pi}{2}\right) \tag{3.35}$$

adding in the sign of the Laguerre polynomial for the correct phase and the Kronecker delta, $\delta_{n,n'}$, to represent coupling back into an incident mode. The coupling between HG modes of different orders is well expressed by this first order approximation. This is demonstrated in figure 3.14, where $a_{n,n'}$ for $n=3$ and $n'=9$ is calculated for different spatial frequencies. The coupling is calculated in two ways: numerically, with no approximation; and using our analytical approximation (equation 3.35). The results are practically identical (see residual in figure B.3). This plot also highlights the Laguerre-Gauss shape of the coupling coefficients. For some spatial frequencies there is significantly more coupling than at others. The spatial frequencies contributing to the coupling will depend on which modes we are coupling between. So we can already see that there are particular types of distortions which

[1]The factors $\sin(|l|\frac{\pi}{2})$ and $\cos(|l|\frac{\pi}{2})$ come from a combination of the factors $(-1)^{|l|/2}$ and $(-1)^{(|l|-1)/2}$ and the fact that the integral including the sine term is 0 for even $n-n'$ and the integral including the cosine term is 0 for odd $n-n'$.

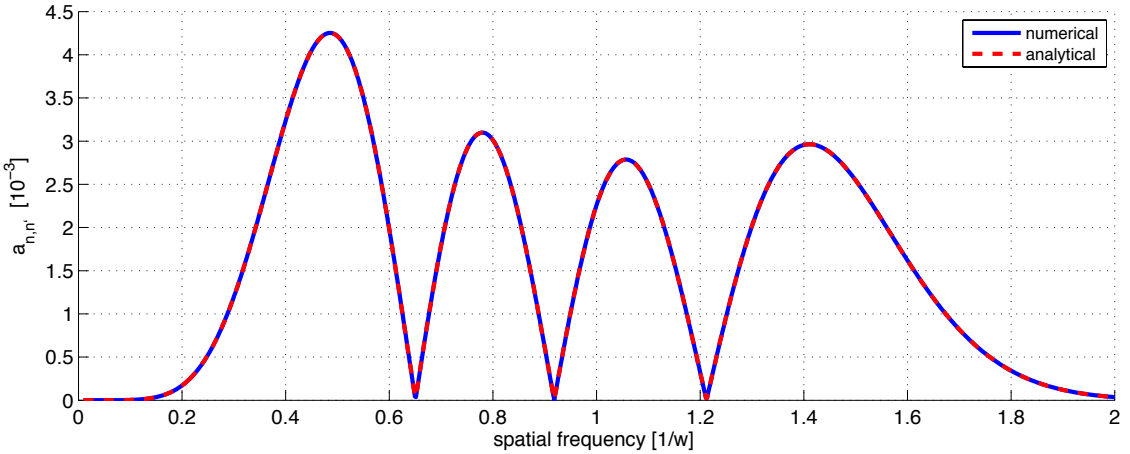

Figure 3.14: Amplitude of the coupling, $a_{n,n'}$, between modes with $n = 3$ and $n' = 9$, due to reflection from a distorted surface. The coupling is calculated for different spatial frequencies of a 1 nm surface distortion. The coupling is calculated numerically and using an analytical approximation (equation 3.35) developed from Winkler's work in [76].

cause particular couplings.

The coupling between HG modes as described by Laguerre-Gauss modes of order $n+n'$ is an elegant solution, from which we can quickly understand some properties of the coupling. For example, in general the higher-order LG modes are spread over wider r (see section 2.3.2). In this case $r = \frac{w}{\Lambda}$, i.e. r is proportional to spatial frequency for a fixed beam size, so we expect the range over which the coupling peaks are spread (see figure 3.14) to increase for larger $n + n'$. This means there is a wider range of spatial frequencies with potential to cause coupling between high order modes. We also observe that the azimuthal index of the LG mode is given by $l = n - n'$. Greater l results in a larger dark spot in the centre of the mode. In terms of the coupling approximation this means that low spatial frequencies couple less between modes with large $n - n'$.

This first order approximation is sufficient for coupling between different HOMs. For coupling back into the same mode ($n = n'$) we require up to second order,

otherwise the power in the mode increases upon reflection. We have:

$$a_{n,n'} \approx a^1_{n,n'} - k^2 h_0^2 \delta_{n,n'} - \text{sign}\left(L_p^{|l|}(4\pi^2 r^2)\right) \frac{k^2 h_0^2}{\sqrt{\pi}} |U_{p,l}(r = \tfrac{w}{\Lambda}, W = \tfrac{1}{\sqrt{2}\pi})| \cos\left(2\phi + |l|\tfrac{\pi}{2}\right) \tag{3.36}$$

where the second order corrections are also described by LG modes of order $n + n'$ but with a beam spot size half that of the LG mode describing first order coupling. An example of this coupling is shown in figure 3.15, where the coupling back into a mode with $n = 4$ is calculated, both numerically and analytically. As before the approximation and numeric results match up. At very low spatial frequencies, compared to beam size, the scatter is very low, as the surface looks essentially flat over the intensity distribution of the beam. In the mid range of spatial frequencies, particular frequencies scatter more power out of the incident mode. Finally, at high spatial frequencies the power scattered from the incident mode remains constant.

Further examples of the coupling approximation are shown in appendix B.4, in particular the coupling from $n = 0$ HG modes into other modes. This more easily demonstrates the coupling into higher-order modes and the dependence on spatial frequency: higher spatial frequencies are responsible for coupling into higher-order

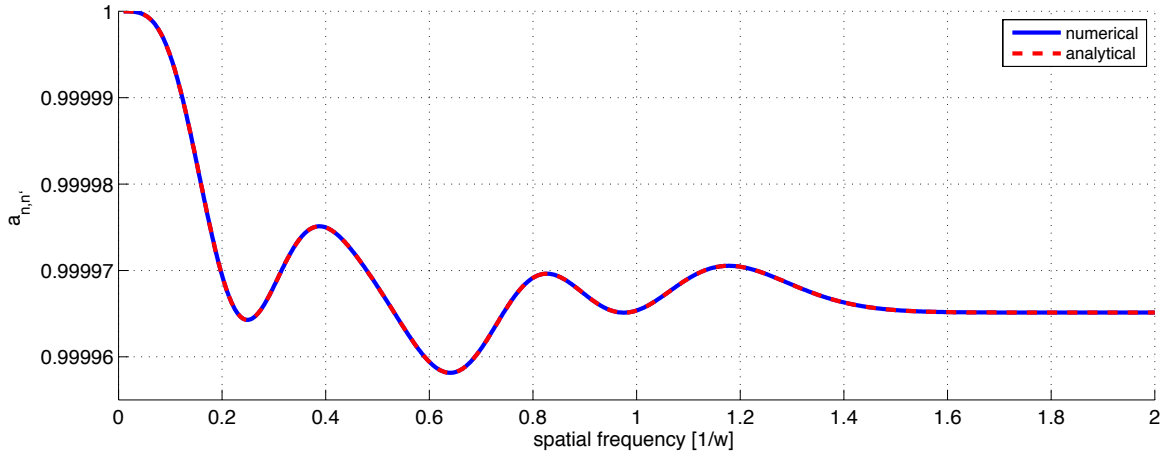

Figure 3.15: The amplitude of the coupling, $a_{n,n'}$, back into a mode with $n = 4$ due to reflection from a 1 nm distorted surface, for a range of spatial frequencies. The coupling is calculated numerically and using an analytic approximation (equation 3.36).

modes.

Figure 3.16 shows plots of the coupling for two different incident modes u_n ($n = 0$ and $n = 3$) into a range of other modes for surfaces described by different spatial wavelengths. For $n = 0$ (left) there is a clear correlation between spatial wavelength and scattering into particular modes. For spatial wavelengths greater than the beam spot size the coupling is predominantly into modes with $n' < 10$. For smaller spatial wavelengths the distorted mirror causes coupling into many higher order modes. In practice this refers to large angle scattering, where the light is scattered out of the path of the beam, and out of the cavity. The power scattered into HOMs is the same order of magnitude for different spatial frequencies. In practice the amplitude of the higher spatial frequencies will be much smaller than the low spatial frequencies (as shown in figure 3.10) and the coupling at these frequencies will be significantly lower.

Figure 3.16 also shows the coupling for an incident HOM, $n = 3$. This is present in the Hermite-Gauss expansion of LG_{33} (see table 3.3). Compared to $n = 0$ there are a wider range of opportunities to couple from the $n = 3$ mode into n' modes. Even for low spatial frequencies modes up to order 10 are present, suggesting that higher-order modes are more susceptible to coupling when incident on distorted

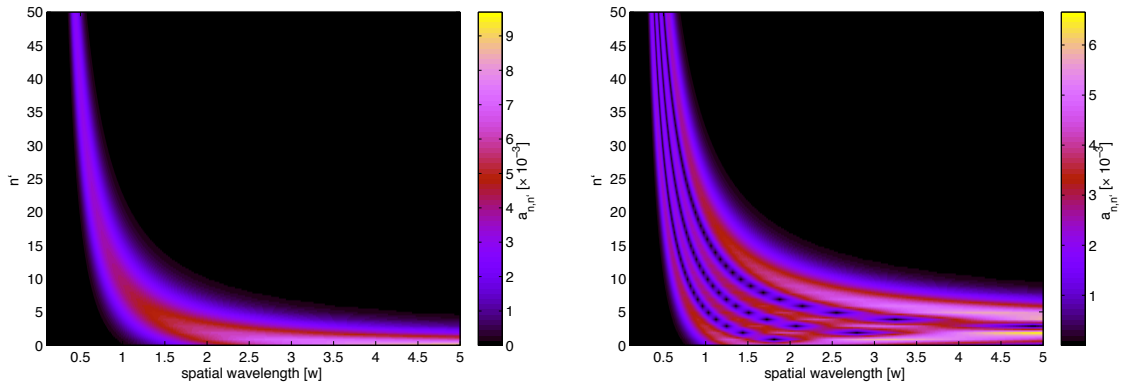

Figure 3.16: Scattering from incident Hermite-Gauss modes $n = 0$ (left) and $n = 3$ (right) into a range of modes n', on reflection from a distorted mirror described by different spatial wavelengths (compared to beam size w). The amplitude of the distorted mirror is 1 nm.

surfaces. This could be a problem for LG_{33}, before even considering the issue of higher-order mode degeneracy.

The approximation detailed in this section expands our understanding of coupling on reflection, using the common approach of considering the spatial frequencies in mirror surfaces. This expansion can be used to determine which modes will be created and helps us select the appropriate number of higher order modes to use in simulations. However, this approach is unsuitable for our investigation in several ways. Firstly, this approximation uses Hermite-Gauss modes, which would involve analysing the 8 individual HG modes which make up LG_{33} and converting these results back into LG modes. This is inefficient. Secondly, this approach, whilst identifying the modes created by a range of spatial frequencies, does not identify specific shapes which will couple between the order 9 modes.

Zernike coupling approximation

Common analysis using spatial frequencies involves taking a statistical approach: performing numerous simulations using randomly generated surfaces to determine the HOM behaviour. Such an approach for the LG_{33} mode is detailed in [77]. We want to take a more analytic approach, calculating the coupling between LG modes from surfaces described by Zernike polynomials. In this way we can identify shapes which will cause problems for LG_{33}.

Zernike polynomials are in polar coordinates, so are compatible with the natural coordinates of the Laguerre-Gauss modes. The coupling between LG modes $u_{p,l}$ and $u_{p',l'}$ on reflection from a mirror described by the Zernike polynomial Z_n^m is given by:

$$k^{n,m}_{p,l,p',l'} = \int_S u_{p,l}\ \exp\left(2\mathrm{i}\, k Z_n^m\right)\ u^*_{p',l'}\ \mathrm{d}S \tag{3.37}$$

The product of the two fields is:

$$u_{p,l}\ u^*_{p',l'} = \frac{1}{w^2}\frac{2}{\pi}\sqrt{\frac{p!p'!}{(|l|+p)!(|l'|+p')!}}\exp\left(\mathrm{i}\ (2p+|l|-2p'-|l'|)\,\psi\right) \left(\frac{\sqrt{2}r}{w}\right)^{|l|+|l'|} L_p^{|l|}\left(\frac{2r^2}{w^2}\right) L_{p'}^{|l'|}\left(\frac{2r^2}{w^2}\right)\exp\left(-\frac{2r^2}{w^2}\right)\exp\left(\mathrm{i}\,\phi\,(l-l')\right) \tag{3.38}$$

If Z is small compared to the wavelength of the laser light we can approximate the exponential to first order:

$$\exp\left(2\mathrm{i}\,kZ\right) \approx 1 + 2\mathrm{i}\,kZ \tag{3.39}$$

This is a valid approximation for advanced gravitational wave interferometers where Z is smaller than 10 nm [74] which gives $2kZ \approx 0.1$ for a wavelength of 1064 nm. Making this approximation we have:

$$\begin{aligned} k^{n,m}_{p,l,p',l'} &= \int_S u_{p,l}u^*_{p',l'}(1+2\mathrm{i}\,kZ^m_n)\ \mathrm{d}S \\ &= \delta_{p,p'}\delta_{l,l'} + \int_0^{2\pi}\int_0^R u_{p,l}u^*_{p',l'}(2\mathrm{i}\,kZ^m_n)\ r\ \mathrm{d}r\ \mathrm{d}\phi \end{aligned} \tag{3.40}$$

where the Kronecker deltas refer to coupling back into the same mode. Generally the limits of the radial integral are 0 and ∞, as the Laguerre-Gauss modes are orthogonal over this range. But since the integrand is proportional to Z^m_n, S becomes the Zernike disc, and as $Z^m_n(\frac{r}{R} > 1) = 0$, the Zernike radius R gives the limit of the integral.

Both Zernike polynomials and Laguerre-Gauss modes can be separated into their angular and radial parts. The angular integrand is:

$$\exp\left(\mathrm{i}\,\phi(l-l')\right)\begin{cases}\cos\left(m\phi\right) & \text{even } Z^m_n \\ \sin\left(m\phi\right) & \text{odd } Z^m_n\end{cases}$$

Considering the even Zernike polynomials, the angular integral becomes:

$$I_\phi = \int_0^{2\pi} e^{\mathrm{i}\,\phi(l-l')} \frac{e^{\mathrm{i}\,m\phi} + e^{-\mathrm{i}\,m\phi}}{2}\,\mathrm{d}\phi = \left[\frac{e^{\mathrm{i}\,\phi(l-l'+m)}}{2\mathrm{i}\,(l-l'+m)} + \frac{e^{\mathrm{i}\,\phi(l-l'-m)}}{2\mathrm{i}\,(l-l'-m)}\right]_0^{2\pi} \tag{3.41}$$

As $e^{\mathrm{i}\,0} = e^{\mathrm{i}\,N\times 2\pi} = 1$, for integer N, the integral, and hence the coupling coefficient, is equal to 0. The only combination of Zernike polynomials and LG modes to give a non-zero result occurs when one of the exponentials disappears before the integration. This occurs when $l - l' + m = 0$ or $l - l' - m = 0$. The same conditions also give the only non-zero results for the odd Zernike polynomials. This forms a *coupling condition* between the azimuthal indices of the Zernike polynomials (m) and the Laguerre-Gauss modes (l/l'):

$$m = |l - l'| \tag{3.42}$$

Unless this condition is satisfied the coupling between modes l and l' is 0, to first order. This is a very useful result and ideal for this investigation, where we are concerned with the coupling between specific modes, in this case the order 9 modes. Already we can identify shapes which will and will not cause problems for LG_{33} (see section 3.3.3). The requirement for m will also give the minimum order, n, of the Zernike polynomial required for such coupling, as $m \leq n$. This simple condition allows quick identification of the modes created from certain mirror shapes. Using this condition we can integrate with respect to ϕ for various combinations of the Zernike polynomials and Laguerre-Gauss modes:

$$I_\phi = \begin{array}{rl} 0 & m \neq |l - l'| \\ \pi & m = |l - l'|, \quad \text{even } Z_n^m \\ \pm\mathrm{i}\,\pi & m = |l - l'|, \quad \text{odd } Z_n^m \\ 2\pi & m = |l - l'| = 0 \rightarrow l = l' \end{array} \tag{3.43}$$

We now look at integrating with respect to r. By making the variable substitution $x = \frac{2r^2}{w^2}$ into equation 3.40 the coupling approximation becomes:

$$k^{n,m}_{p,l,p',l'} = \delta_{p,p'}\delta_{l,l'} + \mathrm{i}\,k\frac{I_\phi}{\pi}\sqrt{\frac{p!p'!}{(|l|+p)!(|l'|+p')!}}\exp\left(\mathrm{i}\,\Delta o\;\psi\right) \int_0^X x^{\frac{|l|+|l'|}{2}} L_p^{|l|}(x)L_{p'}^{|l'|}(x)\;\exp\left(-x\right)R_n^m\left(\sqrt{\frac{x}{2}}\frac{w}{R}\right)\sqrt{\frac{x}{2}}w\;\mathrm{d}x \tag{3.44}$$

with $X = \frac{2R^2}{w^2}$, the limit of the integration and $\Delta o = 2p + |l| - 2p' - |l'|$, the difference in the orders of the incident and coupled modes. Finally the integration of the overall polynomial is solved using the incomplete gamma function, $\gamma(a,x) = \int_0^x t^{a-1}e^{-t}dt$ [75]:

$$\begin{aligned} k^{n,m}_{p,l,p',l'} = \delta_{p,p'}\delta_{l,l'} + A\;\mathrm{i}\,k\frac{I_\phi}{\pi}\sqrt{p!p'!(p+|l|)!(p'+|l'|)!}\;\exp\left(\mathrm{i}\,\Delta o\;\psi\right) \\ \times\sum_{i=0}^{p}\sum_{j=0}^{p'}\sum_{h=0}^{\frac{1}{2}(n-m)}\frac{(-1)^{i+j+h}}{(p-i)!(p'-j)!(|l|+i)!(|l'|+j)!i!j!}\frac{1}{X^{\frac{1}{2}(n-2h)}} \\ \times\frac{(n-h)!}{\left(\frac{1}{2}(n+m)-h\right)!\left(\frac{1}{2}(n-m)-h\right)!h!}\;\gamma(i+j-h+\frac{1}{2}(|l|+|l'|+n)+1,X) \end{aligned} \tag{3.45}$$

We note that the first order direct coupling described here is proportional to the amplitude of the Zernike polynomial, A. The coefficients are not dependent on the individual values of the radius of the mirror, R, or incident beam size, w, but the ratio of these two variables, as contained in X. Finally, as with the scattering approximation outlined in the previous section, the coupling back into the same mode requires expanding the coupling coefficients to second order. The details of this derivation are shown in appendix B.5.

3.3.3 Coupling between order 9 modes

I have developed an analytic expression for the first order coupling between LG modes, outlined above. This approach has yielded a coupling condition, exactly the result we want to identify the shapes which couple between order 9 modes. For coupling to occur between two Laguerre-Gauss modes, $LG_{p,l}$ and $LG_{p',l'}$, the mirror surface must contain Zernike polynomials with azimuthal index:

$$m = |l - l'| \tag{3.46}$$

Table 3.5 summarises the azimuthal index, m, of the Zernike polynomials required to couple from LG_{33} to the other order 9 modes. If these shapes are present in the mirrors of advanced detectors they will couple between the order 9 modes, making the use of LG_{33} unviable if the amplitudes of these polynomials are not sufficiently constrained.

$m = |l - l'|$ also gives the minimum order of the polynomials which will couple between given order 9 modes, since $m \leq n$. As low order mirror surface distortions have, generally, greater amplitude than higher order distortions, this suggests that more coupling will occur into modes coupled via lower m distortions, than those from higher m distortions.

In the left panel of figure 3.17 the coupling from LG_{33} into the order 9 modes is calculated numerically, from a surface described by a 1 nm Z_4^4 polynomial. The numerical coupling does not make the first order approximation used in our ana-

LG mode (p',l')	2, 5	4, 1	1, 7	4,-1	0, 9	3,-3	2,-5	1,-7	0,-9
m	2	2	4	4	6	6	8	10	12

Table 3.5: The azimuthal index (m) required to couple from an incident LG_{33} ($p = 3$, $l = 3$) beam into the other order 9 modes on reflection from a distorted mirror described by a Zernike polynomial. $m = |l - l'|$, where l is the azimuthal index of the incident beam (3 in this case) and l' is the coupled mode.

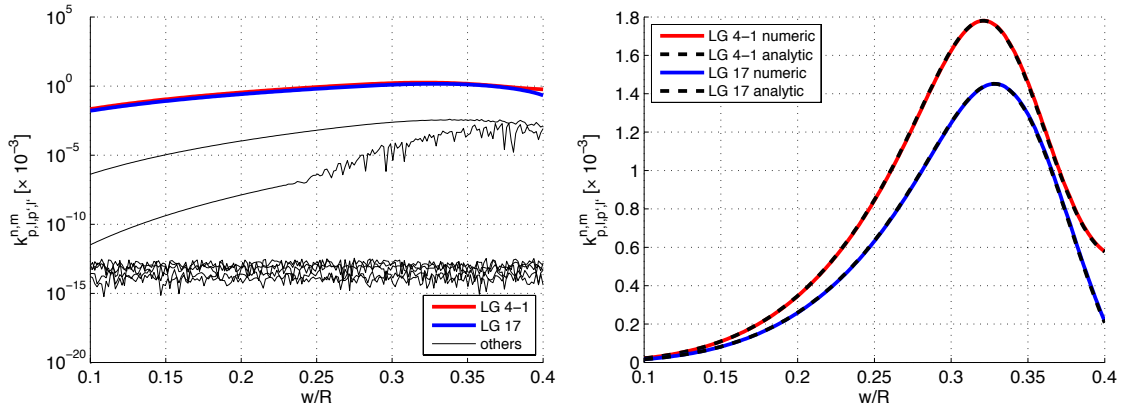

Figure 3.17: Coupling from LG_{33} into the other order 9 LG modes on reflection from a mirror described by a 1 nm Zernike polynomial, Z_4^4. The coupling is calculated for different beam sizes, compared to Zernike radius. **Left:** Coupling calculated numerically for all order 9 polynomials. **Right:** Coupling into LG_{4-1} and LG_{17}, the two modes which satisfy $m = |l - l'|$. The coupling is calculated numerically and with the analytic approximation.

lytical case and coupling occurs into all the other order 9 modes. However, the coupling into the modes which conform to our condition for m (LG_{17} and LG_{4-1}) is significantly larger (a factor of 1000) than the other modes. In the right plot of figure 3.17 a comparison of the coupling approximation and the numerical coupling for this particular case is shown. The two results are practically identical over this range of $\frac{w}{R}$.

3.3.4 Beam size and mirror radius

In figure 3.17 the coupling is calculated over a wide range of $\frac{w}{R}$, the ratio of the beam size to mirror radius. However, this is not a free parameter in the detectors. The beam size, compared to the size of the mirrors, has an impact on many effects in the detectors. For good thermal noise reduction a large beam size is desirable. The beam size is limited by the power lost over the edge of the mirrors, *clipping loss*. For an LG mode this loss is given by:

$$l_{clip} = 1 - \int_S |u_{p,l}|^2 \, \mathrm{d}S \tag{3.47}$$

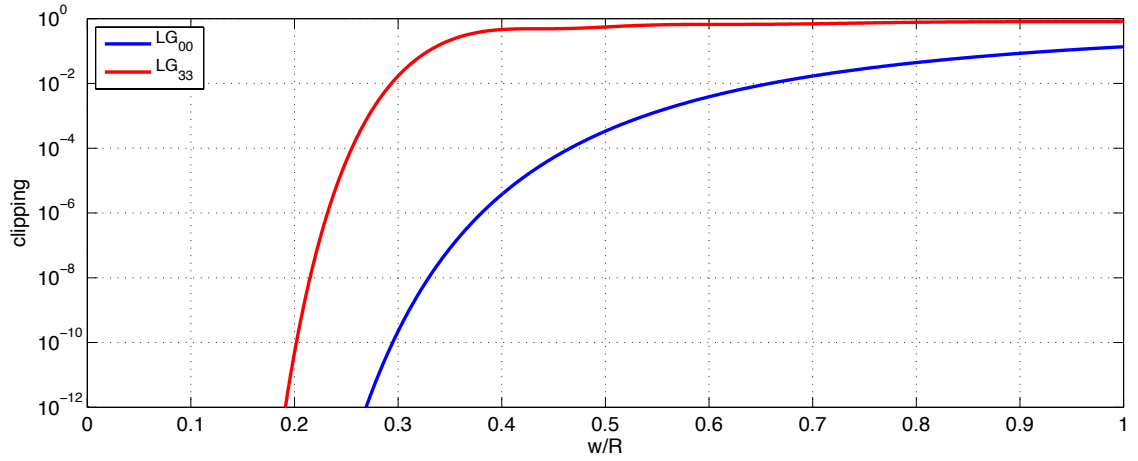

Figure 3.18: The clipping loss, or power loss, due to a beam incident on a finite sized mirror, for different beam sizes (w) compared to the mirror radius (R). The clipping is shown for an LG_{00} beam and LG_{33} beam. Typically a clipping loss < 1 ppm is desirable.

The integral represents the normalised power reflected by a mirror with a finite aperture. For a large mirror the loss is effectively 0. The loss for LG modes is derived as:

$$l_{clip} = 1 - p!(p+|l|)! \sum_{m=0}^{p} \sum_{n=0}^{p} \frac{(-1)^{n+m}}{(p-n)!(p-m)!} \times \frac{1}{(|l|+n)!(|l|+m)!n!m!} \gamma(|l|+n+m+1, X) \tag{3.48}$$

where $X = \frac{2R^2}{w^2}$ and γ is the lower incomplete gamma function [75]. Figure 3.18 shows the clipping experienced by an LG_{33} beam, compared to an LG_{00} beam, as a function of $\frac{w}{R}$. Generally a clipping loss < 1 ppm (10^{-6}) is desired.

3.3.5 Advanced LIGO mirrors

We can apply our analytic expression to the particular mirrors of Advanced LIGO, by decomposing these surfaces into Zernike polynomials, as shown in figure 3.12, for the Advanced LIGO mirror map, ETM08. The coupling into different LG modes can then be calculated using our analytic approximation. In figure 3.19 the total

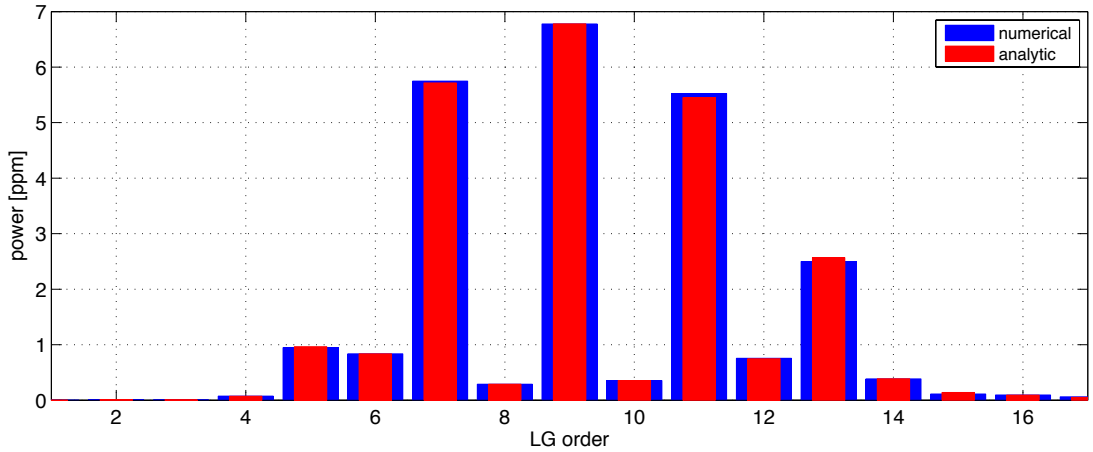

Figure 3.19: The power coupled from an LG_{33} beam into different modes upon reflection from a mirror surface described by the ETM08 mirror map. The coupling back into LG_{33} is omitted (this is close to 1, i.e. 10^6 ppm). The total coupling into each particular mode order is calculated numerically from the total map and analytically by decomposing the map into Zernike polynomials and using an analytic approximation. Both methods yield very similar results.

power coupled from LG_{33} into each order of modes is plotted, using a numerical approach and our analytic approximation to calculate the coupling from ETM08. Both methods give very similar results for the coupling. These results show that a lot of direct coupling occurs into the other order 9 modes, from these realistic mirrors, as well as orders 7 and 11, suggestive of second order distortion terms (i.e. astigmatism). We will adopt this approach in later sections to analyse the coupling caused by specific polynomials, complimenting later simulation results and used for setting requirements for LG_{33}.

3.4 Feasibility study for Advanced LIGO

Our analytical approach can be used to identify the shapes in Advanced LIGO mirrors which will *directly* couple from LG_{33} into the order 9 modes. We now investigate how these modes behave in the high finesse cavities of advanced detectors, to access the impact of higher order mode degeneracy on beam purity within the cavities. This is achieved with simulations of Advanced LIGO arm cavities, using

Figure 3.20: Illustration of an Advanced LIGO arm cavity: 2 curved mirrors, the input test mass (ITM) and end test mass (ETM) separated by 4 km.

mirror	T	l	R_C
ITM	0.014	37.5 ppm	1934 m
ETM	5 ppm	37.5 ppm	2245 m

Table 3.6: Input test mass (ITM) and end test mass (ETM) design parameters for an Advanced LIGO arm cavity. The transmission, T, loss, l and radius of curvature R_C are given for the highly reflective, intra-cavity surfaces of the mirrors. The two mirrors are separated by 4 km, have a thickness of 200 mm and an index of refraction of 1.45. The two mirror cavity produced by these mirrors has a finesse of ~ 450.

FINESSE. We aim to use these results, and the analytical approach outlined above, to derive mirror requirements for the use of LG_{33}. To represent realistic surface distortions Advanced LIGO mirror maps were used.

The arm cavities of Advanced LIGO consist of two curved mirrors, an input test mass (ITM) and end test mass (ETM) separated by ~4 km (figure 3.20). The design parameters are summarised in table 3.6. However, the Advanced LIGO cavities were designed for the fundamental mode. The LG_{33} mode is more spatially extended than the LG_{00} mode and experiences greater clipping loss for a given beam spot size (see section 3.3.4). In the case of the Advanced LIGO parameters, the 34 cm diameter aperture created by the mirrors and a beam size of 6.2 cm on the ETM, the clipping for LG_{33} is unacceptably large, around 31%. Using LG_{33} requires adjusting the beam size, in this case by shortening the length of the cavity in the simulation to 2802.9 m, to achieve similar clipping as experienced by LG_{00} in Advanced LIGO. The results from this setup will be representative of longer cavities with larger mirrors.

3.4.1 Beam purity with Advanced LIGO mirror maps

To model realistic surface distortions maps of the Advanced LIGO mirrors were used in the simulations. At the time of this investigation the cavity mirrors were uncoated and only maps of the polished substrates were available. These are still suitable for our investigation and should be representative of the order of the final distortions. In the simulations reported here the surface map corresponding to the Advanced LIGO end test mass ETM08 was used (see section 3.3.1).

To make some predictions about the modes which are excited in a cavity with this particular mirror, the surface was decomposed into Zernike polynomials. The coupling is predicted using the approximation outlined in section 3.3.2. The decomposition was achieved by performing an inner product between the mirror surface and each polynomial, Z_n^m, up to a given order. Due to the orthogonal nature of the polynomials we have:

$$\int_S Z_{map}\ Z_n^m\ \mathrm{d}S = A_n^m \int_S Z_n^m Z_n^m\ \mathrm{d}S = A_n^m \tag{3.49}$$

where Z_{map} is the mirror surface and A_n^m is the amplitude of the corresponding Zernike polynomial in the surface. The surface was decomposed into Zernikes up to $n = 30$, with the content up to $n = 5$ shown in table 3.7. For the case of LG_{33} we are interested in particular polynomials, which couple between the order 9 modes, as identified in section 3.3.3. For the mirror surface, ETM08, these polynomials are summarised in table 3.8. The polynomials are listed in terms of the power

polynomial (n, m)	2, 2	3, 1	3, 3	4, 0	4, 2	4, 4	5, 1	5, 3	5, 5
amplitude [nm]	0.91	0.23	0.12	0.38	0.20	0.21	0.24	0.08	0.14

Table 3.7: Zernike polynomial content of the mirror map ETM08, describing the measured mirror surface of an Advanced LIGO end mirror. The polynomials up to $n = 5$ are shown, with those corresponding to mirror tuning (Z_0^0), alignment (Z_1^1) and curvature mismatch (Z_2^0) omitted, as these correspond to controllable defects: tuning, misalignment and mode-mismatch.

polynomial (n, m)	2, 2	4, 2	4, 4	6, 2	10, 8	other
amplitude [nm]	0.91	0.20	0.21	0.12	0.12	...
power [ppm]	4.7	0.33	0.043	0.0099	0.0059	< 0.005

Table 3.8: Summary of the Zernike polynomials in the Advanced LIGO mirror map, ETM08, which cause coupling on one direct reflection from LG_{33} into the other order 9 modes. The amplitude of the polynomials and power coupled from LG_{33} (calculated from equation 3.45) is given. The polynomials are ordered by the power they couple between LG_{33} and the other order 9 modes.

coupled, as calculated from the approximation, from LG_{33} into the other order 9 modes. From these results we predict the modes which will have significant power in a cavity simulated with ETM08. The two polynomials which couple the most power from LG_{33} are Z_2^2 and Z_4^2, both polynomials with $m = 2$. These will couple into LG_{41} and LG_{25}, so we expect these modes to have large powers in the cavity. The astigmatic polynomial (Z_2^2) in particular extracts a large amount of power from LG_{33}.

The cavity outlined in section 3.4 was simulated using the interferometer simulation FINESSE. A pure LG_{33} beam was injected into the cavity, with the mirror map ETM08 applied to the end mirror and a perfect input mirror. The circulating field was detected with the cavity on resonance. This field is shown in the left panel of figure 3.21. Comparing this image of the circulating beam with the image of a pure LG_{33} beam in figure 3.3 suggests that the simulated field is not purely LG_{33} and contains other modes. The purity of an LG mode, $u_{p,l}$, in an arbitrary field u is given by $|c_{p,l}|^2$, where:

$$c_{p,l} = \int_S u \; u_{p,l}^* \; \mathrm{d}S \tag{3.50}$$

The purity of the circulating beam, in terms of LG_{33}, is 88.6%. This is significantly lower than the acceptable purity of beams in advanced detectors, where we require a purity greater than 99% [78]. The large impurity in the case of LG_{33} is due to the degeneracy of the cavity for order 9 modes.

The mode content of the circulating beam is summarised in table 3.9. The

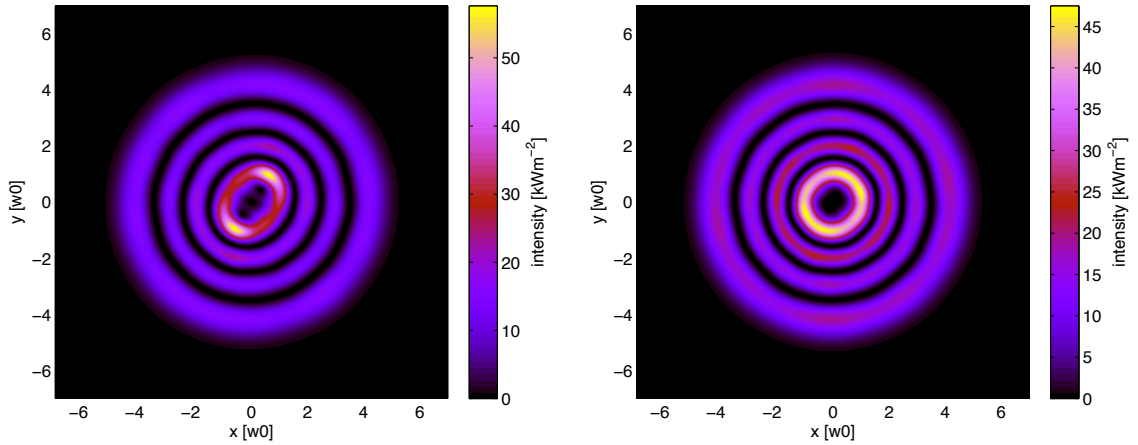

Figure 3.21: Intensity patterns of the circulating beam in Advanced LIGO cavities, simulated with a perfect input mirror, distorted end mirror and an LG_{33} input beam. **Left:**The ETM distortion is described by the original Advanced LIGO mirror map, ETM08. **Right:** The astigmatism is completely removed from the distorted ETM. The circulating beam is distorted in both cases from a pure LG_{33} mode due to coupling into other modes. The removal in astigmatism results in a purer LG_{33} mode.

LG mode (p, l)	3, 3	4, 1	2, 5	4, -1	1,7	other
m_{33}	...	2	2	4	4	...
order	9	9	9	9	9	...
power [%]	88.6	5.70	5.02	0.33	0.31	< 0.05

Table 3.9: Power in the LG modes circulating in a simulated Advanced LIGO cavity, with a pure LG_{33} input beam, a perfect ITM and a mirror map, ETM08, applied to the ETM. m_{33} refers to the azimuthal index of the Zernike polynomial which couples directly between LG_{33} and the particular mode p, l. All the modes with significant power in the cavity are of order 9.

decomposition of the beam shows that the distortion of the end mirror, as described by the ETM08 mirror map, distorts the beam from a pure LG_{33} mode. The distortion of the beam is dominated by the order 9 modes, as these are enhanced in the cavity due to the degeneracy of the cavity resonance. The distortions cause coupling into other order modes but these are not resonant in the cavity and will be relatively suppressed.

After LG_{33} the mode content is dominated by LG_{41} (5.7%) and LG_{25} (5.0%). This agrees with the predictions made by studying the Zernike content of the ETM08

mirror map (table 3.8). This confirms that we can identify particular shapes in mirror surfaces using our coupling expression and this will be a good prediction of the dominant modes in the cavity. The modes LG_{4-1} and LG_{17} also have relatively high power in the cavity. This could be from direct coupling from LG_{33} caused by $m = 4$ polynomials, in particular Z_4^4. These modes could also be generated via cross coupling from the LG_{41} and LG_{25} modes, which can couple into LG_{4-1} and LG_{25} respectively from interactions with $m = 2$ polynomials. Overall the coupling process in a cavity is complicated by these multiple cross couplings, but the results of these simulations, when compared with the coupling approximation, suggest that the direct coupling from a mirror is the dominant effect on the mode content of the circulating beam. A theoretical understanding of the direct coupling has allowed us to make valid predictions about the resulting mode content.

3.4.2 Beam purity with adapted mirror maps

The initial goal of this investigation has been satisfied: to identify particular shapes which couple between order 9 modes and to assess whether the current mirrors result in pure enough LG_{33} beams. We now investigate how the mirrors can be adapted for LG_{33} and calculate requirements on certain Zernike polynomials for sufficient beam purity.

In our initial simulation of an Advanced LIGO cavity, and the analysis of the Zernike content of the ETM08 mirror map, the astigmatism of the mirror appeared to contribute significantly to coupling from LG_{33}. Any reduction in astigmatism should then lead to a significant improvement in LG_{33} purity. To demonstrate this the cavity was simulated again, but this time the ETM08 mirror map was pre-processed to remove any astigmatism from the surface. The circulating beam was detected and decomposed into Laguerre-Gauss beams as before. The circulating beam is plotted in the right panel of figure 3.21. Comparing this with the beam

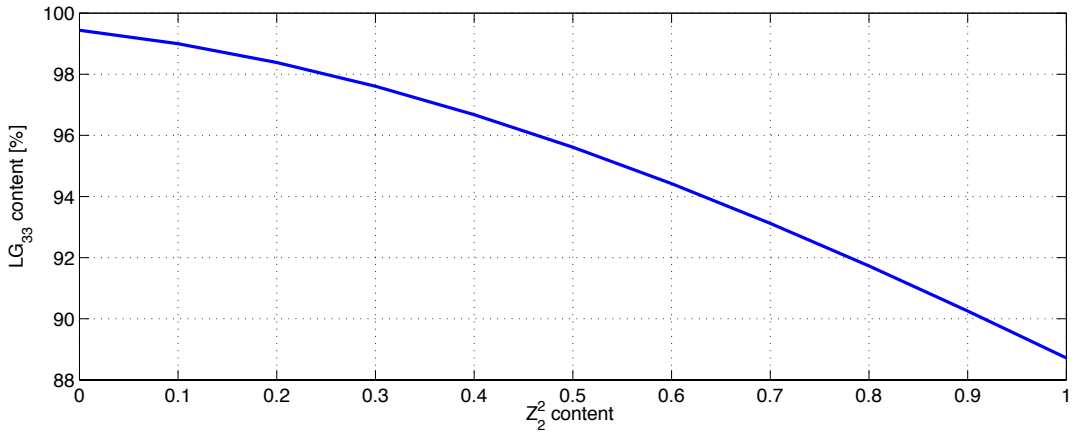

Figure 3.22: The LG_{33} content of a beam circulating in a simulated Advanced LIGO arm cavity as the astigmatic component (Z_2^2) of the end mirror is tuned. The cavity is injected with a pure LG_{33} beam and the distortion of the end mirror is described with an Advanced LIGO mirror map, ETM08. The astigmatic content of the mirror is tuned from 0 to 100% of the astigmatism measured in the ETM08 mirror map.

simulated with the original map (left plot) already shows an improvement in purity: the beam looks much more like LG_{33}. The LG_{33} purity was found to have increased significantly to 99.5%. In figure 3.22 a plot of LG_{33} purity vs. astigmatism is shown, illustrating the strong impact astigmatism has on the beam.

The mode content when the astigmatism is completely removed is summarised in table 3.10. The decomposition shows that the beam is still distorted and the impurities of the beam are still dominated by the order 9 modes. However, the power in specific modes, particularly LG_{41} and LG_{25}, has dropped significantly.

LG mode (p, l)	3, 3	4, 1	2, 5	1, 7	4, -1	0, -9	other
m_{33}	...	2	2	4	4	12	...
order	9	9	9	9	9	9	...
power [%]	99.5	0.231	0.208	0.052	0.017	0.014	< 0.01

Table 3.10: Laguerre-Gauss mode content of the beam circulating in a simulated Advanced LIGO cavity, with a pure LG_{33} input beam and a mirror map applied to the end mirror. The map is measured from the Advanced LIGO mirror ETM08 and has the astigmatism removed to improve the purity of the simulated LG_{33} beam. m_{33} is the azimuthal index of the Zernike polynomial required to couple from LG_{33} into the particular LG mode.

These results demonstrate that astigmatism is a major factor in determining the intra-cavity purity of a higher order LG mode. To use LG_{33} the astigmatism will require more stringent requirements than in the current mirrors.

3.4.3 Mirror requirements for LG_{33}

To use LG_{33} in gravitational wave detectors requires limits on the specific distortions which couple between the order 9 modes. We cannot remove these distortions completely, but we can suggest requirements for the Zernike polynomials in mirror surfaces. Here we investigate the coupling from particular shapes in the mirror surface ETM08 and suggest requirements for the amplitudes of these distortions. The result is an Advanced LIGO mirror map adapted for the use of LG_{33}.

The important shapes to reduce in the mirrors can be identified using our analytic expression (equation 3.45). Zernike polynomials with odd n and with $m > 12$ do not cause coupling between the order 9 modes. To access the impact of the other Zernike distortions the coupling from LG_{33} into the other order 9 modes is calculated for each polynomial present in ETM08. The optical parameters are equivalent to the setup defined in section 3.4, giving a beam size at the ETM of 3.7 cm. For (first order) coupling the condition $m = |3 - l'|$ must be met. For each of the order 9 modes the coupling from LG_{33} is calculated, for each Zernike polynomial with $n = 0$ to $n = 30$ which satisfies $m = |3 - l'|$. This is shown in the left panel of figure 3.23. As previously observed the largest contribution to coupling between the order 9 modes is from astigmatism (Z_2^2) into LG_{41} and LG_{25}. There is also some strong coupling from Z_4^2 and Z_4^4. The other couplings are significantly smaller. Our first step in modifying Advanced LIGO mirrors for LG_{33} is to limit these 3 distortions to give similar couplings to the higher order distortions.

In figure 3.23 (right) the total coupling from the ETM08 mirror map is estimated using our analytical expression to calculate individual Zernike couplings. The cou-

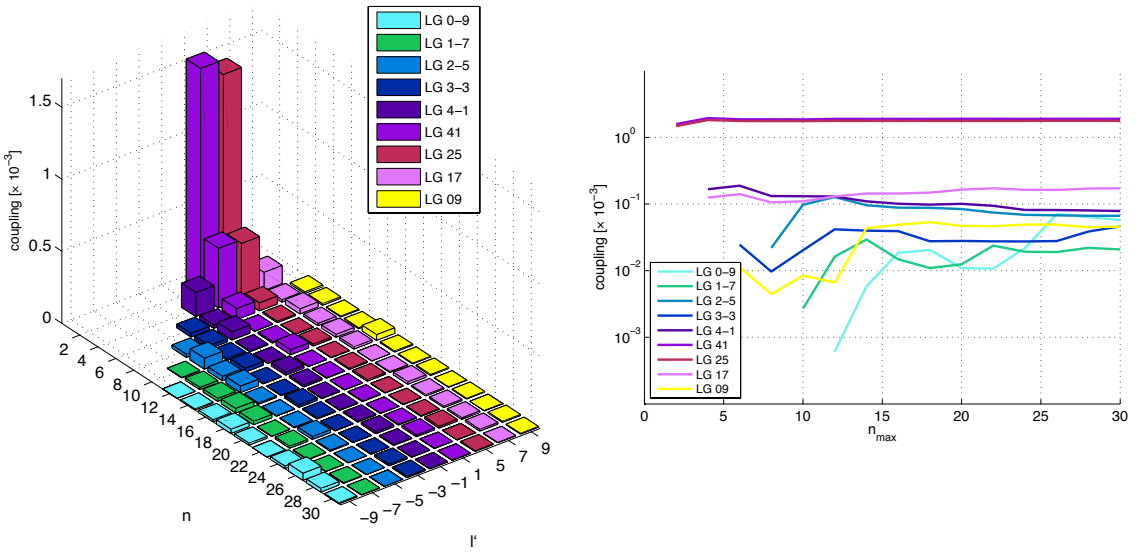

Figure 3.23: Coupling from LG_{33} into the other order 9 modes on reflection from mirrors described by the Zernike polynomials present in the Advanced LIGO mirror surface ETM08. **Left:** Coupling into each order 9 mode from the individual Zernike polynomials in ETM08. The Zernike distortion has order n and satisfies the azimuthal condition $m = |3 - l'|$. **Right:** Cumulative coupling into each order 9 mode, as more Zernike distortions are added to the model: coupling from distortions with $n \leq n_{max}$ are included. The coupling is dominated by LG_{41} and LG_{25}, particularly due to astigmatism ($n = 2$).

pling is calculated as higher order polynomials are added to the model (n_{max} is increased). Generally the higher order polynomials contribute less to the coupling for each mode, and the coupling tends to a particular value as higher n polynomials are added to the approximation. Again, the coupling into LG_{41} and LG_{25} dominates, by at least an order of magnitude. The coupling into these two modes is predominantly the result of low order polynomials. This plot illustrates how this particular map, ETM08, can be adapted for LG_{33}: suppressing the low order distortions can reduce the overall coupling into order 9 modes by a factor of 10. Further reduction will involve limits on multiple distortions.

The total coupling from the ETM08 mirror surface can be calculated numerically. For an LG_{33} incident beam with $w = 3.7$ cm 31 ppm of the reflected power is in modes other than LG_{33}, with 6.8 ppm in the other order 9 modes. In table 3.8 the coupling

polynomial (n, m)	2, 2	4, 2	4, 4
amplitude [nm]	0.042	0.035	0.100

Table 3.11: Amplitude requirements on Zernike distortions in the Advanced LIGO mirror surface ETM08, for the use of an LG_{33} mode. The requirements are calculated to reduce the coupling from LG_{33} into the other order 9 modes to 0.01 ppm, for each individual Zernike surface.

from the individual polynomials which make up the mirror surface is shown, for the order 9 modes. For this particular map we consider the polynomials which cause a large amount of coupling as those which, individually, couple more than 0.01 ppm from LG_{33} into the other order 9 modes: Z_2^2, Z_4^2 and Z_4^4. To achieve sufficient beam purity for a high finesse cavity injected with LG_{33} we require these polynomials to be limited. The requirements for these Zernike polynomials are summarised in table 3.11.

These amplitude requirements were applied to the ETM08 mirror map, resulting in a total coupling of 19 ppm into other modes, with just 0.043 ppm into the other order 9 modes. This adjusted map was used in a simulation of the cavity defined in section 3.4. The result was a much higher LG_{33} purity, with just 815 ppm of the circulating beam in other modes. This is a very good improvement from the original impurity of 0.114, a reduction of over 100, illustrating that a high beam purity is achievable with additional requirements to a few specific shapes in the current mirrors. Using the method reported in this chapter these specific requirements can be calculated. To achieve an even greater purity will involve reducing the amplitudes of these polynomials even further, as well as additional requirements on other distortions.

3.4.4 Improvement in contrast defect

Previously (see figure 3.4) the dark fringe of a Fabry-Perot Michelson was simulated for an LG_{33} beam, with unbalanced distorted arms: specifically an Advanced LIGO

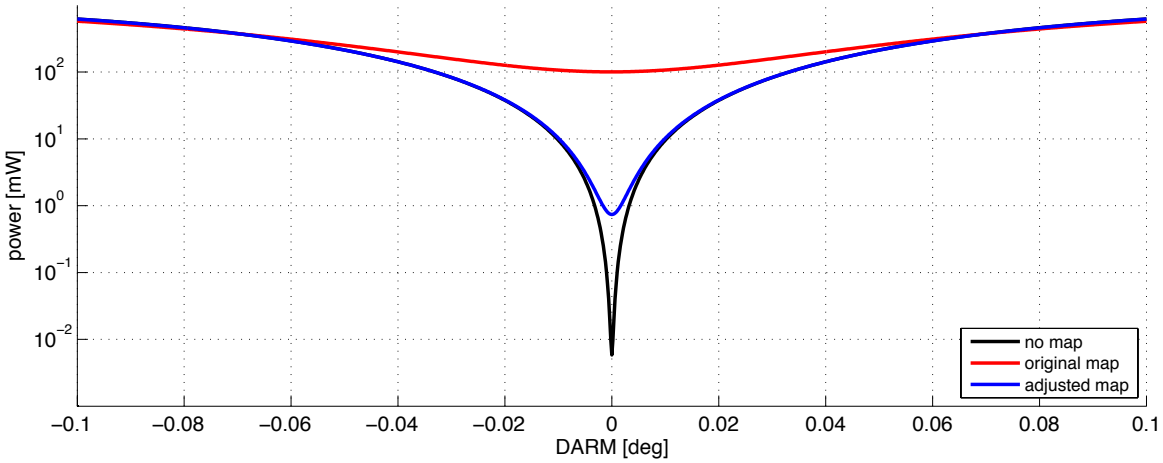

Figure 3.24: The power at the antisymmetric port of an Advanced LIGO style Fabry-Perot Michelson as the differential arm length is tuned (DARM= $\frac{L_x - L_y}{2}$). The interferometer is simulated with a 1 W LG_{33} input beam for 3 cases: 1) perfect mirrors; 2) an Advanced LIGO mirror map applied to the x arm end mirror; and 3) an Advanced LIGO mirror map adapted for LG_{33} applied to the end mirror of the x arm.

mirror map applied to the end mirror of the x arm. Using the adapted map outlined in the previous section we compare the power at the antisymmetric port for the original map and our adapted map. The results are shown in figure 3.24. As expected the adapted map results in a dramatic improvement in the interference of the beams from the two arms and a large reduction in minimum output power. This will significantly improve the contrast defect. The plots here show the minimum output power is reduced by over a factor of 100, the same factor by which the purity of the field circulating in the x arm is improved.

Figure 3.25 shows plots of the output beam from the Fabry-Perot Michelson simulated with the original map (left) and with the adapted map (right). The intensity of the output beam is reduced by 100 when the map is adapted for LG_{33}.

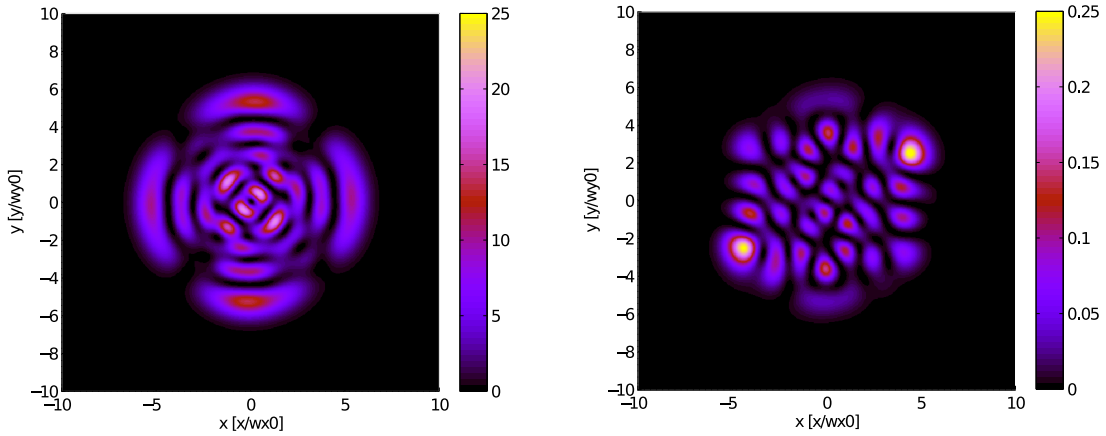

Figure 3.25: Beams at the output of a simulated Advanced LIGO Fabry-Perot Michelson, with LG_{33} input beams. The interferometer is simulated with an Advanced LIGO mirror applied to ETM (x arm) (left) and the same map adapted for LG_{33} (right). The adapted map leads to a significant drop in the power at the antisymmetric port.

3.5 Conclusion

In this chapter I have reported an analytical method with which to calculate the mirror surface requirements for the use of an LG_{33} mode in gravitational wave interferometers. The use of LG_{33} in GW detectors, proposed to suppress mirror thermal noise, is complicated by the degeneracy of the arm cavities for higher order modes. The mirrors produced for Advanced LIGO have been shown to produce an unacceptable beam purity in the high finesse cavities of the arms. Simulations reported here show a beam purity of 88.6%.

To achieve a high beam purity additional requirements of the mirror surfaces are needed. To this end I have derived an analytical approximation of the power coupled into other modes on reflection from individual mirror shapes, described by Zernike polynomials. The most important result presented here is a condition for coupling between two LG modes: $m = |l - l'|$. m refers to the azimuthal index of the mirror shape and l and l' to the azimuthal indices of the incident and coupled mode. Only when this condition is satisfied is power coupled between the two modes. This

simple condition identifies the shapes which will couple between order 9 modes: $m = 2,\ 4,\ 6,\ 8,\ 10,\ 12$. Using this analytical coupling approximation requirements were calculated for specific polynomials, Z_2^2, Z_4^2 and Z_4^4, in the ETM08 mirror map, constituting mirror surface requirements for LG_{33}. This adapted map resulted in a much purer intra cavity beam, with just 815 ppm in other modes, compared to the original 0.114, and an improved contrast defect.

The method outlined in this chapter, and published in [36; 60] demonstrate that a significantly higher beam purity can be achieved with LG_{33} by introducing additional requirements to just 3 mirror shapes. This is unique in the analysis of this mode. The results detailed here compliment work carried out in [77], which takes a statistical approach to investigate the performance of LG_{33} in terms of spatial frequencies.

Throughout my Ph.D I was also involved in experimental demonstrations of LG_{33}. This included a collaborative effort at the Glasgow prototype to test the performance of LG_{33} in environments similar to gravitational wave detectors [72]. This investigation highlighted several technical challenges when using this higher order mode, as well as confirming the need for tighter requirements on astigmatism. As I did not lead this investigation and due to length constraints these results are not included in this thesis, but I point the interested reader to [72] and [79], a video paper detailing the production of a high purity LG_{33} beam.

Finally, recent work on the application of adaptive optics in GW detectors used the analytical method reported in this thesis to identify shapes which, when induced by adaptive optics, can correct the distortion of LG_{33} within the instrument [37; 38]. This is a step towards using LG_{33} in future detectors, using our coupling expression to derive the right requirements.

Chapter 4

Developing and testing modal models

During my Ph.D. the modal model FINESSE has been under development to include higher order mode effects in an efficient and accurate way. On a coding level this work was initiated by Andreas Freise and developed by Daniel Brown. During this period I became the chief user of FINESSE, testing various aspects of the code against expected results and other simulations. The use of higher order modes to describe the effects of misalignment and mode mismatch have long been understood, with analytic equations derived to describe these effects [80]. The main upgrade during the development of FINESSE was the implementation of mirror surface maps, using a modal expansion to describe distortions of the beam caused by arbitrary mirror surfaces. This is achieved by calculating coupling coefficients numerically. The technical details of these numerical integrations can be found in the FINESSE manual [49] and are not the subject of this thesis.

It is necessary to test different aspects of FINESSE, from the simple behaviour of plane wave interferometers to more complicated behaviour involving distorted beams, distorted optics and higher order modes. This is essential for confidence in the results presented here, as well as necessary to convince the wider gravitational

wave community of the validity of our simulations, particularly regarding commissioning work (see chapter 5). Through tests against other simulations we also identify possible issues to be aware of in modal simulations and assess the limitations of these models.

In this chapter the results of these tests are summarised, starting with comparisons of FINESSE with analytic solutions, moving on to tests of the modal model for single components and finally more complicated examples (involving the higher order mode LG_{33} and thermal distortions) are compared with the results of Fast Fourier Transform methods.

4.1 Analytic tests of interferometer responses

Firstly we start with tests of FINESSE against known analytic results, testing the interferometer response functions without higher order mode effects. In 2012 Mengyao Wang led an investigation into the potential of a Sagnac interferometer as the basis for a future gravitational wave detector, comparing this to the standard Michelson interferometer used in current detectors. The results of this effort are detailed in [81]. As part of this investigation I carried out simulations in FINESSE, testing the response of a Sagnac interferometer versus a Michelson and developing a potential control scheme. At this time it was necessary to compare the interferometer responses as modelled in FINESSE with the analytical responses derived from the effect of a gravitational wave on a single space.

4.1.1 Michelson and Sagnac interferometers

The optical layout of a simple Michelson and Sagnac interferometer are shown in figure 4.1. In a Michelson interferometer the light incident on the beam-splitter is split onto two different arms. The light split onto each path will only travel in that particular arm. When the light returns to the beam-splitter the common light

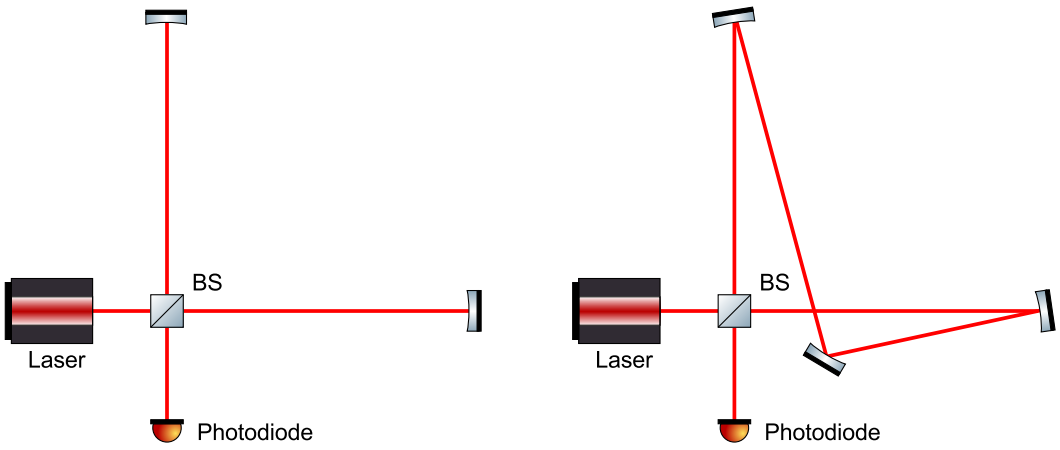

Figure 4.1: Optical layout of a simple Michelson interferometer (left) and a simple Sagnac interferometer (right). A Michelson act as a displacement meter whilst a Sagnac acts as a speed meter.

between the two arms is reflected towards the laser (or power recycling mirror in a recycled interferometer) and the differential light exits the interferometer through the dark port (or towards the signal recycling mirror). In a Sagnac interferometer the light is split at the beam-splitter, but in this case travels through both arms before returning to the beam-splitter (see figure 4.1). This can be achieved using ring cavities or polarising optics. The beams which interfere at the beam-splitter have both travelled through the two arms, the only difference being the order: one beam will travel through the x arm first, then the y arm, whilst the other beam will travel in the opposite direction. The consequence is that Sagnac and Michelson interferometers measure different parameters. A Michelson interferometer measures differential arm length: it is sensitive to the displacement of the mirrors. A Sagnac interferometer is insensitive to any static displacement of the mirrors, as both beams travel through both arms. However, as each beam experiences the arms of the interferometer at different times the Sagnac is sensitive to the speed of the mirrors.

In theory both interferometers can be used to detect the spatial disturbance we expect from a gravitational wave. The response of an interferometer is simply the output signal generated when the arms of a detector are modulated by a gravitational

wave. In this way the expected signals from different interferometer configurations can be compared.

4.1.2 Interferometer response functions

In this section we compare the analytical response of a Michelson and Sagnac interferometer with the response simulated in FINESSE. The derivation of the analytical response and intermediate transfer functions (for linear cavities and simple interferometers without arm cavities) are given in greater detail in appendix A. This is a summary of results published in [82] and [83].

A distance whose length, L, is modulated by a gravitational wave will imprint a phase modulation on any beam propagating along this length:

$$\delta\varphi = \frac{w_0\ h_0}{w_g} \cos\left(w_g t + \varphi_g - w_g \frac{L}{2c}\right) \sin\left(w_g \frac{L}{2c}\right) \tag{4.1}$$

where w_0 is the angular frequency of the laser, h_0 is the amplitude of the gravitational wave, w_g is the angular frequency of the gravitational wave and φ_g is the phase of the gravitational wave. This represents the generation of two sidebands at $w_0 \pm w_g$, with amplitude:

$$A_{sb} = -\frac{w_0\ h_0}{2w_g} \sin\left(\frac{w_g L}{2c}\right) E_0 \tag{4.2}$$

where E_0 is the carrier field amplitude, and phase:

$$\varphi_{sb} = \varphi_0 + \frac{\pi}{2} - \frac{w_0 L}{c} \pm \varphi_g \mp \frac{w_g L}{2c} \tag{4.3}$$

The advantage of expressing the modulation in terms of sidebands is that it is straight forward to propagate these fields through an optical setup to derive the interferometer response: the amplitude of the sidebands at the detector output. The derivation for Sagnac and Michelson interferometers with Fabry-Perot arm cavities

is given in step-by-step detail in appendix A. For a Michelson we have:

$$b_{\mathrm{MICH}} = \mathrm{i}\, t_{bs}\; r_{bs}\; a_0\; \alpha_{sb}^{\mathrm{FP}}\; [\exp\left(-\mathrm{i}\left(2k_0 \pm k_g\right) l_x\right) - \exp\left(-\mathrm{i}\left(2k_0 \pm k_g\right) l_y\right)] \tag{4.4}$$

where t_{bs} and r_{bs} are the (amplitude) transmission and reflection coefficients of the beam-splitter, a_0 is the amplitude of the laser beam, k_0 and k_g are the wave numbers of the laser and gravitational wave, and l_x and l_y are the lengths of the short Michelson arms (between the beam-splitter and ITMs). $\alpha_{sb}^{\mathrm{FP}}$ refers to the response of a Fabry-Perot arm cavity to a gravitational wave (see appendix A for details).

In figure 4.2 the amplitude and phase of the response of a Michelson interferometer with arm cavities is shown, calculated using the analytic result from equation 4.4

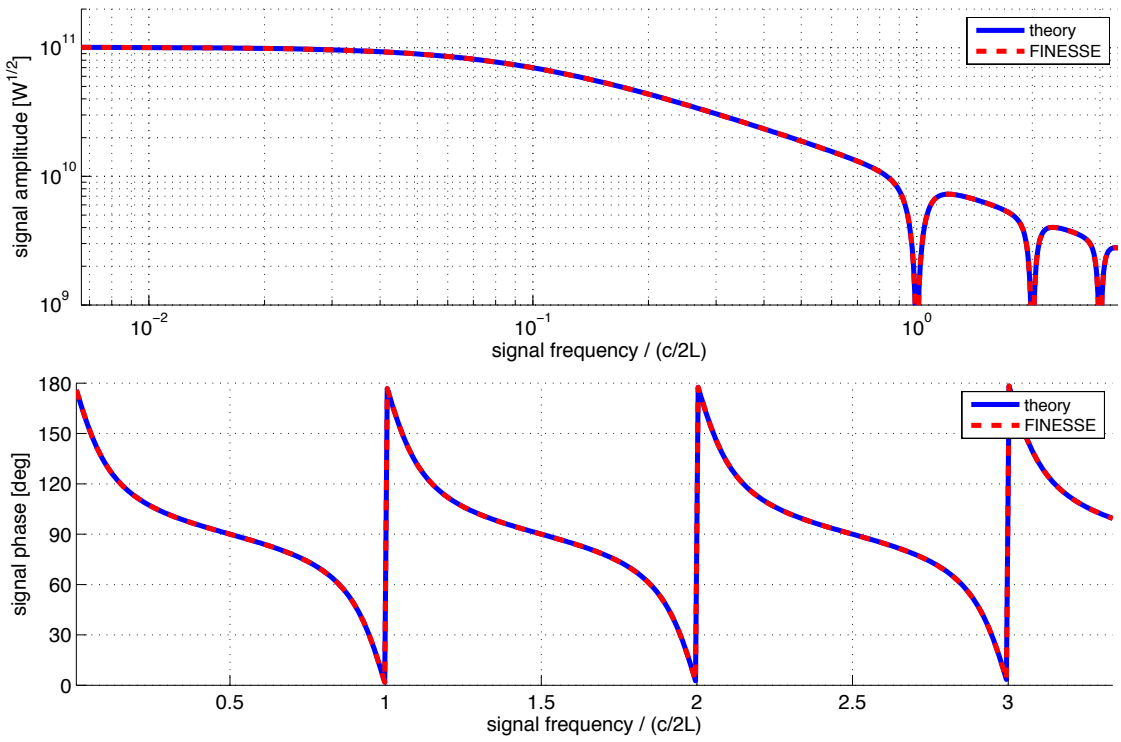

Figure 4.2: Amplitude (top) and phase (bottom) of the response of a Michelson interferometer with Fabry-Perot arm cavities to a gravitational wave. The response is calculated analytically (equation 4.4) and using FINESSE. The frequency of the signal is normalised to the free spectral range of the arm cavities, $\frac{c}{2L}$.

and simulated in FINESSE. The arm cavities are on resonance for the carrier light and the Michelson is tuned to the dark fringe for the carrier. At low frequencies the Michelson exhibits a flat response. The Michelson response drops as the gravitational wave frequency reaches $\frac{c}{2L}$, the free spectral range of the arm cavities. At this frequency one cycle of the gravitational wave signal is equal to the light round-trip time in the arms, so the phase accumulated is equivalent to 0 and the detector is not sensitive to such frequencies. The FINESSE and analytic transfer functions give the same results in amplitude and phase.

For a Sagnac interferometer with Fabry-Perot arm cavities the response is given by:

$$b_{\mathrm{SAG}} = a_0 \; \alpha_{sb}^{\mathrm{FP}} [R_{cav}(k_0) - R_{cav}(k_0 \pm k_g)][R_{bs} + T_{bs}] \tag{4.5}$$

where R_{bs} and T_{bs} refer to the (power) reflection and transmission coefficients of the beam-splitter. R_{cav} refers to the frequency dependent reflection coefficient for a cavity of fixed length. This length is controlled for the carrier, k_0, resonance, so the reflection coefficients for the sidebands ($k_0 \pm k_g$) will be slightly different. R_{cav} differs from $\alpha_{sb}^{\mathrm{FP}}$, in that it refers to the reflection of the signal sidebands from a cavity, where the sidebands are created elsewhere, whereas $\alpha_{sb}^{\mathrm{FP}}$ involves the creation of the gravitational wave sidebands within the cavity. The Sagnac response involves both of these terms as the laser light travels through both arms before it exits the interferometer: sidebands created in one arm will be reflected from the other.

In figure 4.3 the amplitude and phase of the gravitational wave response of a Sagnac interferometer with Fabry-Perot arm cavities is shown. The response is calculated analytically (from equation 4.5) and using FINESSE. The response of the Sagnac interferometer has a distinctive shape, compared to the Michelson. At very low frequencies the response is not flat, as with the Michelson, but slopes upwards, peaking at around $0.1\frac{c}{2L}$ in this example. As with the Michelson response the analytic and FINESSE responses give the same result.

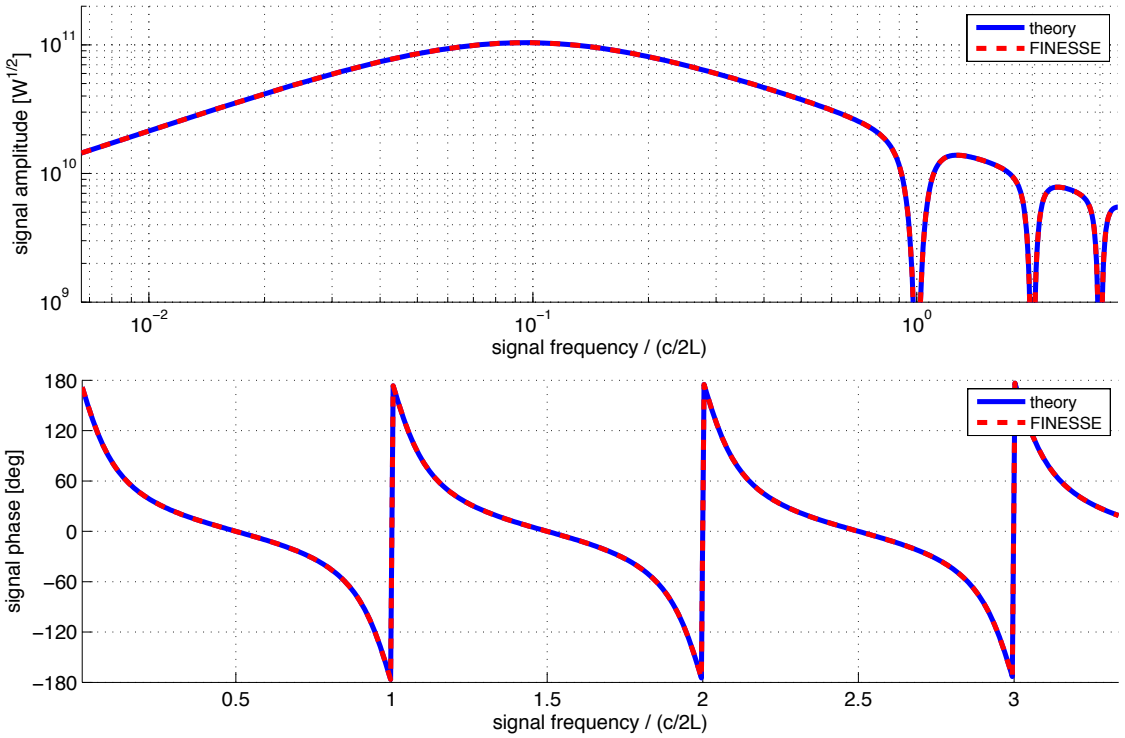

Figure 4.3: Amplitude (top) and phase (bottom) of the gravitational wave response of a Sagnac interferometer with Fabry-Perot arm cavities. The response is calculated analytically (equation 4.5) and simulated in FINESSE. The frequency of the gravitational wave signal is normalised by the free spectral range of the arm cavities, $\frac{c}{2L}$.

4.2 Modal methods vs. FFT methods

The decision to use a modal method to simulate the results presented in this thesis stems from the speed and intuitive nature of the results. The coupling coefficients are calculated numerically for each surface on which a mirror map is applied, for both the reflected and the transmitted field, from the integral [39; 49]:

$$k_{n,m,n',m'} = \int_S u_{n,m}\ A(x,y)\ u^*_{n',m'}\ \mathrm{d}S \tag{4.6}$$

where $u_{n,m}$ is a mode in the incident beam, $u_{n',m'}$ is a mode in the reflected/transmitted beam, S indicates the surface defined by the mirror map and $A(x,y)$ describes the transformation of the beam on reflection/transmission via the distorted mirror. The

most important aspects of performing simulations with modal models are: 1) to use the correct Gaussian basis for the higher-order mode expansion; and 2) to use enough higher-order modes to recreate distortions of the wavefront. A good choice of Gaussian basis means a small number of modes should be sufficient to reproduce the distortions we expect in gravitational wave interferometers.

To robustly test FINESSE it was necessary to compare with simulations using very different methods for simulating light fields in interferometers. For this reason we chose to use a *Fast Fourier Transform* (FFT) method, which uses Fourier transforms of the light fields to propagate them through various optical components [46; 84]. Unlike the modal model an FFT simulation does not express a light field as a sum of individual Gaussian modes, but represents the full field as a 2D grid. This light field is then transformed by functions representing the effect of different optical components, e.g. spaces, mirrors and lenses. A mirror surface is represented as a 2D grid detailing the height of the mirror surface, so it is a simple matter of including a mirror distortion on this grid. In FINESSE the steady-state equations for a particular optical setup are solved, giving the light fields at all points of the interferometer. The effects of distorted optics are included using matrices of coupling coefficients. Light fields interacting with distorted mirrors are transformed by these matrices, computing the mode content of the interferometer at any point.

Using an FFT method requires propagating the light field back and forth within all cavities in the interferometer, in order to simulate the power build up within these cavities. Such FFT methods have been used extensively in gravitational wave modelling [85; 86; 87] and appear a suitable candidate for our comparisons. In the simulations detailed here we use a set of MATLAB functions based on OSCAR [85].

4.2.1 Comparing models: qualitative testing

The comparisons of FINESSE with the FFT models detailed in this chapter will take the form of tests of the overall behaviour, comparing the shape of the beams, the ringing up of higher order modes and cavity losses in a qualitative manner. Both modal models and FFT methods have previously been tested [39; 84] and can describe optics well in the regime of gravitational wave interferometers: paraxial, linear optics. FINESSE in particular has been rigorously tested and can correctly simulate a large range of known results [39; 49]. In this chapter the testing of FINESSE is extended to the higher order mode model developed over the last few years. In most cases we do not have analytical solutions to these higher order mode effects, motivating our comparison with FFT codes. However, although both methods can model the small distortion effects we consider, they do contain some inherent approximations. In the case of modal models this arises from the finite number of modes. In FFT codes the finite grid size and resolution restricts the accuracy. We aim to compare the qualitative results of these two models, as we will expect small discrepancies between the final numbers. We believe this is sufficient for the purposes of supporting the simulations detailed in this thesis and our commissioning work, where the numerical differences are well below the accuracy required.

4.2.2 Reflection from a tilted mirror

In this section we begin with a very simple example, the shape of a beam reflected from a tilted mirror. For such a simple case we can predict the higher-order modes which will be present, namely the order 1 Hermite-Gauss mode HG_{10}. For simple distortion effects, such as misalignment and mode-mismatch, there are two possible methods which can be used in FINESSE. One method is to use a surface map applied to the relevant mirror to depict the tilt or curvature mismatch. We also have an analytic method for calculating such effects, as outlined by Bayer-Helms [80].

For this method misalignment should be specified in FINESSE using the attribute command (`attr`).

Firstly we consider a simple, completely reflective mirror and apply a misalignment of 1 μrad with respect to the incoming beam, placing the mirror at the beam waist. For this simple distortion we simulate the result in three ways: 1) using FINESSE with the misalignment applied using the `attr` command (Bayer-Helms); 2) using FINESSE with a map representing the misalignment; and 3) using an FFT method with a tilt applied to the 2D grid representing the mirror. The reflected beam is detected with the HG_{00} mode removed (using the `mask` command in FINESSE), so only the distortion of the beam is shown. The cross-section of the amplitude and phase of this beam are shown in figure 4.4 for all three simulation methods. As expected the distortion of the beam is dominated by the HG_{10} mode, as seen in the shape of the amplitude. The three methods result in the same amplitude and phase.

The next step is to test the behaviour when the misaligned mirror is used in a more complex setup. In this case the mirror is used in a Fabry-Perot cavity to check

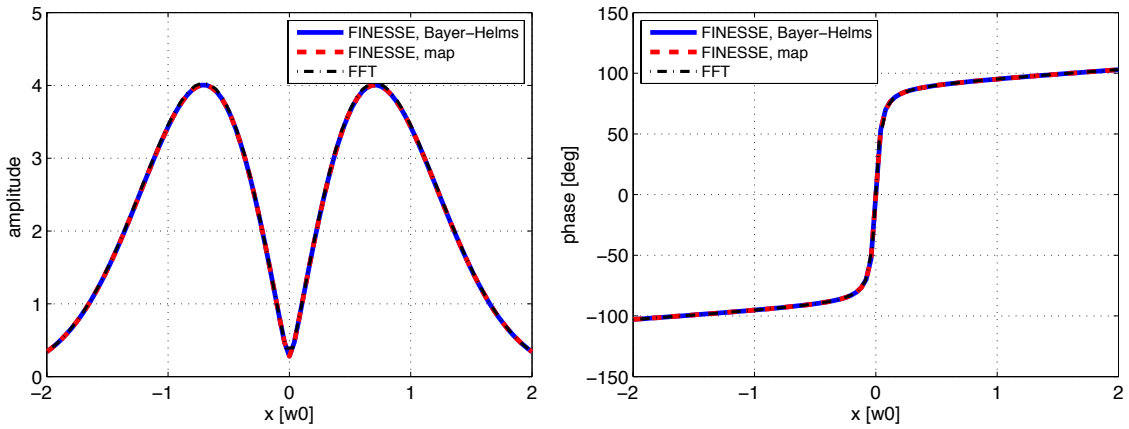

Figure 4.4: Amplitude (left) and phase (right) of the non-HG00 components of the beam reflected from a 1 μrad misaligned mirror placed at the beam waist. The cross-section along the x-axis of the beam is shown. Results from FINESSE simulations using two different methods are shown, an analytic method (Bayer-Helms) and using a mirror map, as well as the results from an FFT propagation simulation. The higher-order mode content is dominated by the order 1 mode HG_{10}, as expected from misalignment.

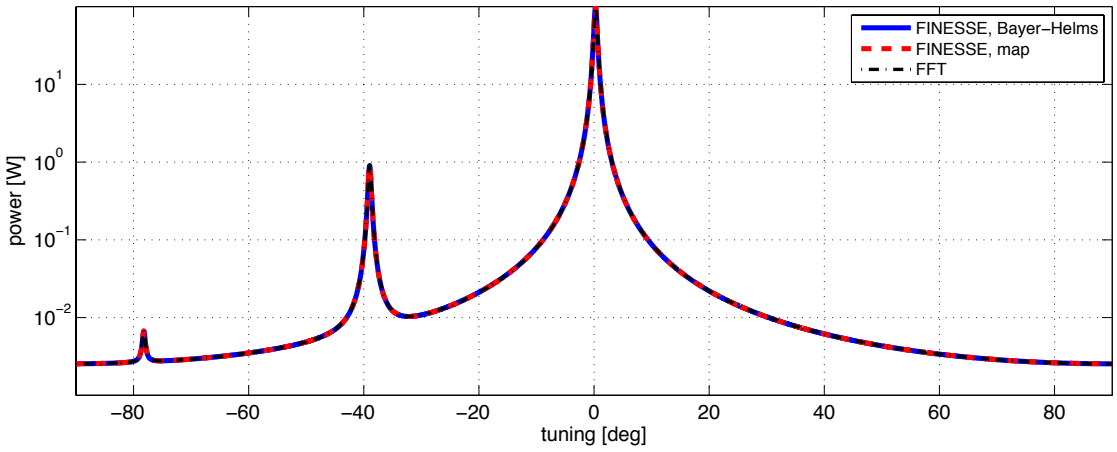

Figure 4.5: Scan of a cavity with a 1 μrad misaligned input mirror. The cavity is simulated in FINESSE using an analytic method (Bayer-Helms) and a tilted mirror map, as well as using an FFT method. The main peak at 0° corresponds to the fundamental mode. The majority of the distortion of the beam is described by the order 1 HG_{10} mode, resonant at $\sim -40°$. Some coupling into an order 2 mode occurs, resonant at $\sim -80°$.

that our modelling of a simple component is correctly extended to behaviour in systems with more complicated interactions. The circulating power detected during a scan of this cavity is shown in figure 4.5. As expected, the majority of the power is in the fundamental mode, resonant at 0°. The misalignment is well described by the addition of the order 1 mode, HG_{10}, which is resonant at around -40°. The peaks are well matched in both tuning and power between the 2 FINESSE methods and the FFT result. All 3 methods also see a second order mode appear, the peak at $\sim -80°$.

4.2.3 Transmission through a thin lens

We have confirmed our simulation approach for first order effects, the next step is to consider second order effects, such as the change in beam size on transmission through a lens. As with misalignment we can simulate this in two ways in FINESSE. Firstly with a lens component, which computes the effect of the lens using an ABCD matrix to transform the Gaussian parameter of the beam, effectively changing the

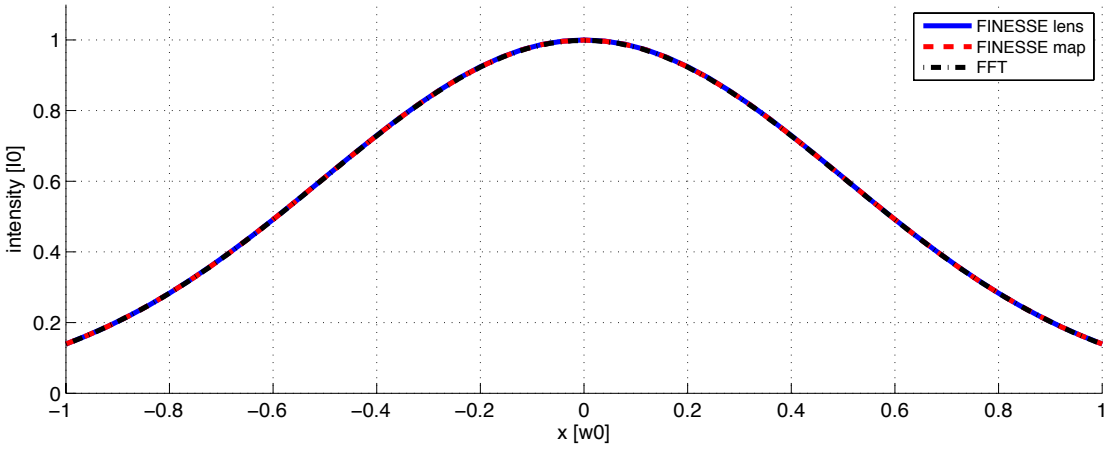

Figure 4.6: Normalised intensity of the cross section of a beam transmitted through a focusing thin lens with a focal length 200 m. The beam was simulated using 3 different methods: 1) using FINESSE with a lens component which uses an ABCD matrix to transform the beam; 2) using FINESSE with a transmission map representing the optical path of the lens; and 3) using a Fast Fourier Transform (FFT) propagation method.

size of the beam. Secondly we use a transmission map to represent the optical path of the lens. We also simulate this effect with an FFT simulation.

Figure 4.6 shows a cross section of the beam transmitted by a convex lens with a focal length of 200 m, as simulated by these 3 methods. The lens changes the size of the beam, which can be described by the addition of an order 2 Laguerre-Gauss mode, LG_{10}. The 3 different methods give the same beam size and shape, even when FINESSE only uses `maxtem 2` (the maximum order of modes used in the simulation) to recreate the beam shape.

4.2.4 Mirror maps in cavities

A lot of simulations for commissioning and investigations such as those detailed in chapter 3 are concerned with the behaviour of optical cavities, so here we concentrate on tests of FINESSE in terms of cavity performance. In particular we want to test the performance when more arbitrary mirror distortions are applied to the cavity mirrors. In these cases there is no analytic solution and the FINESSE results are

only compared with the results of an FFT model. Here we examine the simulated behaviour of an Advanced LIGO arm cavity, with an Advanced LIGO mirror surface map applied to the end mirror, to represent a more generic surface distortion. The map chosen is an Advanced LIGO end mirror map, but for the anti-relective (AR) back surface (for ETM01 [74]). This map is chosen as it has a greater surface distortion than the highly reflective front surface, due to less stringent requirements for the AR surfaces. This will increase the higher order mode effects, making a more effective test of the modal and FFT methods.

In figure 4.7 the power circulating in such a cavity is shown, as simulated in FINESSE and using an FFT code. In this case the FINESSE simulation is carried out with `maxtem 6`. The majority of the power remains in the fundamental mode, but the addition of a surface distortion on the end mirror produces higher order modes, in particular order 1 modes (resonant at $\sim 20°$) and order 2 modes (resonant at $\sim 45°$). Both the FINESSE and FFT results show these additional resonance peaks, at the same power and tuning. Slight peaks at $70°$ and $-85°$ are also observed in both simulations. The agreement of these two simulation methods for this arbitrary

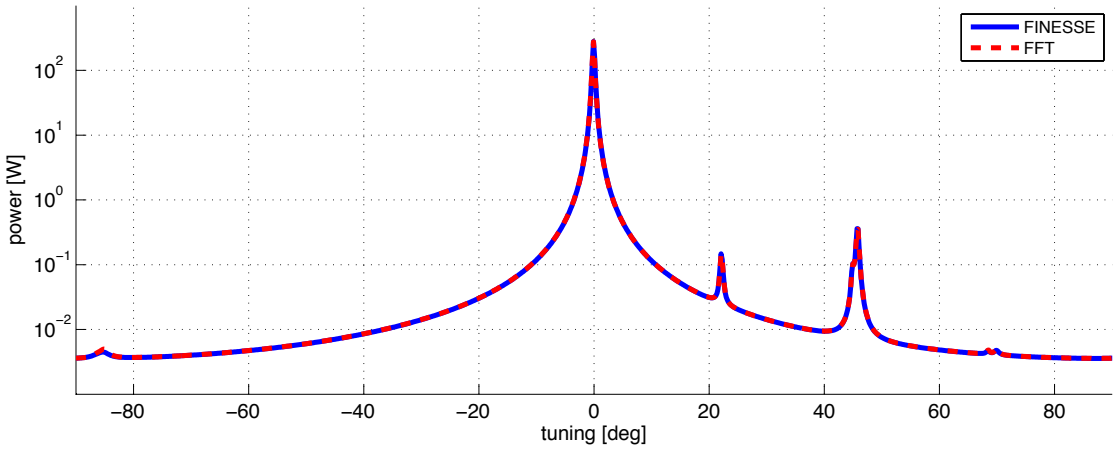

Figure 4.7: The power circulating in a simulated Advanced LIGO cavity as the cavity is tuned. The end mirror has some distorted surface described by an Advanced LIGO mirror map. The cavity is simulated using the modal model FINESSE and an FFT propagation method. The presence of mirror surface distortions results in higher order modes in the cavity: the peaks in power at different tunings.

mirror map, using a relatively low `maxtem`, is good support for the modal model.

A significant simulation campaign undertaken during my Ph.D. was the investigation into the potential of higher order Laguerre-Gauss beams detailed in chapter 3. In particular this focused on the behaviour of the LG_{33} mode in high finesse cavities. It therefore was necessary to test the results of FINESSE simulations using this input mode. The Advanced LIGO cavity simulated above was adapted by reducing the length from 4 km to the 2.8 km required for LG_{33} (see section 3.4). The cavity was simulated in FINESSE and using an FFT method with the mirror map applied to the end mirror but this time with an LG_{33} input beam. The circulating power for a scan of this cavity is shown in figure 4.8. The majority of the power remains in the order 9 modes, resonant at 90°. However, as with the 00 mode there is coupling into other order modes and additional resonance peaks appear in the scan. As expected the use of LG_{33} results in more additional modes than for the 00 mode, as there are more ways in which this mode can couple (see chapter 3). Crucially we see that, as with the 00 mode, the FINESSE and FFT results match up. In this case

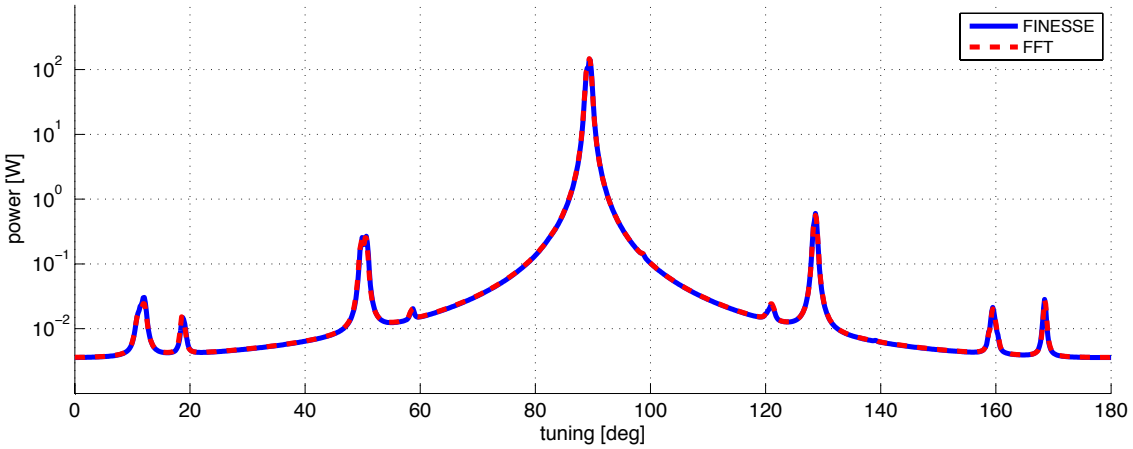

Figure 4.8: Power circulating in an Advanced LIGO style cavity adapted for LG_{33}, with an Advanced LIGO mirror map applied to the end mirror and simulated with the order 9 mode LG_{33} injected into the cavity. The cavity is simulated using FINESSE and an FFT method. The distortion of the end mirror results in coupling into other modes and additional peaks (other than the order 9 peak at 90°) in the circulating power.

the FINESSE simulation used a `maxtem` of 15. This is good confirmation that the results detailed in chapter 3 and published in [36] are modelled correctly, as well as an overall confirmation of the FINESSE model.

Cavities in gravitational wave interferometers are generally operated on resonance. It is crucial that our modal model recreates the correct field on resonance. The effect of coupling into other modes is more easily observed with the LG_{33} input beam, as the effects of mirror distortions are amplified due to cavity degeneracy for higher order modes. In figure 4.9 the intensity of the circulating field in our Advanced LIGO cavity simulated with LG_{33} is plotted, for both the FINESSE and FFT result. The circulating beams are obviously distorted from a pure LG_{33} mode. Significantly, the distorted beam is recreated in both the FINESSE and FFT simulations, with both showing all the same large spatial features. The FFT appears to have some higher spatial frequencies present in the beam which are not present in the FINESSE beam. This is to be expected as a consequence of our modal expansion, which can only be performed with a finite number of higher order modes, purposely omitting very high order distortions. These two beams represent the ability of FI-

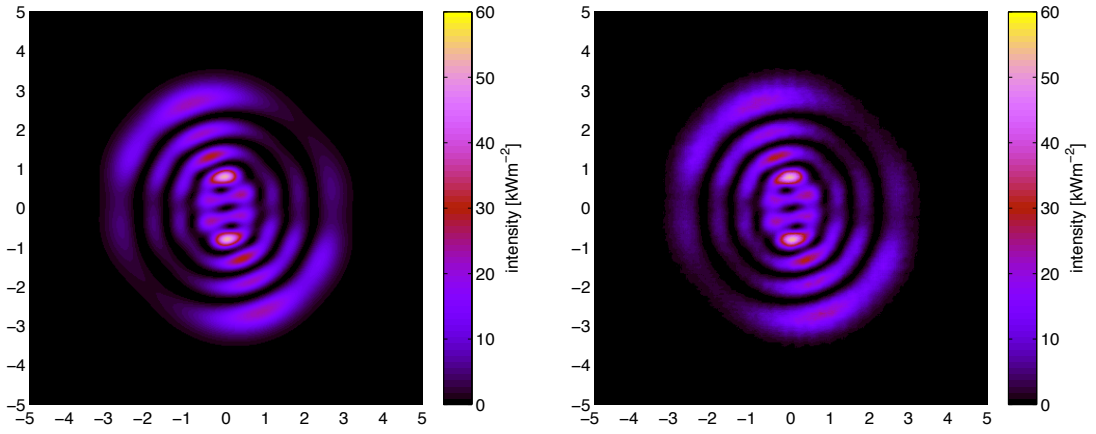

Figure 4.9: Distorted beam circulating in a simulated Advanced LIGO style cavity with a distorted end mirror described by an Advanced LIGO mirror map. The cavity is simulated with an LG_{33} beam injected into it, with the circulating beam detected when the cavity is on resonance. The cavity is simulated using two different methods, the modal model FINESSE (left) and an FFT propagation method (right).

NESSE to recreate the distorted beam shapes, with arbitrary mirror distortions and in cases where there are significant coupling effects.

4.2.5 Thermal distortions in Advanced LIGO cavities

The final tests of the modal model documented here examine the ability to recreate the FFT predicted behaviour of Advanced LIGO arm cavities in the presence of the strong thermal distortions expected during high power operation (as described in section 2.5). As part of the extensive testing of FINESSE we appealed to other simulators in the gravitational wave community for examples they believed would be a good test of FINESSE. We were challenged by Hiro Yamamoto to simulate an Advanced LIGO arm cavity with thermally distorted mirrors and calculate the loss incurred during one round-trip of such a cavity. Previous modal models had not been able to recreate the behaviour predicted by FFT methods, such as the results reported in [88], so this appeared an appropriate test of FINESSE. The expected thermoelastic distortions are relatively large, so if we can recreate the extent of the wavefront distortion caused by such effects we can be confident we are simulating distortions in the right way. Modelling these effects will be crucial for simulations in the later stages of commissioning of advanced detectors, so it is vital FINESSE can perform such simulations robustly. Such setups require some effort to simulate correctly, to achieve accurate results with relatively few higher order modes. This therefore appeared a good test of FINESSE in particular and modal models in general. The examples detailed here form part of the FINESSE manual [49].

Preparing thermal mirror maps

In order to simulate the effects of thermal distortions in FINESSE the expected surface distortions of the mirrors in an Advanced LIGO arm cavity are calculated using the *Hello-Vinet* method [51] (see section 2.5), with the assumption that the

mirrors have reached thermal equilibrium. This distortion is then stored as a mirror map in the FINESSE format. The absorption of laser light by the mirrors has two effects: a distortion of the mirror surface from an ideal sphere and the creation of a lens in the substrate. In this study we only consider the effects of the thermal surface distortions. For simplicity we only deal with absorption in the mirror coatings and not in the substrate, which is relatively small.

For this investigation 3 different coating absorption cases were considered:

1. **No absorption.** The mirrors are represented as perfect spheres, perfectly mode-matched to the incoming beam. The only realistic effect included is the finite apertures of the mirrors.

2. **Unbalanced.** 1 ppm absorption in the end test masses and no absorption in the input test masses.

3. **Balanced.** 1 ppm absorption in the input and end test masses.

For these examples we require two mirror maps, one for the ITM and one for the ETM. Although the mirrors have the same radius, thickness and material properties the distortions will be slightly different for each mirror, due to the different beam sizes at the ITM (5.3 cm) and ETM (6.2 cm). Several MATLAB functions have been developed to calculate the various thermal effects and form part of a package of simulation tools, SIMTOOLS [89] (see section 4.3). In this case the function `FT_mirror_map_from_thermal_distortion.m` was used to produce maps representing the thermal distortions. This function uses the Hello-Vinet formula to calculate the resulting distortion of a mirror surface with given thermal and spatial properties when illuminated with a Gaussian beam of a given size. The dominant effect of the thermal distortion of a mirror is a slight increase in the radius of curvature. In figure 4.10 the expected distortion of the ETM (for 1 ppm coating absorption) is shown. Very similar distortions are predicted for the ITM, scaled to the narrower

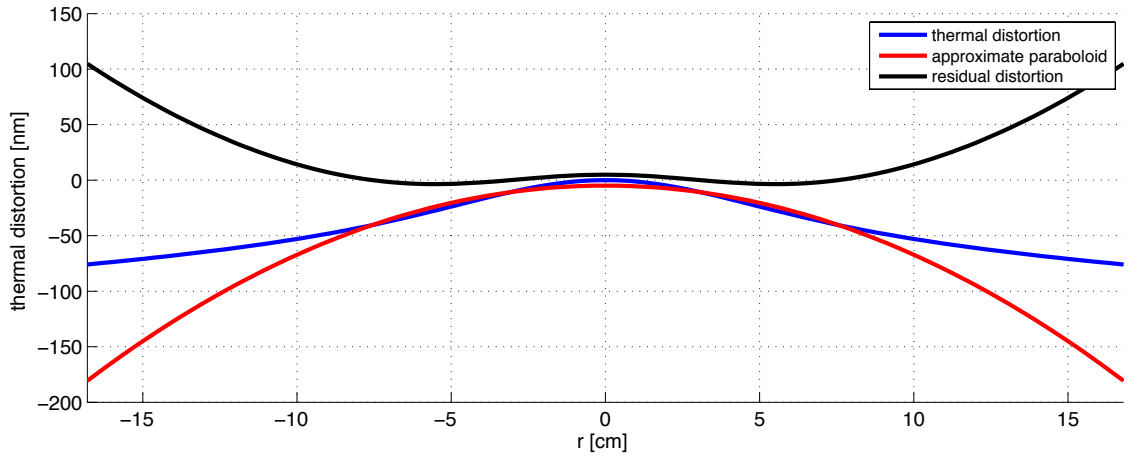

Figure 4.10: Expected thermal distortion of an Advanced LIGO end test mass during high power operation, for 1 ppm coating absorption. The overall thermal distortion is shown, a Gaussian weighted fitted curve (approximate paraboloid) and the residual distortion after this curve is removed.

beam size incident on this mirror, with a steeper distortion due to the concentration of laser power over a smaller area. The central region of the distortion (where the Gaussian beam is most intense) is well described by a simple curved surface (red curve). An Advanced LIGO cavity with thermally distorted mirrors will therefore no longer be mode-matched to the cold cavity and hence to the incoming beam (which we assume is mode matched to the cold case). However, in Advanced LIGO thermal compensation systems have been put in place to correct the change in curvature of the mirrors due to thermal effects (see section 2.5). In this investigation we assume the thermal compensation systems are working perfectly. Using the SIMTOOLS function `FT_remove_curvature_from_mirror_map.m` the curvature is removed from the thermal distortion, weighted by the incident Gaussian beam (see section 4.3.1). The residual distortion is shown in figure 4.10 (black curve). This curvature, or so-called *approximate paraboloid* can be calculated analytically for thermal distortions [53] as in the SIMTOOLS function `FT_approximate_paraboloid_for_thermal_distortion.m`. For the end test mass the removed curvature corresponds to $R_C = -80\,\mathrm{km}$ and for the ITM this corresponds to a curvature of $R_C = -60\,\mathrm{km}$. In most cases this removed curvature would be included in the radius of curvature in the FINESSE script,

in order to calculate the correct cavity eigenmode to use as the Gaussian parameter for the modal expansion (see section 4.3.1). However, in this case we assume the thermal compensation systems are working prefectly to correct the mirrors back to their nominal values of 2245 m (ETM) and 1934 m (ITM).

Simulation setup

The simulation is a simple Fabry-Perot cavity, representing one of the arms of Advanced LIGO and using the design parameters. The cavity setup is defined by 3 lines of code:

```
m1 ITM 0.014 37.5u 0 nITM2 nITM1
s larm 3994.5 nITM2 nETM1
m1 ETM 5u 37.5u 0 nETM1 nETM2
```

where `m1` initiates a mirror component, with a given transmission, loss and tuning, connected to other components via two nodes. The length of the cavity is specified by the space command, `s`. The curvatures of the mirrors are defined with the attribute command:

```
attr ITM Rc 1934
attr ETM Rc 2245
cav armcav ITM nITM2 ETM nETM1
```

where the `cav` command is used to define the cavity eigenmode. In this case this also sets the incoming beam to be mode matched to the cavity specified here, as no other commands are used to set the incoming Gaussian mode. For all 3 cases simulated here (no absorption, unbalanced and balanced) the finite apertures of the mirrors are included:

```
attr ITM r_ap 0.168
attr ETM r_ap 0.168
```

For cases 2 and 3 mirror maps representing the thermal distortions must be applied to the mirrors. E.g. to apply a map to the ETM the following commands are required:

```
# ETM map commands
map ETM etm_thermal_map.txt
knm ETM etm_coupling
conf ETM save_knm_binary 1
conf ETM interpolation_method 2
conf ETM integration_method 3
```

The `map` commands specify the file containing the mirror map in the standard FINESSE format. A file '*etm_coupling*' is created to store the coupling coefficients calculated by FINESSE, stored in binary form for speed of access (`save_knm_binary`). The interpolation of the map (2 = linear) and integration routine (3 = cuba parallel) are also specified.

Results

The chosen figure of merit in this investigation is the round-trip loss for the 3 different cases. It is important that additional losses due to thermal distortions be taken into account in designing and commissioning simulations. In particular we want to compare the losses in the case of distortions on one mirror (unbalanced case) and distortions on both mirrors (balanced case).

In FINESSE the steady state light fields are calculated at all points in a given setup, i.e. it is not simple to simulate one round-trip of a cavity as it is in an FFT simulation. However, we can calculate the round-trip loss from the power circulating in the cavity [88]:

$$L_{arm} = T_{ITM}\left(\sqrt{\frac{P_{FP}(0)}{P_{FP}(L_{arm})}} - 1\right) \tag{4.7}$$

where T_{ITM} is the transmission of the ITM, $P_{FP}(0)$ is the expected circulating power in a loss less cavity (calculated from reflectivity and transmission coefficients) and $P_{FP}(L_{arm})$ is the circulating power in the lossy cavity.

The setups for our 3 cases: no absorption, unbalanced and balanced were simulated for a `maxtem` between 0 and 20. We expect to require relatively high `maxtem` due to the large nature of the thermal distortions. The same simulations are also carried out using an FFT method [85]. The circulating power is detected on resonance and from this the round-trip loss was calculated for each case. Figure 4.11 shows the resulting round-trip losses calculated in FINESSE for different values of `maxtem` for the 3 different cases. For case 1, where no thermal distortions are applied to the mirrors, the result is consistent over a range of `maxtem`. The dominant effect on the round-trip loss in this case is the clipping of the 00 mode due to the finite size of the optics. This effect only requires `maxtem 0`. The number of higher order modes required to model the setup correctly changes when more higher order mode effects are included, i.e. when the thermal distortions of the mirrors are included. This is

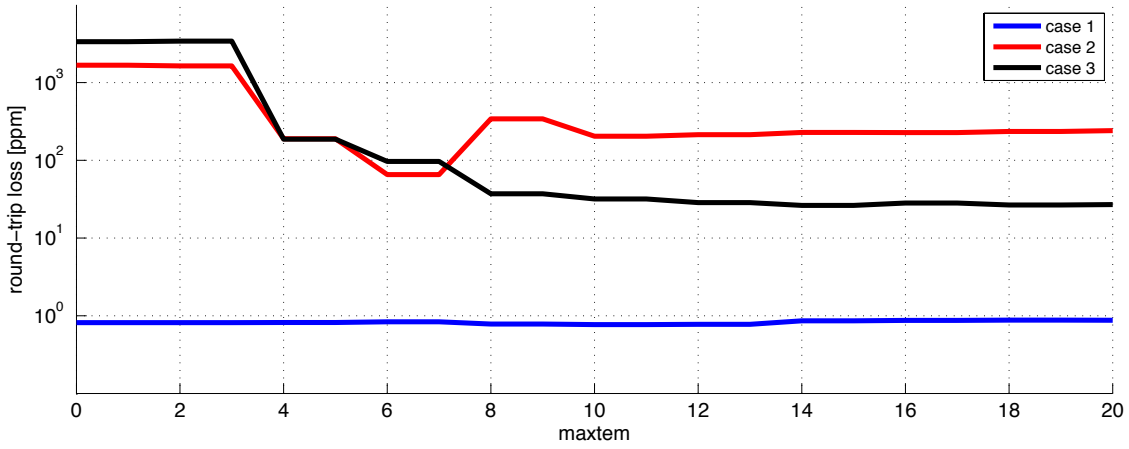

Figure 4.11: Simulated round-trip losses for Advanced LIGO arm cavities with thermally distorted mirrors for different values of maxtem (number of HOMs used in the simulation). 3 different cases are simulated: 1) No thermal distortions, with the beams incurring small losses from the finite size of the mirrors; 2) unbalanced distortions, with a thermally distorted ETM and perfect ITM; and 3) balanced distortions, both mirrors thermally distorted.

shown for cases 2 and 3. The thermal distortions of the mirrors are relatively large, causing a significant amount of coupling into higher order modes. These modes experience greater clipping than the 00 mode, so the round-trip loss is greater than in case 1. The round-trip loss calculated greatly depends on the `maxtem` used. In both cases the calculation of the loss converges when a `maxtem` of 10 or more is used. Less than this could lead to significant over or under estimates of the the loss. This will be significant for future commissioning simulations.

Figure 4.11 also shows that the round-trip losses where both mirrors are thermally distorted are significantly less than those with just the ETM distorted, around an order of magnitude. Naively we might think this should be the other way round, as the case with two distorted mirrors involves coupling into higher order modes at both mirrors. However, as was discussed previously in sections 2.6.2 and 2.6.3, in this case the distortions of both mirrors are very similar to each other, the same shape just scaled to the width of the incident beam on each mirror. When the beam is incident on the end mirror the wavefront is distorted from the curved shape of the Gaussian to fit the distorted shape of the ETM. When this beam propagates to the input mirror, in case 2, the distorted wavefront does not match the perfect surface of the ITM and the wavefront is distorted back to the curved shape. This creates additional higher order modes. In case 3 the distorted wavefront coming from the ETM is a very good match for the distortion of the ITM, and less higher order modes are created.

Finally, in table 4.1 the final FINESSE results are summarised, along with the losses simulated using an FFT method. In this case the results from FINESSE correspond to `maxtem 20`, but very similar numbers are achieved with `maxtem 10`. These numbers agree very well with the results of the FFT. Crucially, the FINESSE simulation now gives the result of a lower round-trip loss for the balanced case (case 3), a result that previous investigations using other modal models were apparently not able to recreate.

Case	FINESSE	FFT
1	0.9	0.9
2	225	234
3	27	27

Table 4.1: Round-trip losses (in parts-per-million) incurred in simulations of Advanced LIGO cavities with thermal distortions of the mirrors. 3 cases are simulated: 1) no thermal distortions; 2) unbalanced thermal distortions, corresponding to 1 ppm absorption in the end test mass; 3) balanced distortions, 1 ppm absorption in both mirrors. The cavity is simulated using a modal model (FINESSE, using maxtem 20) and an FFT method.

The results summarised here suggest that FINESSE is capable of modelling the large distortions expected in high power gravitational wave interferometers. Care should be taken, in both the preprocessing of the mirror maps and the number of higher order modes included, but if the steps detailed here are taken we can produce the correct results.

4.2.6 Apertures

The final distortion effect considered here is the effect of apertures on the beam. In general a large number of higher order modes are required if a beam is incident on the edge of a mirror or any component with a sharp cut-off. However, in the case of well behaved interferometers we expect the beams to be well centred with very little power at the edges of our optics. In this case modal models are adequate to describe aperture effects, as these are dominated by a loss of power in the 00 mode. Tests of such aperture effects have been carried out and for the expected beam sizes in gravitational wave interferometers the relative errors are small enough (see section 4.12 of the FINESSE manual [49]).

4.2.7 Full interferometers

As gravitational wave interferometers are based on optical cavities it did not appear necessary to explicitly test FINESSE against more complicated setups than the cavity examples shown here. As part of commissioning for Advanced LIGO I have simulated more complex setups (power recycled Michelson, complete Advanced LIGO dual recycled configuration, see chapter 5) in conjunction with Hiro Yamamoto's FFT simulations. It is often necessary in commissioning for different groups to simulate the same setup with different models. Both FINESSE and the FFT codes give very similar results, as well as matching what is observed experimentally.

4.3 Simtools

The simulations presented throughout this thesis often required further analytic and numerical tools to perform efficient simulations and to understand the results. These include tools such as those used in 4.2.5 to calculate the expected thermal distortions and process the mirror maps. The functions I have developed generally fell into three categories:

1. Tools required to perform complicated FINESSE simulations in an efficient manner. These involve functions used to preprocess mirror maps to use as few HOMs as possible and tools for running FINESSE in MATLAB to perform more complex tasks.

2. Tools for analysing the output of FINESSE simulations, such as decomposing beams into Gaussian modes (other than the Hermite-Gauss modes used internally by FINESSE).

3. Analytical and numerical tools used to compare FINESSE simulation results with other approaches, such as FFT methods and analytical coupling solutions.

A large part of my work on the simulations of advanced interferometers presented here also involved the development of a range of tools to support FINESSE. These tools were written in MATLAB and form part of the SIMTOOLS package [89]. In particular the tools I have developed focus on the preparation of mirror maps for use in FINESSE and the analysis of surfaces, particularly in terms of Zernike polynomials. Here I will explain the most pertinent groups of functions for this thesis: map preparation tools and those used to calculate Zernike polynomials

4.3.1 Mirror map preparation

Efficient simulations of mirror distortions using modal models are achieved by preparing any mirror maps in such a way as to require as few higher order modes as possible. The most important aspect, when setting up a modal simulation, is to chose the right Gaussian basis with which to perform the modal decomposition. Generally, when dealing with interferometers made up of a series of resonant cavities, the best Gaussian basis is that described by the cavity eigenmodes. These eigenmodes are calculated from the cavity parameters, specifically the curvature of the mirrors and their relative positioning. Using these parameters we calculate the Gaussian mode which resonates in such a cavity.

To calculate these eigenmodes we need the precise curvature of our mirrors, entered into FINESSE as a single number with the attribute command:

```
attr ITM Rc -1934
```

However, in the case where a surface map is applied to a mirror in FINESSE we need to be careful that the map does not contain any curvature. If it does this element of curvature will not be included in calculations of the eigenmode and we are effectively including some mode mismatch in the simulation. This can be avoided by preprocessing the mirror map to remove any curvature, and then including the removed curvature term in the R_C specified by the `attr` command.

The curvature from a surface can be removed by fitting a spherical surface to it, in this case minimising the difference between our reference function, the spherical surface, and our data, the mirror map. This is represented by the function:

$$f = \int_0^{2\pi} \int_0^{R} [Z_{map} - Z_{sphere}]^2 \; r \; \mathrm{d}r \; \mathrm{d}\theta \tag{4.8}$$

where R is the mirror radius, Z_{map} is the surface described by our map and Z_{sphere} is a spherical surface, described by a radius of curvature and offsets in the x, y and z directions. The best fit for the curvature is achieved when f is minimised. This curvature can then be removed from the map surface. In SIMTOOLS this fitting is performed using an in built MATLAB function, `fminsearch`, which minimises our given function, f, by adjusting the parameters, specifically the radius of curvature, which define the reference function Z_{sphere}. In general this fitting algorithm works well when the surface is well described by a curved surface. However, often we want to remove the residual curvatures left in our map data from the measurement process. In this case the maps have relatively small spherical components, compared to the overall curvature of the mirrors. For small curvatures the fitting algorithm can run into problems, as minimising f becomes hard as the majority of the mirror is not described by spherical terms. In these cases it is often quicker and easier to use an inner product with an orthogonal function describing the curvature, generally the Zernike spherical term Z_2^0 (see section 3.4.1).

Another issue to consider when removing some spherical term is the radius over which we should measure this curvature. Naively we could just measure over the entire map surface. However, if we consider the part of the mirror over which the Gaussian beams interact we can measure the curvature the beam 'sees' more effectively. For a typical distorted surface, where the distortion contains components other than the spherical term, the curvature of the surface depends on the area of the surface considered. A Gaussian beam incident on a real mirror will experience

a slightly different curvature depending on the beam size. Therefore, it makes sense for us to weight our fitting routine using a Gaussian function, so that the fitting is tighter at the points on the surface where the incident beam is most intense. This is simply a slight alteration to the previous function:

$$f = \int_0^{2\pi} \int_0^R W(r,\theta)[Z_{map} - Z_{sphere}]^2 \; r \; \mathrm{d}r \; \mathrm{d}\theta \tag{4.9}$$

where $W(r,\theta)$ is the weighting function, in most cases the intensity distribution of the fundamental Gaussian beam. The plots in figure 4.12 show different estimates for the curvature of a mirror surface measured over different regions and using a weighted fitting function. The curvature as measured over the entire map surface (30 cm aperture) is a large, negative radius of curvature. The measurement made over the central 16 cm region gives a different estimate for curvature, changing sign to a positive, smaller radius of curvature. Finally, the curvature calculated using a Gaussian weighting with a beam size of 6.2 cm (the beam size at the end test mass in Advanced LIGO) is similar to the estimate over the central 16 cm, with a slightly

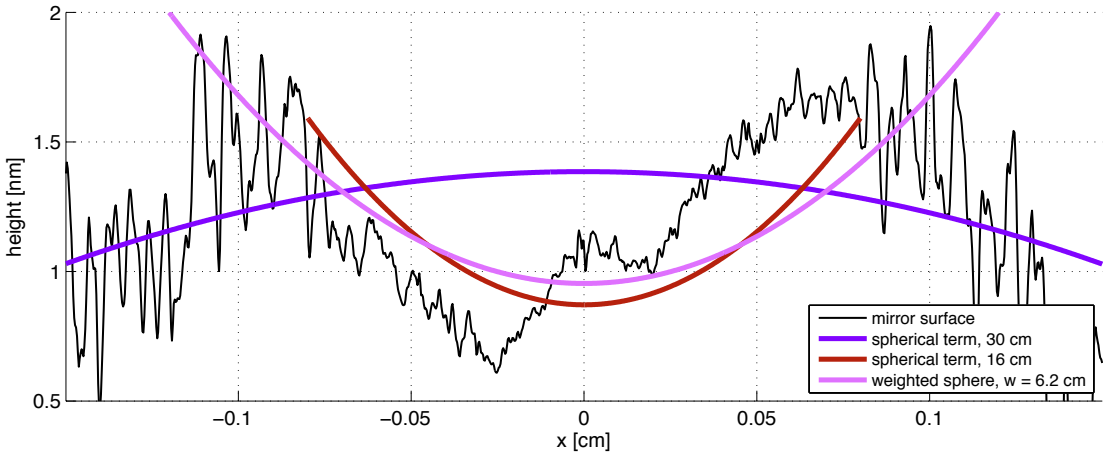

Figure 4.12: Estimates of mirror curvature over different radii and with different weightings. The distorted mirror surface corresponds to the cross section of an Advanced LIGO end test mass, ETM08. 3 different estimates for the curvature of the surface are shown, 1) the Zernike spherical term over the whole 30 cm; 2) the Zernike spherical term over the central 16 cm region; and 3) the Gaussian weighted curvature of the surface, using a weighting beam size of $w = 6.2$ cm.

large R_C as the estimate takes into account data at the edges of the mirror, albeit with a lower contribution to the fitting function.

For modal models the curvature should be removed from mirror maps, and set in the `kat` file to enable the correct calculation of cavity eigenmodes and to avoid unintentionally including mode mismatches. The simulation of mode mismatches can be done separately in FINESSE, using `attr` commands to specify mirror curvatures and `Gauss` commands to specify beam parameters. In the same way any tilt and offset of a map should be removed pre-simulation to avoid simulating misalignments and tuning offsets by mistake. As these parameters will be controlled in the real interferometers, using alignment and longitudinal control signals, including them in any mirror maps can be misleading. These effects can be simulated in FINESSE by specifying a misalignment:

```
attr ETM xbeta 1u
```

which misaligns the ETM by 1 μrad along the x-axis, or by tuning the mirror position. The offset and tilt can be removed using similar methods to curvature removal, specifying the area or weighting with which to measure and remove the defect. In figure 4.13 the Advanced LIGO mirror map, ETM08, is shown for different methods of preparation. The original map is shown along with two prepared versions. The curvature, tilt and offset are removed as measured over the entire surface (centre)

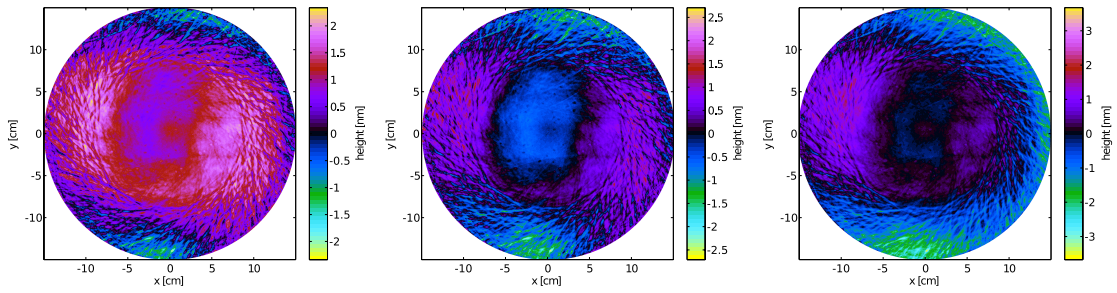

Figure 4.13: Preparing mirror maps for FINESSE: 3 versions of the same mirror map, ETM08, the original map (left); with the offset, tilt and curvature terms removed as measured over the entire map (centre); and with the Gaussian weighted ($w = 6.2$ cm) offset, tilt and curvature terms removed (right).

and as measured using a Gaussian weighted fitting routine (right).

4.3.2 Zernike polynomials

A significant part of the work presented in this thesis concerns the analysis of mirror surfaces, specifically for the investigation of higher order Laguerre-Gauss beams in chapter 3. Although I have also considered and developed tools to look at mirror surfaces in terms of spatial frequencies the majority of my work has used the approach of Zernike polynomials. This approach is particularly compatible with the modal approach used to describe distorted beams, both involving expansions of 2D data in terms of polynomials. To analyse surfaces in terms of Zernike polynomials I wrote a collection of MATLAB tools to calculate the surfaces described by Zernike polynomials as well as decompose mirror maps into these polynomials. In this section some of the technical challenges for writing such tools are detailed, from the implementation of recurrence equations for higher order polynomials, to relations with other optical properties.

Zernike definition

As previously discussed in chapter 3 the Zernike polynomials are orthogonal over the unit disc and have radial index n and azimuthal index m, with $0 \leq m \leq n$. For each n, m polynomial there is an even polynomial:

$$Z_n^{+m}(\rho, \phi) = A_n^{+m} \cos(m\phi) R_n^m(\rho) \tag{4.10}$$

and an odd polynomial:

$$Z_n^{-m}(\rho, \phi) = A_n^{-m} \sin(m\phi) R_n^m(\rho) \tag{4.11}$$

Here we refer to the even polynomial by $+m$ and the odd polynomial by $-m$. $R_n^m(\rho)$ refers to the radial function, given by:

$$R_n^m(\rho) = \sum_{h=0}^{\frac{1}{2}(n-m)} \frac{(-1)^h (n-h)!}{h!(\frac{1}{2}(n+m)-h)!(\frac{1}{2}(n-m)-h)!} \rho^{n-2h} \tag{4.12}$$

for $n-m$ even, and 0 otherwise, giving $n+1$ non-zero polynomials for each order n. To normalise the Zernike polynomials (giving 1 for the inner product of a Zernike polynomial with itself) the constant:

$$N_n^m = \sqrt{\frac{2(n+1)}{1+\delta_{m0}}} \tag{4.13}$$

can be used. Our approach was to use the un-normalised polynomials, as this gives a maximum amplitude of each Zernike surface of $A_n^{\pm m}$, making the amplitudes of the polynomials easier to compare.

For $m \neq 0$ we have an odd and even polynomial, which are identical apart from some relative rotation of $\frac{90^\circ}{m}$. In SIMTOOLS the polynomials are defined as separate odd and even functions when performing an inner product with a mirror map. However, it often makes sense to deal with the resulting polynomial which is a combination of odd and even functions. This combination is the same shape but with a specific amplitude and rotation. The amplitude of the overall polynomial is:

$$A_n^m = \sqrt{(A_n^{-m})^2 + (A_n^{+m})^2} \tag{4.14}$$

The relative rotation of the polynomial (relative to the the even polynomial, i.e. 0° rotation gives the even polynomial) is:

$$\theta = \text{sign}(A_n^{-m}) \frac{1}{m} \cos^{-1}\left(\frac{A_n^{+m}}{\sqrt{(A_n^{-m})^2 + (A_n^{+m})^2}}\right) \tag{4.15}$$

where a positive rotation is equivalent to the even polynomial being rotated anti-

clockwise.

Recurrence relations

For very large order (n) Zernike polynomials we find that the factorials in equation 4.12 can become very large numbers, which can then lead to errors when these polynomials are generated numerically. This can be easily illustrated by 2 values: z_{max} the maximum of the (un-normalised) polynomials which should be 1; and the inner product of the normalised Zernike polynomials with themselves, which should also be 1. However, we find large deviations for higher order polynomials. The plots in figure 4.14 illustrate this. We observe that there is a dramatic increase in both the inner product and z_{max} for $n > 40$ and we can conclude that we are no longer calculating the correct radial polynomials. These large errors occur when n and $n - m$ is large, i.e. Z_{50}^{0}, which is illustrated in the plots by oscillations, at large n, between extreme values and 1 (the true value). We find that R_n^n and R_n^{n-2} can be calculated simply and accurately and we will use this as the basis for our recurrence relations.

To deal with errors such as these we use recurrence relations, which can generate

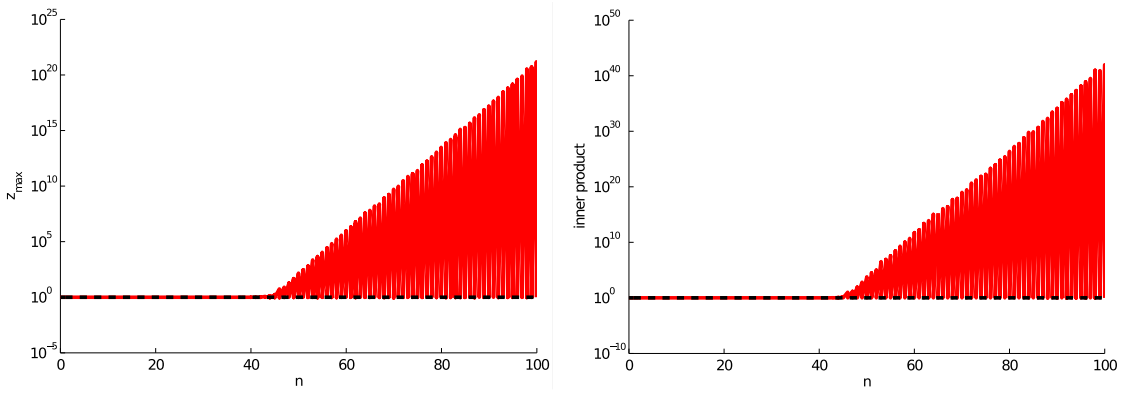

Figure 4.14: Plots illustrating the large numbers occurring when high order (n) Zernike polynomials are calculated numerically. **Left:** The maximum amplitude of any point on the Zernike surface, which should be 1 for the un-normalised polynomials considered here. **Right:** The inner product of each Zernike surface with itself, which should be 1 for the normalised case shown here.

higher order polynomials from the lower order ones. The low order polynomials can be calculated from the standard formula. In our MATLAB package of tools, SIMTOOLS, the recurrence relations outlined below are used to calculate polynomials with $n > 25$.

The radial polynomials obey the following recurrence relation, as proposed by Chong [90]. In this relation the order (n) of the polynomial is fixed and the recurrence calculates polynomials with different m from known polynomials with $m' = m + 2$ and $m'' = m + 4$:

$$R_n^m = H_1 R_n^{m+4}(\rho) + \left(H_2 + \frac{H_3}{\rho^2} \right) R_n^{m+2}(\rho) \tag{4.16}$$

where:

$$\begin{aligned} H_1 &= \frac{(m+4)(m+3)}{2} - (m+4)H_2 + \frac{(n+m+6)(n-m-4)}{8} H_3 \\ H_2 &= \frac{(n+m+4)(n-m-2)}{4(m+3)} H_3 + (m+2) \\ H_3 &= -\frac{4(m+2)(m+1)}{(n+m+2)(n-m)} \end{aligned} \tag{4.17}$$

Using this relation we can calculate any polynomial once we have two polynomials with the same order and different m. However, as we do not want to calculate polynomials with $n > 25$ directly we require some other method to get the desired polynomial order. Chong also proposes two relations which are a modified form of a recurrence relation known as Kinter's method [90]. Chong proposes two relations, one with $m = n$ and one with $m = n - 2$:

$$\begin{aligned} R_n^n &= \rho^n \\ R_n^{n-2} &= n\rho^n - (n-1)\rho^{n-2} \end{aligned} \tag{4.18}$$

Using these relations we can calculate polynomials for any given order n. Then, using Chong's recurrence relations, the polynomial for any m can be calculated

from the $m = n$ and $m = n - 2$ polynomials.

These recurrence methods were implemented in SIMTOOLS for polynomials for $n > 25$. Figure 4.15 shows plots of our figures of merit, the maximum surface height and inner product, for the polynomials as defined in SIMTOOLS. There is a significant improvement from the very large numbers shown in figure 4.14. In the case of z_{max} there is some variation at very large n, due to accumulative errors in the recurrence relations. However, these are very small, with the largest error between orders 0 and 100 being 3.65×10^{-11}, which is small enough to be negligible. The inner product is calculated for several different grid resolutions. The deviation from 1 is much smaller than that achieved using the original Zernike definition. There is some notable error, particularly for high n. This error greatly depends on the resolution of the grid, where there are not enough points to represent the high spatial frequencies represented by high order polynomials. Therefore we must consider the grid resolution when looking at high order polynomials, in particular when decomposing mirror maps into Zernike polynomials. However, as seen in the investigations presented in this thesis, we are primarily interested in low order Zernike polynomials to characterise our mirror surfaces, generally orders < 10. The

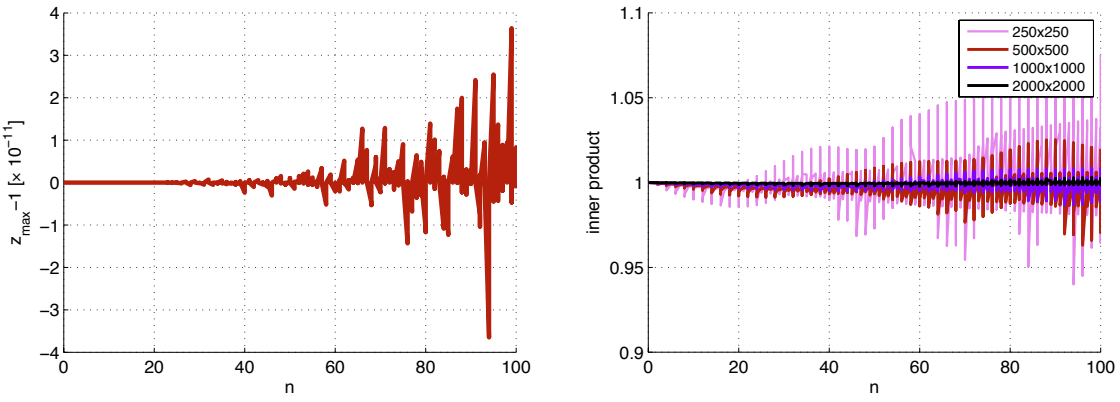

Figure 4.15: Difference from 1 of the surface maximum of the un-normalised Zernike polynomials ($z_{max} - 1$) (left) and the inner product of the normalised Zernike polynomials (right) when calculated numerically using a recurrence routine for $n > 25$, where the expected value is 1. The error on the inner product depends on the resolution of the grid.

higher orders can be represented by spatial frequencies. The inner product errors in these cases should be small, but we should still take care to use a high enough resolution during any analysis.

Equivalent optical properties

Certain low order Zernike polynomials represent specific optical features, or defects, which are often characterised by variables other than the amplitude of the corresponding Zernike polynomial. For example, the curvature of a mirror could be referred to by the Zernike polynomial Z_2^0 or by some radius of curvature. It is often convenient to refer to these other properties and here we will consider the four Zernike terms pertaining to offset (Z_0^0), tilt ($\mathrm{Z}_1^{\pm 1}$) and constant curvature (Z_2^0).

The offset is the simplest defect and is just given by the amplitude of the Z_0^0 term, A_0^0.

The tilt of a mirror surface is described in the x direction by the even order 1 polynomial (Z_1^{+1}) and in y by the odd polynomial (Z_1^{-1}). This is often referred to as the angle of the surface, or misalignment of the surface, which is related to the amplitude of the order 1 polynomials by:

$$\theta = \tan^{-1}\left(\frac{A_1^1}{R}\right) \tag{4.19}$$

where A_1^1 is the amplitude of the order 1 polynomial and R is the radius of the mirror.

The radius of curvature of a mirror is more commonly used to describe its curvature. This is related to the amplitude, A_2^0, of the Zernike polynomial Z_2^0 by:

$$R_C = \frac{4(A_2^0)^2 + R^2}{4A_2^0} \tag{4.20}$$

It should be noted that the Z_2^0 term is not an exact match for a curved surface in

the standard definition. However, for the curvatures of Gaussian beam wavefronts, and hence the curvature of the interferometer mirrors, the two are to all intents and purposes identical. This equivalence fails for highly curved mirror surfaces, i.e. when $R_C \sim R$.

4.4 Conclusion

It is crucial that the modal method used throughout this thesis is properly tested and understood in order to perform meaningful simulations, particularly in anticipation of commissioning. In this chapter the various tests of our particular modal model, FINESSE, have been summarised.

A consequence of an investigation into the potential of a Sagnac interferometer as a future GW detector [81] was testing of the plane wave interferometer response generated in FINESSE against analytic response functions. The results match for complex interferometers: Michelson and Sagnac interferometers with arm cavities. Moving on to testing the simulation of distorted optics using modal models, we have compared FINESSE results with those achieved using a different simulation, the Fast Fourier Transform (FFT) method. In this chapter I have demonstrated the two simulation methods give the same distortions of a beam when interacting with single components: a misaligned mirror and thin lens. Expanding on this the behaviour of linear cavities was throughly tested, using measured mirror maps and injecting the mode LG_{33} into a cavity to test the performance of FINESSE with significant higher order mode effects. In all cases the behaviour matches that shown by our FFT model. Finally, FINESSE was tested on its ability to correctly recreate the round-trip losses which occur when strong distortions are applied to the cavity mirrors, the thermal distortions of the mirrors during high power operation. This definitive test of FINESSE highlighted the need to prepare maps carefully before they are used in simulations and the necessity of including enough higher order modes.

As before the results for this investigation matched those produced using an FFT simulation, when enough HOMs were included. From the results detailed here we can be confident in the validity of the simulation results presented in this thesis and else where.

In this chapter some of the technical issues when using mirror maps and analysing surface distortions are discussed. In particular we focus on the preparation of mirror maps, before they are used in FINESSE, and the use of Zernike polynomials to describe mirror surfaces. Mirror maps are processed to remove any offset, tilt or curvature from a surface, as these features are included explicitly in the FINESSE input files. The most important of these features is the curvature, as this determines the eigenmodes of any cavities and, in most cases, the Gaussian basis with which to perform our modal expansion. The removal of this feature should be treated with care, so as not to un-knowingly simulate a mode mismatch.

The analysis of mirror surfaces in terms of Zernike polynomials requires accurate calculation of the Zernike surfaces. To this end a recurrence relation is used to calculate the polynomials with $n > 25$, to avoid the large errors which occur when the traditional equations are used numerically. In general we are concerned with lower order polynomials, for modal behaviour. However, care should be taken, especially with the resolution of the mirror surface data, when performing such an analysis.

Chapter 5

Commissioning and simulation support for Advanced LIGO

The commissioning of Advanced LIGO is a crucial process in which the behaviour of different sub-sytems are sequentially tested and the detectors are brought to design sensitivity. In this chapter the results of several different commissioning tasks carried out during my Ph.D. are reported.

My first experience with commissioning involved tests of the input mode cleaner as summarised in section 5.2 and reported in more detail in [91]. This was a crucial stage for testing the Advanced LIGO model and preparing for more intense commissioning tasks.

In section 5.3 the results of an investigation into power loss at the beam-splitter are reported. Measurements made during installation of the power recycled Michelson in Livingston showed lower power than expected in the power recycling cavity [92]. The simulations detailed in this section explain this low power buildup: large beams at the beam-splitter result in excess power clipped by the finite size of the optic. Experimentally a maximum power buildup of 37 is achieved by mode matching the two Michelson arms using the x arm thermal compensation system. The simulations return a maximum buildup of 34-36, depending on the matching of

the input beam. Taking into account subsequent measurements of the cavity stability a maximum gain between 37-38 is calculated. We conclude that the addition of the end mirrors will reduce the size of the beam, and the replacement of the beamsplitter is not yet necessary. We also suggest a potential way to reduce the beam sizes: adjusting the power recycling mode matching telescope. These results were originally reported in [40] and presented at the March 2014 LVC conference [41].

Section 5.4 details an extension of the modelling of the Livingston detector: comparing simulations of the contrast defect and output beam with experimental results [92]. This includes matching the contrast defect achieved using the x arm thermal compensation system and the recent measurement using the y arm thermal compensation system, achieving mode matching at a smaller beam size [93].

In section 5.5 an ongoing task is discussed: predicting the effect of mode mismatches present in the Livingston interferometer on the performance of the full control system [43].

Finally, in section 5.6 the full Advanced LIGO dual recycled configuration is modelled to predict the higher order mode content due to coating distortions of the end mirrors. For this task Hiro Yamamoto requested a comparison with his model [94] in order to accept or reject the coating of the ETMs. The simulations predict 100 ppm in higher order modes in the arm cavities, 2000 ppm in the power recycling cavity and a contrast defect of the order of 1 ppm [44]. This agrees with Yamamoto's results and are acceptable HOM levels. We conclude that the coatings can be accepted.

5.1 Preparing for commissioning

Simulating Advanced LIGO for commissioning is a complex process. Before any specific task can be carried out the model must be built and tested against expected behaviour. This process is a long and technical one, which requires understanding

of the optical design of the interferometer and comparison with other models. A summary of the steps I took to prepare the Advanced LIGO FINESSE files [95] for commissioning is detailed in appendix C.

5.2 First commissioning task: the input mode cleaner

My first direct experience of commissioning began in 2012, during the commissioning of the input mode cleaner, the first set of mirrors the laser interacts with. Although I did not lead this commissioning effort, unlike later tasks, this provided a good opportunity to learn about the commissioning process and to check that our models, which have been rigorously tested against other simulation methods (see chapter 4) can match experimental results. The results are reported in the LIGO document [91] and were presented at the Livingston commissioning workshop in January 2013 [96].

5.3 Power loss at the beam-splitter: experience with the Livingston power recycled Michelson

During December 2013 I led a concentrated commissioning effort to explain the observed low power buildup in the power recycling cavity at the LIGO Livingston Observatory (LLO), during commissioning of the power recycled Michelson (PRMI). This task required additional spatial information about the beam: to model the 'clipping' of large beams in the interferometer by the finite size of the beam-splitter. Such a task is ideally suited to the modal model and my experience. The results of this investigation are detailed in the LIGO document [40] and have been presented at the LVC conference in March 2014 [41].

5.3.1 State of the interferometer

Having installed the optics comprising the power recycled Michelson (PRMI) the commissioning team at Livingston were able to lock the PRMI. During the commissioning and installation of the output mode cleaner (OMC) it had been observed that the output mode of the PRMI did not match well to the eigenmode of the OMC as expected [97]. This suggests the eigenmode of the power recycling cavity is not as expected. It was also noted that the two arms of the PRMI were not well mode matched. The most plausible explanation for the mismatch between the two arms is differences between the ITM substrates, as ITMX and ITMY were specifically selected for the similarity of their highly reflective (HR) surfaces.

Measurements of the ITMs taken before they were installed at Livingston identified differences in the curvature of the HR surface, when measured via the AR (anti-reflective) surface (with the measurement beam passing through the substrate) and a direct reflection from the HR surface [98]. This suggests their is some second order distortion in the ITM substrates: effective lenses inside the ITMs. We will refer to these lenses measured under controlled, cold conditions as ITM *non-thermal* substrate lenses, to distinguish them from the thermal lensing of the ITMs during operation (see section 2.5). The focal lengths of these non-thermal lenses were calculated as 305 km for ITMX and -82.4 km for ITMY [40]. The difference in lensing between the two ITMs can explain the mismatch of the two arms. The mismatch between the output mode and OMC eigenmode is due to the difference of these cold lenses to the expected 50 km thermal lenses at 12.5 W input power that the interferometer is designed for [16]. These differences between the current Livingston setup and the Advanced LIGO design are illustrated in figure 5.1. The design is a dual recycled Michelson with 50 km thermal lenses in the ITMs (left). The thermal lenses have a greater focusing power than the non-thermal lenses in the cold optics, as experienced in the current Livingston power recycled Michelson configuration

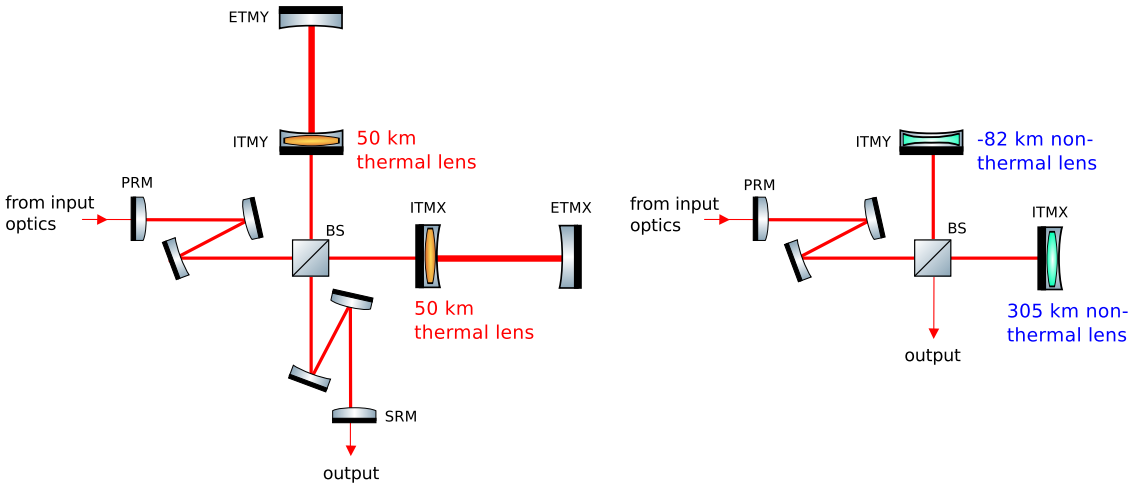

Figure 5.1: Diagrams of different optical setups for Advanced LIGO. **Left:** The Advanced LIGO design, a dual recycled Michelson interferometer with Fabry-Perot arm cavities. The interferometer is designed to be mode-matched to the 50 km thermal lenses which are expected with an input power of 12.5 W. **Right:** Livingston power recycled Michelson (PRMI) configuration, including the non-thermal lenses present in the cold ITMs.

(right). We would therefore expect larger beams in the power recycling cavity of the Livingston configuration than for the design.

It is possible to correct some of the differences between the two arms using the thermal compensation systems (TCS) designed to correct for thermal lensing. By actuating on an ITM ring heater a negative lens is produced in the substrate to counteract the positive lens produced by internal heating (see 2.5.4). In this case the ITMX ring heater can be used to match the arms. Actuating on the ITMY ring heater will increase the mismatch, as the already negative lensing in the substrate will increase.

The ITM ring heaters were actuated on in the Livingston PRMI, whilst the power recycling gain, reflected power and contrast defect were monitored. The results of these measurements over a period of ∼5 hours are shown in figure 5.2, taken from LLO aLOG entry 9733 [92]. When the heaters are switched on or off it takes time for the ITMs to reach thermal equilibrium and the lensing to stabilise. At time $t = 0$ the ITMX ring heater is switched off while the ITM cools down.

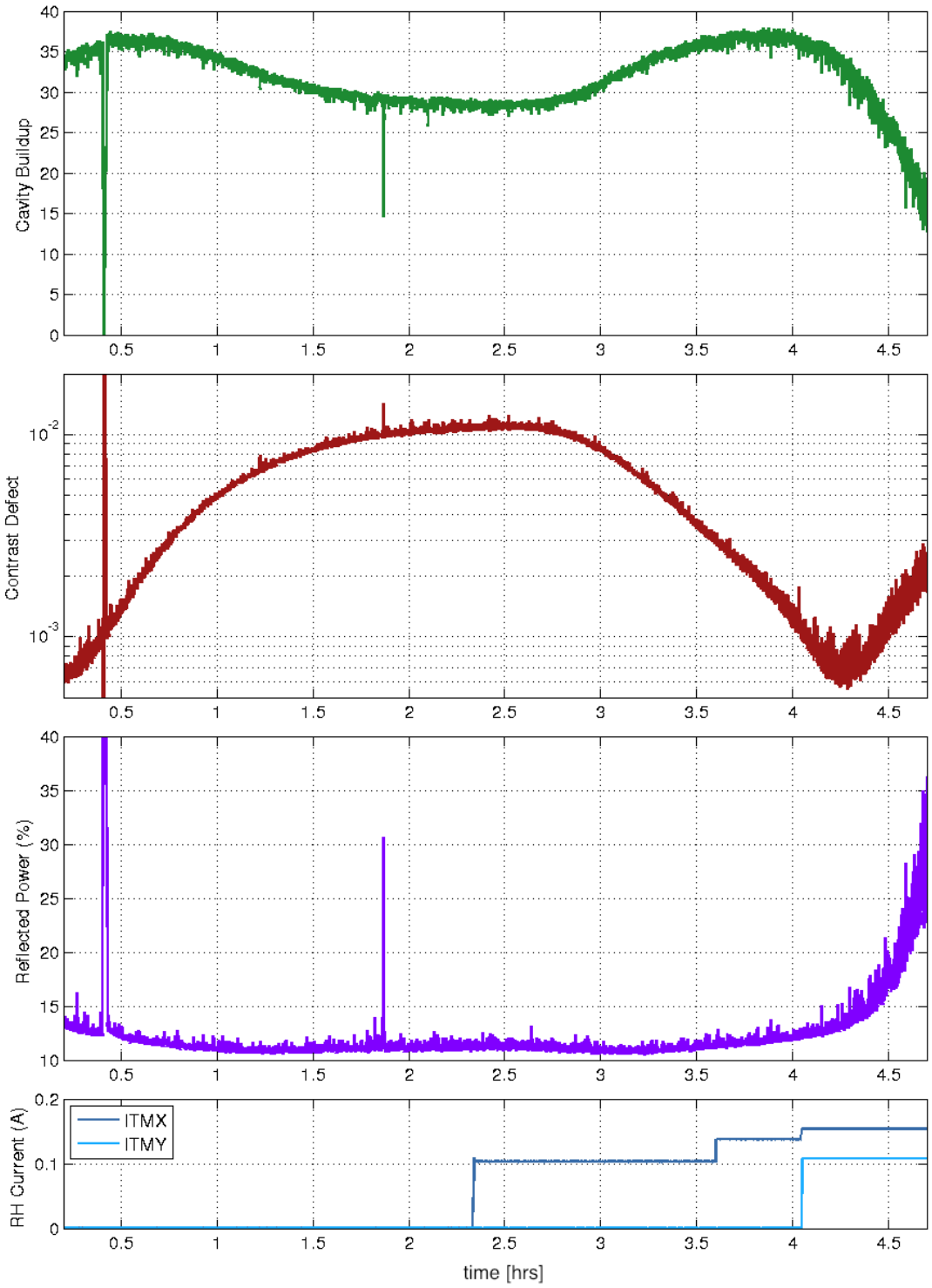

Figure 5.2: Plots showing (from top to bottom) the power build up in the PRC, contrast defect, reflected power and the current applied to the ring-heaters on the ITMs over time. At time 0 the ITMX ring heater is switched off. At around 2 hours ITMX has cooled down and the ITMX ring heater is switched back on. At ∼4 hours the ITMY ring heater is switched on. Image courtesy of Denis Martynov and Chris Mueller [92].

The arms are observed to be well matched at this point, as the contrast defect is at a minimum. This is due to the negative lens created in ITMX, matching it to the constant negative lens in ITMY. As ITMX cools down the substrate gradually returns to it's natural state: a positive non-thermal lens. At ~ 2 hours ITMX has cooled down and a maximum contrast defect is observed. At this point the ring heater for ITMX is switched back on, gradually matching the arms again. After ~ 4 hours the ITMY ring heater is switched on. This increases the negative lensing in ITMY and increases the mismatch between the arms. The contrast defect increases and ultimately the interferometer lost lock.

The behaviour of the contrast defect as the ITM ring heaters are actuated agrees with our qualitative arguments and the measurements of the non-thermal lensing in the ITMs. However, during this operation it was noted that the power recycling gain did not behave as expected. Even at its maximum of ~ 37, the observed power recycling gain is significantly lower than the expected value of 58 calculated from the Advanced LIGO design parameters [31]. Also noteworthy is the fact that the minimum in contrast defect does not coincide exactly with the maximum in PRC gain, as we would expect if the only contributory effects were mode-mismatches.

This problem is inherently an issue of distorted beams. We were tasked with investigating possible explanations for these observed effects, in particular the drop in power recycling gain. The most likely explanation for this low power is clipping in the power recycling cavity, specifically at the beam-splitter where the beams are largest compared to the size of the optic.

5.3.2 The Livingston Finesse file

In preparation for commissioning, 'core' FINESSE files corresponding to the two sites, Livingston and Hanford, were prepared [95]. These files consist of all the core optics, modelling the mirrors and beam-splitter as thick optics, with surfaces

corresponding to the highly reflective (HR) and anti-reflective (AR) sides, and including compensation plates in the arms (part of the TCS). The measured optical parameters (reflectivities, losses etc.) and geometric properties (radii of curvature, thickness etc.) are the measurements of the cold optics installed at Livingston [74]. The distances between different optics are taken from the master coordinate list [99]

For this particular investigation there are several particular parameters which are varied whilst the other optical and geometric properties are kept as given in [74] and [99]. These include:

- Simulating the effect of the ring heaters by tuning the radius of curvature of the ITMs. In practice the ring heater will change the lensing in the substrate and the curvature of the HR surface but as they are both order 2 distortions, and the arm cavities are not included, changing R_C is a reasonable approximation.
- Using apertures to model the finite size of the central beam-splitter.
- The centring of the beam on the beam-splitter.
- Radius of curvature of PR3.

In all simulations reported in this section we assume no thermal lensing, as the low input power (2 W) corresponding to these measurements gives negligible thermal lensing.

5.3.3 Mode-matching: simulating thermal compensation

The expected power recycling gain of 58 was calculated from models of the Advanced LIGO design. The maximum possible PRC gain from the measured Livingston optics is ~ 53. This is calculated from a plane wave model, omitting any higher order mode effects but including the measured losses and reflectivities of the Livingston mirrors. This is still significantly greater than the maximum of 37 measured experimentally,

so the model is extended from simple plane waves to include parameters which effect the size and shape of the beam (i.e. mirror curvatures).

The power recycling cavity forms a split coupled cavity between the individual cavities formed between the PRM and ITMX/Y (PRX/Y). Individually these cavities form resonators for particular eigenmodes. In the current Livingston setup PRX and PRY are substantially mode mismatched, due to the differing non-thermal lenses in the ITMs. This is illustrated in figure 5.3, which shows the beam sizes of the two cavity eigenmodes at the beam-splitter as the ITMX ring heater is actuated (simulated by tuning ITMX R_C). The far left of the plot represents the cold optics, with the ring heater switched off. At this point the eigenmodes of the two arms are strongly mismatched, with the eigenmode of PRX significantly smaller than PRY. It should also be noted that these beam sizes are larger than the design size of 5.3 cm. As ITMX R_C is tuned, mimicking the action of the ring heater, the PRY eigenmode remains the same, whilst the beams in PRX increase. Eventually the beams are mode matched at ~ 1901.5 m.

Using the ring heaters can achieve good mode matching. However, this pushes

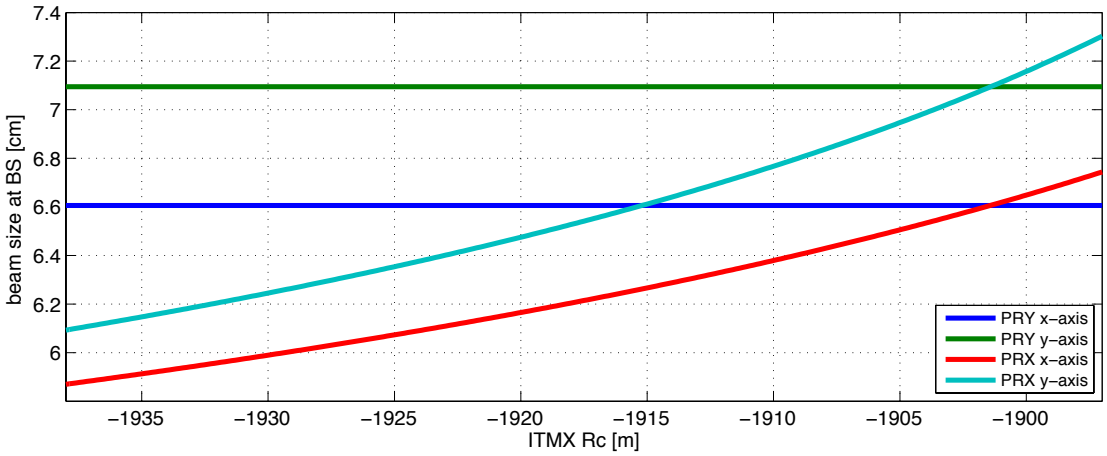

Figure 5.3: Beam sizes of the eigenmodes of the two cavities which make up the Livingston power recycled Michelson: PRX (between the PRM and ITMX) and PRY (between the PRM and ITMY). The radius of curvature of ITMX is tuned, mimicking the action of the ring heater and changing the size of the PRX eigenmode. Equal beam sizes occur when ITMX $R_C = 1901.5$ m.

the overall beams in the PRC to much larger sizes than the design values, which will increase any clipping of the beam in the PRC.

5.3.4 Modelling the beam-splitter

In the Advanced LIGO design the size of the beam, compared to the size of the optics, is largest at the central beam-splitter. In this case, where the beam at the beam-splitter is likely to be significantly larger, it is sensible to investigate clipping losses at the beam-splitter as the discrepancy between our current models and the observed behaviour.

The Advanced LIGO beam-splitter

Figure 5.4 shows a diagram of the central beam-splitter in Advanced LIGO, highlighting the relevant dimensions and the incident beams. The incoming beam (coming from the power recycling cavity) is incident at 45° on the centre of the highly reflective front surface. The transmitted beam travels through the beam-splitter at an angle

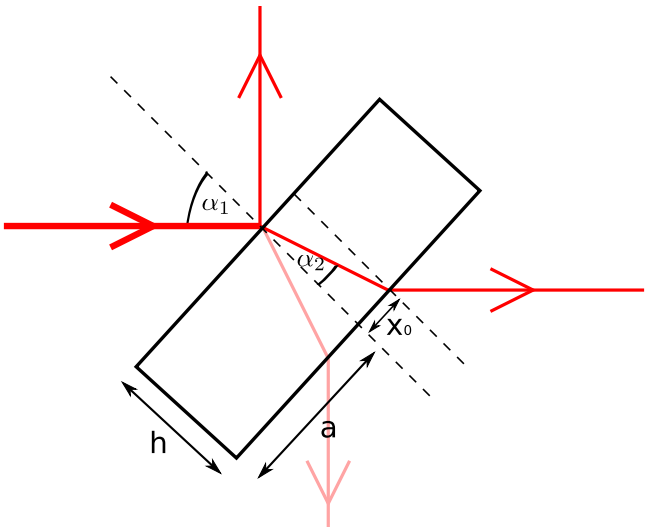

Figure 5.4: Central aLIGO beam splitter geometry. The different beams are shown and their points of incidence at the front and back surface. α_1 and α_2 are the angles of incidence from the power recycling cavity (direct) and x arm (through the BS substrate) respectively. h is the BS thickness, a is the radius and x_0 is the offset of the beam incident on the back surface of the beam-splitter.

of:

$$\alpha_2 = \sin^{-1}\left(\frac{1}{1.44963}\sin\left(45°\right)\right) = 29.195° \tag{5.1}$$

The beam-splitter has a thickness of 6 cm, so the transmitted beam travels a length of:

$$\delta L = \frac{6\,\mathrm{cm}}{\cos\alpha_2} = 6.873\,\mathrm{cm} \tag{5.2}$$

inside the beam-splitter. The beam exits through the AR surface slightly off-centre. Assuming the incoming beam is exactly centred on the HR surface this offset is:

$$x_0 = h\tan\left(\alpha_2\right) = 3.35\,\mathrm{cm} \tag{5.3}$$

The beam-splitter has a diameter of $2a = 37\,\mathrm{cm}$.

Clipping at the front surface

The beam-splitter is a cylindric optic, presented at an angle of 45° to the beam. In the frame of the beam-splitter the beam looks elliptical and to calculate the clipping occurring here we work in the frame of the optic. The clipping loss due to one interaction with the BS is calculated. To do this a mask is created in the shape of the beam-splitter aperture and applied to the incident light field, masking the light outside the aperture. The clipping is calculated using:

$$l_{clip} = 1 - \int_S |u|^2\,\mathrm{d}S \tag{5.4}$$

where u is the normalised masked field. This is calculated numerically for the Advanced LIGO design parameters ($w = 5.3\,\mathrm{cm}$) and for the as-built LLO parameters, with ITMX R_C tuned to 1901.5 m to match the two arms ($w_x = 6.6\,\mathrm{cm}$, $w_y = 7.1\,\mathrm{cm}$). The results are summarised in table 5.1. In figure 5.5 the amplitude of the beams incident on the front surface of the beam-splitter are shown, with

w_x [cm]	w_y [cm]	clipping [ppm]
5.3	5.3	1
6.6	7.1	120

Table 5.1: Clipping on the front of the beam-splitter in the Advanced LIGO power recycled Michelson. The clipping is given for the design parameters ($w = 5.3\,\mathrm{cm}$) and for the current LLO parameters, with the ITMX R_C tuned to 1901.5 m to mode match the arms.

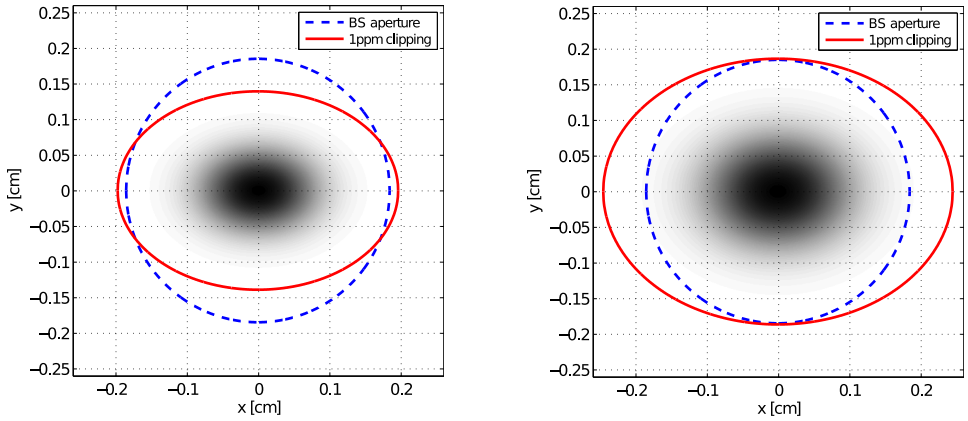

Figure 5.5: Beam amplitude on the front surface of the beam-splitter in the Advanced LIGO power recycled Michelson. **Left:** Advanced LIGO design parameters ($w = 5.3\,\mathrm{cm}$). **Right:** LLO as-built parameters with ITMX $R_C = 1901.5\,\mathrm{m}$ for optimum mode-matching between the arms ($w_x = 6.6\,\mathrm{cm}$, $w_y = 7.1\,\mathrm{cm}$). The beam is shown as a projection onto the BS surface and so appears elliptical. The aperture of the BS and the aperture which would achieve 1 ppm clipping are both shown.

the aperture of the beam-splitter displayed, as well as the aperture corresponding to 1 ppm clipping. These results demonstrate how the increase in beam size, compared to the design parameters, results in significantly increased clipping at the beam-splitter. The clipping on the front surface is increased by over 2 orders of magnitude. In both the design and as-built cases the majority of the beam clipping occurs along the x-axis, as the aperture is effectively smaller along this axis due to the 45° incident angle.

Clipping at the back surface

On the back surface of the beam-splitter the incident beam is slightly off-centre (by 3.35 cm), but the aperture of the optic remains the same. The off-centring will

result in increased clipping at this surface. The clipping at the back of the beam-splitter (table 5.2) is significantly greater than at the front, around an order of magnitude, even for the design parameters. The offset of the beam on this surface also introduces some anti-symmetric clipping of the beam (see figure 5.6) and again most of the clipping happens along the x-axis. The overall clipping at the beam-splitter is dominated by this off-centring on the back surface. In total the current as-built model suggests an increase in clipping at the beam-splitter of at least an order of magnitude.

w_x [cm]	w_y [cm]	clipping [ppm]
5.3	5.3	35
6.6	7.1	840

Table 5.2: Clipping losses on the back surface of the beam-splitter, in an Advanced LIGO power recycled Michelson. Calculated for the design parameters ($w = 5.3\,\mathrm{cm}$) and as-built LLO parameters, with ITMX R_C tuned to match the arms ($w_x = 6.6\,\mathrm{cm}$, $w_y = 7.1\,\mathrm{cm}$).

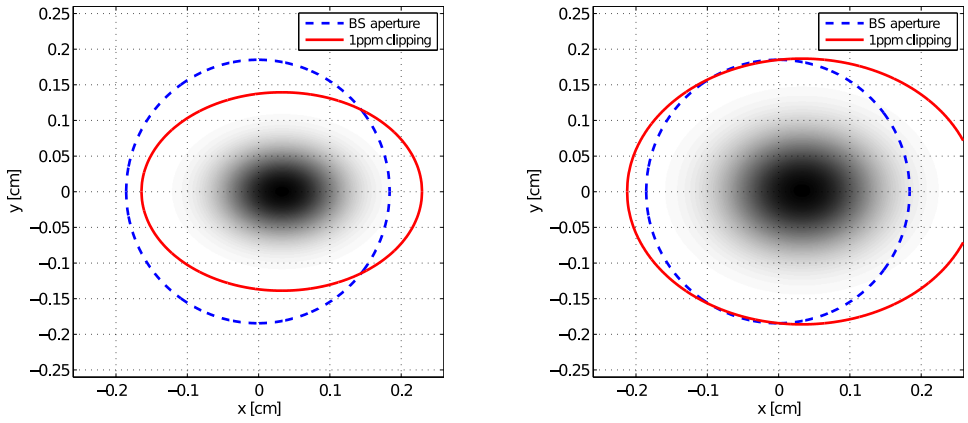

Figure 5.6: Beam amplitude on the back of the beam-splitter in the Advanced LIGO power recycled Michelson. **Left:** Design parameters ($w = 5.3\,\mathrm{cm}$). **Right:** as-built LLO parameters, with ITM R_C tuned to 1901.5 m to match the two arms ($w_x = 6.6\,\mathrm{cm}$, $w_y = 7.1\,\mathrm{cm}$). The beams are shown as projections onto the BS, including the offset of the beam on the back surface. The aperture of the BS and the aperture for 1 ppm clipping of the beam is shown.

5.3.5 Power build up with thermal compensation

The clipping at the beam-splitter described above is calculated for mode matched Michelson arms, achieved in practice using the thermal compensation systems. In the cold state the eigenmode of the cavity between ITMX and the PRM (PRX) will have a smaller beam (see figure 5.3) and the clipping at the BS will be slightly lower. However, for this state of operation the mode-matching will be worse.

Figure 5.7 shows the power recycling gain and contrast defect as the radius of curvature of ITMX is tuned, simulating the effect of the ring heater and attempting to recreate the measurement in figure 5.2. As ITMX is heated (R_C decreases) the positive lensing in ITMX (300 km non-thermal lens) is corrected and gradually matched to the negative lens in ITMY (-80 km non-thermal lens). In the model with no aperture effects the maximum PRC gain is ~ 53, which occurs at the point where the arms are mode matched. However, when the BS apertures are included we see a drop in maximum gain, as well as a shift in the x-axis position of the maximum. The aperture representing the front surface of the BS produces little clipping and consequently only a a small reduction in PRC gain. When the apertures created by the back surface are included the maximum power is significantly reduced and the position of the peak is shifted to a colder ring heater state (higher R_C). This can be explained by considering what happens to the size of the beams in the PRC. As ITMX is heated the lens changes from a cold positive lens to a negative lens. This results in a larger beam size for the PRX cavity eigenmode and overall in the power recycling cavity. As ITMX is heated there is more clipping at the beam-splitter due to larger beam sizes. The maximum in power recycling gain is some compromise between good mode-matching between x and y, and a smaller beam for less clipping.

The setup is also simulated with a mismatched input beam, using a beam which would match the Advanced LIGO design as our best guess for the output of the input mode cleaners. This reduces the gain further as less light is coupled into the

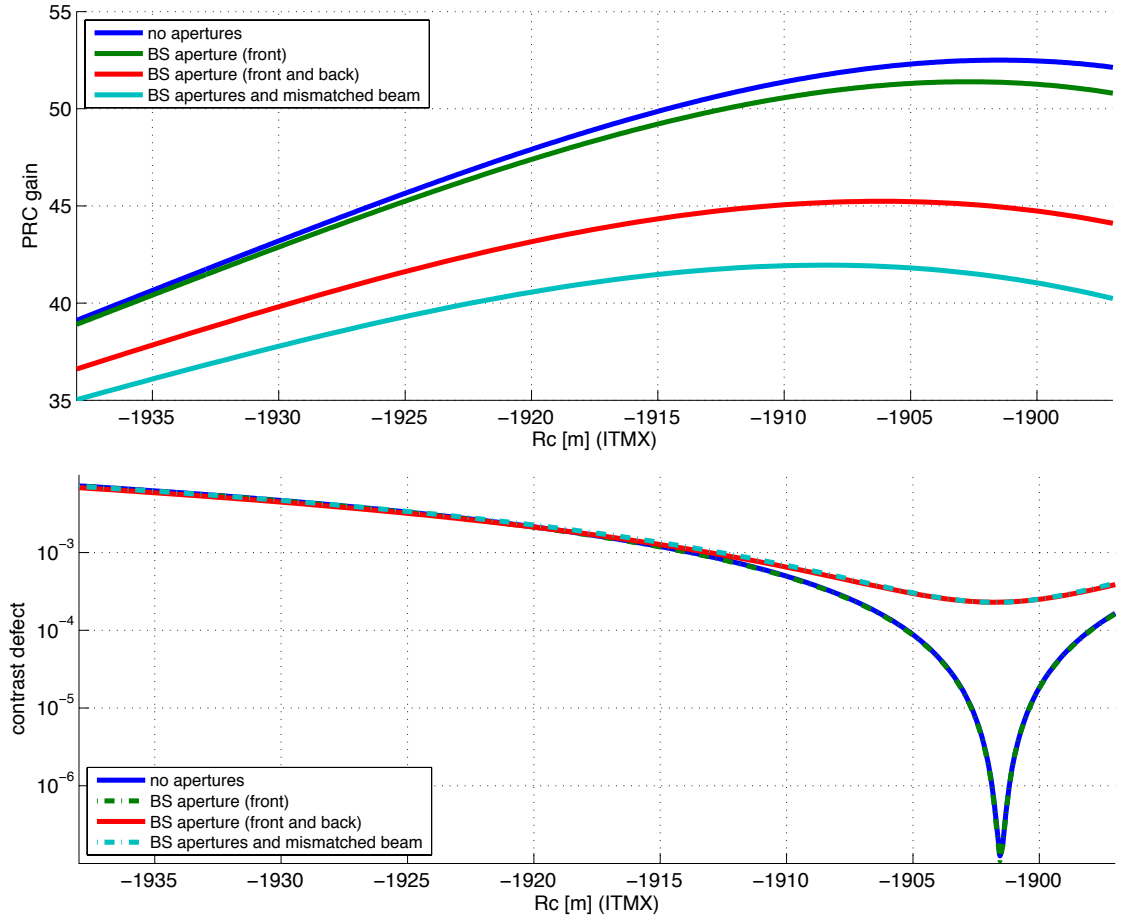

Figure 5.7: Simulated power recycling cavity (PRC) gain (top) and contrast defect (bottom) in the power recycled Michelson at Livingston (configuration as of November 2013). The ITMX R_C is tuned to mimic the effect of the ITMX ring heater. 4 different cases are modelled: 1) no apertures; 2) including the apertures representing the front of the beam-splitter; 3) including the apertures for the front and back of the BS; 4) all BS apertures and a mismatched input beam (the expected beam from the input mode cleaner). The maximum PRC gain observed experimentally was ~ 37.

interferometer. The results shown here do not exactly match the maximum gain of ~ 37 observed at Livingston, but they do illustrate how clipping at the BS reduces the gain. To get the final numbers the BS baffles will have to be included (see section 5.3.8). These results show, qualitatively, the effect of clipping when the beams are larger than expected.

The second plot in figure 5.7 shows the contrast defect for the same setup. For all 4 cases the minimum in contrast defect corresponds to the point at which the

arms are matched (ITMX $R_C = -1901\,\mathrm{m}$). This suggests the contrast is dominated by the mode matching of the two arms. This explains the experimental observation that the minimum in contrast defect does not correspond to the maximum in gain, as the gain is a compromise between mode matching and smaller beams for less clipping. The contrast defect is dominated by mode matching. The plot also shows that the back surface aperture causes significantly higher contrast defect. This is due to the asymmetric nature of the beam-splitter for beams coming from the x or y arm into the signal recycling cavity (or dark port). The beam coming from the y arm is clipped by the BS, but this clipped light passes into the SRC. The beam coming from the x arm is clipped and this light passes to the PRC. The clipped light from y has no x arm field to interfere with, so appears at the dark port. This effect is corrected with the addition of baffles around the BS.

In figure 5.8 the power recycling gain is shown as both ITM ring heaters are used, as is observed in the last hour in figure 5.2. This includes all the BS apertures. As

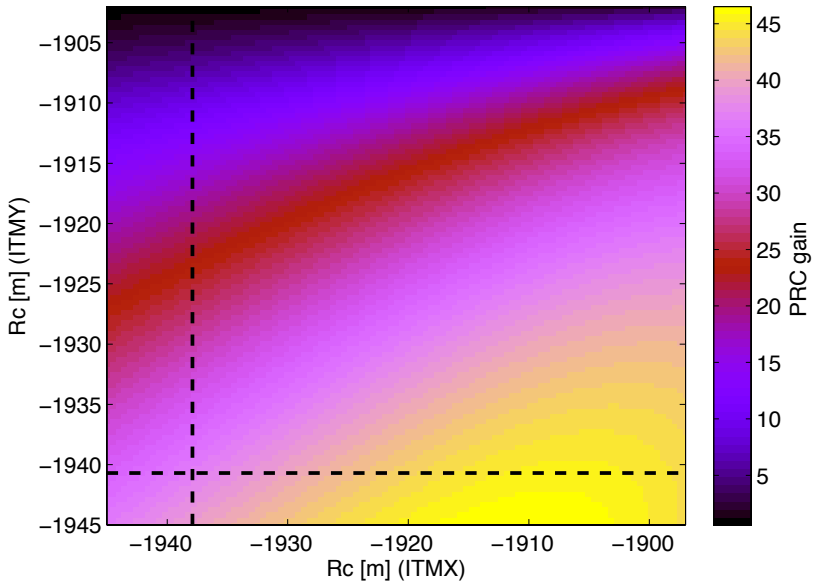

Figure 5.8: Power build up in the PRC of the Livingston PRMI as the curvatures of the two input mirrors are tuned. This simulates the action of the ring heaters on the ITMs. The dotted lines refer to the measured values of the cold optics. The effect of heating the ITMs from this value is shown in the top right square.

is observed, the action of the ring heater on ITMY pushes the interferometer further away from mode matched arms as the negative lens in ITMY becomes stronger. The beam size of the eigenmode for PRY, and the combined beam in the PRC, become larger as ITMY is heated, creating even more clipping at the beam-splitter. In order to recover more of the PRC gain some method for producing a positive lens in the ITMs is needed, to match both arms to a smaller beam size. This would reduce the clipping and increase the PRC buildup.

5.3.6 Centring the beam

The maximum buildup in the power recycling cavity has been shown to be dominated by the clipping at the back surface of the beam-splitter, due to the offset of the effective aperture to the beam. By off-centring the beam on the front surface of the beam-splitter it should be possible to recover some of the PRC gain. The results of a simulation of this effect are shown in figure 5.9. This suggests around 5 in PRC gain can be recovered by off-centring the beam on the BS. The maximum

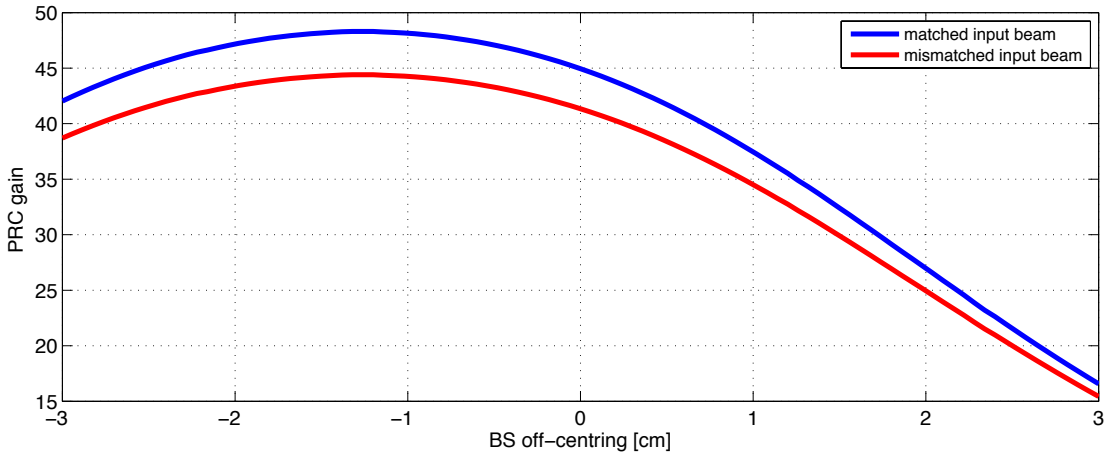

Figure 5.9: Simulated power build up in the PRC as the beam is offset from the centre of the beam-splitter. Here the centring refers to the front surface of the beam-splitter. The interferometer was simulated for optimum mode matching between the arms (ITMX $R_C = 1901.5\,\mathrm{m}$) with an input beam matched to the PRC (blue curve) and with a mismatched input beam (red curve), using the optimum beam for the Advanced LIGO design, as a best guess for the beam coming from the input optics.

is achieved when a balance between clipping at the front and back of the BS is achieved. However, as the clipping is minimised in the power recycling cavity it will be maximised in to the signal recycling cavity, reducing any potential signal. This is, therefore, not a sustainable method to maximise the PRC gain.

5.3.7 Possible mitigation of large beam sizes

The reduction in power recycling gain from the expected 53 discussed above is due to larger beams at the beam-splitter, caused by different lenses in the ITMs than the 50 km thermal lenses of the design. However, there are other parameters which can have a large effect on the beam size: the positioning and curvatures of the power recycling optics.

The radius of curvature of PR3 and distance between PR2 and PR3 in particular have a strong effect on the beam size in the power recycling cavity. The folded recycling cavities act to provide stable recycling cavities, rather than the marginally stable PRC of Enhanced LIGO, and to expand the beam from the mm size of the input optics to the cm size of the main interferometer [16; 27]. The majority of the beam expansion occurs between PR2 and PR3, where the beam size increases by almost a factor of 10. Any changes in this distance or the curvatures of these mirrors can have a dramatic effect on the beam size. By either increasing the distance between the mirrors, or decreasing the radius of curvature of PR3, the PRC eigenmode becomes more stable, with smaller beams at the beam-splitter. This will reduce the clipping at the BS. This effect is illustrated in figure 5.10, where power buildup in the PRC is detected as the R_C of PR3 is tuned around the measured reference value, with the arms matched.

For larger PR3 R_C the beam at the beam-splitter is larger and experiences greater clipping: for larger PR3 R_C the power recycling gain is lower. Around the measured value for the Livingston setup the PRC build up changes quite dramatically with

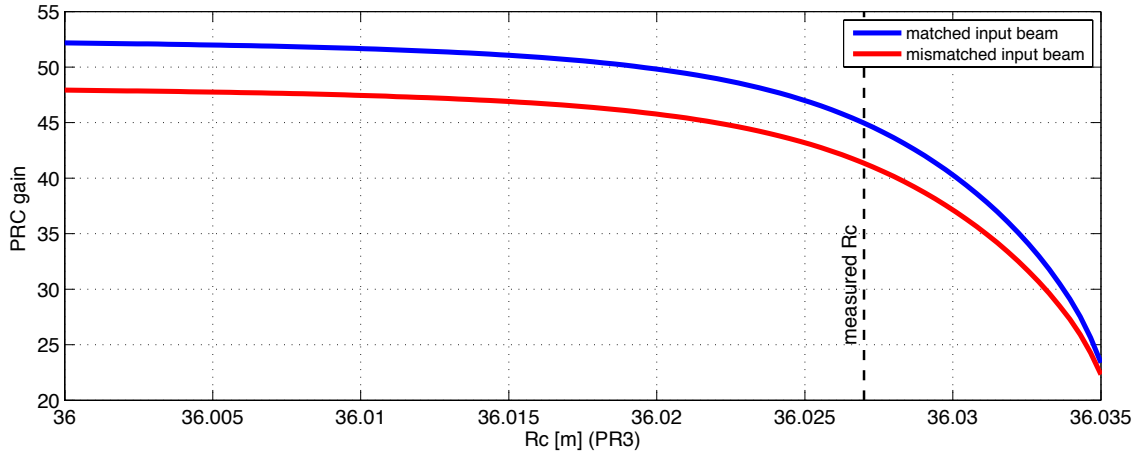

Figure 5.10: Power recycling cavity gain vs. curvature of PR3, one of the mirrors in the folded power recycling cavity. The measured value of the R_C is 36.027 m [74]. The simulation is carried out with mode matched x and y arms (ITMX $R_C = -1901.5$ m), for an input beam matched to the PRC and for a mismatched input beam (matched to the original design).

small changes of R_C. For example, changes in the range of 1 cm can result in changes of 5-10 in PRC gain. We also find a very similar trend when tuning the PR2-PR3 distance, with a scaling factor of 2 for the change in distance compared to the change in R_C. For example, a 5 mm change in this distance gives a similar change in buildup as a 1 cm change in R_C. This trend could be useful, as it suggests we can reduce the clipping at the beam-splitter, and recover some of the PRC gain by moving PR2 or PR3 to increase this distance. If clipping continues to be a problem in the full interferometer setup this is a possible solution.

5.3.8 Final numbers: additional losses due to baffles

For the final numbers in this investigation we add in the baffles which are placed around the beam-splitter to conserve contrast defect from the unbalanced effect of the beam-splitter on the light from each arm [100]. The baffles are included in the simulation by applying absorption maps which represent the apertures. The results are shown in figure 5.11.

The inclusion of the baffles increases the clipping of the beam in the power

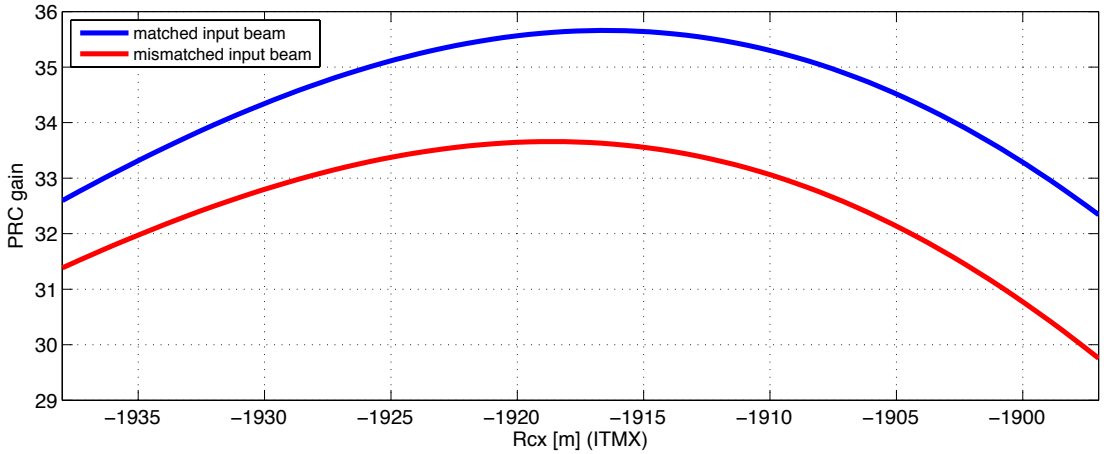

Figure 5.11: Final simulation of the PRC gain, with the beam-splitter baffles included to give the overall clipping of the beam at the BS. The PRC gain is predicted as ITMX R_C is tuned to mimic the effect of the ring heater on the ITM and to match the ITMX lens to ITMY. Two cases are shown, one with the input beam matched to the y arm and one with a mismatched input beam, using a beam matched to the design case.

recycling cavity. In this case the maximum gain looks very similar to the 37 observed experimentally. The slight discrepancies can easily be explained by a combination of the factors investigated above: beam centring on the BS or slight errors in our values of the curvature and positioning of the power recycling optics. In fact, a latter measurement of the Gouy phase of the power recycling cavity [101] suggested that the cavity is slightly closer to stability than the model parameters suggest. This can be explained by either an extra 4 mm between PR2 and PR3 or an 8 mm shorter PR3 [102]. From figure 5.10 this would give a $\sim 10\%$ increase in PRC gain. If we apply this to the baffle results the maximum gain is between 37 and 38, depending on the matching of the input beam.

As before the maximum in PRC gain does not occur with maximum mode matching between the arms (ITMX $R_C = 1901.5$ m) but is a compromise between good arm mode matching, reduced clipping with smaller beams and mode matching between the input beam and the arms (the mismatched beam is smaller than the matched beam). These final numbers form a convincing argument that the observed PRC

gain is due to large beams being clipped at the beam-splitter.

5.3.9 Thermal compensation using the CO_2 laser

The thermal compensation system is made up of two parts, ring heaters applied to the back surfaces of the ITMs and a compensation plate/ CO_2 laser projection system [57]. Whilst the ring heaters can only correct positive lensing the CO_2 laser can be used to project specific heating profiles onto the compensation plate. In theory this can be used to correct any lensing in the ITMs, when combined with the ring heaters. This allows correction of the ITMY negative lens, and a way to match ITMY to ITMX by pushing towards more positive lensing and matching the arms at a smaller beam size. This would reduce the clipping and increase the PRC gain.

Just such an approach was attempted in Livingston [93]. The CO_2 laser power was gradually increased to match ITMY to ITMX. The contrast defect and power recycling gain are shown in the plots in figure 5.12. As the CO_2 laser power is increased the PRC gain increases, as the arms are mode matched. In this case the mode matching occurs at smaller beam sizes, which reduces the clipping and leads to a maximum buildup of ~ 44. In order to recover more of the buildup predicted by our plane wave models (53) the ITMY and ITMX CO_2 lasers would need to be used to correct the effective lensing to the design 50 km lenses, matching both arms to the smaller beam sizes of the design.

Figure 5.12 also shows the contrast defect as the CO_2 laser power is increased. This reduces to a minimum of ~ 400 ppm when the arms are well matched.

5.3.10 Conclusion

I have demonstrated that the low power buildup observed in the Livingston PRMI can be explained by larger than expected beams in the power recycling cavity, due to non-thermal lenses in the ITMs which differ significantly from each other and

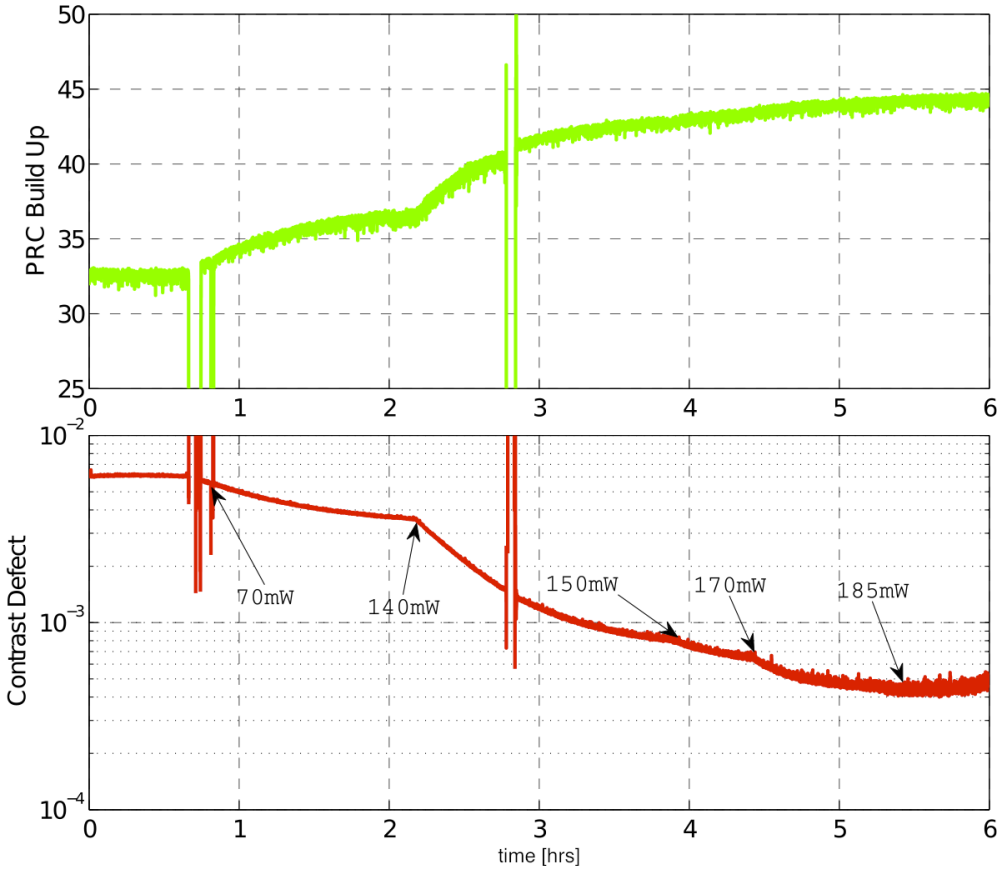

Figure 5.12: Power buildup and contrast defect in the Livingston PRMI as the CO_2 laser is used on the y arm compensation plate to compensate the negative lens in ITMY and match ITMY to the positive lens in ITMX. Both the buildup and contrast defect are detected over time as the CO_2 laser power is increased (labels on contrast defect refer to the CO_2 laser power). Image courtesy of Denis Martynov [93].

from the assumed thermal lensing of 50 km in the design. These larger beams experience greater power loss at the beam-splitter, due to its finite size. The results of this simulation task have confirmed the mechanism by which the power buildup is reduced and the commissioning team can account for this in future measurements.

We conclude that the size of the beams in the PRC must be reduced or the beam-splitter replaced with one with a larger aperture to reduce the loss and recover the PRC gain. With the inclusion of the end mirrors for the full interferometer the beams will be smaller, as the beam size is dominated by the eigenmode of the arm cavities. These are a closer match to the design size of 5.3 cm at the BS. Therefore, we do not yet propose the replacement of the beam-splitter. In the event that

the beam sizes remain too large we have proposed a potential mitigation strategy: extending the distance between PR2 and PR3 in the PR mode matching telescope to reduce the beam size in the power recycling cavity.

5.4 Higher order modes at the dark port: the Livingston power recycled Michelson

The previous investigation focused on explaining the observed power recycling gain at Livingston. However, the contrast defect also depends on many of the higher order mode effects (mode mismatches and apertures) present in the Livingston PRMI. In this section an effort to simulate the contrast defect seen experimentally is described, as reported in [92; 93; 103].

The minimum contrast defect observed when actuating on the ITMX ring heater is between 600 ppm and 800 ppm from [92; 93] (see figure 5.2) One measurement recorded a contrast defect as low as 200 ppm [103]. Hiro Yamamoto carried out simulations using FFT codes to check if the current models agreed with these observations. He asked me, to provide a modal comparison with his results, which slightly over predict the contrast defect at 1300 ppm [58].

5.4.1 Transmission of the input mirrors

The contrast defect is effectively:

$$C = \frac{|a_x - a_y|^2}{|a_x + a_y|^2} \tag{5.5}$$

where a_x and a_y refer to the light fields reflected from the x and y arm. The contrast defect, unlike the power recycling gain, is much more dependent on higher order distortions in the PRMI, specifically differential distortions between the two

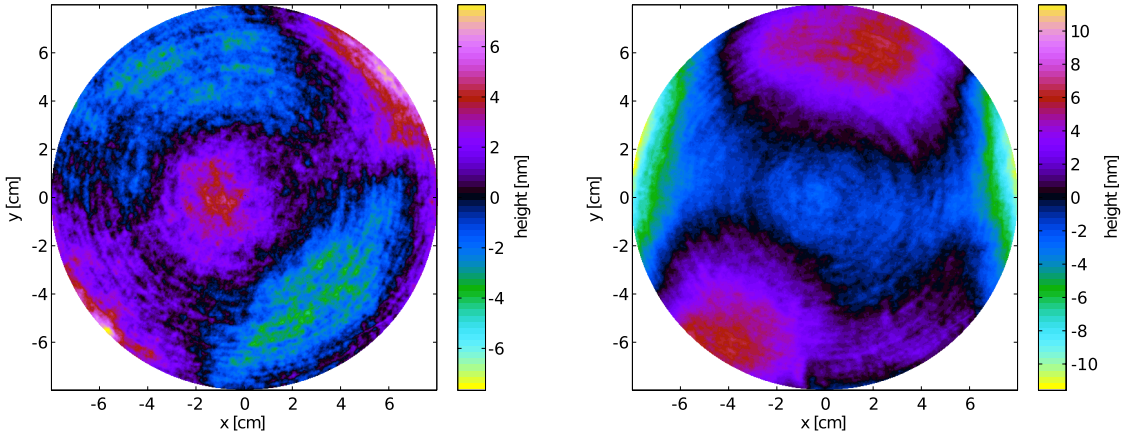

Figure 5.13: Transmission maps for the ITMs installed at Livingston, describing the distorted optical path of light travelling through the substrates. ITM04 (x arm, left) and ITM08 (y arm, right). The central 16 cm region is shown, with the curvature term (the non-thermal lens) removed [74].

arms. With this in mind the model was adapted to include 'transmission maps' on the ITMs. These are maps describing the optical path of fields travelling through the ITM substrates, including the second order effect from the non-thermal lenses and other higher order aberrations. The measured maps for the Livingston ITMs are shown in figure 5.13 [74].

5.4.2 Optimising mode matching with the x arm ring heater

In figure 5.14 the simulated contrast defect is shown for several different cases, as ITMX R_C is tuned to simulate the ring heater, recreating the experimental result shown in figure 5.2. Three different cases are shown. Firstly the BS baffles aren't included and the clipping due to the finite size of the beam-splitter is uneven between the two arms, resulting in a contrast defect of 200 ppm. Including the baffles suppresses this. When the ITM transmission maps are included the contrast defect increases due to differential higher order mode effects. The minimum contrast defect is $\sim$ 800 ppm. This agrees with the values quoted in [92; 93] but we do not see the 200 ppm minimum seen [103].

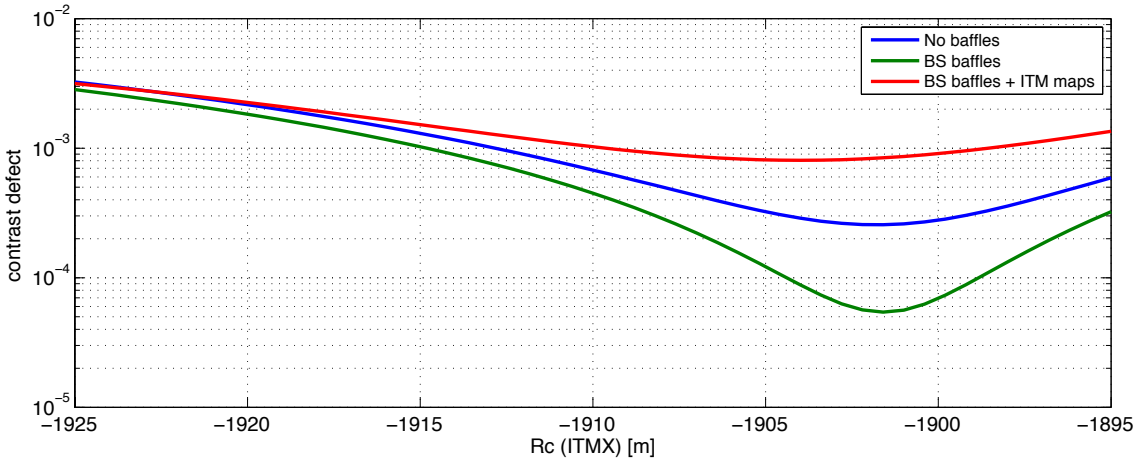

Figure 5.14: Contrast defect in the Livingston PRMI as ITMX R_C is tuned to simulate the ITMX ring heater. Three cases are considered: 1) finite size of the BS included with no BS baffles; 2) BS baffles included; and 3) baffles and ITM transmission maps included.

5.4.3 Optimising mode matching with the y arm CO_2 laser

A greater PRC gain was achieved using the CO_2 laser on the y arm compensation plate to effectively correct the lensing in ITMY to match ITMX, with a smaller beam size (see figure 5.12). In this case the maximum PRC gain is 44 and the minimum contrast defect is around 400 ppm. In figure 5.15 these results are recreated using FINESSE, simulating the thermal compensation of ITMY by tuning the curvature. The maximum PRC gain is 45 whilst the minimum contrast defect is 600 ppm. This agrees well with the observations made experimentally, and the range of contrast defect and PRC gain looks very similar to that seen experimentally [93] (see figure 5.12).

5.4.4 Simulated vs. measured output beam

The final result I will present for this task is a more qualitative result: the output beam generated with our models, compared to that detected at Livingston [93]. These two beams are shown in figure 5.16, when the CO_2 laser is used to match the two arms. The two beams exhibit similar features, the cross-like nature of the beam

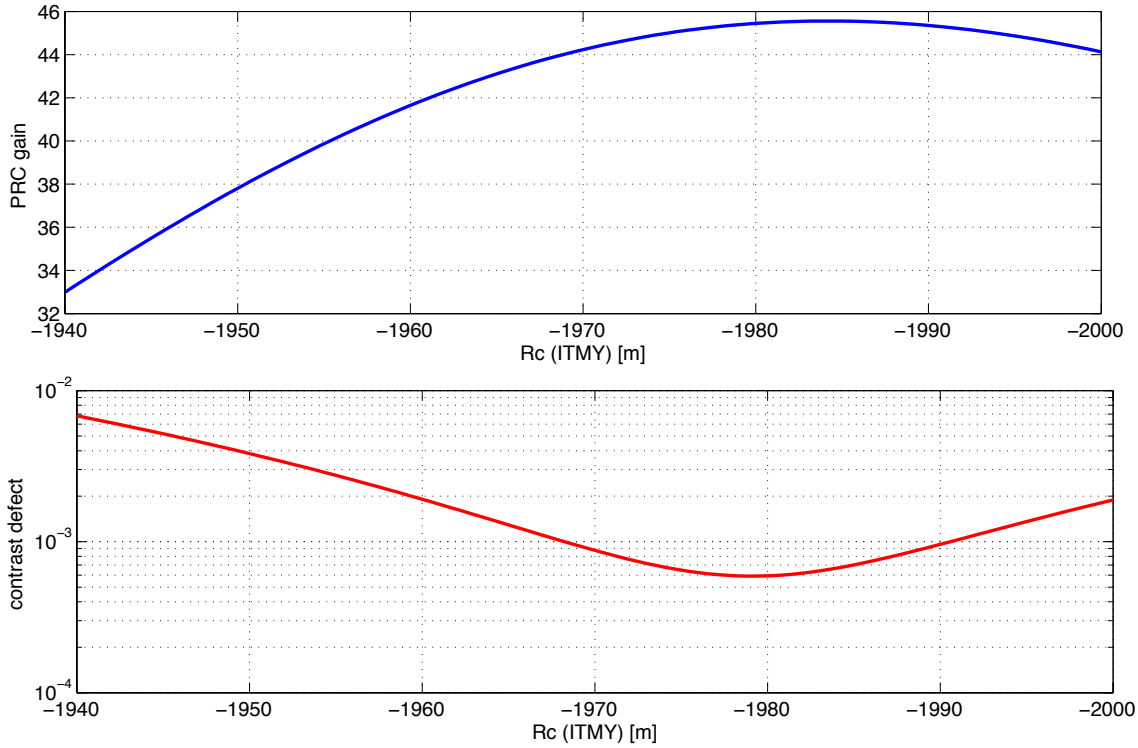

Figure 5.15: PRC gain (top) and contrast defect (bottom) for the Livingston PRMI as the curvature of ITMY is tuned to simulate the thermal compensation system: the CO_2 laser projected onto the y arm compensation plate. This corrects the negative lens in ITMY.

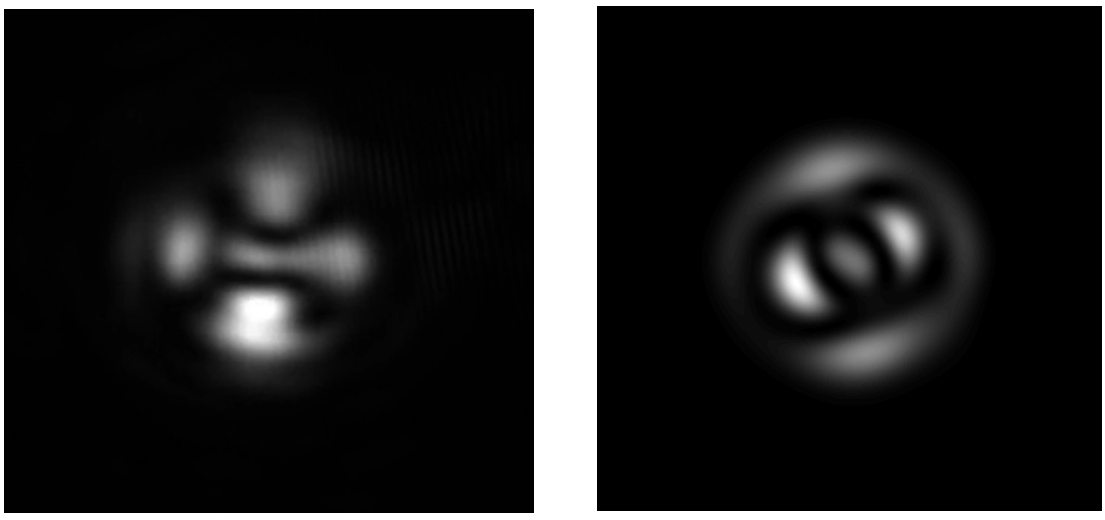

Figure 5.16: Beam detected at the output of the Livingston PRMI when the CO_2 laser is used to match ITMY and ITMX. **Left:** measured beam [93]. **Right:** simulated beam.

as well as some sharper edges which resemble clipping of the beam, though this is more obvious in the simulated beam. However, there are some notable differences. Achieving exactly the same beam shape at the output is complex as only a finite number of higher order modes (up to order 10) are used and not all the distortions present in the detector are included for simplicity. In this case the ITM transmission maps and BS baffles are the only spatial effects included, with all other optics considered perfectly spherical. However, even with this simplified model the main features are recognisable in both the measured and simulated beams and correspond to similar contrast defect levels.

5.4.5 Conclusion

This results of this simulation task confirmed Yamamoto's results in terms of simulated beam shape and order of magnitude contrast defect [58]. The higher order modes at the output are similar to that seen experimentally, in both power and observed beam shape. However, the output at the dark port will be more sensitive to beam distortions than the power in the PRC and more work is needed to include all the defects which could impact this result. Extensions of this work will attempt to explain the minimum 200 ppm contrast defect observed in [103] and the discrepancy between the results presented here and Yamamoto's FFT results.

5.5 Effect of mode mismatches on control signals: ongoing investigation for Advanced LIGO

In section 5.3 the low power build up in the Livingston PRMI was successfully explained: larger than expected beams experience greater clipping at the beamsplitter. When the arm cavities are included the carrier field beam size will be dominated by the eigenmode of the arm cavities, due to the high finesse of the

arms, which are much closer to the smaller beams of the design. Any thermal lensing will also reduce the beam sizes. We therefore expect to reduce the clipping and recover the PRC gain. However, the clipping could still have an impact on fields in the interferometer: specifically the radio frequency sidebands used for interferometer control. The longitudinal control scheme for Advanced LIGO is described in appendix C.2.3. The control sidebands are chosen so they do not enter the arm cavities of the detector and will only see the power (or dual) recycled Michelson. Therefore they will remain in the large beam, PRMI state. This has the potential to reduce the overlap between the control sidebands and carrier and adversely impact the control scheme. The effect of mode mismatch between the arms and the PRMI, and between each arm of the PRMI, should be investigated in preparation for this stage of commissioning.

In this section I outline an ongoing investigation into the effect of Livingston mode mismatches on the control scheme. Preliminary results for this task are presented in [43].

5.5.1 Advanced LIGO control

The operation of gravitational wave detectors such as Advanced LIGO requires tight control of the position of the mirrors to keep the interferometer on the *operating point*. This requires the arm and power recycling cavities to be resonant for the carrier, with the Michelson tuned to the dark fringe (with some small offset for DC read out). The positioning of the signal recycling mirror depends on the mode of operation. These can be represented by 5 degrees of freedom (dofs):

- CARM: common, or average, arm length.
- DARM: differential arm length.
- MICH: differential Michelson length (between the BS and ITMs).

- PRCL: power recycling cavity length.
- SRCL: signal recycling cavity length.

These dofs and their associated operating points are discussed in more detail in appendix C.

The interferometer is kept on the operating point using *error signals* similar to a Pound-Drever-Hall error signal (see appendix C.2.2 and figure 5.17). The operating point of each degree of freedom corresponds to some distinct phase relation for the carrier light. By beating the carrier with some reference field (control sidebands at specific frequencies) the phase of the carrier is extracted. An example of a Pound-Drever-Hall error signal for a single cavity is shown in figure 5.17. The central zero crossing corresponds to the resonance of the carrier (the operating point of the cavity). The zero crossings either side represent the resonance of the upper and lower sidebands. Using signals such as these Advanced LIGO can be 'locked' to the operating point. The Advanced LIGO control scheme is described in detail in appendix C.2.3.

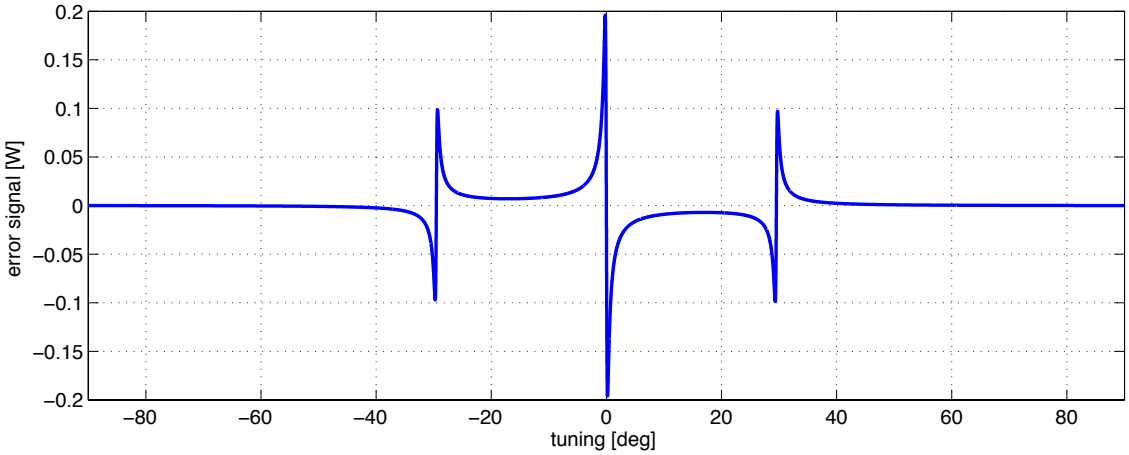

Figure 5.17: Example of a Pound-Drever-Hall error signal for control of an single cavity. The central zero crossing corresponds to the operating point of the carrier. The two zero crossings either side correspond to the operating points of the upper and lower sidebands.

5.5.2 Operating points in distorted cavities

The error signal shown in the previous section refers to a perfect cavity, with perfect mode-matching. The introduction of mode mismatches and beam distortions can change the position of the operating point and magnitude of the signal. In this section we consider the error signal for a single cavity for two cases: 1) a mode mismatch of the input beam; and 2) misalignment of the input mirror. The results are plotted in figure 5.18. In case 1 the distortion of the beam occurs outside the cavity, when describing the beam in the cavity eigenmode. The operating point (the zero crossing of the error signal) is unchanged from that of a cavity with no HOM effects. The magnitude of the error signal is reduced (the peak signal decreases from 0.25 to 0.15) for greater mismatch as the overlap between the Gaussian mode of the sidebands and carrier is degraded.

In case 2 the distortion of the beam occurs inside the cavity. The misalignment of the input mirror creates a slightly longer cavity and so the operating point is

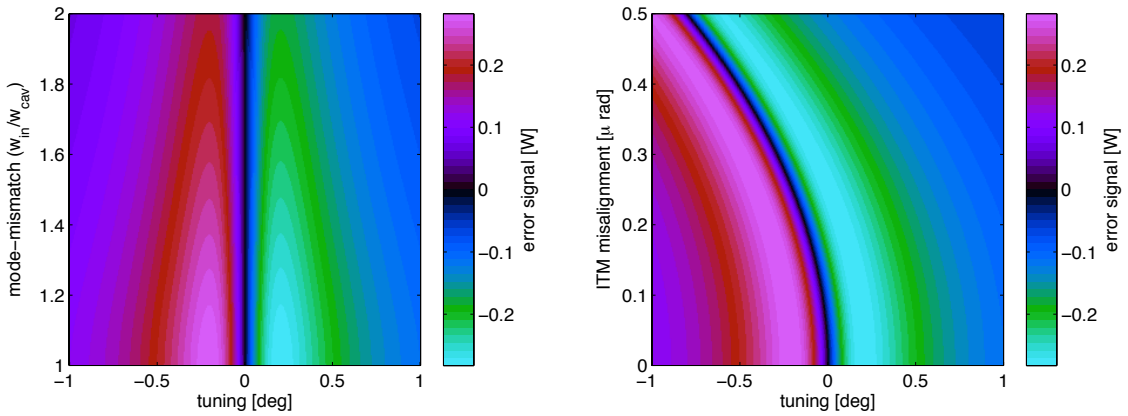

Figure 5.18: Examples of cavity error signals with simple higher order mode effects. The operating point is at the zero crossing of the error signal (black in the surface plot). 0° tuning refers to the resonance of the 00 mode in an un-distorted cavity. **Left:** Error signal vs. mode mismatch of the input beam, in terms of the size of the waist (w_{in}) compared to the cavity eigenmode waist (w_{cav}). The operating point is that of the undistorted cavity (0°). **Right:** Error signal vs. misalignment of the input mirror. The misalignment shifts the operating point from the un-distorted case (0°) as the misalignment changes the effective cavity length.

shifted from that of the un-distorted cavity (0°). In this case the magnitude of the error signal is unaffected as the carrier and sidebands are mode matched.

5.5.3 Coupled cavity operation: Livingston PRMI example

Predicting the operating point becomes complicated with additional mirrors. The simplest example of this is a coupled cavity such as a power recycled Michelson. Consider the operating point of the power recycling cavity in the PRMI defined by the Livingston cold optics, as outlined in the commissioning task in section 5.3. In the cold state the arms are substantially mode mismatched. In this example there is not a clearly defined eigenmode.

Figure 5.19 shows the power recycling cavity length (PRCL) error signal for such a setup when modelled with different eigenmodes. ITMX R_C is tuned to match the two arms. 3 eigenmodes are considered: the x arm eigenmode (PRX); the y arm eigenmode (PRY); and an average of the two. The surface plots in figure 5.19 show the result for PRX. In the left panel the zero crossing of the error signal

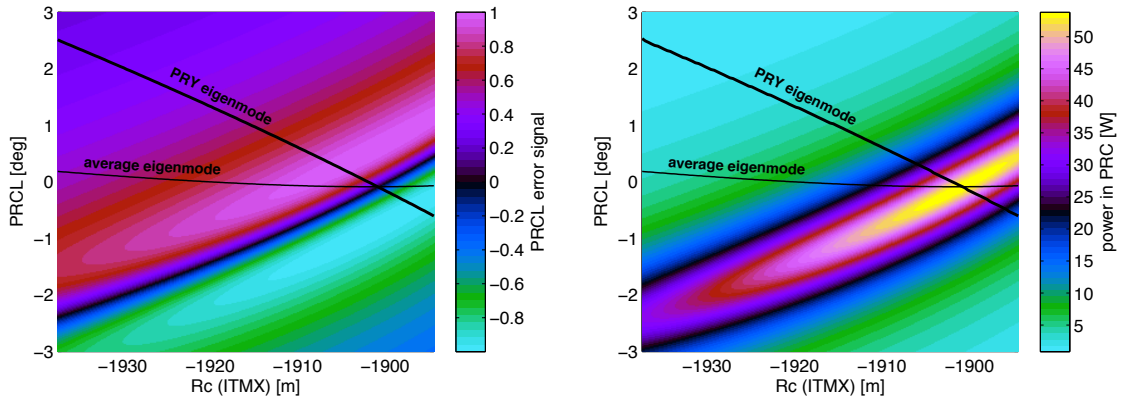

Figure 5.19: Operating points for coupled cavities. **Left:** PRCL error signal for the mode mismatched Livingston PRMI, modelled using the eigenmode of the x arm and tuning the curvature of ITMX to match the two arms. The zero crossing represents the operating point in the x eigenmode and the black traces represent the operating point using the y arm eigenmode and an average eigenmode. **Right:** Power in the PRC, when modelled with the x arm eigenmode. The black traces represent the maximum power using the y arm eigenmode and an average eigenmode.

(the operating point) is in black. The operating points when modelled using the PRY and average eigenmodes are shown. The results of simulations using any of these eigenmodes should give identical results, as long as enough HOMs are used to recreate the mode mismatch and the interferometer is locked on the the right operating point for the eignmode. The zero crossings for the 3 eigenmodes intersect at the point where the arms are matched (ITMX $R_C = 1901.5\,\mathrm{m}$). The operating points for all 3 cases coincide with the maximum buildup of power in the power recycling cavity (right panel). So although the operating point in our model depends on the eigenmode an initial guess of this point can be made by maximising the power.

5.5.4 Error signals in the power recycled, Fabry-Perot Michelson

The addition of Fabry-Perot cavities to the Livingston PRMI adds more complexity and, for the current measurements, additional mode-mismatches. Not only are the short Michelson arms mismatched, but the arm cavities are mismatched to PRX and PRY. In figure 5.20 the some of the consequence of these mismatches are shown. Looking again at the operating point of the PRC, but this time in the cold, mis-

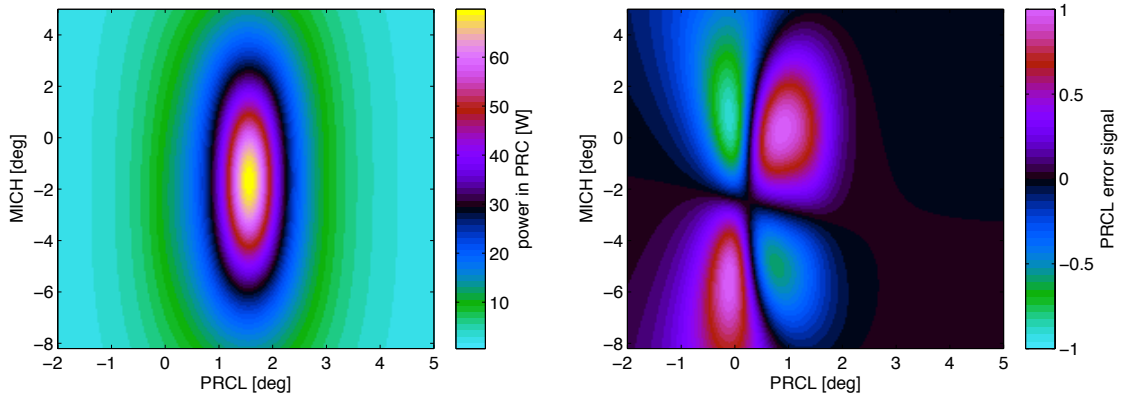

Figure 5.20: Power (left) and PRCL error signal (right) for the Livingston power recycled Fabry-Perot Michelson as the power recycling cavity length (PRCL) and differential Michelson length (MICH) are tuned.

matched state as two degrees of freedom are tuned: PRCL and MICH. In the left panel the maximum power is shown. The maximum in power occurs at PRCL$\sim 1.5^\circ$ independent of MICH. However, the zero crossing of the error signal (right panel) does not correspond to the maximum in power and is not independent of MICH. This is a result of coupling between the two dofs from the mode mismatches. The PRCL error signal also exhibits a zero crossing for MICH, which should not occur for a well designed control system.

5.5.5 Conclusion

Discussed and illustrated in this section are several consequences of beam distortions on the error signals, mode mismatch in particular. The impact of these effects is complex, but generally we are concerned that the interferometers will lock to the wrong point, impacting the sensitivity, or that the interferometer will easily lose lock. Additional details on Advanced LIGO control and this investigation are given in appendix C.

Here I have motivated the need to investigate the error signals in the presence of these mode mismatches. This is an ongoing investigation which still requires significant work. Preliminary results are detailed in [43].

5.6 Accepting end mirror coatings

During the commissioning workshop in Livingston in January 2013 I carried out simulations to predict the higher order mode content in the dual-recycled Advanced LIGO configuration in the presence of the expected distortions of the end test masses. This was at the request of Hiro Yamamoto, to confirm his results [94]. The expected distortions of the ETMs are measured mirror maps of the coated mirrors and the purpose of these tests was to accept or reject the coated ETMs.

5.6.1 Expected distortions of coated mirrors

Figure 5.21 shows plots of the mirror surface measured from a particular mirror, ETM01. This optic served as a test of the coatings applied to the mirrors at LMA (Laboratoire des Matériaux Avancés) and is the map used in this investigation. The plots of the map in this figure show firstly the map over a 30 cm aperture, with the offset, tilt and curvature removed using a Gaussian weighted fitting function (see section 4.3.1). The central 16 cm region, where the requirements are strongest, is shown, with just the weighted terms removed (centre) and with all Zernike terms with $n \leq 5$ removed (right). Here we see a distinctive, high frequency spiral pattern on the mirror surface. This is a consequence of the coating process and was not present on the uncoated, polished substrate [74].

It is important that the effect of this spiral distortion, and the overall distortion of the mirror, does not significantly increase the number of higher order modes in Advanced LIGO. The current coating process uses a planetary method [94] to coat mirrors in pairs. The motivation for this is to produce matching pairs of ETMs and ITMs to be used in the same detector, with common surface distortions to avoid a large number of higher order modes in the signal recycling cavity and dark port. However, it is important to test that such distortions won't result in large HOM

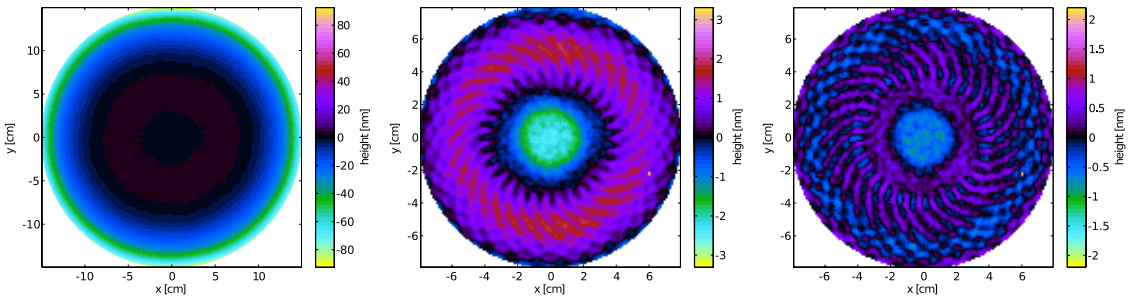

Figure 5.21: Maps of the surface height of the coated end test mass ETM01 with Gaussian weighted ($w = 6.2$ cm) offset, tilt and curvature removed. **Left:** Map over 30 cm region. **Centre:** Map over 16 cm region. **Right:** Central 16 cm region with all Zernike polynomials with $n \leq 5$ removed. A high spatial frequency spiral pattern is evident [74].

contents in the arms and recycling cavities.

5.6.2 Individual arm test: mode content

The first test is the behaviour of an individual arm cavity, in terms of the higher order mode content. An Advanced LIGO arm was simulated, using design reflective properties but the measured test mass curvatures of 1938 m (ITM) and 2249 (ETM). The ETM01 mirror map shown above was applied to the end test mass. The cavity was locked using a Pound-Drever-Hall error signal and the circulating beam was detected. The beam was then decomposed into Laguerre-Gauss modes. The mode content is summarised in table 5.3. Around 100 ppm is in modes other than the 00 mode, with the majority of this power in the order 4 mode LG_{20}. This level of higher order mode content in the arm cavities is acceptable [78] and is consistent with that seen using the FFT based simulation SIS [87].

mode (p, l)	0, 0	2, 0	3, 0	other
power in arm	0.9999	70 ppm	10 ppm	< 3 ppm

Table 5.3: Laguerre-Gauss mode content of the beam circulating in an Advanced LIGO arm cavity with the coated mirror map, ETM01, applied to the end mirror.

5.6.3 Recycled Fabry-Perot Michelson: mode content and contrast defect

The next test is the recycled Michelson with Fabry-Perot arm cavities. We not only want to check that the higher order mode content in the arms is not significantly different to the single arm test but want to investigate how the higher order modes propagate to other parts of the interferometer: the power and signal recycling cavities. The operation of the signal recycling mirror is complicated so we start with the power recycled Fabry-Perot Michelson.

Apart from the curvature of the cavity mirrors and application of the ETM mirror map the setup is the Advanced LIGO design. The results are summarised in table 5.4. The arm cavity mode content remains almost the same as the single

mode (p, l)	0, 0	2, 0	3, 0	other
arms	0.9999	72 ppm	9 ppm	< 4 ppm

mode (p, l)	0, 0	2, 0	other (total)
PRC	0.998	1600 ppm	230 ppm

configuration	contrast defect
power recycled	3.5 ppm
dual recycled	2.0 ppm

Table 5.4: Higher order mode content in Advanced LIGO with expected coating distortions applied to the ETMs. **Top:** Mode content of the arms. **Bottom left:** Mode content of the power recycling cavity. **Bottom right:** Contrast defect with and without signal recycling.

arm test. The higher order mode content in the PRC is around 2000 ppm, an acceptable [78] value which agrees with other results [94]. As expected the distortions of the beam head to the power recycling cavity, as they are common to both arms. There is a small number of higher order modes in the SRC, from asymmetries between the two arms, but these are not dominated by any one mode. Significantly the higher order modes in the SRC are not enhanced by the signal recycling mirror (in fact we see some mode healing of the beam, as described in section 2.8).

5.6.4 Conclusion

From the results detailed in this section and reported in [44] I was able to confirm Yamamotos results and the ETM coatings were accepted.

5.7 Conclusion

This chapter has detailed several specific commissioning tasks. The main results presented here concern the power recycled Michelson interferometer installed at Livingston. The simulations detailed in section 5.3 explain the mechanism for the drop in power recycling cavity buildup observed in [92]: lenses in the substrates result in a mismatch with the design, producing large beams in the PRC with increased clipping at the beam-splitter. To recover the power buildup the beam size must be reduced or the beam-splitter replaced with a larger optic. As the addition of the ETMs will have a significant effect on the beam size it is not necessary to replace the beam-splitter. In the event that the beams are still too large in the PRC a potential mitigation strategy is proposed: adjusting the optics in the power recycling telescope to reduce the beam size.

The investigations at Livingston were extended in sections 5.4 and 5.5. The contrast defect at Livingston (for the power recycled Michelson) was simulated, successfully matching experimental results. This requires further work to explain the details of the contrast defect and HOM content of the output beam. The Livingston model was then extended to include the arm cavities and in section 5.5 the motivation for an investigation of the effect of mode mismatches on interferometer control was laid out. This is the basis of an ongoing commissioning task.

Finally, the full Advanced LIGO configuration was modelled to predict the effect of distortions on the coated ETMs (see section 5.6). The higher order mode content in the arm cavities and power recycling cavity is acceptably low. The distortion is common to both arms (common mode) and is reflected towards the PRM, with few modes sent to the signal recycling cavity. The confirmation of these acceptably low higher order mode powers resulted in the acceptance of the coated ETMs.

Chapter 6

Conclusion

6.1 Summary

In this thesis I have reported on the effects of beam and mirror distortions in gravitational wave interferometers. The extensive work presented here can act as a description of the higher order mode behaviour of interferometers, but also provides answers for specific tasks: commissioning for Advanced LIGO; developing technologies for future detectors; and providing the models which are needed for current and future commissioning and design.

The modal model, as detailed in chapter 2, is used to model the effects of distorted beams and optics, using higher order modes to describe deviations from an ideal Gaussian beam. A finite number of modes is sufficient for the small distortions in gravitational wave detectors. In chapter 2 the higher order mode behaviour of different setups is modelled, building from individual optics to the final dual recycled, Advanced LIGO configuration. This provides a backdrop to the quantitative results presented in chapters 3 and 5.

In chapter 3 the behaviour of the higher order mode LG_{33} is studied, in realistic interferometric setups, as reported in [36] and [60]. This particular task is aimed at future detectors, for which this mode has been proposed to reduce mirror thermal

noise. The degeneracy of the arm cavities in Advanced LIGO for the LG_{33} mode was shown to excite distortions of the beam and result in an unacceptable beam purity of 88.6%. A novel approach taken in this investigation was to derive an expression for the power coupled on reflection from individual mirror shapes: the Zernike polynomials. This approach identified the shapes which excite the other order 9 modes from an incident LG_{33} mode, from which mirror requirements for LG_{33} were derived. This is an elegant solution which has since been used in the modelling of adaptive optics to correct the distortion of an LG_{33} beam inside the interferometer.

Chapter 4 details the testing of our modal model, FINESSE and some technical subtleties for efficient, accurate simulations [49]. Although not necessary to understand the results presented in this thesis, the details discussed in this chapter form an instruction manual for anyone wishing to carry out their own simulations. The tests reported here serve to support the science results presented in this thesis and elsewhere.

Finally, in chapter 5 I report on several commissioning tasks involving distortions of the beam, where plane wave models would not be sufficient. Due to the current stage of commissioning the majority of these tasks have focused on the power recycled Michelson interferometer in Livingston. For this configuration I identified the source of the low power build up in the interferometer: power loss at the beam-splitter, due to large beams in the power recycling cavity. We conclude that it is not yet necessary to replace the beam-splitter as the addition of the ETMs will have a strong impact on the beam size: favouring a smaller beam.

In several commissioning tasks I predict the higher order mode content at points in the interferometer. For commissioning of the Livingston power recycled Michelson the contrast defect was modelled and is found to agree with most measurements. This investigation is still ongoing. For the full dual recycled Fabry-Perot Michelson the higher order mode content in each of the arms and recycling cavities was

modelled with distortions corresponding to coated end mirrors. The result of this commissioning task was an acceptance of the coated ETMs.

6.2 Future work

Commissioning of Advanced LIGO will continue, and we expect to see increased distortion effects to come as we move to the full configuration and enter high power operation. The higher order mode behaviour of the interferometer will become more complicated, with processes such as mode healing occurring. This is an exciting time for commissioning, particularly in the area of beam and mirror distortions, as the combinations of high laser power and high finesse cavities will result in significant beam shape evolution.

One project I hope to work on outside of commissioning is an experimental demonstration of the losses in a near-unstable optical cavity. It is the aim of such an experiment to provide some comparison with the modal model, by measuring the mirrors before installation for use in simulations. There is also the potential to inject an LG_{33} beam into such a cavity, to confirm our predictions for this mode and further probe the higher order mode behaviour of the cavity.

List of publications

Papers and proceedings

2014 A. Freise et al., *Interferometer techniques for gravitational wave detection*, Living Reviews in Relativity, in preparation.

2013 L. Carbone et al., *The generation of higher-order Laguerre-Gauss optical beams for high-precision interferometry*, J. Vis. Exp. **78**, e50564.

2013 M. Wang et al., *A realistic polarizing Sagnac topology with DC readout for the Einstein Telescope*, Phys. Rev. D **87**, 096008.

2013 B. Sorazu et al., *Experimental test of higher-order Laguerre-Gauss modes in the 10 m Glasgow prototype interferometer*, Classical and Quantum Gravity **30**, 035004.

2012 C. Bond et al., *The effect of mirror surface distortions on higher order Laguerre-Gauss modes*, Journal of Physics: Conference Series **363**, 012005.

2012 P. Fulda et al., *Review of the Laguerre-Gauss mode technology research program at Birmingham*, Journal of Physics: Conference Series **363**, 012010.

2011 C. Bond et al., *Higher order Laguerre-Gauss mode degeneracy in realistic, high finesse cavities*, Phys. Rev. D **84**, 102002.

Technical notes and presentations

2014 C. Bond et al., *Simulation investigation of beam clipping and power recycling gain in Livingston PRMI*, talk at the March LIGO-Virgo Collaboration (LVC) meeting, Nice. LIGO Document G1400222.

2014 C. Bond et al., *Simulations of effects of LLO mode-mismatches on PRFPMI error signals*, talk at LIGO simulation meeting 28/02/2014. LIGO Document T1400182.

2013 C. Bond et al., *Investigation of beam clipping in the Power Recycling Cavity of Advanced LIGO using Finesse*, LIGO Document T1300954 (2013).

2013 K. Arai et al., *Finesse simulation for the alignment control signal of the aLIGO input mode cleaner*, LIGO Document T1300074 (2013).

2013 C. Bond et al., *Mode healing in GW interferometers*, poster presented at the 10th Amaldi conference, Warsaw. LIGO Document G1300711.

2013 C. Bond et al., *Interferometer responses to gravitational waves: Comparing* Finesse *simulations and analytical solutions*, LIGO Document T1300190, ArXiv e-prints, 1306.6752 (2013).

2013 C. Bond et al., *Higher order modes in aLIGO cavities*, talk at the Advanced LIGO commissioning meeting, Livingston, January 2013. LIGO Document G1400464.

2013 C. Bond, D. Brown and A Freise, *Introduction to Finesse and associated tools*, talk at the Advanced LIGO commissioning meeting, Livingston, January 2013. LIGO Document G1300199.

2012 C. Bond et al., *Modeling deviations from perfect optics using modal methods*, talk at the March LVC meeting, Rome. LIGO Document G1200284.

2011 C. Bond et al., *Laguerre-Gauss mode degeneracy*, talk at the 9th Amaldi conference, Cardiff. LIGO Document G1100821.

Appendix A

Interferometer responses to gravitational waves

A.1 Introduction

This section details comparisons of analytic calculations and FINESSE [39; 49] simulations of interferometer responses to gravitational wave strain. FINESSE includes the possibility to model gravitational wave signals by modulating the 'space' between optical components. For the validation of the code we could not find an easily available document showing example responses for various interferometer types. Thus in this section, based on the note recorded in [82] we present the analytical results for several simple interferometers and show that FINESSE gives the same results. This should provide useful examples for other people who find themselves looking for a reference calculation.

A.2 Phase modulation in the sideband picture

Generally we can describe a light field at a given point:

$$E_{\text{in}} = E_0 \exp\left(\mathrm{i}\left(w_0 t + \varphi_0\right)\right) \tag{A.1}$$

where φ_0 is a constant phase term. Applying a phase modulation we get:

$$E_{\text{out}} = E_0 \exp\left(\mathrm{i}\left(w_0 t + \varphi_0 + \phi(t)\right)\right) \tag{A.2}$$

where $\phi(t)$ is the phase modulation:

$$\phi(t) = m\cos\left(\Omega t + \varphi_s\right) \tag{A.3}$$

m is the modulation index and φ_s is the modulation signal's phase. E_{out} can then be expanded as a series of Bessel functions of the first kind, $J_k(m)$:

$$\exp(\mathrm{i}\, m\cos\varphi) = \sum_{k=-\infty}^{\infty} \mathrm{i}^{\,k} J_k(m)\exp(\mathrm{i}\, k\varphi), \tag{A.4}$$

This implies the creation of an infinite number of upper ($k > 0$) and lower ($k < 0$) sidebands around the carrier ($k = 0$). For small modulation indices ($m < 1$) the Bessel functions decrease rapidly with increasing k and so we can use the approximation:

$$J_k(m) \;= \left(\frac{m}{2}\right)^k \sum_{n=0}^{\infty} \frac{\left(-\frac{m^2}{4}\right)^n}{n!(k+n)!} = \frac{1}{k!}\left(\frac{m}{2}\right)^k + O\left(m^{k+2}\right). \tag{A.5}$$

For $m \ll 1$, as is the case for modulation by a gravitational wave, we can express the phase modulation as the addition of two sidebands at frequencies $w_0 \pm \Omega$ ($k = \pm 1$) and a small correction to the amplitude of the carrier ($k = 2$):

$$\begin{aligned} E_{\mathrm{out}} = E_0\left(1 - \frac{m^2}{4}\right)\exp\left(\mathrm{i}\left(w_0 t + \varphi_0\right)\right) \\ + E_0\frac{m}{2}\exp\left(\mathrm{i}\left(\left(w_0 - \Omega\right)t + \varphi_0 + \frac{\pi}{2} - \varphi_s\right)\right) \\ + E_0\frac{m}{2}\exp\left(\mathrm{i}\left(\left(w_0 + \Omega\right)t + \varphi_0 + \frac{\pi}{2} + \varphi_s\right)\right) \end{aligned} \tag{A.6}$$

where the first term is the carrier, the second term is the lower sideband and the third term the upper sideband. Hence we have sideband amplitudes of:

$$A_{sb} = \frac{m}{2}E_0 \tag{A.7}$$

and sideband phases of:

$$\varphi_{sb} = \varphi_0 + \frac{\pi}{2} \pm \varphi_s \tag{A.8}$$

where φ_0 is the phase of the carrier and φ_s is the phase of the modulation signal.

A.3 Modulation of a space by a gravitational wave

A gravitational wave modulates the length of a space. In [18] the phase change for a round trip between two test masses separated by length L is given by:

$$\varphi(t) = \frac{2w_0 L}{c} \pm \frac{w_0}{2} \int_{t-2L/c}^{t} h_+(t)\mathrm{d}t \tag{A.9}$$

As stated here the equation refers to a round trip between two points separated by length L. For the phase change for a one-way trip between the two points, and adjusting to our definition of the phase accumulated between two points ($\exp(-\mathrm{i}\,kL)$), we have:

$$\varphi = -\frac{w_0 L}{c} \mp \frac{w_0}{2} \int_{t-L/c}^{t} h(t) = -\frac{w_0 L}{c} \mp \delta\varphi \tag{A.10}$$

We assume we have a gravitational wave signal:

$$h(t) = h_0 \cos(w_g t + \varphi_g) \tag{A.11}$$

where w_g and φ_g are the user-defined frequency and phase of the gravitational wave. Thus we get:

$$\begin{aligned} \delta\varphi &= \tfrac{w_0 h_0}{2} \left[\tfrac{1}{w_g} \sin(w_g t + \varphi_g)\right]_{t-L/c}^{t} \\ &= \tfrac{w_0 h_0}{2w_g} \left(\sin(w_g t + \varphi_g) - \sin\left(w_g t - w_g \tfrac{L}{c} + \varphi_g\right)\right) \end{aligned} \tag{A.12}$$

Using the trigonometric identity $\sin u - \sin v = 2\cos((u+v)/2)\sin((u-v)/2)$ we can write:

$$= \tfrac{w_0 h_0}{w_g} \cos\left(w_g t + \varphi_g - w_g \tfrac{L}{2c}\right) \sin\left(w_g \tfrac{L}{2c}\right) \tag{A.13}$$

This represents a phase modulation with an amplitude of

$$m = -\frac{w_0 h_0}{w_g} \sin\left(\frac{w_g L}{2c}\right) \tag{A.14}$$

and a phase of:

$$\varphi = -\frac{\omega_g L}{2c} + \varphi_g \tag{A.15}$$

From equations A.7 and A.8 we can state the amplitude and phase of the generated sidebands as:

$$A_{\mathrm{sb}} = -\frac{w_0 h_0}{2w_g} \sin\left(\frac{w_g L}{2c}\right) E_0 \tag{A.16}$$

and:

$$\varphi_{\mathrm{sb}} = \varphi_0 + \frac{\pi}{2} - \frac{w_0 L}{c} \pm \varphi_g \mp \frac{w_g L}{2c} \tag{A.17}$$

Figure A.1 shows plots of the amplitude and phase of the upper sideband for a single space ($L = 10\,\mathrm{km}$), comparing the equations above with the actual FINESSE result. The FINESSE output has been created with this simple file:

```
l l1 1 0 n1
s s1 10k 1 n1 n2
fsig sm s1 1 0
ad upper 1 n2

xaxis sm f lin 1 100k 1000
put upper f $x1
yaxis abs:deg
```

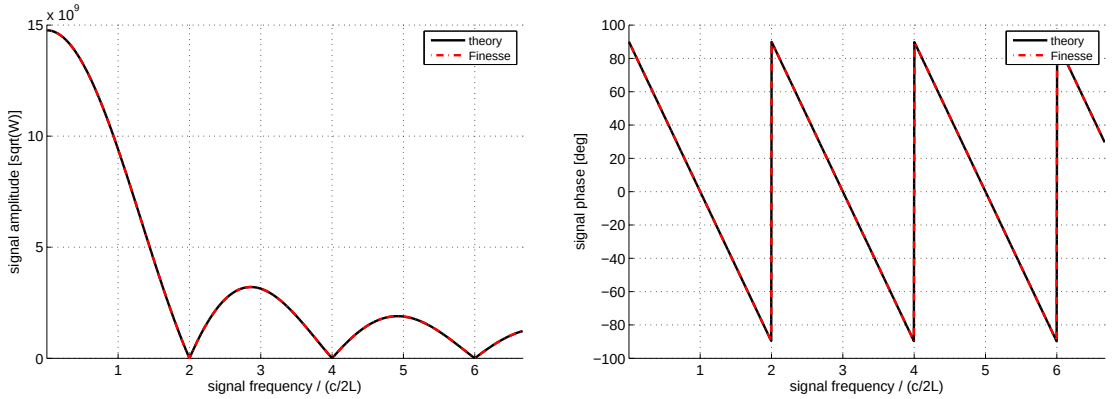

Figure A.1: Plots showing the amplitude and phase of the upper sideband produced when a gravitational wave modulates a space of length $L = 10\,\mathrm{km}$ against the signal frequency of the gravitational wave. The signal frequency is normalised with respect to the of the light round-trip of space L, or the *free-spectral-range* of a cavity of length L.

The 'theory' curves have been created in MATLAB with the following function:

```
%-------------------------------------------------------------------------
% function [Abs] = FT_GW_sidebands(lambda,h0,fsig,L,n)
%
% A function for Matlab which calculates the amplitude of the sidebands
% created when a light beam travels along a path modulated by a
% gravitational wave.
%
% lambda:   Wavelength of carrier light [m]
```

```
% h0:       Gravitational wave amplitude
% fsig:     Frequency of the gravitational wave [Hz]
% L:        Length of the path [m]
% n:        Index refection of the medium through which the beam travels
%
% Asb:      Amplitude of the sidebands [sqrt(W)]
%
% Part of the Simtools package, http://www.gwoptics.org/simtools
% Charlotte Bond    07.11.2012
%------------------------------------------------------------------------
%

function [Asb] = FT_GW_sidebands(lambda,h0,fsig,L,n,sb_sign)
    % Carrier light parameters
    c = 299792458;
    f0 = c/lambda;
    w0 = 2*pi*f0;
    % Signal anglar frequency
    wsig = 2*pi*fsig;
    % Sideband amplitude
    Asb = (w0*h0./(2*wsig)) .* sin(wsig*L*n/(2*c));
    % Phase
    phi_sb = pi/2 - w0*L*n/c - sb_sign * wsig*L*n/(2*c);
     % Final sideband
    Asb = Asb.*exp(1i*phi_sb);
end
```

A.4 Reflection from a mirror

We now consider the effect of a gravitational wave on a beam propagating through a space of length L where it is then reflected from a mirror and propagates back through the space (see figure A.2). *Is this just equivalent to a space of double the length, taking into account the reflectivity of the mirror?*

In this case the effect of the gravitational wave is calculated by considering the sidebands added at different points in the setup, after each length propagation. As the modulation index, m, is small we assume the carrier field amplitude is unchanged due to the gravitational wave. Referring to the fields in figure A.2, where a refers to the field of the carrier

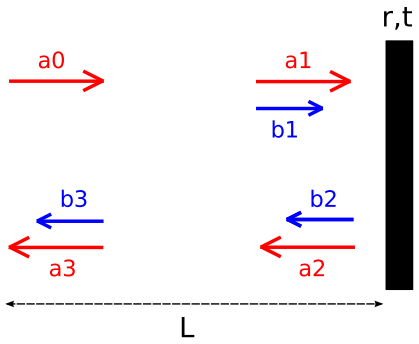

Figure A.2: A diagram of a single reflection from a mirror. a represent the carrier field, b represent the upper and lower sidebands produced by a gravitational wave.

and b refer to the field of the sidebands we have:

$$\begin{aligned} a_3 &= a_2 \exp\left(-\mathrm{i}\, k_0 L\right) \\ a_2 &= r a_1 \\ a_1 &= a_0 \exp\left(-\mathrm{i}\, k_0 L\right) \end{aligned}$$

So the reflected carrier field is given by:

$$a_3 = r a_0 \exp\left(-\mathrm{i}\, 2 k_0 L\right) \tag{A.18}$$

For the sideband fields we have:

$$\begin{aligned} b_3 &= b_2 \exp\left(-\mathrm{i}\, (k_0 \pm k_g) L\right) + a_2\ \alpha_{sb}^{\text{space}} \\ b_2 &= r b_1 \\ b_1 &= a_0\ \alpha_{sb}^{\text{space}} \end{aligned}$$

where $\alpha_{sb}^{\text{space}}$ describes the relative amplitude and phase of the sideband created from the modulation of the space. This gives the reflected field of the sidebands as:

$$\begin{aligned} b_3 &= r a_0\ \alpha_{sb}^{\text{space}} \exp\left(-\mathrm{i}\, (k_0 \pm k_g) L\right) + r a_0\ \alpha_{sb}^{\text{space}} \exp\left(-\mathrm{i}\, k_0 L\right) \\ &= r a_0\ \alpha_{sb}^{\text{space}} \exp\left(-\mathrm{i}\, k_0 L\right) \left[1 + \exp\left(\mp \mathrm{i}\, k_g L\right)\right] \end{aligned} \tag{A.19}$$

The sidebands produced from the round-trip propagation and single reflection have combined amplitude and phase $a_0\ \alpha_{sb}^{\text{arm}}$ where:

$$\alpha_{sb}^{\text{arm}} = r \alpha_{sb}^{\text{space}} \exp\left(-\mathrm{i}\, k_0 L\right) [1 + \exp\left(\mp \mathrm{i}\, k_g L\right)] \tag{A.20}$$

and if we assume the space is 'resonant' for the carrier wave we can simplify this to:

$$\alpha_{sb}^{\mathrm{arm}} = r\alpha_{sb}^{\mathrm{space}}[1 + \exp(\mp \mathrm{i}\, k_g L)] \tag{A.21}$$

Figure A.3 shows plots of the amplitude and phase of the upper sideband for propagation back-and-forth from a mirror ($L = 10\,\mathrm{km}$, $r = 1$), comparing these analytical equations and the result from FINESSE. The FINESSE output is generated by the following commands:

```
l l1 1 0 n1
s s1 10k 1 n1 n2
m m1 1 0 0 n2 n3
fsig sm s1 1 0
ad upper 1 n1

xaxis sm f lin 1 50k 400
put upper f $x1
yaxis abs:deg
```

The plots illustrate that this propagation back-and-forth is equivalent to the modulation of a space of double the length (the plots are identical to those shown in figure A.1 except the x-axis is scaled by 2).

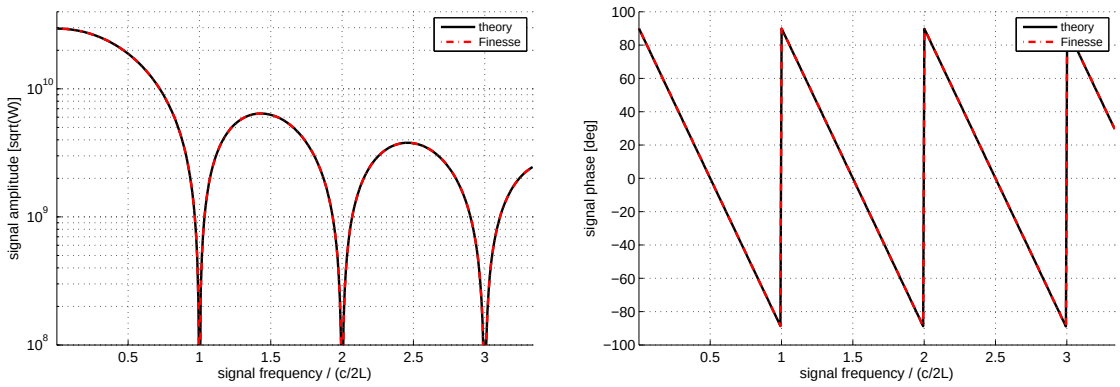

Figure A.3: Plots showing the amplitude and phase of the upper sideband produced when a gravitational wave modulates a carrier field which propagates along a space of length $L = 10\,\mathrm{km}$ and is then reflected by a mirror ($r = 1$) and travels the same 10 km back again. This is the same result as shown in Figure A.1 except for the fact that the x-axis is scaled by a factor of two (and in this plot the y-axis uses a log-scale).

A.5 Linear cavities

We now consider the sidebands reflected from a Fabry-Perot cavity when the cavity space is modulated by a gravitational wave. Figure A.4 shows the different fields at different points in a linear cavity.
The sideband field reflected from a linear cavity is:

$$b_4 = \mathrm{i}\, t_1 b_3' \tag{A.22}$$

where

$$\begin{aligned} b_3' &= a_1 \alpha_{sb}^{\mathrm{arm}} + r_2 b_1 \exp\left(-\mathrm{i}\, 2(k_0 \pm k_g)L\right) \\ b_1 &= r_1 b_3' \\ b_3' &= \frac{a_1 \alpha_{sb}^{\mathrm{arm}}}{1 - r_1 r_2 \exp\left(-\mathrm{i}\, 2(k_0 \pm k_g)L\right)} \end{aligned}$$

and $\alpha_{sb}^{\mathrm{arm}}$ refers to the relative amplitude and phase of the sidebands after propagation back-and-forth from the end mirror. The carrier fields are solved by the usual simultaneous equations:

$$\begin{aligned} a_1 &= \mathrm{i}\, t_1 a_0 + r_1 a_3' \\ a_3' &= a_3 \exp\left(-\mathrm{i}\, k_0 L\right) \\ a_3 &= r_2 a_1' \\ a_1' &= a_1 \exp\left(-\mathrm{i}\, k_0 L\right) \end{aligned}$$

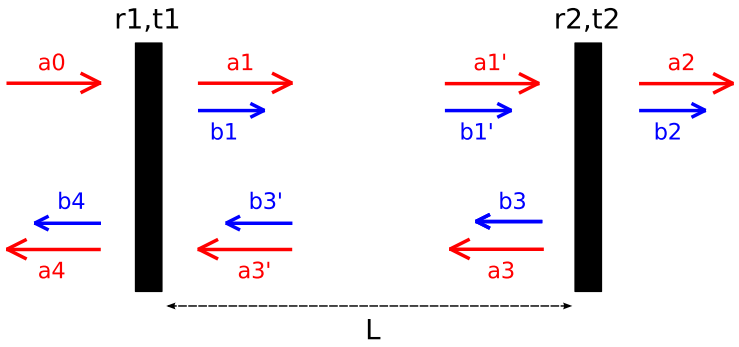

Figure A.4: A diagram showing the carrier and sideband fields at different points in a linear cavity. a represent the carrier field, b represent the upper and lower sidebands produced by a gravitational wave.

from which we have:

$$\begin{aligned} a_1 &= \mathrm{i}\, t_1 a_0 + r_1 r_2 a_1 \exp\left(-\mathrm{i}\, 2k_0 L\right) \\ a_1 &= \frac{\mathrm{i}\, t_1 a_0}{1 - r_1 r_2 \exp\left(-\mathrm{i}\, 2k_0 L\right)} \end{aligned} \tag{A.23}$$

Finally:

$$b_4 = \frac{-T_1 a_0}{1 - r_1 r_2 \exp\left(-\mathrm{i}\, 2k_0 L\right)} \frac{1}{1 - r_1 r_2 \exp\left(-\mathrm{i}\, 2(k_0 \pm k_g) L\right)} \alpha_{sb}^{\mathrm{arm}} \tag{A.24}$$

The sidebands reflected from a Fabry-Perot cavity are given by the field $a_0\ \alpha_{sb}^{\mathrm{FP}}$, where:

$$\alpha_{sb}^{\mathrm{FP}} = \frac{-T_1}{1 - r_1 r_2} \frac{\alpha_{sb}^{\mathrm{arm}}}{1 - r_1 r_2 \exp\left(\mp \mathrm{i}\, 2k_g L\right)} \tag{A.25}$$

if we assume the cavity is on resonance. In figure A.5 plots of this analytic result for a 10 km long cavity are compared with the result from FINESSE. The FINESSE output is generated with the following file:

```
l l1 1 0 nin

s s0 1 nin n1

const T_ITM 700e-3
const T_ETM 100e-6

m1 ITM $T_ITM 0 0 n1 n2
s sarm 10k n2 n3
m1 ETM $T_ETM 0 180 n3 n4

fsig sig1 sarm 1 0
ad upper 0 n1

xaxis sig1 f lin 100 50k 400
put upper f $x1
yaxis lin abs:deg
```

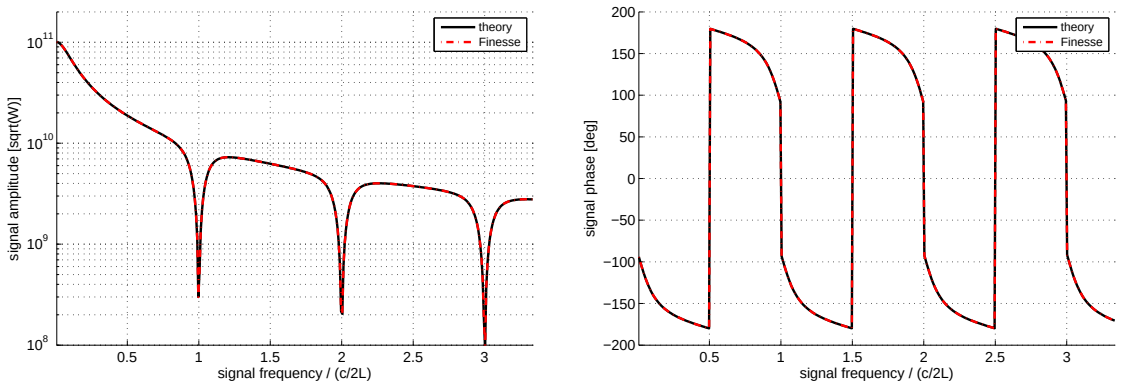

Figure A.5: Plots showing the amplitude and phase of the upper sideband produced by a gravitational wave modulating a Fabry-Perot cavity of length $L = 10\,\mathrm{km}$ at frequency against the signal frequency. The sideband is detected in the light reflected from the cavity.

A.6 Michelson interferometer

We now look at the effect of a gravitational wave on the output of a Michelson interferometer. The amplitude of the sidebands at the output of the detector is given by:

$$b_{out} = r_{bs} b_x + \mathrm{i}\ t_{bs} b_y \tag{A.26}$$

where r_{bs} and t_{bs} refer to the reflection and transmission coefficients of the beam-splitter and b_x and b_y are the sideband fields reflected from the x and y arms. If we consider a gravitational wave in the ideal polarisation for a Michelson (a gravitational wave, h_+, modulating the space in the y arm 180° out of phase with the x arm) we have:

$$\begin{aligned} b_x &= \mathrm{i}\ t_{bs}\ (a_0 \exp(-\mathrm{i}\, k_0 l_x))\ \alpha_{sb}^{\mathrm{FP}} \exp(-\mathrm{i}\,(k_0 \pm k_g) l_x) \\ b_y &= r_{bs}\ (a_0 \exp(-\mathrm{i}\, k_0 l_y))\ (-\alpha_{sb}^{\mathrm{FP}}) \exp(-\mathrm{i}\,(k_0 \pm k_g) l_y) \end{aligned}$$

where l_x and l_y refer to the Michelson lengths, which should be much smaller than the cavity lengths. In order to operate on the dark fringe we must have $|l_x - l_y| = (2N+1)\frac{\lambda}{4}$, where N is an integer. Finally, at the output of the interferometer we have:

$$b_{out} = i\ t_{bs} r_{bs} a_0 \alpha_{sb}^{\mathrm{FP}} \left[\exp(-\mathrm{i}\,(2k_0 \pm k_g) l_x) - \exp(-\mathrm{i}\,(2k_0 \pm k_g) l_y)\right] \tag{A.27}$$

For the case of no arm cavities (i.e. just a single mirror at the end of the arm) we just replace the $\alpha_{sb}^{\mathrm{FP}}$ factor with $\alpha_{sb}^{\mathrm{arm}}$. In figure A.6 this analytic result and the result from a FINESSE simulation of the same setup are plotted, for a simple Michelson and a Michelson with arm cavities. The FINESSE output is generated using the following code:

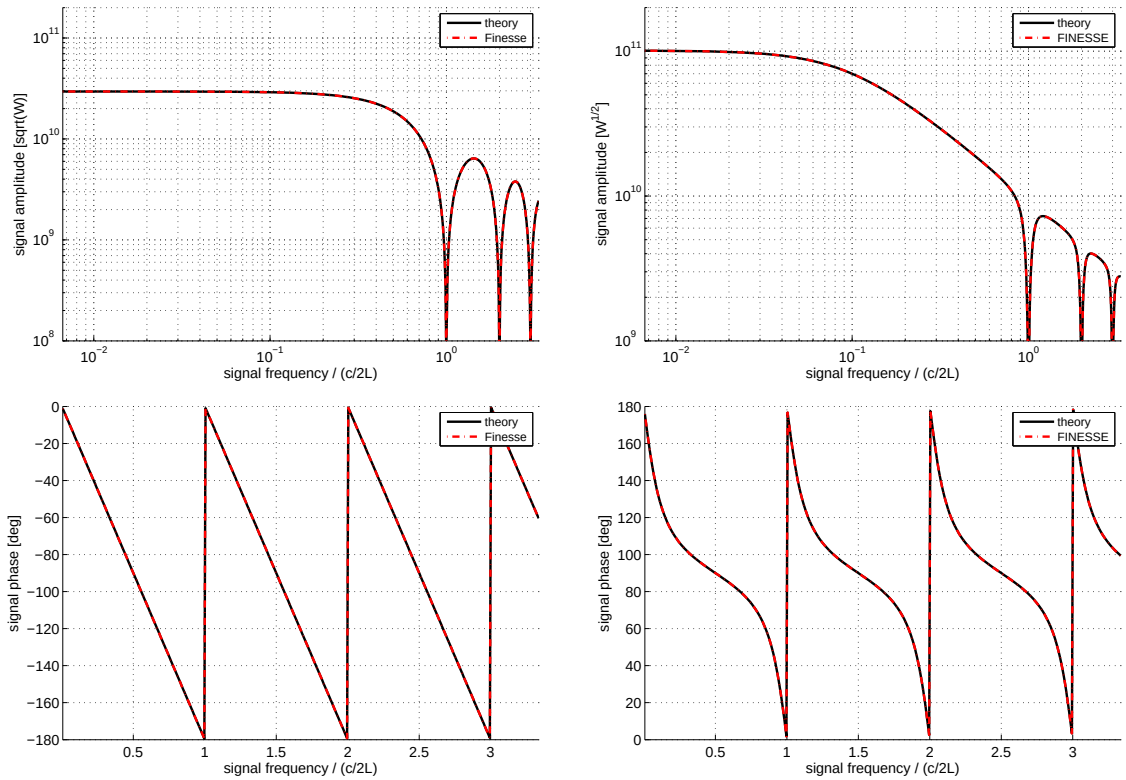

Figure A.6: Plots showing the amplitude and phase of the upper sideband produced by a gravitational wave modulating the 10 km long arms of a Michelson interferometer. Left: Plots of the amplitude (top) and phase (bottom) of the sidebands at the output of a simple Michelson with no arm cavities. Right: Plots of the amplitude (top) and phase (bottom) of the sidebands at the output of a Michelson with Fabry-Perot arm cavities.

For a simple Michelson without arm cavities:

```
l l1 1 0 nin

s s0 1 nin n1

const T_ETM 100e-6

bs BS 0.5 0.5 0 45 n1 ny1 nx1 nout

s syarm 10k ny1 ny2
m1 ETMy $T_ETM 0 0 ny2 ny3

s sxarm 10k nx1 nx2
m1 ETMx $T_ETM 0 90 nx2 nx3

fsig sig1 syarm 1 180
fsig sig1 sxarm 1 0

ad upper 0 nout

xaxis sig1 f lin 100 50k 400
put upper f $x1
yaxis lin abs:deg
```

For a Michelson with arm cavities:

```
l l1 1 0 nin

s s0 1 nin n1

const T_ITM 700e-3
const T_ETM 100e-6

bs BS 0.5 0.5 0 45 n1 ny1 nx1 nout

s sy 1 ny1 ny2

m1 ITMy $T_ITM 0 0 ny2 ny3
s syarm 10k ny3 ny4
m1 ETMy $T_ETM 0 0 ny4 ny5

s sx 1 nx1 nx2

m1 ITMx $T_ITM 0 90 nx2 nx3
s sxarm 10k nx3 nx4
m1 ETMx $T_ETM 0 90 nx4 nx5

fsig sig1 syarm 1 180
fsig sig1 sxarm 1 0

ad upper 0 nout

xaxis sig1 f lin 100 50k 400
put upper f $x1
yaxis lin abs:deg
```

A.7 Sagnac interferometer

We now look at the gravitational wave effect on the output of a Sagnac interferometer. The sideband fields at the output of the detector are given by:

$$b_{\text{out}} = \mathrm{i}\, t_{bs} b_a + r_{bs} b_c \tag{A.28}$$

b_c and b_a refer to the sidebands generated travelling clockwise and anti-clockwise through the interferometer. Travelling clockwise through the interferometer we have:

$$b_c = b_c^x + b_c^y R_{cav}(k_0 \pm k_g) \tag{A.29}$$

where b_c^x and b_c^y refer to the sidebands created in the x and y arms. R_{cav} is the complex number describing the reflected field from a cavity:

$$R_{cav}(k) = r_1 - \frac{T_1 r_2 \exp(-2\mathrm{i}\, kL)}{1 - r_1 r_2 \exp(-2\mathrm{i}\, kL)} \tag{A.30}$$

If there is no arm cavity $T_1 = 1$ and $r_1 = 0$ and an additional 180° needs to be added to R_{cav} (mitigating the 90° phase incurred for each transmission through the input mirror). The sidebands created travelling clockwise through the y arm are given by:

$$b_c^y = r_{bs} a_0 (-\alpha_{sb}^{\text{FP}}) \tag{A.31}$$

The minus refers to the relative phase of the modulation by the gravitational wave. The sidebands created travelling clockwise through the x arm are given by:

$$b_c^x = r_{bs} a_0 R_{cav}(k_0) \alpha_{sb}^{\text{FP}} \tag{A.32}$$

So we have:

$$b_c = r_{bs}\ a_0\ \alpha_{sb}^{\text{FP}}\ [R_{cav}(k_0) - R_{cav}(k_0 \pm k_g)] \tag{A.33}$$

The sidebands created travelling anti-clockwise through the interferometer are given by:

$$b_a = b_a^x R_{cav}(k_0 \pm k_g) + b_a^y \tag{A.34}$$

We have the sidebands created travelling anti-clockwsie through the x-arm:

$$b_a^x = \mathrm{i}\, t_{bs}\ a_0\ \alpha_{sb}^{\text{arm}} \tag{A.35}$$

The sidebands created travelling anti-clockwise through the y-arm ($-\alpha_{sb}^{\text{arm}}$ to take into account h_+ is out of phase by π with respect to the x arm):

$$b_a^y = \mathrm{i}\, t_{bs} a_0 R_{cav}(k_0)(-\alpha_{sb}^{\text{arm}}) \tag{A.36}$$

Which gives the total anti-clockwise sideband field as:

$$b_a = \mathrm{i}\ \ t_{bs}\ a_0\ \alpha_{sb}^{\text{FP}}\left[R_{cav}(k_0 \pm k_g) - R_{cav}(k_0)\right] \tag{A.37}$$

Finally the sidebands at the output of the interferometer are given by:

$$\begin{aligned} b_{out} &= a_0\ \alpha_{sb}^{\text{FP}}\left[R_{cav}(k_0) - R_{cav}(k_0 \pm k_g)\right]\left[R_{bs} - \mathrm{i}^{\,2} T_{bs}\right] \\ &= a_0\ \alpha_{sb}^{\text{FP}}\left[R_{cav}(k_0) - R_{cav}(k_0 \pm k_g)\right]\left[R_{bs} + T_{bs}\right] \end{aligned} \tag{A.38}$$

In figure A.7 this analytical solution is plotted, as well as the result for a FINESSE simulation, for a simple Sagnac and a Sagnac with arm cavities. The FINESSE simulation is detailed in the following kat files:

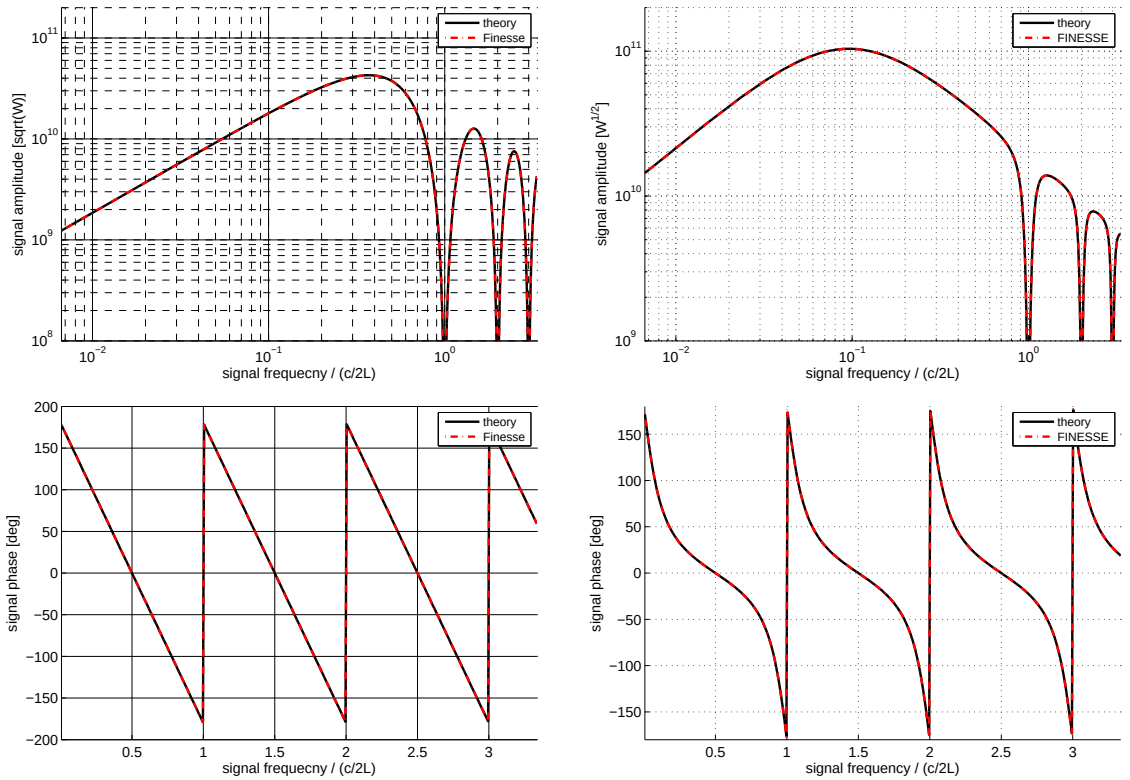

Figure A.7: Plots showing the amplitude and phase of the upper sideband produced by a gravitational wave modulating the arms of a Sagnac interferometer. Left: Plots of the amplitude (top) and phase (bottom) of the sidebands at the output of a simple Sagnac with no arm cavities. Right: Plots of the amplitude (top) and phase (bottom) of the sidebands at the output of a Sagnac with Fabry-Perot arm cavities. The arms in both cases have alength L =10 km.

For a simple Sagnac without arm cavities:

```
 l1 1 0 nin

s s0 1 nin n1

const T_ETM 100e-6

bs BS 0.5 0.5 0 45 n1 ny1 nx1 nout

s syarm1 10k ny1 ny2
bs1 ETMy $T_ETM 0 0 0 ny2 ny3 nytrans
dump1
s syarm2 10k ny3 ny4

bs TM 1 0 0 45 ny4 nx4 dump2 dump3

s sxarm1 10k nx1 nx2
bs1 ETMx $T_ETM 0 0 0 nx2 nx3 nxtrans
dump4
s sxarm2 10k nx3 nx4

fsig sig1 syarm1 1 180
fsig sig1 syarm2 1 180
fsig sig1 sxarm1 1 0
fsig sig1 sxarm2 1 0

ad upper 0 nout

xaxis sig1 f lin 100 50k 400
put upper f $x1
yaxis lin abs:deg
```

For a Sagnac with arm cavities:

```
l l1 1 0 nin

s s0 1 nin n1

const T_ITM 700e-3
const T_ETM 100e-6

bs BS 0.5 0.5 0 45 n1 ny1 nx1 nout

s sy 1 ny1 ny2

bs1 ITMy $T_ITM 0 0 0 ny2 ny3 ny4 ny5
s syarm1 10k ny4 ny6
bs1 ETMy $T_ETM 0 0 0 ny6 ny7 ny8 dump1
s syarm2 10k ny7 ny5

bs TM 1 0 0 45 ny3 nx3 dump2 dump3

s sx 1 nx1 nx2

bs1 ITMx $T_ITM 0 0 0 nx2 nx3 nx4 nx5
s sxarm1 10k nx4 nx6
bs1 ETMx $T_ETM 0 0 0 nx6 nx7 nx8 dump4
s sxarm2 10k nx7 nx5

fsig sig1 syarm1 1 180
fsig sig1 syarm2 1 180
fsig sig1 sxarm1 1 0
fsig sig1 sxarm2 1 0

ad upper 0 nout

xaxis sig1 f lin 100 50k 400
put upper f $x1
yaxis lin abs:deg
```

Appendix B

Expanding fields in terms of Gaussian modes

B.1 Converting between Hermite-Gauss and Laguerre-Gauss modes

This section is a summary of the coefficients required to express Laguerre-Gauss (LG) modes as sum of Hermite-Gauss (HG) modes and vice versa. Alterations to equations in [48], which describe LG modes in terms of HG modes, are shown to be consistent with our LG mode definition, which differs to that defined in [48] in two ways. We also adapt the equations for a negative azimuthal index LG mode. Finally these coefficients are re-arranged to get the coefficients required to express an HG mode as a sum of LG modes.

B.2 LG to HG

In [48] an LG mode can be described by:

$$u^{\mathrm{LG}}_{n,m}(x,y,z) = \sum_{k=0}^{N} \mathrm{i}^{\,k} b(n,m,k) u^{\mathrm{HG}}_{N-k,k}(x,y,z) \tag{B.1}$$

where $N = n + m$ and the LG indices are $p = \min(n,m)$ and $|l| = n - m$. However, our definition of an LG mode [17] (equation 2.13) differs from the definition given in [48]:

$$\begin{aligned} u^{\mathrm{LG}}_{\mathrm{ours}} &= u^{\mathrm{LG}}_{\mathrm{com.}} \exp\left(\mathrm{i}\, l\phi\right) \\ u^{\mathrm{LG}}_{\mathrm{ref}} &= u^{\mathrm{LG}}_{\mathrm{com.}} (-1)^p \exp\left(-\mathrm{i}\, l\phi\right) \end{aligned} \tag{B.2}$$

where $u^{\mathrm{LG}}_{\mathrm{com.}}$ is the common factor between the two definitions. We have the coefficient for the HG mode as:

$$c = \int_S u^{\mathrm{LG}}_{p,l} (u^{\mathrm{HG}}_{n,m})^* \, \mathrm{d}S \tag{B.3}$$

For $u^{\mathrm{LG}}_{p,l}(u^{\mathrm{HG}}_{n,m})^*$, where both modes are the same order, the only imaginary factor is contained in $\exp(\pm il\phi)$. The coefficients for the LG modes in our representation will be:

$$c_{\mathrm{ours}} = (-1)^p \, c^*_{\mathrm{ref}} \tag{B.4}$$

for positive l and:

$$c_{\mathrm{ours}} = (-1)^p \, c_{\mathrm{ref}} \tag{B.5}$$

for negative l, where c_{ref} are the coefficients from [48]. As $b(n, m, k)$ is real we finally have (in terms of LG indices p and l):

$$u^{\mathrm{LG}}_{p,l}(x, y, z) = \sum_{k=0}^{N} (-1)^p (\mp \mathrm{i})^k b(|l| + p, p, k) u^{\mathrm{HG}}_{N-k,k}(x, y, z) \tag{B.6}$$

where $\mp$ is negative for positive l and positive for negative l. The coefficients b are given by:

$$b(|l| + p, p, k) = \sqrt{\frac{(N-k)!k!}{2^N(|l|+p)!p!}} (-2)^k P_k^{|l|+p-k,p-k}(0) \tag{B.7}$$

where P is a Jacobi polynomial. In figure B.1 the sum recreates an LG_{33} beam very well, with only a small difference between the original mode and the sum of HG modes.

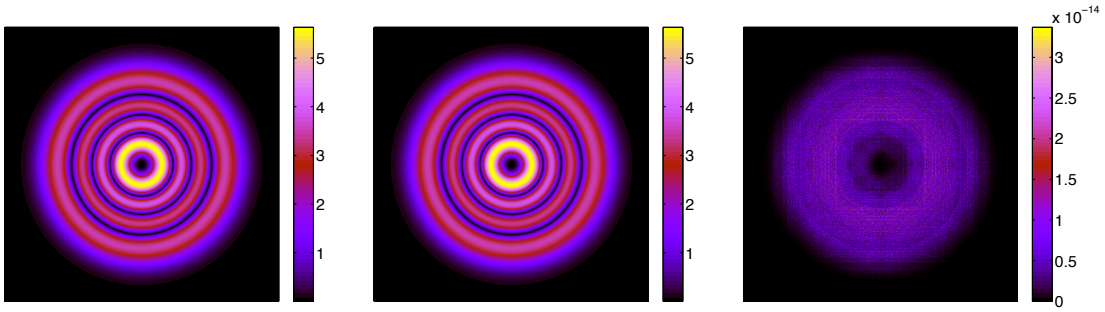

Figure B.1: Plots showing the amplitude of the Laguerre-Gauss mode LG_{33} from the original equation (left), a sum of HG modes (centre) and the difference between the two (right).

B.3 HG to LG

We can also describe an HG mode as a sum of LG modes:

$$u^{\mathrm{HG}}_{n,m}(x,y,z) = \sum_{j=0}^{N} a_{p,l} u^{\mathrm{LG}}_{p,l}(x,y,z) \tag{B.8}$$

where N is the mode order ($N = n+m$), $p = \frac{1}{2}(N-|2j-N|)$, $l = 2j-N$. The coefficients $a_{p,l}$ can be extracted by looking at the equation B.6. The coefficient for a particular LG mode is given by:

$$a_{p,l} = \int_S u^{\mathrm{HG}}_{n,m}\ u^{\mathrm{LG}*}_{p,l}\ \mathrm{d}S \tag{B.9}$$

As we have:

$$u^{\mathrm{LG}}_{p,l}(x,y,z) = \sum_{k=0}^{N} c_{n,m} u^{\mathrm{HG}}_{n,m}(x,y,z) \tag{B.10}$$

$$c_{n,m} = \int_S u^{\mathrm{LG}}_{p,l}\ u^{\mathrm{HG}*}_{n,m}\ \mathrm{d}S \tag{B.11}$$

We find that:

$$a_{p,l} = c^*_{n,m} \tag{B.12}$$

Finally we have:

$$u^{\mathrm{HG}}_{n,m}(x,y,z) = \sum_{j=0}^{N} (-1)^p (\pm \mathrm{i})^m b(|l|+p,p,m) u^{\mathrm{LG}}_{p,l}(x,y,z) \tag{B.13}$$

where we have $l = 2j-N$ and $p = \frac{1}{2}(N-|2j-N|)$, and $\pm$ is the sign of l. In figure B.2 you can see that the sum recreates an HG_{47} beam very well, with again only a small difference between the original mode and the sum of LG modes.

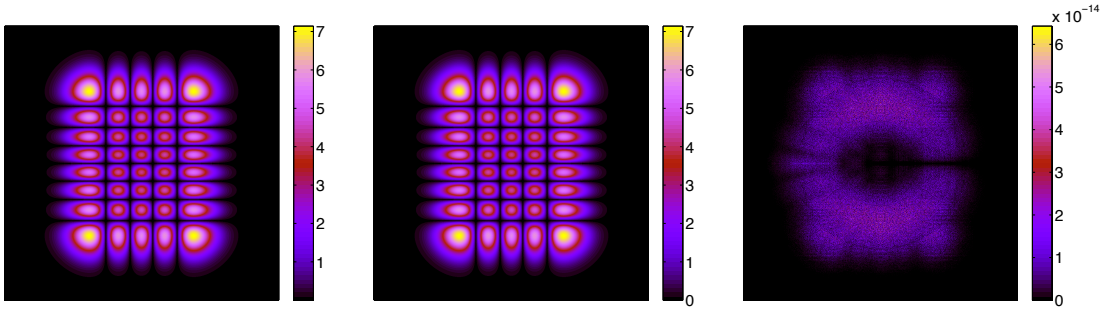

Figure B.2: Plots showing the amplitude of the Hermite-Gauss mode HG_{47} from the original equation (left), a sum of LG modes (centre) and the difference between the two.

B.4 Scattering into higher-order modes

In section 3.3.2 the coupling between different Hermite-Gauss modes, in 1 dimension, was derived for an arbitrary incident mode on a surface distortion described by a single spatial frequency. Here we show some more detailed examples of this coupling approximation.

In figure 3.14 in section 3.3.2 the coupling between HG modes with $n = 3$ and $n = 9$ was calculated, for a range of spatial frequencies, both numerically and using our first order analytical approximation. In figure B.3 the residual for this example is plotted, showing the very small difference between the two methods.

Figure B.4 shows the amplitude of the coupling from an incident $n = 0$ HG mode into modes with $n' \neq 0$, as calculated from our coupling approximation, for reflection from a distorted mirror described by a single spatial frequency. Recall that coupling such as this is described by a Lagurre-Gauss mode of the order $n + n'$, which in this case is simple n'. In this case the azimuthal index of the mode is $l = n'$. The coupling into each mode peaks at a particular spatial frequency, showing that particular mirror surface distortions are related to coupling into particular modes. The peak in coupling occurs at a higher spatial frequency for higher n'. This is consistent with our experience that higher order distortions cause coupling into higher-order modes.

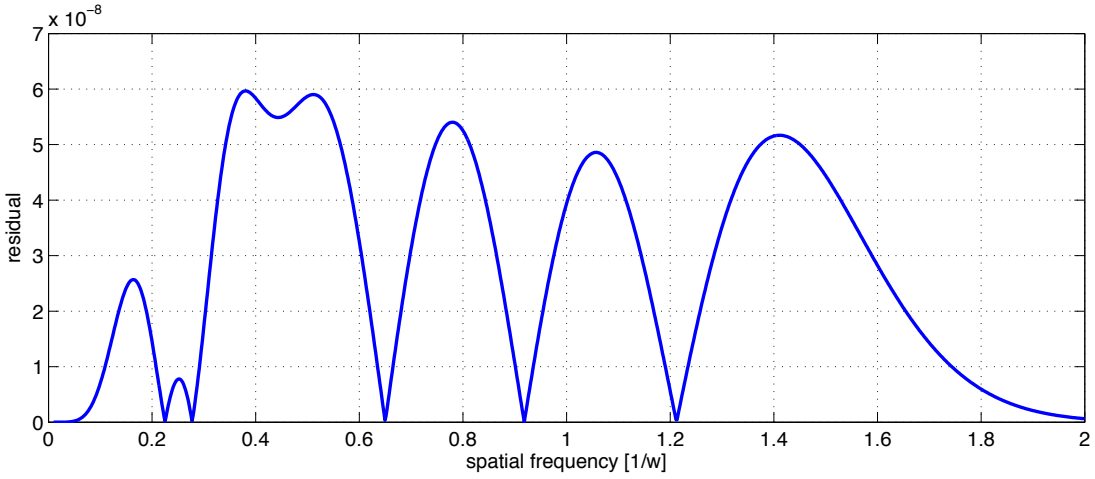

Figure B.3: Plot showing the residual (difference) between coupling coefficients calculated numerically and coupling coefficients calculated using the first order analytical approximation derived in section 3.3.2. In this example the coupling is between HG modes with $n = 3$ and $n = 9$, for a range of spatial frequencies.

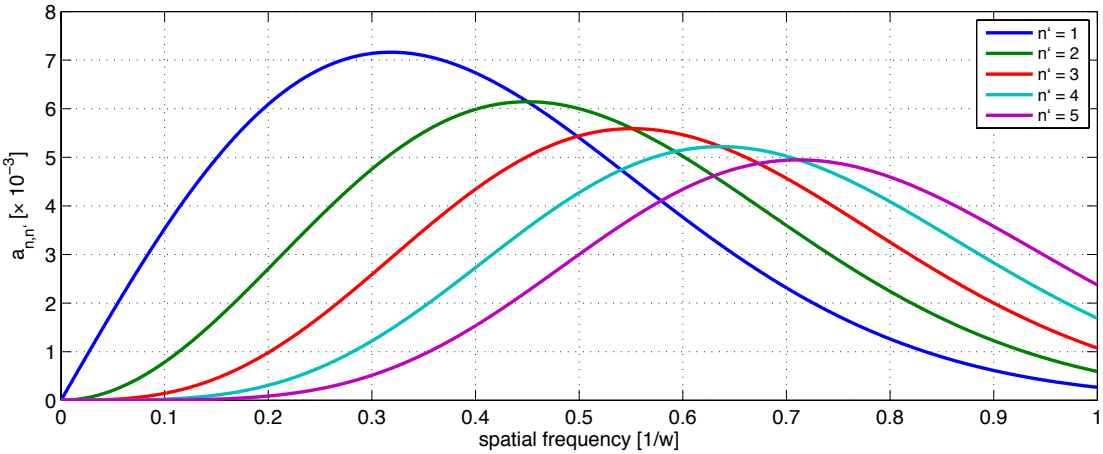

Figure B.4: Amplitude of the coupling from an HG mode with $n = 0$ into modes with $n' = 1$, 2, 3, 4 and 5, from coupling upon reflection from a distorted mirror, described by a single spatial frequency. The spatial frequency is normalised with respect to $1/w$, where w is the beam radius.

B.5 Second order Zernike coupling

In section 3.3.2 the first order coupling between LG modes reflected from a distorted mirror surface described by a single Zernike polynomial was derived. As with the coupling from a distortion described by a single spatial frequency, the coupling back into the same mode requires the second order term as well. We have:

$$\begin{aligned} k^{n,m}_{p,l,p',l'} &= \int_S u_{p,l} \exp\left(2\mathrm{i}\, k Z^m_n\right) u^*_{p',l'}\ \mathrm{d}S \\ &\approx \delta_{p,p'}\delta_{l,l'} + k^{n,m,1}_{p,l,p',l'} + k^{n,m,2}_{p,l,p',l'} \end{aligned} \tag{B.14}$$

where $k^{n,m,1}_{p,l,p',l'}$ is the first order coupling as calculated in section 3.3.2 and $k^{n,m,2}_{p,l,p',l'}$ is the second order coupling, given by:

$$k^{n,m,2}_{p,l,p',l'} = \int_S u_{p,l}\ u^*_{p',l'}(-2k^2(Z^m_n)^2)\ \mathrm{d}S \tag{B.15}$$

The product of the two beams is:

$$\begin{aligned} u_{p,l}\ u^*_{p',l'} = \frac{1}{w^2}\frac{2}{\pi}\sqrt{\frac{p!p'!}{(|l|+p)!(|l'|+p')!}} \exp\left(\mathrm{i}\left(2p+|l|-2p'-|l'|\right)\psi\right) \\ \left(\frac{\sqrt{2}r}{w}\right)^{|l|+|l'|} L^{|l|}_p\left(\frac{2r^2}{w^2}\right) L^{|l'|}_{p'}\left(\frac{2r^2}{w^2}\right) \exp\left(-\frac{2r^2}{w^2}\right) \exp\left(\mathrm{i}\,\phi(l-l')\right) \end{aligned} \tag{B.16}$$

As with the first order coupling we can split the integration into the radial and angular parts. The angular integration is:

$$I_\phi = \int_0^{2\pi} \begin{matrix}\cos^2(m\phi)\\ \sin^2(m\phi)\end{matrix} \exp\left(\mathrm{i}\,\phi(l-l')\right)\,\mathrm{d}\phi \tag{B.17}$$

Taking the even Zernike polynomial we have:

$$\int_0^{2\pi} \frac{1}{4}\left(e^{\mathrm{i}\,m\phi} + e^{-\mathrm{i}\,m\phi}\right)^2 e^{\mathrm{i}\,\phi(l-l')}\,\mathrm{d}\phi = \int_0^{2\pi} \frac{1}{4}\left[e^{\mathrm{i}\,\phi(l-l'+2m)} + e^{\mathrm{i}\,\phi(l-l'-2m)} + 2e^{\mathrm{i}\,\phi(l-l')}\right]\,\mathrm{d}\phi \tag{B.18}$$

As with the angular integration for the first order coupling, a non-zero value is only achieved when the exponentials disappear before the integration. We therefore have conditions for non-zero second order coupling:

$$\begin{aligned} &2m = |l-l'| \\ &\text{or} \\ &l = l' \end{aligned} \tag{B.19}$$

Integrating with respect to ϕ we have:

$$I_\phi = \begin{cases} 0 & 2m \neq |l-l'|, \quad l \neq l' \\ \frac{\pi}{2} & 2m = |l-l'|, \quad \text{even } Z_n^m \\ -\frac{\pi}{2} & 2m = |l-l'|, \quad \text{odd } Z_n^m \\ \pi & l = l', \quad m \neq 0 \\ 2\pi & l = l', \quad m = 0 \end{cases} \tag{B.20}$$

For the radial integration we make the variable substitution $x = \frac{2r^2}{w^2}$ which gives:

$$\begin{aligned} k_{p,l,p',l'}^{n,m,2} = &-2k^2 \frac{1}{w^2}\frac{2I_\phi}{\pi}\sqrt{\frac{p!p'!}{(|l|+p)!(|l'|+p')!}}\exp\left(\mathrm{i}\,\Delta o\;\psi\right) \\ &\int_0^X x^{\frac{|l|+|l'|}{2}} L_p^{|l|}(x) L_{p'}^{|l'|}(x)\exp(-x)\left[R_n^m\left(\sqrt{\frac{x}{2}}\frac{w}{R}\right)\right]^2\sqrt{\frac{x}{2}}w\;\mathrm{d}x \end{aligned} \tag{B.21}$$

where Δo is the difference in order between the incident and coupled mode and $X = \frac{2R^2}{w^2}$ is the limit of the exponential. As with the first order coupling we use the lower incomplete

gamma function, $\gamma(a,x) = \int_0^x t^{a-1}e^{-t}\mathrm{d}t$ to get the final solution:

$$k_{p,l,p',l'}^{n,m,2} = -\frac{I_\phi}{\pi}k^2A^2\sqrt{p!p'!(p+|l|)!(p'+|l'|)!}\exp\left(\mathrm{i}\,\Delta o\;\psi\right)$$
$$\sum_{i=0}^{p}\sum_{j=0}^{p'}\sum_{h=0}^{\frac{1}{2}(n-m)}\sum_{g=0}^{\frac{1}{2}(n-m)}\frac{(-1)^{i+j+h+g}(n-h)!(n-g)!X^{h+g-n}}{(p-i)!(p'-j)!(|l|+i)!(|l'|+j)!i!j!h!g!} \tag{B.22}$$
$$\frac{\gamma(i+j+n-h-g+\frac{1}{2}(|l|+|l'|)+1,X)}{(\frac{1}{2}(n+m)-h)!(\frac{1}{2}(n+m)-g)!(\frac{1}{2}(n-m)-h)!(\frac{1}{2}(n-m)-g)!}$$

Using this derivation of the second order term, combined with our previous derivation of the first order coupling, the amplitude/ power coupled back into the incident mode can be calculated. In figure B.5 this coupling back into the same mode is calculated in the case of reflection from a surface described by Z_2^0, the curvature mismatch polynomial. The power coupled back into this mode, $|k_{p,l,p,l}|^2$, is calculated for the LG_{00} mode and LG_{33} mode.

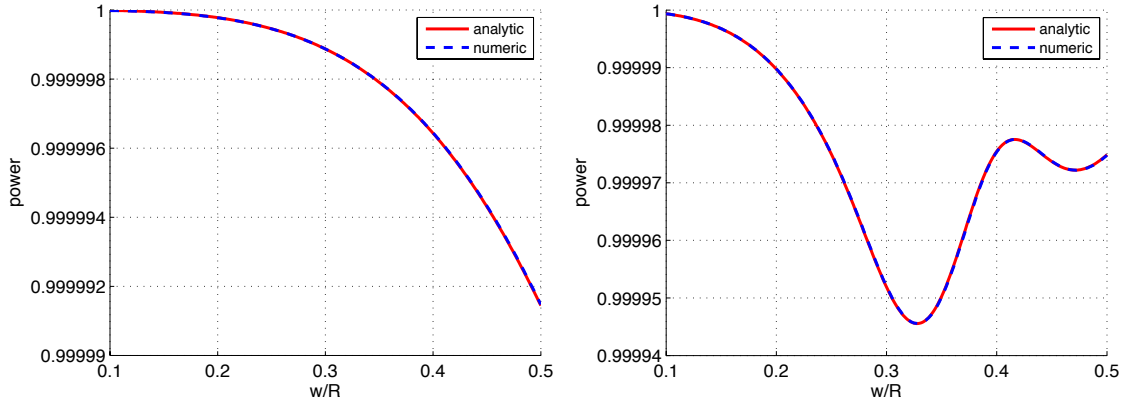

Figure B.5: Power coupled back into the same mode on reflection from a distorted mirror surface described by the curvature mismatch Zernike polynomial, Z_2^0. The coupled power is calculated numerically and using an analytic approximation expanded to second order, for an LG_{00} beam (left) and LG_{33} beam (right).

Appendix C

Preparation for commissioning

C.1 Preparing aLIGO input files

Preparing Advanced LIGO input files is a long, technical process. Firstly, it is important to understand the optical design. The motivation for the dual recycled, Fabry-Perot Michelson is understood in a generic sense but we need to understand the choice of parameters for Advanced LIGO, as well as checking FINESSE simulations of the design agree with results and arguments presented in the design documents, specifically [16; 27; 34; 78]. We want to identify the most important parameters; which have to be tightly controlled and which have larger tolerances. This will go a long way towards predicting future behaviour and identifying parameters which will have certain effects.

C.1.1 Basic parameters

Firstly we look at the core parameters, specifically lengths and the reflectivity of different mirrors. The majority of the parameters and arguments presented in this section come from [34], with several plots re-created to illustrate specific parameter choices.

Arm cavity finesse

The first consideration is the arm cavities. The length of the arms is automatically set to $\sim 4\,\mathrm{km}$, from the existing LIGO infrastructure. This gives a free spectral range of $37.5\,\mathrm{kHz}$. The choice of the reflectivity of the mirrors, or the finesse of the arm cavities, will impact other aspects of the design, so is chosen with care. The decision to have $\sim 800\,\mathrm{kW}$ circulating in the arms (during high power operation) was made early on, in order to reduce shot noise in the interferometer, the limiting noise source at most frequencies for initial LIGO. A combination of parameters determine this intra-cavity power: input laser power, power recycling gain and arm cavity finesse. A finesse of 450 was chosen [104].

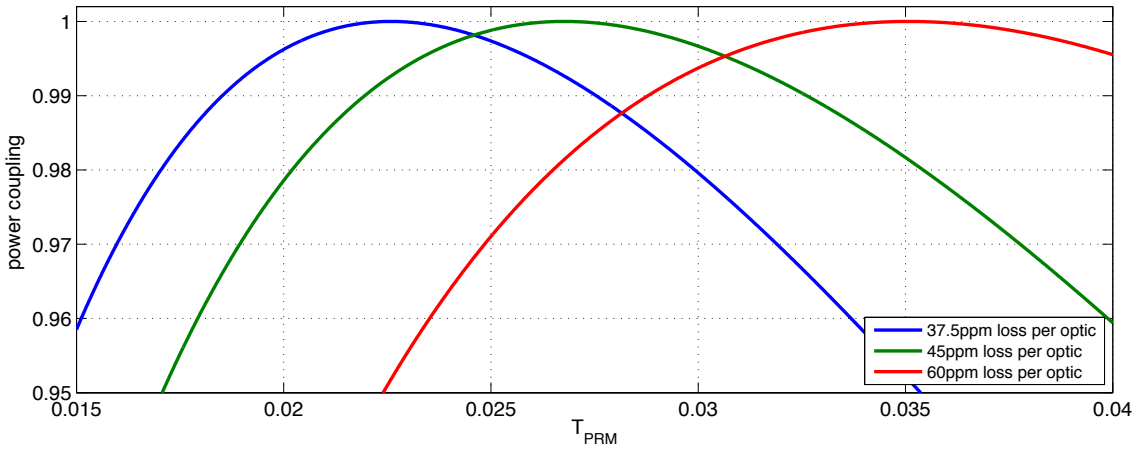

Figure C.1: Power coupled into an Advanced LIGO interferometer versus power recycling mirror transmission. The power coupled is simulated for 3 different values of scattering loss per optic, 37.5 ppm (nominal value), 45 ppm and 60 ppm.

PRM transmission

The transmission of the power recycling mirror (PRM) is carefully chosen to ensure the majority of the power is coupled into the interferometer, not reflected (i.e. close to impedance matched). In figure C.1 the power coupled into the interferometer is shown, for different PRM transmissions (recreated from [34]). The power coupling is considered for different losses at each optic, 37.5 ppm (the target loss) 45 ppm and 60 ppm. These larger losses are considered to make sure the choice of T_{PRM} will not result in significantly different coupling if the losses are larger than 37.5 ppm. The final transmission chosen was 3%, giving slight over-coupling for 37.5 ppm losses, providing robustness against greater losses and the potential to detect error signals in reflection. It should be noted that most of the power is 'transmitted' through the losses in the arms, rather than through the end mirrors.

DARM offset

Advanced LIGO will not be operated exactly on the dark fringe but with a slight offset in the differential arm length (DARM= $L_x - L_y$), a so called *DC offset*. This provides some carrier light at the detector output with which the signal sidebands can beat against to read out the gravitational wave signal [33]. In Advanced LIGO 100 mW will be used. In figure C.2 the power at the detector output (or anti-symmetric port) is shown, as DARM is tuned. This result is recreated from [34] and [104] The minimum output power (at 0 DC offset) depends on the difference in round-trip arm loss in x and y. The output for differential losses of 30 ppm and 60 ppm are shown. Away from 0 DC offset the two loss cases give very similar results, and 100 mW of carrier power is achieved at around 10 pm.

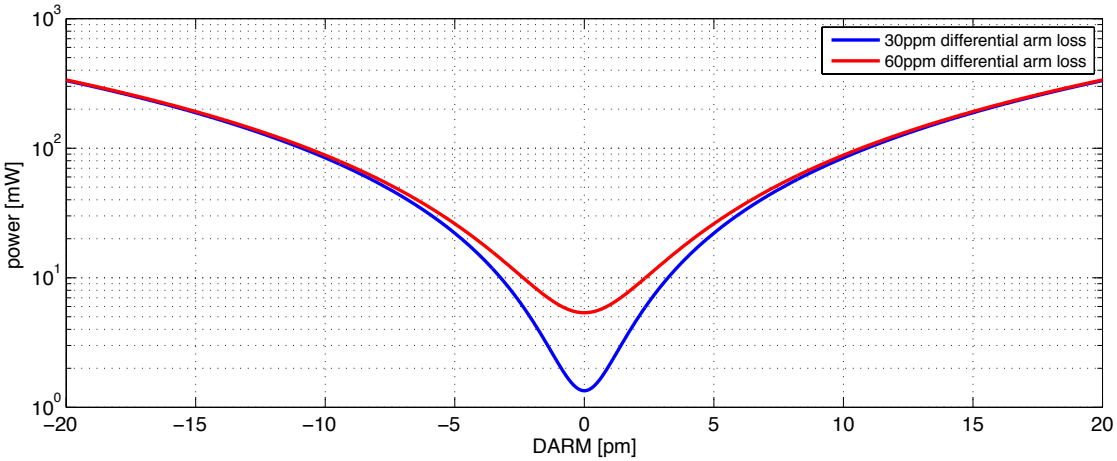

Figure C.2: The carrier power at the anti-symmetric (AS) port as the differential arm length ($L_x - L_y$) is tuned. The output is simulated for two possible differential arm losses, 30 ppm and 60 ppm. 100 mW at the output is achieved at a DARM offset of around 10 pm.

In FINESSE this is equivalent to a tuning offset of $+0.002°$ on ETMX and $-0.002°$ on ETMY.

Recycling cavity lengths

The choice of lengths for the power and signal recycling cavities are closely linked to the control scheme of Advanced LIGO. This involves injecting 2 pairs of control sidebands into the interferometer, at two different frequencies. The choice of these sideband frequencies stems from the geometry of the arm cavities. The 2 sidebands have (design) frequencies of 9099471 Hz (f_1) and 45497355 Hz ($f_2 = 5 \times f_1$), which are chosen to be anti-resonant in the arm cavities when the carrier is resonant (i.e. they are reflected by the arm cavities) and to avoid coinciding with any higher order mode resonances in the arms.

As discussed later the design of the control scheme has strict requirements on the condition of the sidebands in different parts of the interferometer. Both sidebands must be resonant in the power recycling cavity when it is locked to the carrier. This puts a strict condition on the PRC length:

$$l_{PRC} = \left(N + \frac{1}{2}\right) \frac{c}{2f_1} \tag{C.1}$$

The factor of $\frac{1}{2}$ is included as the sidebands are 180° out of phase with the carrier, as the carrier enters the arm cavities. A power recycling cavity length of 57.6557 m ($N = 3$) was chosen to be compatible with the opto-mechanical layout for a stable recycling cavity [34].

For control of Advanced LIGO one of the sidebands should exit the Michelson into the signal recycling cavity and eventually the output port. However, in a Michelson where

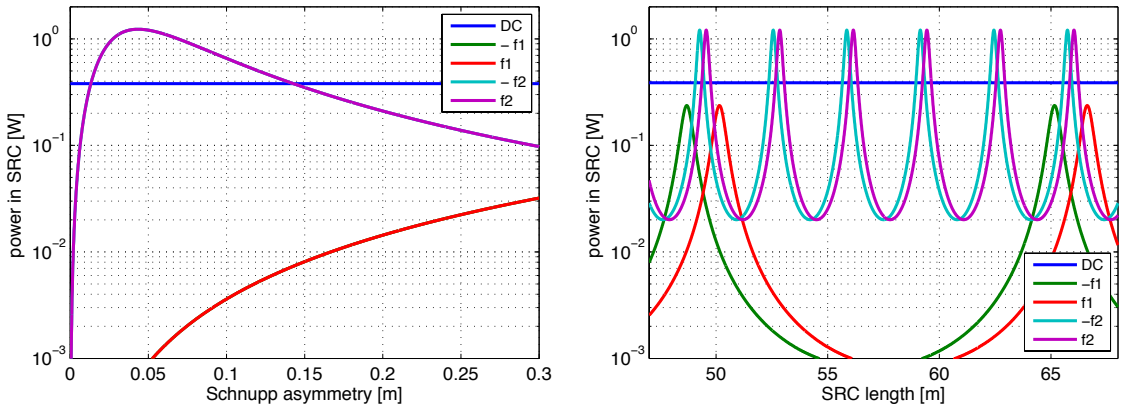

Figure C.3: Power in the signal recycling cavity in the carrier (DC) and upper (f_1, f_2) and lower ($-f_1$, $-f_2$) control sidebands. **Left:** The asymmetry of the short Michelson arms (Schnupp asymmetry) is tuned, with the signal recycling cavity resonant for the f_2 sideband and tuned for broadband operation. **Right:** The length of the signal recycling cavity is tuned, with the SRM tuned for NS-NS operation.

the short arms between the beam-splitter and ITMs (l_x/l_y) are the same length the dark fringe for the carrier will also be the dark fringe for the sidebands. In order for one of the sidebands (f_2) to leak into the signal recycling cavity we need some *Schnupp asymmetry*, $l_{Sch} = l_x - l_y \neq 0$ [33]. Figure C.3 shows the power of the carrier and sidebands in the signal recycling cavity versus Schnupp asymmetry (left plot), recreated from [34]. In this case the signal recycling cavity is resonant for f_2. The Schnupp asymmetry is chosen to maximise the coupling of f_2 into the signal recycling cavity while keeping f_1 small, to ensure a high finesse for f_1 in the PRC. The chosen Schnupp asymmetry is 5 cm, a compromise between the result shown here, for broadband signal recycling, and the result for neutron star – neutron star in-spiral (NS – NS) operation. In the right panel of figure C.3 the length of the signal recycling cavity is tuned, with the signal recycling mirror tuned for NS – NS operation. An SRC length of 56.0084 m is chosen, fulfilling the conditions of resonance for f_2, non-resonance for f_1 and consistent with the layout constraints for a stable, folded signal recycling cavity [34].

C.1.2 Mode-matching

Now we understand the more basic parameters of the design we can move onto the parameters which concern the size and shape of the resonating beam: namely the curvatures of the mirrors and the mode-matching between different cavities. This is a complicated process as the four different cavities (power recycling, signal recycling and two arms) all need to match up well to get maximum power build up and avoid high contrast defects.

The eigenmode of the arm cavities is selected to produce large beams at the ITM (5.3 cm) and ETM (6.2 cm) to reduce thermal noise, with slightly smaller beams at the

ITM as the thermal noise is lower here (fewer coating layers) and to prevent scattering into the recycling cavities. The curvatures are also carefully selected for a specific Gouy phase to avoid higher order modes easily ringing up in the arms: $R_C = 1934\,\mathrm{m}$ (ITM) and $R_C = 2245\,\mathrm{m}$ (ETM).

In initial LIGO the power recycling cavity was marginally unstable, as it shared the eigenmode of the arm cavities but is located in the far field, meaning the spacing between higher order mode resonances was small (11 kHz compared to the 350 kHz linewidth of the cavity) enhancing the power in higher order modes in the control sidebands and causing problems for control [105]. To avoid this in Advanced LIGO the interferometer was designed with stable recycling cavities: folded cavities which do not share the arm cavity eigenmode [27]. These folded cavities expand the beam from the small beams of the input optics (i.e. mode-cleaner) to the larger beams needed for the arms. This requires 3 mirrors for each recycling cavity: the primary mirrors, PRM and SRM, and two additional mirrors which shape and direct the beam, PR2/3 and SR2/3. The greatest change in the beam occurs between PR2/3 (and SR2/3) where the beam size increases by around a factor of 10 over a short distance ($\sim 16\,\mathrm{m}$). Because of this the distance between these two mirrors and the curvature of P/SR3 has a strong effect on the size of the beam entering the arms and the stability of the recycling cavities. Any small changes in these parameters could lead to substantially larger or smaller beams.

The mode matching of the beams between the recycling cavities and arms is complicated by thermal effects, specifically thermal lensing and the change in mirror curvatures. Although this will be corrected by thermal compensation systems [55] it was decided to match the recycling cavities to the arms in the presence of 50 km lenses in the ITMs, as expected for an input power of $\sim$ 12.5 W with coating absorptions of 0.5 ppm [16]. This will potentially mitigate the use of TCS at low power. In the end the cavities were designed for a 50 km lens inside the substrate (effective 34.5 km lens) corresponding to 18 W input power.

C.2 Simulating the right operating point

The design sensitivity of advanced detectors will only be achieved when the interferometers are 'locked': the arm and power recycling cavities are on resonance, and the Michelson is tuned to the dark fringe (with some small offset for DC readout). The operating point of the signal recycling cavity is variable and depends on the mode of operation. For real interferometers with complicated higher order mode effects the maximum in power may not coincide with the resonance of the cavities. We also consider that there may be some discrepancy between the ideal operating point and the point the control systems will lock to. We must include routines representative of the real locking schemes in our simulations and not just use some static operating point determined by the power buildup in the

interferometer.

C.2.1 Degrees of freedom

The operation of Advanced LIGO requires very tight control of the position of the mirrors, to ensure that the interferometer is kept on the operating point. In theory the alignment and microscopic position of all the mirrors needs to be controlled. For longitudinal control this is more easily represented as the control of several degrees of freedom. In figure C.4 a simplified diagram of the Advanced LIGO dual recycled configuration is shown, with the lengths which require control labelled. The microscopic degrees of freedom associated with these lengths are:

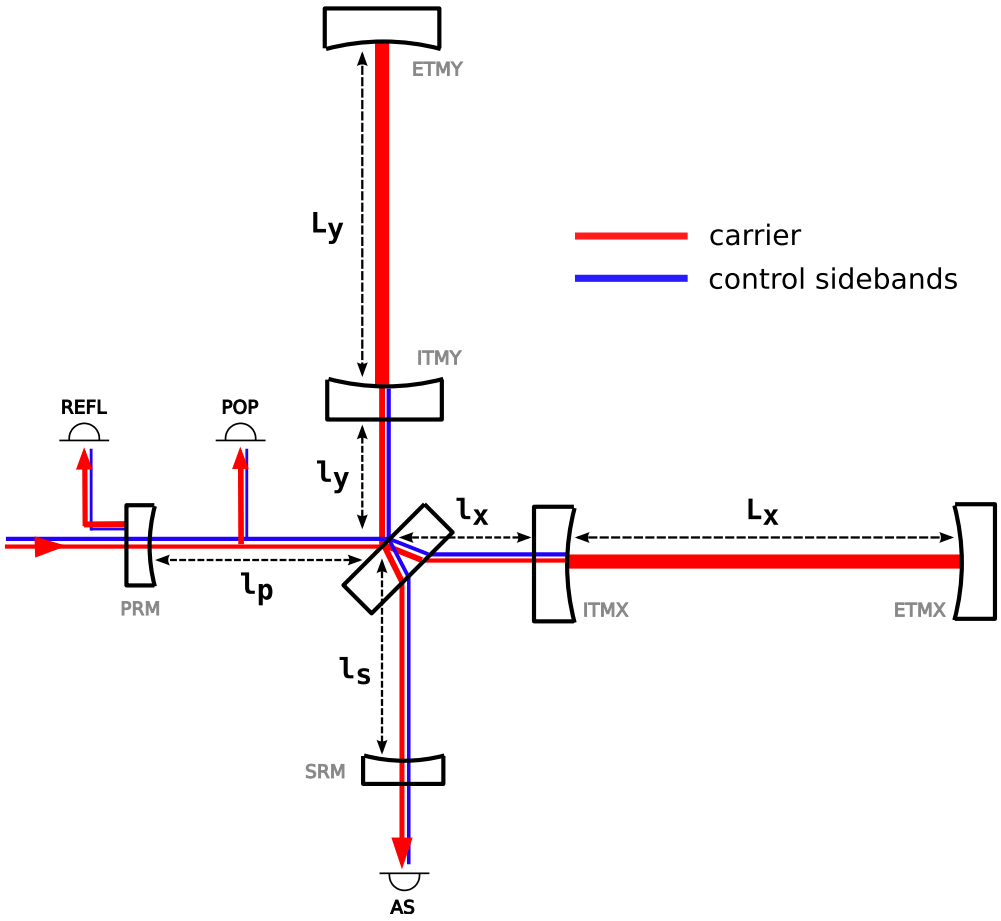

Figure C.4: Diagram of Advanced LIGO lengths and control ports. The 3 detection ports used for control are shown, the reflection port (REFL), the PRC pick-off port (POP) and the anti-symmetric port (AS). The paths of the carrier light and control sidebands are shown, the sidebands only travel in the dual recycled Michelson. The lengths which have to be controlled are highlighted: $l_p + \frac{l_x+l_y}{2}$, $l_s + \frac{l_x+l_y}{2}$, the length of the power and signal recycling cavities; l_y, l_x, the small Michelson lengths between the beam-splitter and ITMs and L_y, L_x the length of the arm cavities.

- **CARM** Common-mode arm motion, CARM $= L_x + L_y$. This tunes the average length of the arm cavities and is used to keep the arms on resonance.
- **PRCL** Power recycling cavity length, PRCL $= L_p + \frac{l_x + ly}{2}$. The power recycling cavity is operated on resonance to maximise the power coupled into the central interferometer.
- **MICH** Michelson arm length, MICH $= l_x - l_y$. MICH controls the short arms of the Michelson (between the ITMs and beam-splitter) and determines the fringe at the output port. Generally the Michelson is operated on the dark fringe.
- **DARM** Differential arm motion, DARM $= Lx - Ly$. This controls the difference in length of the two arm cavities and is used to get the best interference between the two arms at the dark port.
- **SRCL** Signal recycling cavity length, SRCL $= L_s + \frac{l_x + l_y}{2}$. Used to control the operation of the signal recycling cavity. The operating point of SRCL depends on the mode of operation of the interferometer. It can be tuned for a particular frequency of gravitational wave or for broadband operation.

C.2.2 Error signals

To control Advanced LIGO standard error signals are produced to feed back into actuators and control the mirror positions. In interferometry a very effective method for producing such error signals is the Pound-Drever-Hall method [106]. The Advanced LIGO control scheme follows similar principles.

The Pound-Drever-Hall (PDH) method explicitly refers to the control of a single cavity. For this method two sidebands are imprinted on the incoming light, by means of, for example, an EOM (electro-optic modulator) which phase modulates the carrier light at a given frequency (f_{SB}). As long as the modulation is small this is equivalent to the addition of 2 sidebands at $f_0 \pm f_{SB}$, where f_0 is the carrier frequency. Figure C.5 shows an example of the circulating amplitude and reflected phase of the carrier and 9 MHz sidebands in an Advanced LIGO arm cavity. The sidebands chosen for PDH should not be resonant at the same time as the carrier (i.e. $f_{SB} \neq n \times \text{FSR}$) and common sideband frequencies in interferometry are at radio frequencies. The tuning at which the cavity is resonant for each light field corresponds to a sign flip of the reflected phase. When the cavity is not resonant for a particular field it has effectively not entered the cavity and the amplitude and phase response is flat. The phase around resonance looks like a very nice potential error signal, with a distinctive zero crossing. The basis of the Pound-Drever-Hall method is to use the sidebands as a reference field with which to interfere the reflected carrier and produce a signal proportional to the carrier phase. The photodiode signal will contain several

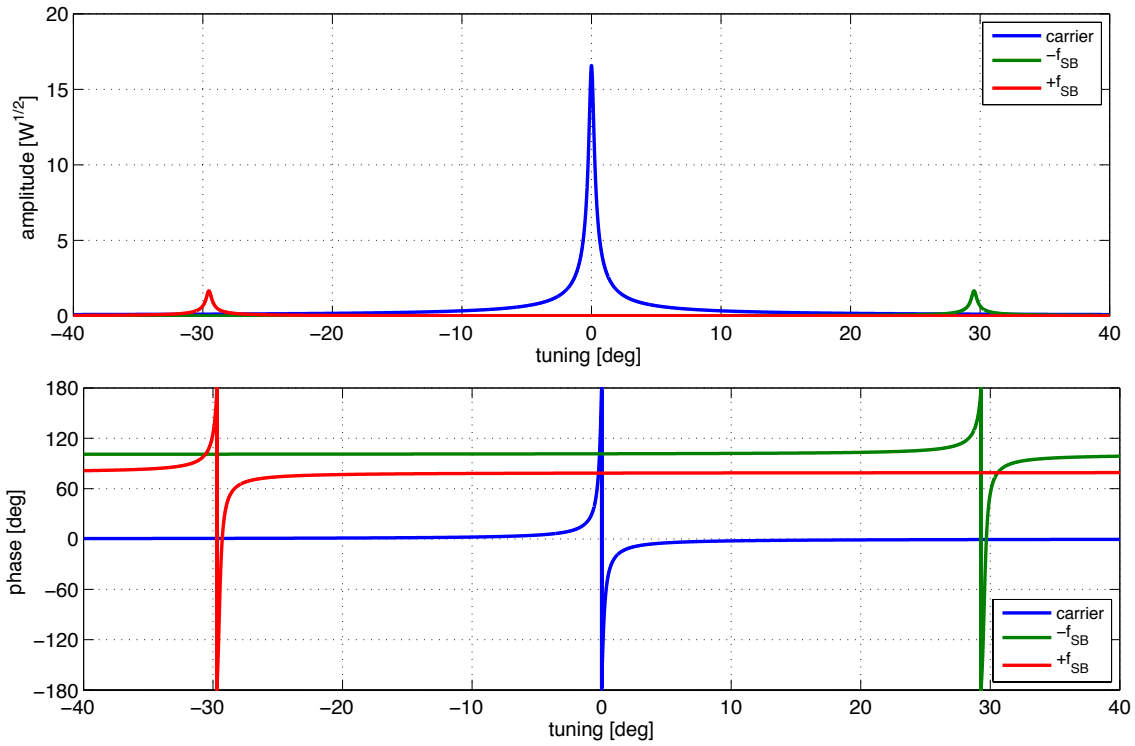

Figure C.5: Circulating amplitude (top) and reflected phase (bottom) of 3 different light fields circulating in an Advanced LIGO arm cavity. The carrier light as well as the upper and lower sidebands from a phase modulator are shown. The sidebands are chosen so they do not enter the cavity with the carrier. The resonance of each field circulating in the cavity corresponds to a sign flip of reflected phase.

frequency components, one at the frequency of the phase modulation f_{SB}. This term is also proportional to the reflected carrier amplitude and reflected sideband amplitude and contains our error signal. This term is isolated by mixing with the same signal used for the phase modulation (i.e. $\sin(2\pi f_{SB} t)$), producing a DC signal proportional to reflected sideband and carrier which is extracted by means of a low pass filter [106].

Figure C.6 shows a plot of a Pound-Drever-Hall error signal, detected in reflection. This shows the classic shape of a PDH signal, with a central zero crossing corresponding to the resonance of the carrier, and two zero crossings either side of this corresponding to the resonance of the sidebands. With such a signal we can lock the cavity to the carrier, or sideband, operating points, or alternatively lock the laser frequency to the cavity. This type of error signal forms the basis of the more complicated control scheme of Advanced LIGO. Although PDH signals are specifically generated in reflection, error signals can be generated in a similar way in transmission. In this case the sidebands need to be chosen so that they are at least partially transmitted with the carrier.

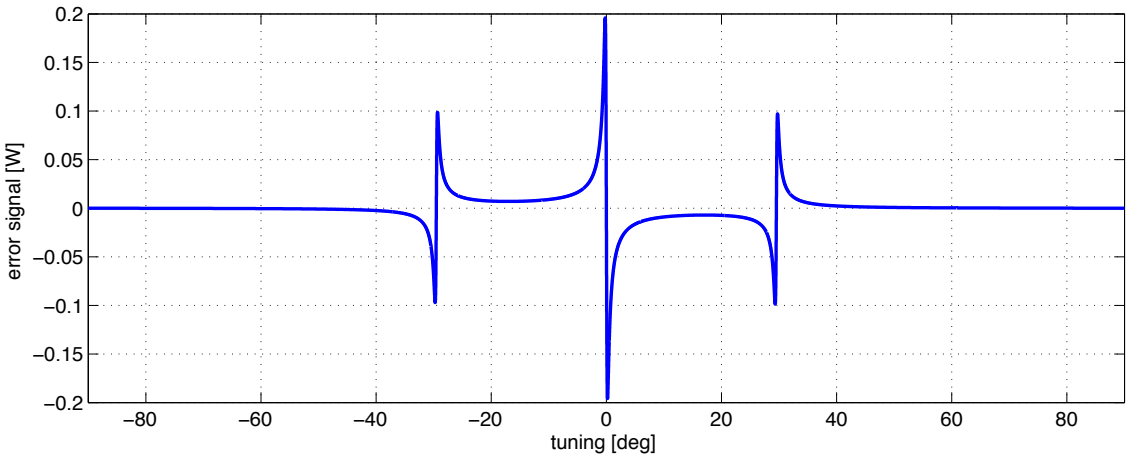

Figure C.6: Example of a standard Pound-Drever-Hall error signal produced in reflection from an Advanced LIGO cavity. The central zero crossing corresponds to the operating point of the carrier, with the two zero crossings either side corresponding to the operating points of the upper and lower sideband.

C.2.3 Advanced LIGO control scheme

The control scheme for Advanced LIGO is detailed in [34]. The final state of Advanced LIGO will be controlled using a combination of error signals from 3 ports: REFL (the reflection port), POP (PRC pick-off port) and AS (the anti-symmetric port), as shown in figure C.4. 2 control sidebands are used, one at 9 MHz, f_1, and one at 45 MHz, f_2, $(5 \times f_1)$. These sideband frequencies are carefully chosen to fulfil certain requirements and to follow a certain path within the interferometer (see figure C.4). Firstly, both sidebands are not resonant inside the locked arm cavities. This allows control of CARM by demodulating the signal in reflection (REFL), similar to a Pound-Drever-Hall error signal. The length of the power recycling cavity is chosen so both sidebands are resonant inside the PRC (see section C.1.1). This enables them to probe different degrees of freedom, not just PRCL. For control the signal recycling cavity at least one of the sidebands should be present in the SRC and close to resonance. The f_2 sideband is chosen for SRCL control, whilst the f_1 sideband is used for control of CARM and PRCL, so should not leak out of the Michelson or be resonant in the SRC (see C.1.1). This will reduce the finesse of the PRC for f_2. The control of SRCL is more complicated than the other degrees of freedom as it does not have a set operating point and needs to be locked in different modes.

The error signals for each degree of freedom are summarised in table C.1 [34]. These signals are chosen as the best possible combination of signals for isolation between the degrees of freedom. The control of SRCL is dependent on the detuning and different error signals will have to be used for different states of operation. In practise the acquisition of the final lock is a more complicated process.

d.o.f.	freq.	port
CARM	f_1	REFL
PRCL	f_1	POP
MICH	f_2	POP
DARM	DC	AS
SRCL (broadband)	f_2	REFL
SRCL (NS-NS)	$f_2 + f_1$ or $f_2 - f_1$	REFL

Table C.1: Summary of the error signals for the Advanced LIGO control scheme (design). The degrees of freedom (d.o.f.) are controlled by error signals taken at the given ports: REFL (reflection), POP (PRC pick-off) and AS (anti-symmetric). The error signals are produced by mixing and demodulating the carrier light with control sidebands $f_1 = \pm 9099471\,\text{Hz}$ and $f_2 = \pm 45497355\,\text{Hz}$, with the exception of DARM which is controlled by the DC light at AS. The control of SRCL depends on the detuning of the signal recycling cavity [34].

C.2.4 Simulating control systems

An important aspect when performing realistic simulations is to use the operating point achieved by the real interferometer control systems. This is an iterative process which requires several steps similar to those required to lock the interferometer experimentally. In complicated interferometers such as Advanced LIGO any offset in one degree of freedom (from the true operating point) will effect the error signals of other degrees of freedom. In cases with large higher order mode effects (such as the large mode-mismatches seen during commissioning in chapter 5) an offset in one degree of freedom can couple into another and lead to multiple zero crossings in the error signals. If we try and lock with such a signal we can easily lock to the wrong point. This is illustrated by the error signals shown in figure C.7. Here the signals for the Livingston Advanced LIGO power recycled configuration are shown (see section 5.5). This includes a substantial mode-mismatch between the two short Michelson arms, which results in significant coupling between the PRCL and MICH degrees of freedom, especially when offset from the operating point. In figure C.7 the error signals are shown over several iterations, as the interferometer is tuned towards the operating point. The starting point for the simulation tunes the arm cavities and power recycling cavity to maximise the power. The Michelson is tuned to minimise the power at the output port. At this initial tuning the error signals for MICH, PRCL and CARM do not have a good shape, exhibiting multiple zero crossings, some non-symmetric behaviour and smaller magnitude error signals. Cross coupling occurs between MICH and PRCL in particular. The simulation was tuned by hand to put the interferometer at the point suggested by these error signals. Of course altering the positioning of one degree of freedom will have an effect on the others, so this requires several iterations before the systems converges to the operating point and the shape of the error signals is as expected.

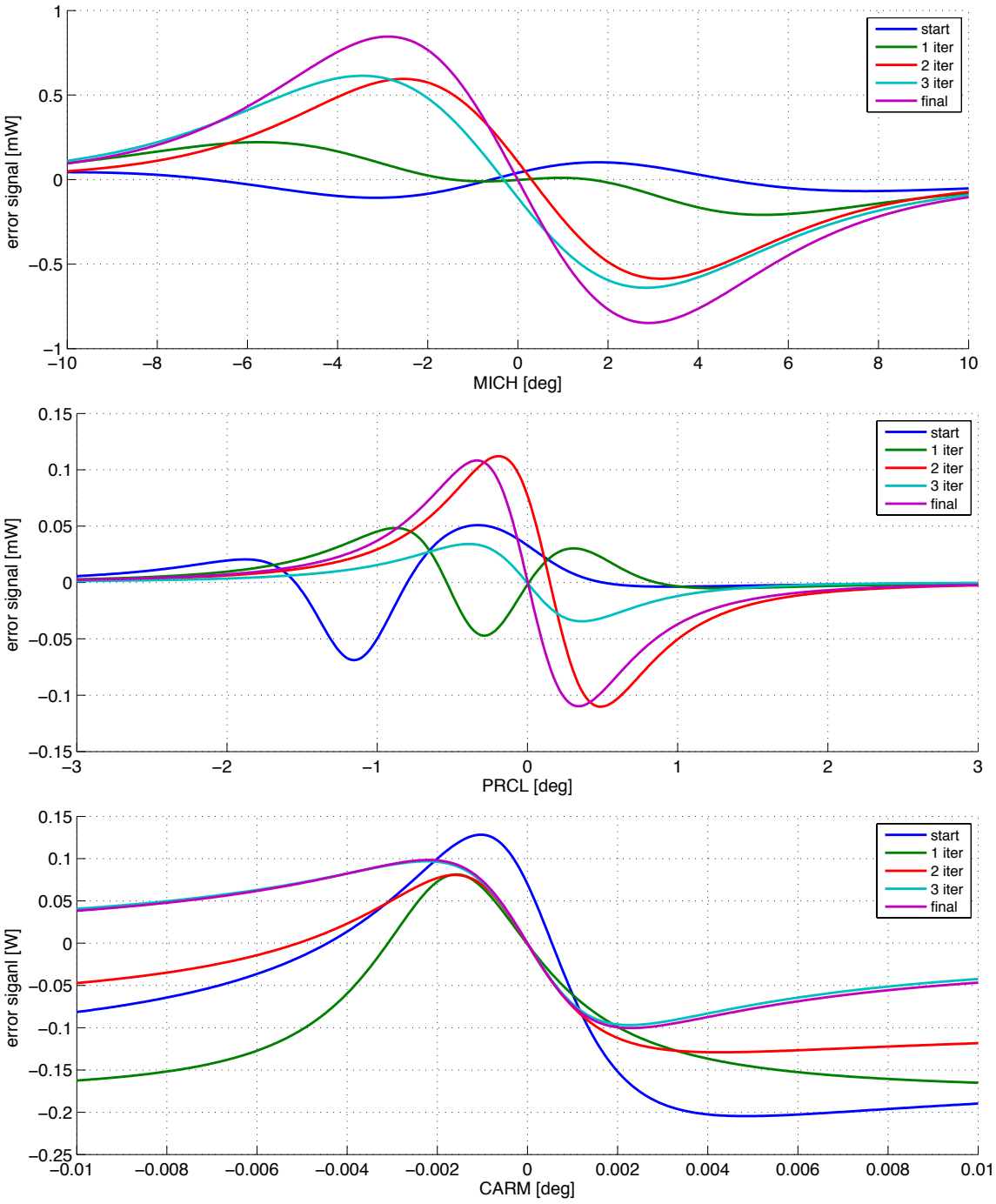

Figure C.7: Simulated error signals for, from top to bottom, MICH, PRCL and CARM for the Livingston power recycled Michelson with Fabry-Perot cavities. The error signals are shown for several iterations as the interferometer is brought closer to the operating point. The starting point is determined by maximising the power in the arm cavities and power recycling cavity, whilst tuning the Michelson to minimise the power at the output port. The error signals for each degree of freedom are then used to iterate towards the operating point, where the error signals are well behaved.

This is a good illustration of potential problems when locking the interferometer. Care should always be taken with such complicated setups and for accurate simulation results the appropriate error signals should be used.

C.2.5 Tests against Optikle

Before taking the lead on particular commissioning tasks it was necessary to test our Advanced LIGO files against results achieved using other simulations, in this case Optikle [107]. These tests took the form of comparisons of the behaviour of the control sidebands in the power and dual recycled Michelson interferometer, without Fabry-Perot cavities as detailed in [108]. This involves not only the 9 MHz and 45 MHz sidebands used for control but the sidebands at double the demodulation frequencies ($2f$).

The results of this study matched the Optikle results, in both behaviour and numbers. The results are summarised in [109]. We can now move onto specific commissioning tasks confident that we are simulating the interferometer correctly.

Power recycled Michelson

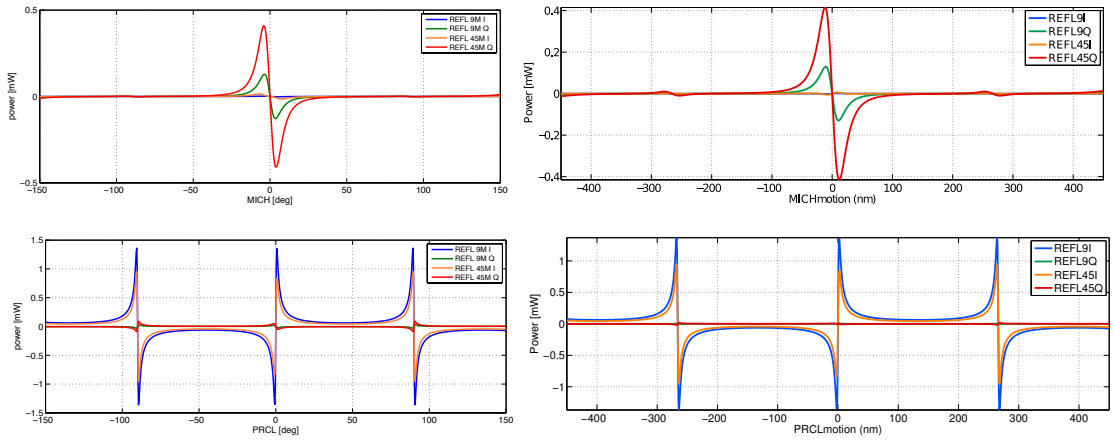

Figure C.8: MICH (top) and PRCL (bottom) error signals for FINESSE (left) and Optickle (right).

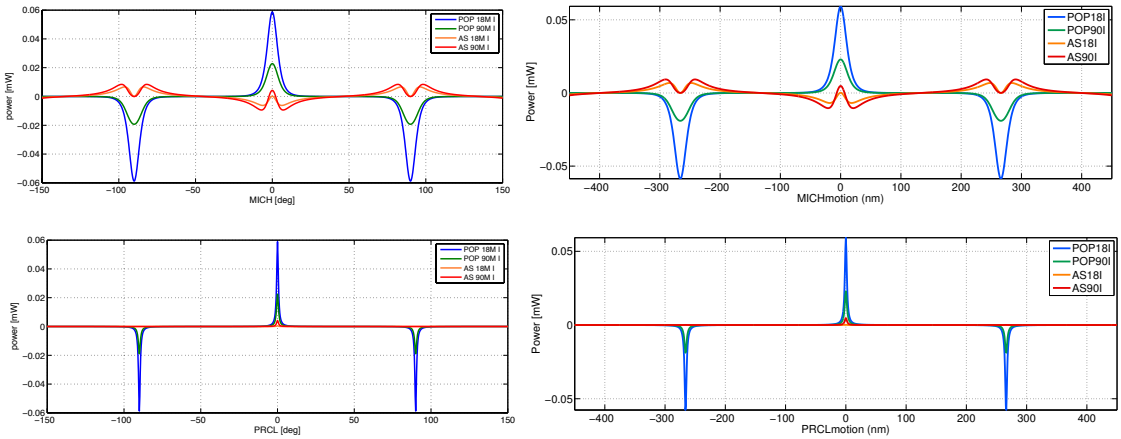

Figure C.9: MICH (top) and PRCL (bottom) 2f signals for FINESSE (left) and Optickle (right).

Dual recycled Michelson

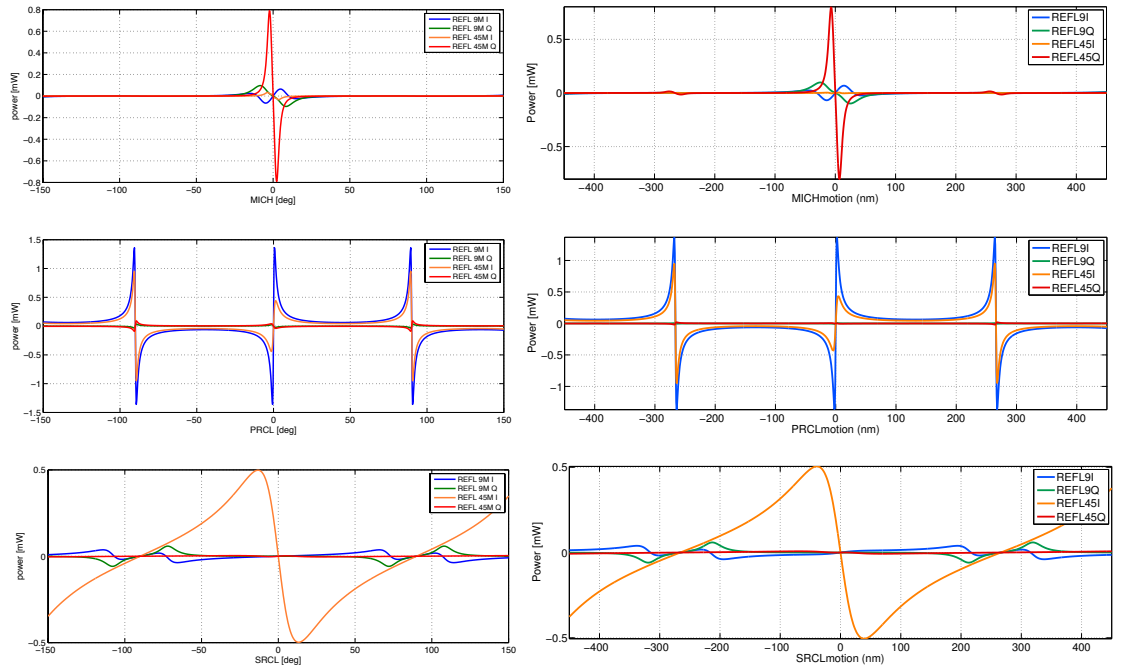

Figure C.10: MICH (top) and PRCL (centre) and SRCL (bottom) error signals for FINESSE (left) and Optickle (right).

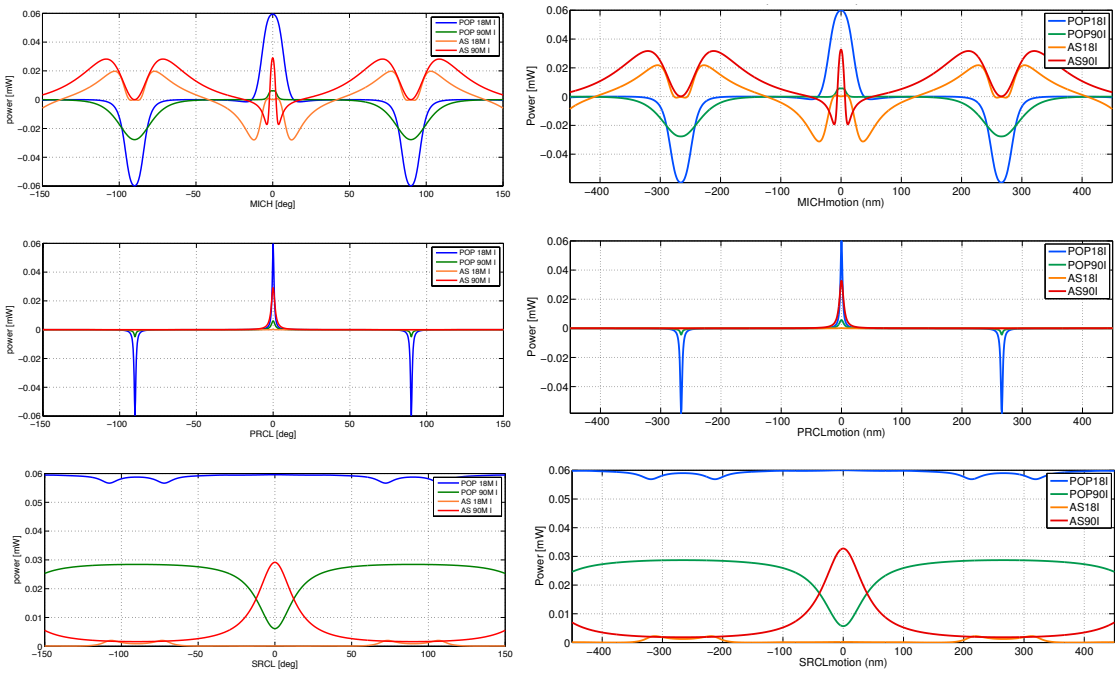

Figure C.11: MICH (top) and PRCL (centre) and SRCL (bottom) 2f signals for FINESSE (left) and Optickle (right).

References

[1] A. Einstein. Die Grundlagen der Allgemeinene Relativitätstheorie. (German) [The foundations of the Theory of General Relativity]. 354(7), 1916. 1

[2] B. S. Sathyaprakash and B. F. Schutz. Physics, astrophysics and cosmology with gravitational waves. *Living Reviews in Relativity*, 12(2), 2009. 1, 2, 4

[3] G. Hammond, S. Hild, and M. Pitkin. Advanced technologies for future laser-interferometric gravitational wave detectors. *ArXiv e-prints*, February 2014. 1, 4, 16

[4] R. A. Hulse and J. H. Taylor. Discovery of a pulsar in a binary system. *Astrophysical Journal*, 195:L51–L53, January 1975. 2, 3, 4

[5] J. M. Weisberg and J. H. Taylor. The relativistic binary pulsar b1913+16: Thirty years of observations and analysis. *Binary Radio Pulsars*, *ASP Conference Series*, 328(25), 2005. 2, 3

[6] B. C. Barish and R. Weiss. LIGO and the detection of gravitational waves. *Physics Today*, 52:44–50, 1999. 4

[7] D. Sigg and the LIGO Scientific Collaboration. Status of the LIGO detectors. *Classical and Quantum Gravity*, 25(11):114041, 2008. 4, 5, 6

[8] T Accadia, et al. Status of the Virgo project. *Classical and Quantum Gravity*, 28(11):114002, 2011. 4

[9] H. Grote and the LIGO Scientific Collaboration. The status of GEO600. *Classical and Quantum Gravity*, 25(11):114043, 2008. 4

[10] K. Somiya and the KAGRA Collaboration. Detector configuration of KAGRA - the Japanese cryogenic gravitational-wave detector. *ArXiv e-prints*, 2011. 4, 67

[11] C. S. Unnikrishnan. IndIGO and Ligo-India Scope and Plans for Gravitational Wave Research and Precision Metrology in India. *International Journal of Modern Physics D*, 22:41010, 2013. 4

[12] S. Fairhurst. Triangulation of gravitational wave sources with a network of detectors. *New Journal of Physics*, 11(12):123006, 2009. 5

[13] S. E. Whitcomb. Ground-based gravitational-wave detection: now and future. *Classical and Quantum Gravity*, 25(11):114013, 2008. 6

[14] R. Adhikari, P. Fritschel, and S. J. Waldman. Enhanced LIGO. LIGO Document T060156, 2006. 6

[15] G. M. Harry and the LIGO Scientific Collaboration. Advanced LIGO: the next generation of gravitational wave detectors. *Classical and Quantum Gravity*, 27(8):084006, 2010. 6, 12, 15

[16] M. A. Arain and G. Mueller. Optical layout and parameters for the Advanced LIGO cavities. LIGO Document T0900043, 2009. 7, 15, 37, 38, 46, 49, 155, 169, 218, 222

[17] A. Freise and K. Strain. Interferometer Techniques for Gravitational-Wave Detection. *Living Reviews in Relativity*, 13, February 2010. 8, 10, 11, 21, 27, 29, 31, 33, 34, 71, 76, 89, 211

[18] J. Mizuno. *Comparison of optical configurations for laser-interferoemtric gravitational-wave detectors*. PhD thesis, Universität Hannover, 1995. 10, 197

[19] http://www.gwastro.org/forscientists/gravitational-wave-interferometer-noise-calculator 12, 66

[20] S M Aston. Update on quadruple suspension design for Advanced LIGO. *Classical and Quantum Gravity*, 29(23):235004, 2012. 13

[21] N.A. Robertson et al. Quadruple suspension design for Advanced LIGO. *Classical and Quantum Gravity*, 19(15):4043 –4058, 2002. 13

[22] M Punturo. The einstein telescope: a third-generation gravitational wave observatory. *Classical and Quantum Gravity*, 27(19):194002, 2010. 13

[23] V. B. Braginsky, V. P. Mitrofanov, and K. V. Tokmakov. On the thermal noise from the violin modes of the mass suspension in gravitational wave antennae. *Phys. Letters A*, 186:18–20, 1993. 13

[24] G. Gonzalez. Suspensions thermal noise in the LIGO gravitational wave detector. *Classical and Quantum Gravity*, 17:4409–4435, 2000. 13

[25] G. M. Harry et al. Thermal noise from optical coatings in gravitational wave detectors. *Appl. Opt.*, 45(7):1569–1574, 2006. 14

[26] G. Harry, T. P. Bodiya, and R. DeSalvo. *Optical Coatings and Thermal Noise in Precision Measurement*. Cambridge University Press, 2012. 14

[27] M.A. Arain and G. Mueller. Design of the Advanced LIGO recycling cavities. *Optics Express*, Vol. 16, Issue 14:10018–10032, 2008. 15, 169, 218, 222

[28] B. J. Meers. Recycling in laser-interferometric gravitational-wave detectors. *Phys. Rev. D*, 38:2317–2326, 1988. 16

[29] M. Pitkin, S. Reid, S. Rowan, and J. Hough. Gravitational wave detection by interferometry (ground and space). *Living Reviews in Relativity*, 14(5), 2011. 16, 17

[30] S. Goßler et al. Mode-cleaning and injection optics of the gravitational-wave detector GEO600. *Review of Scientific Instruments*, 74:3787–3795, 2003. 16

[31] M. A. Arain, G. Mueller, R. Martin, V. Quetschke, D. H. Reitze, D. B. Tanner, and L. Williams. Input optics subsystem design requirements document. LIGO Document T020020, 2009. 16, 74, 158

[32] K. Arai, S. Barnum, P. Fritschel, J. Lewis, and S. Waldman. Output mode cleaner design. LIGO Document T1000276, 2013. 17

[33] S. Hild et al. DC-readout of a signal-recycled gravitational wave detector. *Classical and Quantum Gravity*, 26(5):055012, 2009. 17, 219, 221

[34] R. Abbott. Advanced LIGO length sensing and control final design. LIGO Document T1000298, 2010. 17, 218, 219, 220, 221, 226, 227

[35] A. Freise, K. Strain, C. Bond, and D. Brown. Interferometer techniques for gravitational-wave detection. *Living Reviews in Relativity*, in preparation, 2014 19, 20

[36] C. Bond, P. Fulda, L. Carbone, K. Kokeyama, and A. Freise. Higher order Laguerre-Gauss mode degeneracy in realistic, high finesse cavities. *Phys. Rev. D*, 84:102002, 2011. 19, 66, 73, 115, 130, 189

[37] R. A. Day, G. Vajente, M. Kasprzack, and J. Marque. Reduction of higher order mode generation in large scale gravitational wave interferometers by central heating residual aberration correction. *Phys. Rev. D*, 87:082003, 2013. 19, 115

[38] G. Vajente and R. A. Day. Adaptive optics sensing and control technique to optimize the resonance of the Laguerre-Gauss 33 mode in Fabry-Perot cavities. *Phys. Rev. D*, 87:122005, 2013. 19, 115

[39] A. Freise, G. Heinzel, H. Lück, R. Schilling, B. Willke, and K. Danzmann. Frequency-domain interferometer simulation with higher-order spatial modes. *Classical and Quantum Gravity*, 21(5):S1067–S1074, 2004. 19, 32, 122, 124, 195

[40] C. Bond, P. Fulda, D. Brown, and A. Freise. Investigation of beam clipping in the power recycling cavity of Advanced LIGO using Finesse. LIGO Document T1300954, 2013. 19, 153, 154, 155

[41] C. Bond, P. Fulda, D. Brown, and A. Freise. Simulation investigation of beam clipping and power recycling gain in Livingston PRMI. LIGO Document G1400222, 2014. Presentation at the March 2014 LVC conference. 19, 153, 154

[42] C. Bond. Simulations of contrast defect in LLO PRMI. LIGO Document G1400465, 2014. 19

[43] C. Bond, P. Fulda, D. Brown, and A. Freise. Simulations of effects of LLO mode-mismatches on PRFPMI error signals. LIGO Document T1400182, 2014. Slides for simulation meeting 28/02/2014. 19, 153, 179, 184

[44] C. Bond, D. Brown, L. Carbone, and A. Freise. Higher order modes in aLIGO cavities. LIGO Document G1400464, 2013. 19, 153, 187

[45] C. Bond, D. Brown, and A. Freise. Mode healing in GW interferometers. LIGO Document G1300711, 2013. Presented at the Amaldi conference in July 2013. 21, 43, 61

[46] A. E. Siegman. *Lasers*. University Science Books, 1986. See also: Errata List for LASERS, `http://www.stanford.edu/~siegman/lasers_book_errata.pdf`. 22, 23, 25, 76, 123

[47] H. Kogelnik and T. Li. Laser beams and resonators. *Appl. Opt.*, 5(10):1550–1567, 1966. 27, 76

[48] M. W. Beijersbergen, L. Allen, H. E. L. O. van der Veen, and J. P. Woerdman. Astigmatic laser mode converters and transfer of orbital angular momentum. *Optics Communications*, 96:123–132, 1993. 30, 211, 212

[49] A. Freise, D. Brown, and C. Bond. Finesse, Frequency domain INterferomEter Simulation SoftwarE. *ArXiv e-prints*, 2013. 32, 63, 116, 122, 124, 131, 138, 190, 195

[50] P. Hello and J. Y. Vinet. Analytical models of transient thermoelastic deformations of mirrors heated by high power cw laser beams. *J. Phys. France*, 51(20):2243–2261, 1990. 44

[51] P. Hello and J. Y. Vinet. Analytical models of thermal aberrations in massive mirrors heated by high power laser beams. *J. Phys. France*, 51(12):1267–1282, 1990. 44, 131

[52] J. Y. Vinet and the Virgo Collaboration. *The Virgo Book of Physics: Optics and Related Topics*. Virgo, 2001. 44

[53] J. Y. Vinet. On special optical modes and thermal issues in advanced gravitational wave interferometric detectors. *Living Reviews in Relativity*, 12(5), 2009. 44, 45, 46, 68, 70, 133

[54] J. Degallaix. *Compensation of strong thermal lensing in advanced interferometric gravitational wave detectors*. PhD thesis, The University of Western Australia, 2006. 46, 49

[55] P. Willems, A. Brooks, M. Smith, and K. Mailand. Advanced LIGO thermal compensation system preliminary design. LIGO Docuemnt T0900304, 2009. 49, 222

[56] M. A. Arain, G. Ciani, M. Jacobson, G. Mueller, S. O'Connor, and P. Willems. Final design and installation plans for the aLIGO TCS ring heaters. LIGO Document G1100222, 2011. 49

[57] A. Brooks, A. Cole, A. Heptonstall, M. Jacobson, A. Lynch, S. O'Connor, Z. Shao, and C. Vorvick. Thermal compensation systems (TCS): Co2 laser projection system (CO2P): Final design document. LIGO Document T1100570, 2012. 49, 172

[58] H Yamamoto. Core optics related loss hierarchy of aLIGO - LVC2014. LIGO Document G1400198, 2014. 52, 57, 174, 178

[59] S Hild. Experience with signal-recycling in GEO600. 2006. GWADW, Elba, 2006. 60

[60] C. Bond, P. Fulda, L. Carbone, K. Kokeyama, and A. Freise. The effect of mirror surface distortions on higher order Laguerre-Gauss modes. *Journal of Physics: Conference Series*, 363:012005, 2012. 66, 73, 115, 189

[61] B. Mours, E. Tournefier, and J.-Y. Vinet. Thermal noise reduction in interferometric gravitational wave antennas: using high order TEM modes. *Classical and Quantum Gravity*, 23:5777–5784, 2006. 67

[62] J.-Y. Vinet. Mirror thermal noise in flat-beam cavities for advanced gravitational wave interferometers. *Classical and Quantum Gravity*, 22:1395–1404, 2005. 67

[63] M Lorenzin et al. Silicate bonding properties: investigation through thermal conductivity measurements. *Journal of Physics: Conference Series*, 228:012019, 2010. 67

[64] LSC Advanced Detector Committee for the LSC. LSC instrument science white paper. LIGO Document T1000416, 2010. 69

[65] S. Chelkowski, S. Hild, and A. Freise. Prospects of higher-order Laguerre-Gauss modes in future gravitational wave detectors. *Phys. Rev. D*, 79(12):122002, 2009. 70, 72

[66] P. Fulda, K. Kokeyama, S. Chelkowski, and A. Freise. Experimental demonstration of higher-order Laguerre-Gauss mode interferometry. *Phys. Rev. D*, 82(1):012002, 2010. 72, 77

[67] M. Granata, C. Buy, R. Ward, and M. Barsuglia. Higher-order Laguerre-Gauss mode generation and interferometry for gravitational wave detectors. *Phys. Rev. Lett.*, 105(23):231102, 2010. 72

[68] G. A. Turnbull, D. A. Robertson, G. M. Smith, L. Allen, and M. J. Padgett. The generation of free-space Laguerre-Gaussian modes at millimetre-wave frequencies by use of a spiral phaseplate. *Optics Communications*, 127:183–188, 1996. 72

[69] J. Arlt, K. Dholakia, L. Allen, and M. J. Padgett. The production of multiringed Laguerre-Gaussian modes by computer-generated holograms. *Journal of Modern Optics*, 45:1231–1237, 1998. 72

[70] M. Galimberti and R. Flaminio. Mirror requirements for 3rd generation GW detectors. Technical report, 2010. Talk at GWADW 2010. 73

[71] J. Miller. New beam shape with low thermal noise. Technical report, 2011. Talk at GWADW, Elba, 2011. 73

[72] B. Sorazu et al. Experimental test of higher-order laguerregauss modes in the 10 m glasgow prototype interferometer. *Classical and Quantum Gravity*, 30(3):035004, 2013. 77, 78, 115

[73] J. Degallaix, M. Galimberti, and R. Flaminio. Maximum astigmatism for ET arm cavity mirrors, Internal document, 2011. 79

[74] G. Billingsley. LIGO core optics reference page. `https://galaxy.ligo.caltech.edu/optics/`. 82, 83, 97, 128, 159, 170, 175, 185

[75] I. S. Gradshteyn and I. M. Ryzhik. *Tables of integrals, series, and products*. Academic Press, 1994. 5th Edition. 86, 91, 99, 102

[76] W. Winkler, R. Schilling, J. Mizuno, A. Rüdiger, K. Danzmann, and K. A. Strain. Light scattering described in the mode picture. *Appl. Opt.*, 33:7547–7550, 1994. 89, 93

[77] T. Hong, J. Miller, H. Yamamoto, Y. Chen, and R. Adhikari. Effects of mirror aberrations on Laguerre-Gaussian beams in interferometric gravitational-wave detectors. *Phys. Rev. D*, 84:102001, 2011. 96, 115

[78] G. Billingsley, G. Harry, and W. Kells. Core optics components design requirements. LIGO Document T000127, 2010. 106, 186, 187, 218

[79] L. Carbone, C. Bogan, P. Fulda, A. Freise, and B. Willke. Generation of high-purity higher-order Laguerre-Gauss beams at high laser power. *Phys. Rev. Letters*, 110:251101, 2013. 115

[80] F. Bayer-Helms. Coupling coefficients of an incident wave and the modes of spherical optical resonator in the case of mismatching and misalignment. *Appl. Opt.*, 23:1369–1380, 1984. 116, 124

[81] M. Wang, C. Bond, D. Brown, F. Brückner, L. Carbone, R. Palmer, and A. Freise. Realistic polarizing Sagnac topology with dc readout for the Einstein Telescope. *Phys. Rev. D*, 87:096008, 2013. 117, 150

[82] C. Bond, D. Brown, and A. Freise. Interferometer responses to gravitational waves: Comparing Finesse simulations and analytical solutions. *ArXiv e-prints*, 2013. 119, 195

[83] C. Bond, D. Brown, and A. Freise. Interferometer responses to gravitational waves: Comparing Finesse simulations and analytical solutions. LIGO Document T1300190, 2013. 119

[84] J. Y. Vinet, P. Hello, C. N. Man, and A. Brillet. A high accuracy method for the simulation of non-ideal optical cavities. *Journal de Physique I*, 2:1287–1303, 1992. 123, 124

[85] J. Degallaix. Oscar: a Matlab based FFT code. Matlab Central File Exchange, 2008. 123, 136

[86] J. Y. Mikael Laval, J. Y. Vinet. *DarkF User Guid.* Artemis Department, Oberservatory of the 'Cote d'Azur', Nice, France, 2006. 123

[87] H Yamamoto. SIS (stationary interferometer simulation) manual. LIGO Document T070039, 2013. 123, 186

[88] H Yamamoto. Mode matching and diffraction loss of FP cavity with thermal deformations. LIGO Document T0900306, 2010. 131, 135

[89] A. Freise and C. Bond. Simtools. `http://www.gwoptics.org/simtools/`. 132, 140

[90] S. K. Hwang and W. Y. Kim. A novel approach to the fast computation of Zernike moments. *Pattern Recognition*, 39(11):2065 – 2076, 2006. 147

[91] K. Arai, C. Bond, D. Brown, L. Carbone, S. Doravari, A. Freise, P. Fulda, and K. Kokeyama. Finesse simulation for the alignment control signal of the aLIGO input mode cleaner. LIGO Document T1300074, 2013. 152, 154

[92] C. Mueller and D. Martynov. LLO alog 9733, 15/11/2013. https://alog.ligo-la.caltech.edu/aLOG/index.php?callRep=9733, 2013. 152, 153, 156, 157, 174, 175, 188

[93] D. Martynov. LLO alog 11140, 27/04/14. https://alog.ligo-la.caltech.edu/aLOG/index.php?callRep=11140, 2014. 153, 172, 173, 174, 175, 176, 177

[94] H Yamamoto. Example and experience using SIS for aLIGO designing and commissioning. LIGO Document G1300054, 2013. 153, 184, 185, 187

[95] A. Freise, C. Bond, P. Fulda, D. Brown, L. Carbone, and K. Kokeyama. Finesse input files for Advanced LIGO. LIGO Document L1300231, 2013. 154, 158

[96] L Carbone et al. Examples and experience from using finesse in the early aLIGO commissioning. LIGO Document G1300058, 2013. Presented at the Livingston commissioning workshop, January 2013. 154

[97] C. Mueller, L. Barsotti, P. Fritschel, and H. Yamamoto. Mode matching investigation at LLO. LIGO Document G1300909, 2013. 155

[98] G. Billingsley. ITM04 input test mass final polishing data package. LIGO Document C1000472, 2010. 155

[99] L. Williams. ALIGO IO L1 master coordinate list. LIGO Document E1200274, 2012. 159

[100] H. Yamamoto. Advanced LIGO baffle design using SIS. LIGO document T1000090, 2012. 170

[101] C. Mueller. LLO alog 10762, 06/02/2014. https://alog.ligo-la.caltech.edu/aLOG/index.php?callRep=10762. 171

[102] C. Mueller, L. Barsotti, and P. Fulda. aLIGO mode matching situation. LIGO Document G1400107, 2014. 171

[103] W Korth. LLO alog 8629, 07/09/13. https://alog.ligo-la.caltech.edu/aLOG/index.php?callRep=8629. 174, 175, 178

[104] P. Fritschel, R. Adhikari, S. Ballmer, and M. Evans. Arm cavity finesse for Advanced LIGO. LIGO Document T070303, 2007. 218, 219

[105] A. M. Gretarsson, E. D'Ambrosio, V. Frolov, B. O'Reilly, and P. K. Fritschel. Effects of mode degeneracy in the LIGO Livingston Observatory recycling cavity. *Journal of the Optical Society of America B Optical Physics*, 24:2821, 2007. 222

[106] E. Black. Notes on the Pound-Drever-Hall techniques. LIGO Document T980045, 1998. 224, 225

[107] R. L. Ward. Optickle webpage. http://www.ligo.caltech.edu/~rward/Optickle/. 229

[108] A. Effler. alog 8102. https://alog.ligo-la.caltech.edu/aLOG/index.php?callRep=8102, 2013. 229

[109] C. Bond, P. Fulda, D. Brown, and A. Freise. Comparing Finesse and optickle simulations of the Advanced LIGO dual-recycled Michelson. LIGO Document T1400270, 2013. 229